Czech Technical University in Prague

F3

Faculty of Electrical Engineering
Department of Measurement

Master Thesis

Measurement of radiation shielding from carbon composites for protection of electronics in Low Earth Orbit

Bc. Dominika Labudová

Aerospace Engineering

January 2023
Supervisor: Ing. Ladislav Sieger, CSc.
Supervisor–specialist: Doc. Ing. Carlos Granja, PhD.

ZADÁNÍ DIPLOMOVÉ PRÁCE

I. OSOBNÍ A STUDIJNÍ ÚDAJE

Příjmení: **Labudová** Jméno: **Dominika** Osobní číslo: **498879**

Fakulta/ústav: **Fakulta elektrotechnická**

Zadávající katedra/ústav: **Katedra fyziky**

Studijní program: **Letectví a kosmonautika**

Studijní obor: **Avionika**

II. ÚDAJE K DIPLOMOVÉ PRÁCI

Název diplomové práce:

Měření radiačního stínění z uhlíkových kompozitů pro ochranu elektroniky na nízké oběžné dráze Země

Název diplomové práce anglicky:

Measurement of radiation shielding from carbon composites for protection of electronics in Low Earth Orbit

Pokyny pro vypracování:

1) Proveďte rešerši stínících vlastností materiálů pro různé druhy kosmického záření na LEO
2) Proveďte rešerši radiační odolnosti polovodičových struktur (OPA, FET, lineární prvky-tranzistory do zdrojů, CPU, RAM, FRAM ...)
3) Popište vlastnosti stínících uhlíkových kompozitů
4) Prověďte měření vlastností testovaných uhlíkových kompozitů pro různé typy záření s využitím senzorů typu SXD, Timepix ...
5) Zpracujte naměřená data a interpretujte výsledky. Navrhněte vhodnou kombinaci materiálů pro požadované radiační zatížení elektroniky s ohledem na parametry dráhy družice a délku mise.

Seznam doporučené literatury:

1) Dereniak, E.; Growe, D. Optical Radiation Detectors; John Wiley & Sons, 1984.
2) VITUS Silicon Drift Detectors, 2021.
https://www.ketek.net/wp-content/uploads/2017/10/KETEK_Manual_VITUS_SDD_REV6_201
7-10.pd
3) Brezina, C.; Gaspari, Y.; et al. The Timepix3 chip, 2021.
https://indico.cern.ch/event/267425/attachments/477859/661149/Timepix3_final.pdf
4) Granja, C.; Oancea, C.; Jakubek, J.; et al. Wide-range tracking and LET-spectra of energetic light and heavy charged particles. Nuclear Instruments and Methods in Physics Research Section A: Accelerators, Spectrometers, Detectors and Associated Equipment 2021, 988 (1), DOI: https://doi.org/10.1016/j.nima.2020.164901.

Jméno a pracoviště vedoucí(ho) diplomové práce:

Ing. Ladislav Sieger, CSc., katedra fyziky FEL

Jméno a pracoviště druhé(ho) vedoucí(ho) nebo konzultanta(ky) diplomové práce:

Datum zadání diplomové práce: **12.07.2021** Termín odevzdání diplomové práce: _____

Platnost zadání diplomové práce:
do konce zimního semestru 2022/2023

Ing. Ladislav Sieger, CSc.	prof. Ing. Ondřej Jiříček, CSc.	prof. Mgr. Petr Páta, Ph.D.
podpis vedoucí(ho) práce	podpis vedoucí(ho) ústavu/katedry	podpis děkana(ky)

III. PŘEVZETÍ ZADÁNÍ

Diplomantka bere na vědomí, že je povinna vypracovat diplomovou práci samostatně, bez cizí pomoci, s výjimkou poskytnutých konzultací. Seznam použité literatury, jiných pramenů a jmen konzultantů je třeba uvést v diplomové práci.

. _____
Datum převzetí zadání

_____
Podpis studentky

Acknowledgements

I thank my supervisor Ing. Ladislav Sieger, CSc. for his time, experience and numerous advice, and for providing the computational resources needed to complete this thesis. I thank Doc. Ing. Carlos Granja, PhD. for the suggestion of the topic, the material, data and experiments performed together. Also the knowledge, experience and guidance throughout the process of the preparation of the samples, the realization of the experiments and data acquisition, the operation of the pixel detectors, the extensive and complex data processing and evaluation of results, and guidance and advice in creating this thesis. I thank the work and help by the colleagues at the accelerators and at the X-ray sources including X-ray scanner. The teams of 5M, VZLU and Rigaku manufactured and provided the composite samples studied. Last, I thank my family, friends and colleagues for their understanding and support.

Declaration

I declare that I have written the submitted master's thesis independently, under the guidance of the master's thesis supervisor and specialist supervisor, and that I have listed all the information sources used in accordance with the Methodical Instruction on the observance of ethical principles in the preparation of university studies final theses.

In Prague, 10. January 2023

.....

Abstract

Spacecraft in Low Earth Orbit (LEO) are continuously exposed to the harsh, complex and highly dynamic near Earth space radiation environment. Satellite components, in particular those using standard and COTS electronics are especially susceptible to the large fluences and resulting large doses and radiation effects of the space environment. To mitigate part of the radiation damage effects on electronics, space industry uses materials for radiation shielding. In this work, a novel high-resolution experimental technique to measure, examine and evaluate the radiation shielding properties of materials is developed and applied on novel composite materials produced and provided by material research teams in Czech Republic. Dedicated scientific experiments using a microtron electron accelerator, a robotic X-ray scanner and an X-ray micro imaging setup were conducted as part of this thesis. Additionally, data from a cyclotron proton accelerator were also analyzed. Alltogether, an extensive amount of data was processed given by the large number of samples examined (41 samples in total) and several radiation environments and setups studied. The data was processed in high detail using several algorithms and software scripts. The output of data processing is provided in the form of physical products (flux, dose rate, composition). These results are evaluated and produced as both graphic plots and table format with values normalized for the material's planar density. The studied samples are also compared with conventional nuclear materials standardly used for radiation shielding (e.g. Al, Cu, Ta, Pb). Given the radiation environment in LEO, the best shielding properties belong to specific carbon composites.

Keywords: LEO, radiation environment, radiation effects, radiation shielding, carbon composites, pixel detectors

Supervisor: Ing. Ladislav Sieger, CSc.
Department of Physics FEE CTU

Abstrakt

Kozmické lode na nízkej obežnej dráhe Zeme sú nepretržite vystavené neľútostnému, zložitému a vysoko dynamickému prostrediu vesmírneho žiarenia blízko Zeme. Satelitné komponenty a najmä štandardná elektronika netolerantná voči radiačnému žiareniu sú obzvlášť citlivé na veľké fluktuácie a výsledné veľké dávky a radiačné účinky vesmírneho prostredia. Na zmiernenie niektorých účinkov radiačného škodenia na elektroniku používa vesmírny priemysel materiály na tienenie žiarenia. V tejto práci je vyvinutá experimentálna technika na meranie, skúmanie a vyhodnocovanie vlastností tienenia materiálov voči žiareniu a aplikovaná na nové kompozitné materiály vyrábané a poskytované tímami materiálového výskumu v Českej republike. V rámci tejto práce sa uskutočnili špecializované vedecké experimenty s mikrotrónovým elektrónovým urýchľovačom, robotickým röntgenovým skenerom a zostavou röntgenového mikrozobrazovania. Okrem toho sa analyzovali aj údaje z cyklotrónového protónového urýchľovača. Celkovo bolo spracované veľké množstvo dát dané veľkým počtom skúmaných vzoriek (spolu 41 vzoriek) a viacerými študovanými radiačnými prostrediami a nastaveniami. Dáta boli veľmi podrobne spracované pomocou niekoľkých algoritmov a softvérových skriptov. Výstup spracovania dát je poskytovaný vo forme fyzikálnych produktov (tok, dávkový príkon, zloženie). Tieto výsledky sú vyhodnocované a prezentované vo forme grafov a taktiež tabuliek s hodnotami normalizovanými pre rovinnú hustotu materiálu. Študované vzorky sa porovnávajú s konvenčnými jadrovými materiálmi štandardne používanými na tienenie žiarenia (napr. Al, Cu, Ta, Pb). Vzhľadom na radiačné prostredie na nízkej obežnej dráhe Zeme majú najlepšie tieniace vlastnosti špecifické skúmané uhlíkové kompozity.

Kľúčové slová: Nízka obežná dráha Zeme, radiačné prostredie, účinky radiačného žiarenia, tienenie radiačného žiarenia, uhlíkové kompozity, pixelové detektory

Preklad názvu: Meranie radiačného tienenia z uhlíkových kompozitov na ochranu elektroniky na nízkej obežnej dráhe Zeme

Contents

Figures

Tables

Chapter 1

Introduction and motivation

The space radiation environment in Low Earth Orbit (LEO) exhibits a complex, highly variable and dynamic nature in terms of composition (particle types - electrons, protons, X-rays, gamma rays, neutrons, ions), spectrum (kinetic energy, deposited energy), direction, fluence and intensity, often differing by orders of magnitude [1] [2] [3] [4] [5] [6]. The sources of radiation and radiation-related phenomena (called space weather) [2] [7] are similarly varied: trapped radiation in Earth's magnetic field, solar radiation including solar particle events (SPEs) and their interplay in the form of geomagnetic storms as well as galactic and extragalactic cosmic rays [8] [9] [2]. The dynamic processes like SPEs and geomagnetic storms produce large gradients and dynamic variability of the mixed radiation field. Satellites and their components, including solar panels, structure and electrical components are affected by the large fluences and resulting large doses and radiation effects [10] [11] [12] [13] [14] [15] [16] [17] as well as the harsh physical environment (vacuum, temperature gradients e.g. -70°C to +80°C in LEO, mechanical stress, UV radiation, plasma charging) [18] [19] [20]. The nanosatellites in LEO [21] [22] [15] often use Commercial of the shelf (COTS) components, which are not radiation hard nor radiation tolerant. To mitigate some of the radiation damage effects on electronics, space industry uses materials for radiation shielding [7] [22] [23] [1] [24] [25]. Such materials should also be light, small, of light weight and of suitable mechanical and thermal properties as well as be cost-efficient.

The goal of this thesis is to develop an experimental technique to measure, examine and evaluate the radiation shielding properties of materials, especially novel composite materials that are used in orbit, including Czech nanosatellites VZLUSAT-1[1] (2017) [21] and VZLUSAT-2[2] (2022). For this task, several scientific experiments using radiation sources in Czech Republic were conducted, including a cyclotron accelerator (NPI CAS, Rez near Prague) for protons, microtron accelerator (NPI CAS, Rez near Prague) for electrons, table top X-ray unit and a robotic X-ray scanner both at Advacam Prague. The technique and the measurements made use of advanced, high-resolution semiconductor pixel detectors of type Medipix/Timepix (Advacam Prague/CERN). Extensive data was measured and collected for a large number of samples (41 samples in total), including novel composite materials produced and provided by material research teams in Czech Republic (5M, Rigaku, VZLU, Advacam). In addition, conventional nuclear materials standardly used for radiation shielding (e.g. Al, Cu, Ta, Pb) were measured and used as reference and calibration samples. Most of the experiments were performed as part of this master thesis. The cyclotron accelerator proton experiment was performed prior to this thesis by the specialist supervisor.

[1] `http://www.vzlusat1.cz`
[2] `https://www.vzlusat2.cz`

Extensive amounts of data were collected during the experiments given the large number of samples investigated, several radiation environments studied in terms of their type, energy and spectrum, and different experimental measuring conditions (beam direction, geometry, setup). The data was processed in high detail (each of the pixelated tracks of single particles is analyzed in high resolution) using several algorithms and software scripts developed in Advacam by the thesis supervisor and this team. Extensive and detailed calculations were performed on a personal laptop and additionally also on a high-performance computing cluster at the FEE CTU in Prague. The results of data processing are presented in the form of physical products (flux, dose rate, composition) folded in terms of image-detector spatial distribution and radiation beam-sample-detector geometry/setup settings. These results are evaluated and produced as both table and graphic plots format. The graphical results presented in the main part of this thesis are given only for four selected samples, consisting of two representative composites and two referential materials. The rest of the samples are given in the appendices.

The text of this thesis is structured into consecutive sections. Chapter 2 outlines the harsh radiation and physical environment in LEO, both challenging to nanosatellites, their components and payload instruments. In chapter 3, the radiation sources in the near Earth environment, their composition and spectral characterization are introduced. The effects of radiation on electronics are presented in Chapter 4, with an introduction to materials shielding properties provided in Chapter 5. Chapter 6 presents the conducted experiments, including the detectors used, the radiation sources and the description of selected investigated samples. The developed method for data processing is explained in Chapter 7. The evaluation and interpretation of results and knowledge acquired are given in Chapter 8. The evaluation of analysed samples against a typical LEO CubeSat mission radiation environment is given in Chapter 9. Discussion of results and future work considerations are given in Chapter 10. Conclusions are in Chapter 11. Supplementary material and extensive results are given in the appendices. A short description of the radiation sources and accelerators used is given in Appendix A. The detailed list of shielding samples investigated and used in experiments is given in Appendix B. Detailed results in the form of radiograms or 2D imaging maps of the extensive samples used are given in Appendix C. The exhaustive measurement results for the proton experiment are given in Appendix D. Contents of attached CD are described in Appendix F. Extensive results of measurements in table form are given in Appendix E.

Chapter 2
CubeSats

A nanosatellite is considered to be any satellite that weighs between 1–10 kg. A CubeSat, a type of nanosatellite, must conform to specific criteria in terms of its shape, size, and weight. They are typically built up from standard cubic units each measuring 10 cm × 10 cm × 10 cm [26]. The main motivation for CubeSats is to provide standardized and affordable access to space for small companies, research institutes and universities. Thanks to their small size and flexible architecture, they can use extra space available on rockets, resulting in greater and flexible opportunities for launches at low launch costs.

To maintain a low prize, rather than using radiation hard and conventional space engineering parts, which are expensive but also bulky and can have long delivery times, CubeSats often use COTS components that are not necessarily radiation hard or space-qualified. For a CubeSat to properly function for a required period of time, all it's parts must be ideally at least damage tolerant to specific threats of the harsh space radiation environment in LEO. In addition, they must be designed to resist and survive further physical hazards, such as temperature fluctuations, high vacuum, mechanical stress nad shock vibrations and radiation, several of which are outlined in this chapter.

2.1 Temperature, vacuum and heat transfer

Solar radiation, namely UV, IR, thermal and plasma directly hit all exposed surfaces of a satellite, which leads to very high temperatures, depending on the materials reflectivity, absorptivity and heat capacity. On the other hand, when no solar radiation is present, including the non-illuminated rear parts of the satellite or component, the temperatures might drop to several tens of degrees below zero. This leads to large gradients or jumps in temperature, and therefore to repeating thermal expansion and contraction, which can result in degradation, material fatigue and damage to materials. Because of the space vacuum, it is not possible to transfer heat by convection, thus the only way to dissipate heat is often by conduction, where the heat is transferred to a different component, and/or by radiation only. Countermeasures to this problem can be categorized as passive or active. Passive measures include multi layer insulation, reflective layers, radiators or heat pipes. Electric band heaters or cryocoolers can be used as active protections [18].

2.2 Plasma charging

Spacecrafts in LEO are surrounded by space plasma, made up of charged particles, both electrons and ions. Since the orbital velocity of satellites in LEO is generally greater than thermal velocity of the plasma ions, the effect of plasma ions is insignificant [27]. Solar

UV illumination can also produce photoelectrons while interacting with the spacecraft, as well as secondary electrons and backscattered electrons from energetic electron impingement [28]. These particles continuously interact with spacecrafts in LEO, resulting in build-up of charge on spacecraft surfaces or in the spacecraft interior, referred to as spacecraft charging. It is the result of a spacecraft or a spacecraft component balancing incoming charged particles and assuming a potential. Surface charging is caused by energetic electrons with energies less than about 100 keV [28]. This can lead to electrostatic discharges, which can cause degradation of components, structural damage and operational anomalies as a result of damage to electronics [10]. Internal dielectric charging is caused by electrons with energies greater than about 500 keV [28]. Internal discharge is the buildup of charge within dielectric materials or on insulated conductors that results in an arc discharge, damaging sensitive electronic circuitry [29].

2.3 Outgassing

Many plastic, composite and organic materials contain fractional amounts of volatile chemicals, either on the surface or dispersed through the material. These volatile chemicals may over time migrate to the surface and escape into the local environment. This process is called outgassing and can cause contamination and other undesired issues to spacecrafts and/or their sub-systems [30].

The gases escaped out of the satellite materials might create a thin layer of coating covering the optical sensors lenses or cause an arc in the electronic components [31]. Similarly, an outgassing material can develop material fatigue or exhibit erosion, which can affect the operation and also decrease the life expectancy of spacecraft components.

2.4 Vibrations

The level of damage to spacecraft hardware potentially caused by vibrations depends heavily on the launch conditions and rocket vehicle, as it passes through the atmosphere [11]. The vibrations can be classified as: *I*) acoustic vibrations, caused by differences in pressure during launch and by the turbulence in the surrounding air created by the gases exiting the nozzle of the rocket, *II*) random vibrations, caused by dynamic force exerted on the vehicle and *III*) pyrotechnic shock, caused by staging and on-orbit brief ignitions [18]. The vibration damage to hardware is usually mitigated by using external mounts [18].

2.5 Significance of radiation

Satellites in LEO are exposed to significant and large levels of radiation. This radiation is caused by energetic charged particles (electrons, protons, light ions) trapped by the earth's magnetic field, solar radiation, including SPEs, solar storms and solar flares and galactic cosmic rays [6]. According to Koons et al. in year 2000, around 38 % of investigated incidents related to space system damage were caused by some type of radiation effect [12]. As shown in Figure 2.1, according to NASA publication from 1996,

45 % of spacecraft anomalies caused by space environment were due to radiation [32]. Considering this high percentage, the research into effects and risks associated with exposure to radiation and subsequent mitigation is necessary.

Considering CubeSats, the need for financially low solutions demands the use of COTS components. As these electronic components are not designed to handle the harsh radiation environment in LEO, one solution is to use material shielding. Besides having good radiation shielding efficiency, the shielding material in general has to be light, easy to manufacture, and should be resistant to the other non-radiation hazards mentioned above. While choosing appropriate shielding, it is necessary to consider the radiation field composition (particle types, energy spectrum), relevant radiation exposure, the level of acceptable risk and it is necessary to determine the radiation shielding efficiency of the material.

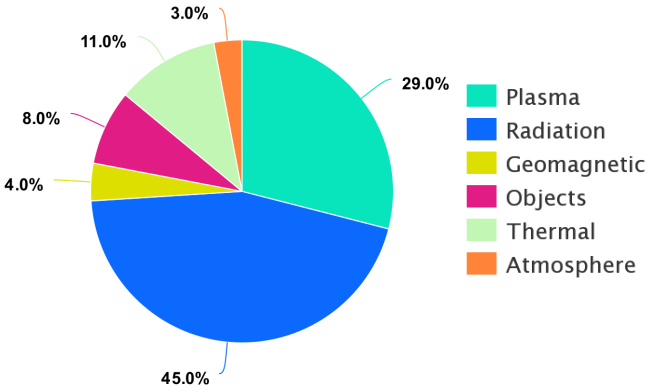

Figure 2.1: Distribution of spacecraft anomalies caused by **space environment** (not all anomalies). Source: NASA.

Chapter 3

Radiation environment in LEO

The sources of radiation in near-Earth space can be divided into three groups. Solar radiation, which originates from the Sun, including solar storms from solar fluxes and solar particles events (SPEs), galactic radiation originating from energetic processes in our Galaxy and trapped particles in the Earth's magnetic field, creating the Van Allen Belts [4]. The primary radiation environment is a complex mixture of these phenomena and sources of solar, planetary and cosmic origin, as illustrated in Figure 3.1. Jupiter is a source of electrons to the solar system, including Earth's radiation belts. As can be seen in Figure 3.2, radiation components and individual types of particles vary greatly in energy and flux.

In addition to the primary radiation component of space radiation (described above), there also occurs so-called secondary radiation. This results from interaction of primary radiation on Earth's upper atmosphere as well as on material and structures of satellites and also human tissue on board spacecrew missions. Several such interactions, such as *Bremmstrahlung* secondary radiation (further explained in Chapter 5.5), are illustrated in Figure 3.3. In this chapter, the radiation sources, their composition and spectral characterization are introduced in relation to the radiation environment in LEO.

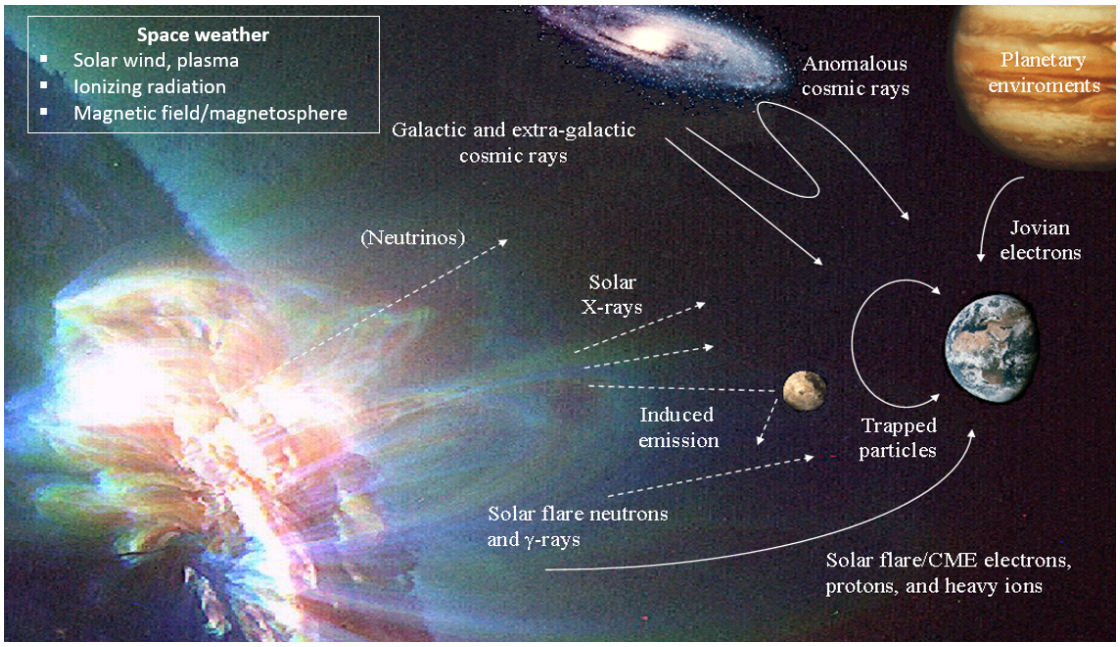

Figure 3.1: Illustration of the near-Earth space radiation environment. Sources are the Sun, the trapped radiation in Earth's radiation belts, galactic and extragalactic cosmic rays and also electrons from Jupiter. Source: ESA.

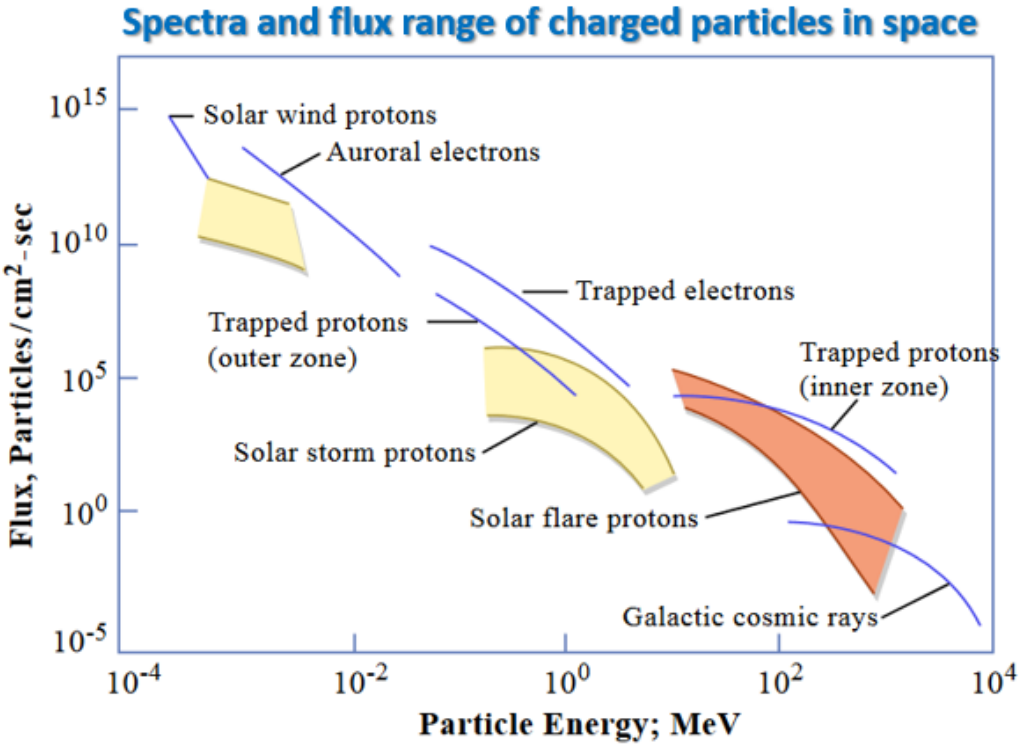

Figure 3.2: Radiation-source components of primary space radiation in the near-Earth environment, the particle energy spectra and flux range. Note the axes in logarithmic scale, covering a wide range of particle flux and energy. Source: ESA.

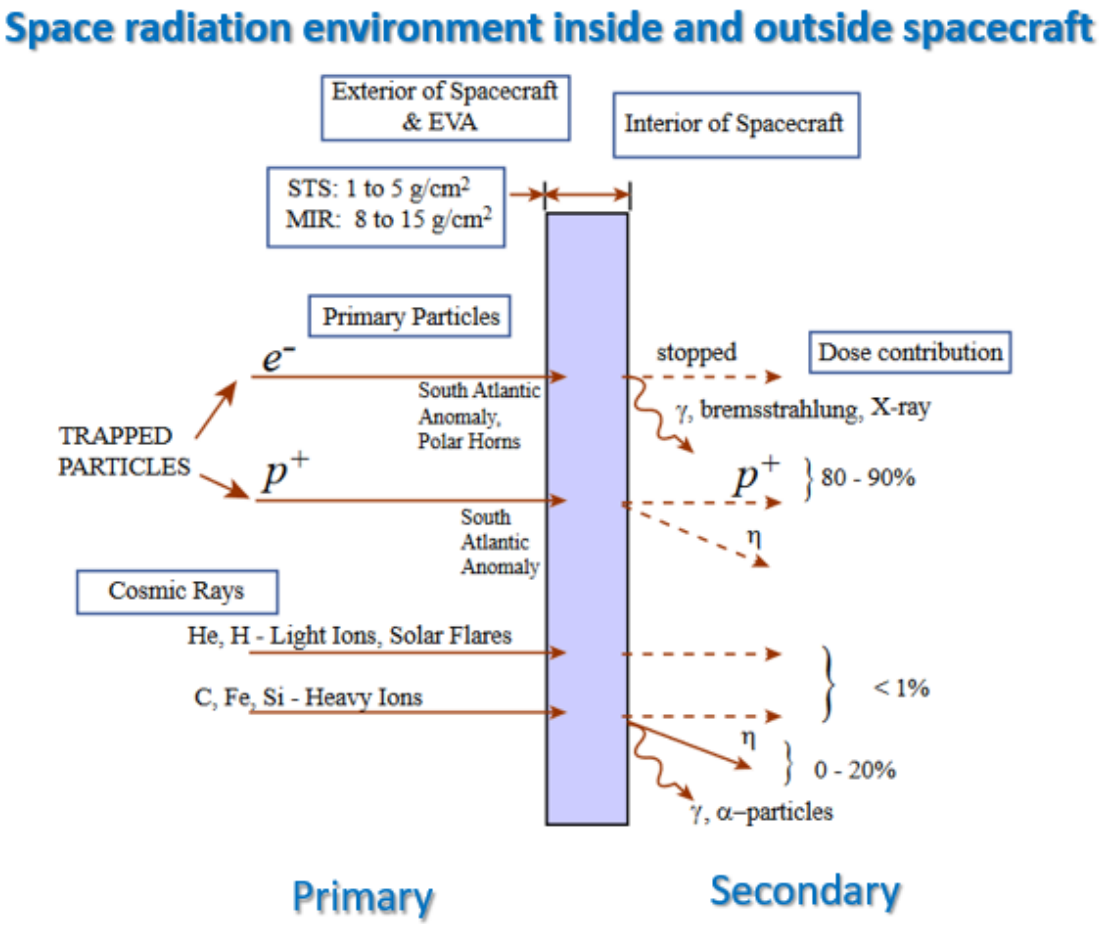

Figure 3.3: Illustration of the space radiation environment outside (left side) and inside (right side) of a spacecraft wall/material. The environment outside is made of primary radiation of solar, Earth radiation belts and cosmic origin. The environment inside of the spacecraft consists of transmitted and scattered primary particles with addition of secondary radiation from radiation interactions and nuclear reactions by the incident energetic primary radiation in matter - such as the spacecraft walls or material. Source: ESA.

3.1 Galactic cosmic rays

Galactic cosmic radiation (GCR) originates from outside of our solar system, from our own galaxy and beyond - extragalactic origin. The distribution is isotropic throughout interstellar space [4]. The charged particle composition of GCR is 98 % protons and heavier ions (baryon component), and 2 % electrons and positrons (lepton component), with the baryon component consisting of 87 % protons, 12 % helium ions (alpha particles) and 1 % heavy ions [4]. GCRs contain also photons - namely gamma rays and X-rays, from cosmic and stellar sources.

The energies of cosmic radiation cover a wide range from GeV to more than 10^{20} eV. Direct measurements using balloon and satellite-borne experiments are possible below $\approx 10^6$ GeV. At high energies above $\approx 10^6$ GeV, ground-based experiments have carried out measurements of the all-particle energy spectrum and the composition of cosmic rays [33]. Figure 3.4 shows the detailed composition of measured GCR, where the thick line represents the total supernova remnants cosmic rays (SNR-CRs). It can be seen, that direct measurements end at $\approx 10^5$ GeV.

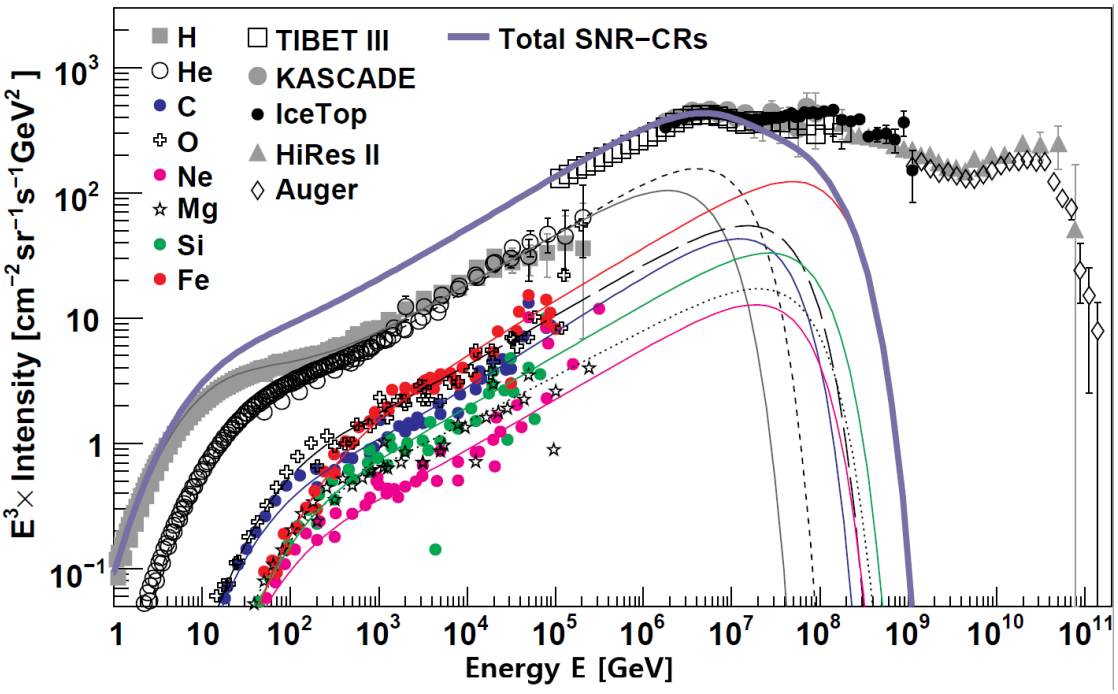

Figure 3.4: Spectra and charged particle composition of GCRs. The thin lines represent spectra for the individual elements, and the thick-solid line represents the total contribution [33].

The flux of GCR below 1 GeV is affected by the solar cycle. The galactic cosmic rays entering the solar system interact with the solar wind and magnetic field and are partially modified. Measurements show that the attenuation is greatest during the solar maximum, when the solar wind is the most intense. In contrary, GCR flux is the greatest during the solar minimum [6]. Compared to other sources of radiation, namely solar radiation (Section 3.2) and trapped radiation (Section 3.3), GCRs overall exhibit low flux.

They are however highly energetic and are responsible for SEEs in electronics, especially by the proton and namely the ion components.

GCRs composed of charged particles are greatly affected by the Earth's magnetic field, which acts as a shield. Charged particles have the tendency to bend and follow the lines of the geomagnetic field. As illustrated in Figure 3.5, the geomagnetic field lines are parallel to the Earth's surface near the equator and point towards the Earth's surface at north and south magnetic poles. This means that most GCR particles are deflected away from the equator and part are funneled towards the poles at high altitudes. Many of these GCR charged particles along with their secondary charged particle products become trapped in the Earth's magnetosphere, creating the Earth's radiation belts, also known as Van Allen radiation belts (Section 3.3). These belts cover a wide space above Earth, stretching from over few hundred kilometers up to ≈ 40,000 km. The exposure to radiation belts depends on the satellite's orbit. The main three orbits are the Low Earth Orbit (LEO), with altitude from 500 km to 1,200 km, the Medium Earth Orbit (MEO), with altitude from 5,000 km to 20,000 km and the Geosynchronous Equatorial Orbit (GEO), with altitude around 36,000 km.

Spacecraft in LEO, according to their orbit and altitude, are exposed to large and varying radiation fields, receiving the greatest exposures near the poles (near the so-called polar horns) and a minimum near the equator, with the exception of the South Atlantic Anomaly (SAA). Low-inclination orbits such as the 28.5° orbit of the Hubble Space Telescope and many early Space Shuttle missions are exposed to high energy GCR [4].

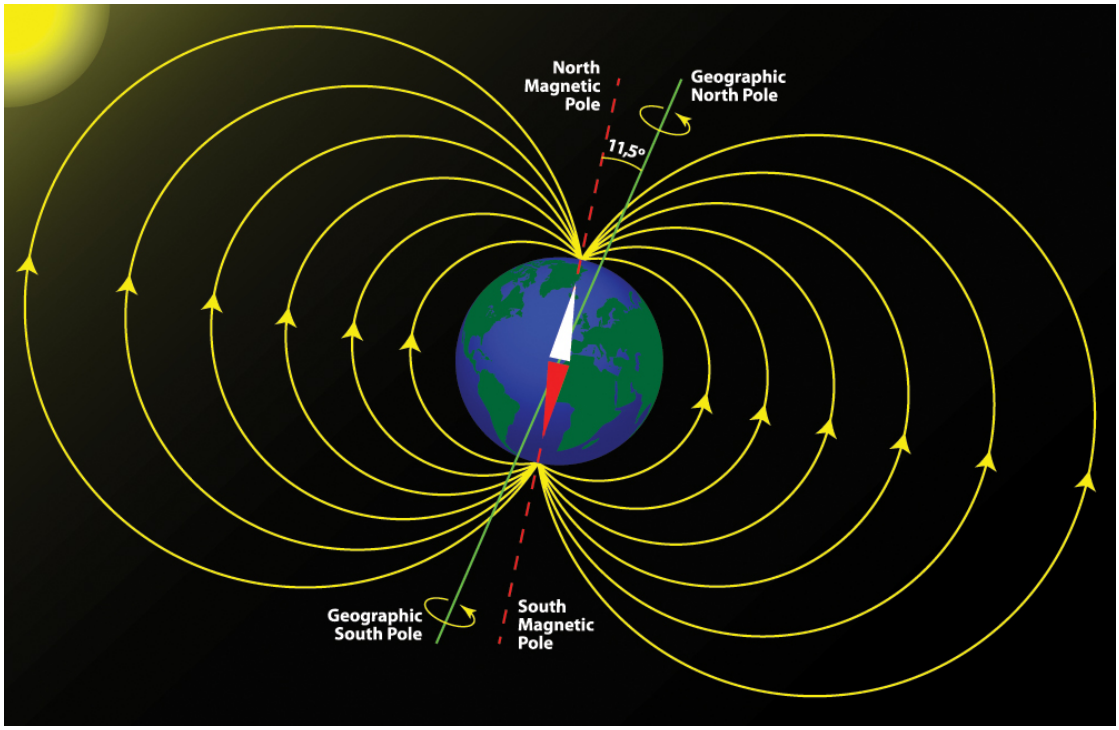

Figure 3.5: The Earth's magnetic field, magnetic poles and geographic poles. Image source: Milagli/Shutterstock.com.

3.2 Solar radiation

In addition to electromagnetic radiation, the sun continuously emits particle radiation, the low-energy component of which makes the solar wind. Solar wind consist mainly of protons and electrons, with intensities ranging between 10^{10} and 10^{12} particles per $\mathrm{cm}^{-2} \cdot \mathrm{s}^{-1} \cdot \mathrm{sr}^{-1}$. The velocity of this particle stream varies between 300 km $\cdot$ s^{-1} and 800 km $\cdot$ s^{-1} and more. These particles have low energies, between 100 eV and 3.5 keV for protons [5], which have limited and superficial effect on components and electronics.

The part of the ionizing radiation relevant for LEO satellites coming from the sun has the form of energetic particles, called Solar Particle Events (SPEs), solar flares and Coronal Mass Ejections (CMEs), emitted by the sun. These events are illustrated in Figure 3.1. The composition of their fluxes is primary electrons, protons and light ions up to iron [4]. Part of these events, namely the SPEs, occur most often during the solar maximum of the 11-year solar cycle, with their total proton fluence being larger than 30 MeV at 10^6 protons per cm^{-2} [4]. Over the course of one solar cycle, approximately 50 such SPEs occur.

SPEs generally associated with solar flares usually only last in the order of hours. They are made up by relatively large fluxes of electrons, with total fluence at Earth orbit between 10^7 and 10^8 particles per cm^{-2}. The SPEs coming from large CMEs, on the other hand, usually last in the order of days and are characterized by a much larger fluxes of protons. Their total fluence can exceed 10^9 particles per cm^{-2} [4].

3.3 Van Allen belts

The Earth is surrounded by two regions of energetic charged particles, trapped at high altitudes by the Earth's geomagnetic field. Referred to as the Van Allen belts, or the Earth's trapped radiation belts, illustrated in Figure 3.6, they are a result of the interaction of GCR and solar charged particles with the Earth's magnetic field. The present electron component originates from Jupiter.

The belts spread over a large region around the Earth, with the flux of the particles showing areas of maximum density. There are namely two belts. The inner belt, ranging from $\approx$ 1,000 km (500 km for SAA) to $\approx$ 13,000 km, consists mainly of highly energetic protons, exceeding 30 MeV, and electrons with energies less than few MeV. It is partly formed by decaying neutrons, formed in cosmic particle interaction in the upper atmosphere, producing electrons and protons [5]. The second belt, called the outer belt, ranging up to 75,000 km, is formed primarily by trapped electrons of solar and Jupiter origin, with energies up to $\approx$ 10 MeV.

The trapped particles, mainly protons and electrons, follow a complex motion revolving around a geomagnetic field line in what is called a cyclotron motion, see Figure 3.7. The particles move back and forth along the field lines, with the directions reversing near the poles, see illustration in Figure 3.7. The protons tend to drift to the west and electrons to the east [4]. As the geomagnetic field is not uniform and the field lines converge near the poles, the Van Allen belts are most intense over the Equator and are effectively absent above the poles.

The radiation belts are affected by the solar cycle. With high solar activity, the

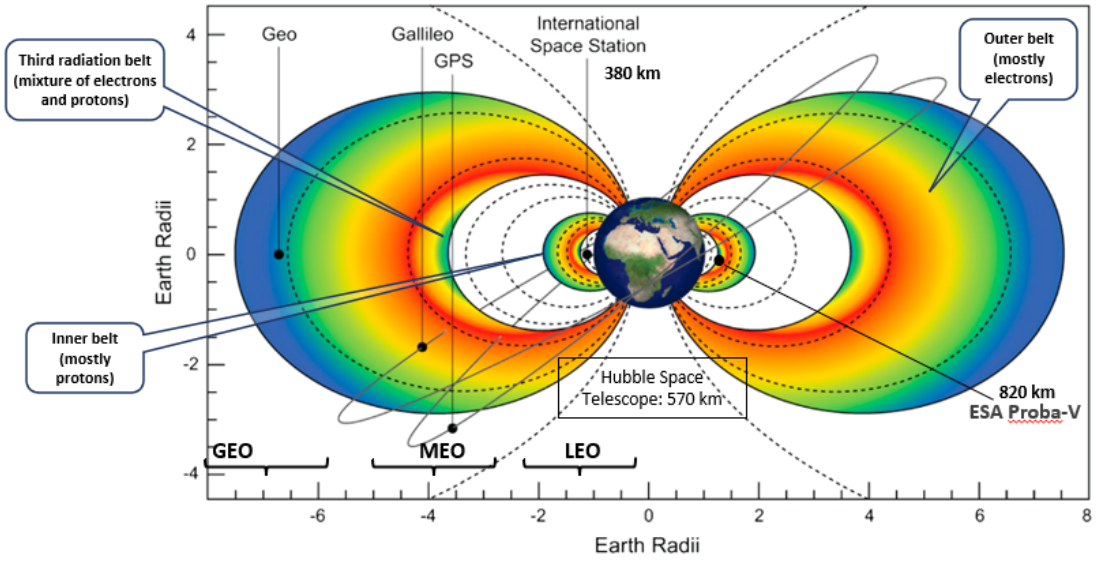

Figure 3.6: The Earth's trapped radiation belts (Van Allen belts) [13]. The inner belt, ranging from ≈ 1,000 km (500 km) to ≈ 13,000 km, consisting mainly of highly energetic protons and the outer belt, ranging up to 75,000 km, is formed primarily by trapped electrons of solar and Jupiter origin. An additional third transient radiation belt detected in 2021, contains a variable mixture of electrons and protons.

proton intensity decreases, while electron intensity increases. In LEO, the dominant contribution to the radiation exposure is delivered by protons, especially over the SAA (see Section 3.3) and the polar horns crossings of intense electron exposure. While the center of the inner belt is fairly stable, the intensity of protons and electrons at the lower edge of the belt may vary by up to a factor of 5 [5]. In 2021, NASA launched Van Allen Probes to study particle behaviour in the belts. This mission found a third, temporary belt in the region between the inner and outer belts. The belt lasted only a month, but appeared again later in the mission with major solar activity [4].

South Atlantic Anomaly

There is a region of weakened geomagnetic field over the coast of Brazil, where the inner radiation belt extends down to altitudes of few hundred kilometers, as shown in Figure 3.8. This area is called the South Atlantic Anomaly (SAA) and is caused by a displacement (shift and tilt) of the axis of Earth's magnetic field from it's axis of rotation. Because of the weakened magnetic field, the inner radiation belt particles reach lower altitudes increasing the local particle flux [34]. Traversing the SAA, although taking only 15 minutes, causes the dominant fraction of total exposure for satellites in LEO at low inclinations [5]. This is evidenced in the measurements of dose rate on board the PROBA-V satellite shown in Figure 3.9. It shows the spatial radiation map of measured dose rates during 220 days (3,100 orbits), where the logarithmic color gradient clearly shows the greater dose rate values in the SAA region, as well as near the magnetic poles.

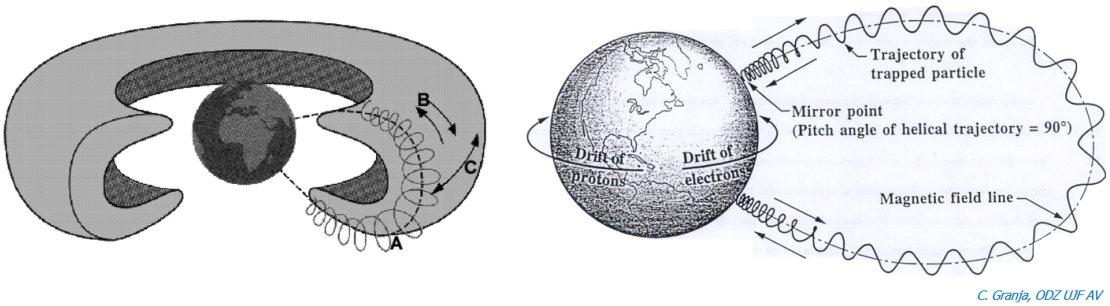

Figure 3.7: Illustration of the dynamic motion of the trapped charged particles in the Earth's radiation belts. On the left, **A** points to the gyration motion - a spiral motion around a magnetic field line, **B** points to bouncing of the particles between the magnetic poles and **C** to drift motion of the particles, where they travel equatorially around the Earth. On the right, a detailed illustration of the trajectories is shown. Image source: C. Granja, ODZ UJF AV, ESA.

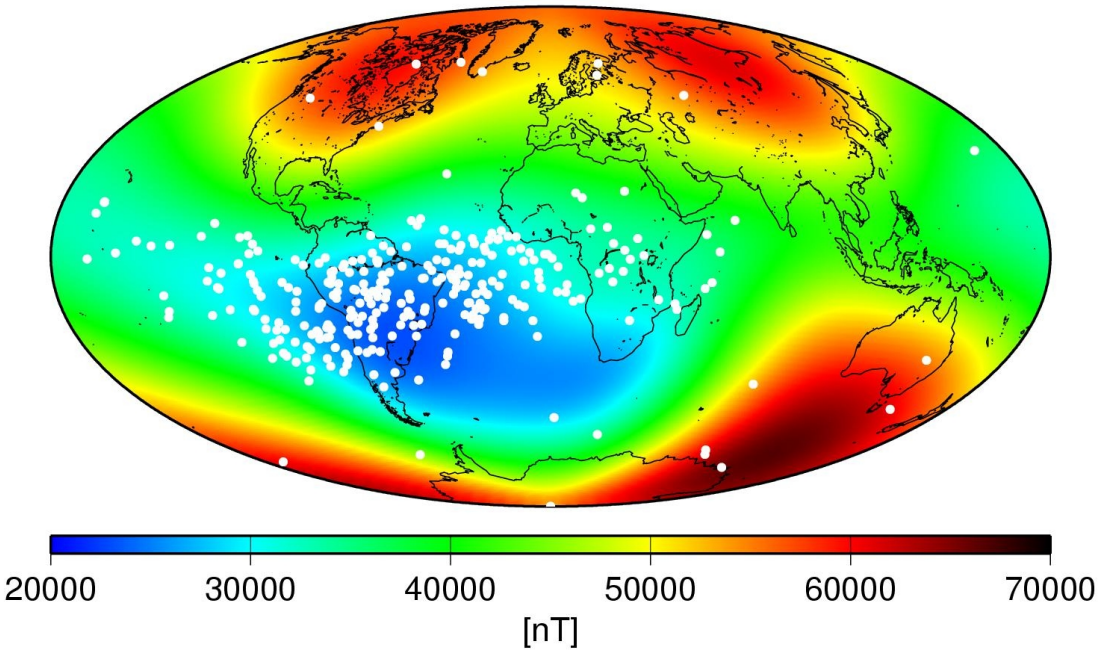

Figure 3.8: The intensity of the magnetic field of Earth at LEO exhibiting the South Atlantic Anomaly (SAA). The white spots on the map indicate where electronic equipment on a satellite (TOPEX/Poseidon) was affected by radiation in LEO orbit. Image source: ESA/DTU Space.

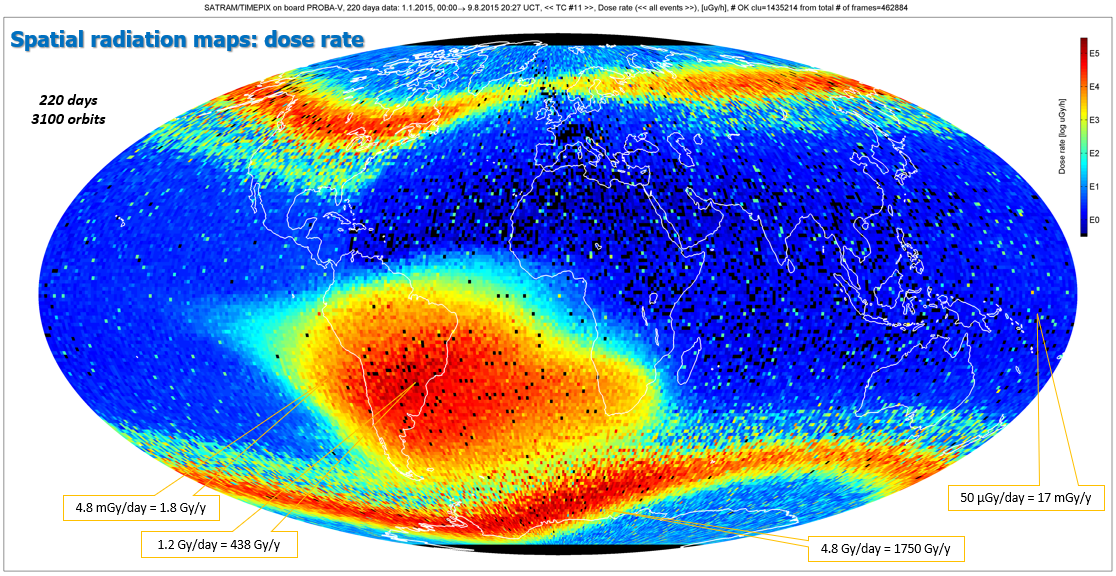

Figure 3.9: Earth spatial radiation map of dose rate measured by SATRAM/TIMEPIX on board the PROBA-V satellite between 1.1.2015 and 9.8.2015. Note the logarithmic scale of the color gradient, showing the wide range of dose rate based on geographical location. Image source: Carlos Granja, IEAP CTU Prague, 2016.

Neart-earth space radiation exposure profile

Figure 3.10 illustrates the near-Earth space radiation environment for altitudinal range from 0.1 km to 250,000 km [35]. The three described parameters are absorbed dose rate in $\mu Gy \cdot h^{-1}$ (solid black line), flux in $cm^{-2} \cdot s^{-1}$ (dashed red line) and specific dose (SD) in $nGy\ cm^2 \cdot particle^{-1}$ (dashed blue line). The left axis represents the altitudinal range in kilometers on logarithmic scale. Next to the left axis, the carriers, instruments, date ranges and averaged geographic coordinates of the measured values are listed. On the right side, the predominant radiation sources and their composition are listed, with blue arrows pointing to places where they occur.

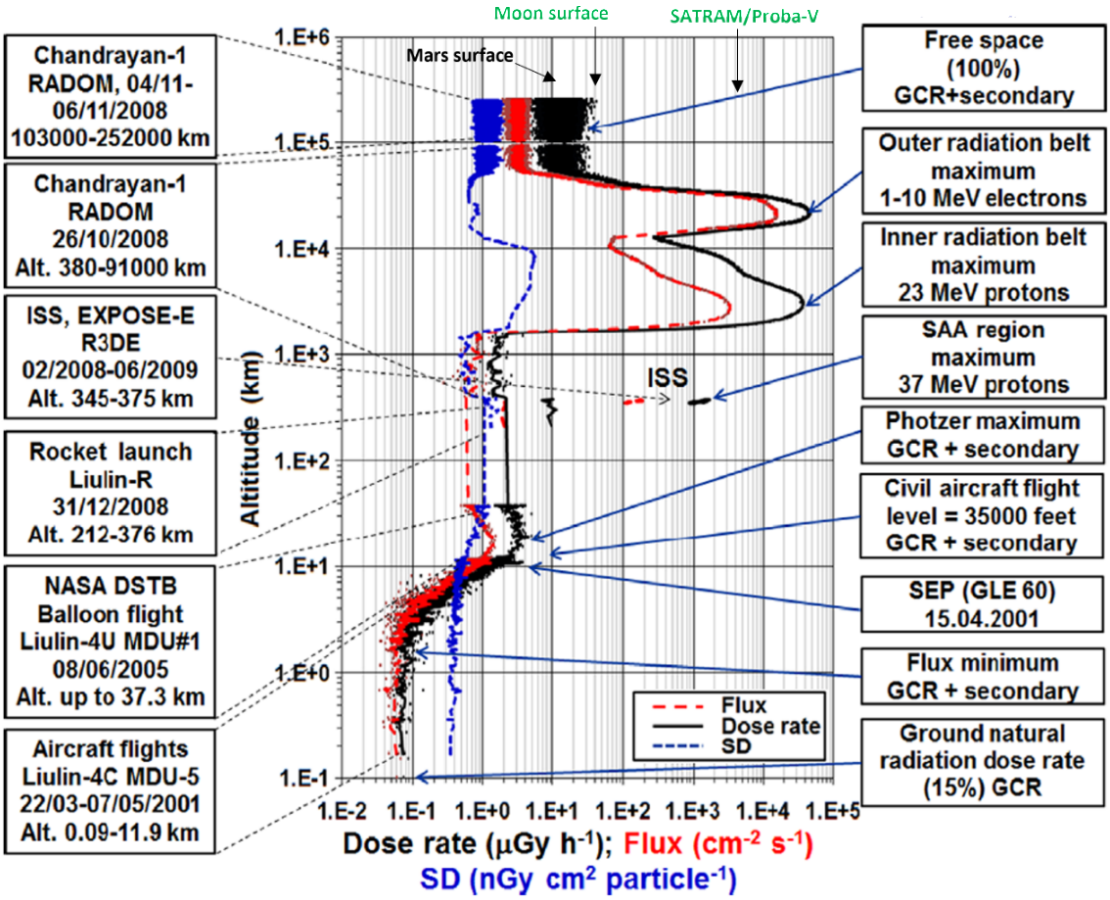

Figure 3.10: Intensity and flux profile between Earth and free space. Variations of the absorbed dose rate (solid black line), flux (dashed red line) and specific dose (dashed blue line) are shown for altitudinal range from 0.1 to 250,000 km. Note the logarithmic scale of the axes. Next to the left axis, the carriers, instruments, date ranges and averaged geographic coordinates of the measured values are listed. On the right side, the predominant radiation sources and their composition are listed, with blue arrows pointing to places where they occur [35].

Chapter 4

Radiation effects on electronics

Radiation can damage materials and electronic components. It can degrade the operation and can cause reduced availability of a system, error in or destruction of critical components in modules, potentially resulting in module and subsystem failure, or in worst-case scenario, components or subsystem failure, or even total mission loss [14] [12].

The degradation in performance of electronics caused by radiation can follow a number of courses. The overall effect on the electronic component will depend on the type of radiation, its mode and rate of interaction with the material, the type of the material and its contribution to the function of the device and the physical principles upon which the device functions [16] [25]. This has particular significance to electrical, electronic and electro-mechanical components (EEECs) and the use of COTS components in CubeSats [10].

This chapter provides a general information about types of radiation interactions and the specific radiation effects on electronic devices. The rest of this chapter is dedicated to the effects of radiation on specific semiconductor devices and known radiation resistance of electronics.

4.1 Radiation interactions and effects

Energetic particles, such as energetic charged particles as well as photons (gamma rays) lose energy while passing through matter by a variety of interactions and scattering mechanisms. The two major damage mechanisms as consequences of energy transfer from radiation to electronic materials are atomic displacement and ionization [14]. Both of these mechanisms are important to electronic devices. While certain devices can be more sensitive to one type of damage, most devices are sensitive to both. While both these mechanisms cause long-term effects in electronics, ionization can further cause transient, or single event effects, to occur [10]. Three main types of damage to EEECs are examined: Total Ionizing Dose (TID), Displacement Damage (DD) and Single Event Effects (SEEs) [23] [14].

4.1.1 Total Ionizing Dose

As an incident particle passes through a semiconductor, it can cause direct or indirect ionization. An example of direct ionization taken from [23] can be seen in Figure 4.1, where:

(a) a charged particle passes through a semiconductor material,

(b) the charged particle interacts with the semiconductor,

(c) electron–hole pairs are generated along the path of the particle due to its energy loss,

(d) holes that are created remain trapped in the integrated circuit oxides (such as passivation, gate oxides, etc.).

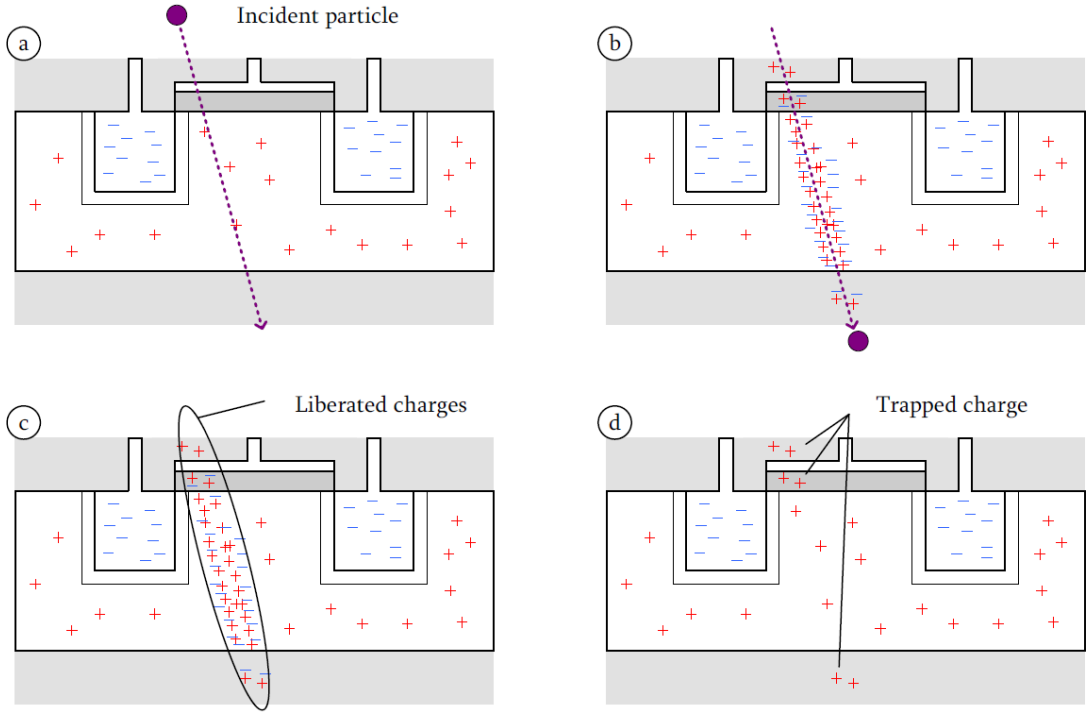

Figure 4.1: Illustration of the total ionizing dose process [23]. The interaction of incident particles and energy-dose transfer is illustrated in several steps, described in the text.

Ionization can cause changes to the device characteristics and performance / operation. The total ionizing dose, or absorbed dose, is a cumulative long term ionizing damage, usually due to protons and electrons. It increases over time causing gradual degradation of the performance of EEECs such as semiconductors [23]. This effect is usually measured in Grays [Gy] (1 gray = 1 Joule per kilogram). In United States, the unit rad is also sometimes still used, where 1 gray = 100 rad.

TID effect on electronics

The effects of TID on EEECs are for example threshold shifts, leakage current, timing changes and functional failures, for an overview see Table 4.1 [36]. An example can be taken from [23], where the positive charge collected in the gate oxides is considered. As the gate is progressively activated by the slow build-up of trapped positive charges, an NMOS semiconductor will have a decrease in switch-on voltage. Similarly, a PMOS device will exhibit an increase in switch-on voltage, as the positive charges progressively inhibit the switch-on of the gate. NMOS devices will eventually fail as they will be permanently activated, and PMOS devices will be permanently de-activated.

Technology category	Sub-category	Effects
MOS	NMOS PMOS CMOS CMOS/SOI/SOS	Threshold voltage shift Decrease in drive current Decrease in switching speed Increased leakage current
BJT		hFE degradation, particularly for low-current conditions
JFET		Enhanced source-drain leakage currents
Digital microelectronics (general)		Enhanced transistor leakage Logic failure from reduced gain (BJT) or threshold voltage shift and reduced switching speeds (CMOS)
CCDs		Increased dark currents Effects on MOS transistor elements Some effects on CTE
MEMS		Shift in response due to charge build-up in dielectric layers near to moving parts

Table 4.1: Technologies susceptible to TID effects [36] [25].

4.1.2 Displacement Damage

Displacement Damage (DD) is a long term non-ionizing damage effect due to high-LET particles such as protons, electrons, and neutrons. It is caused by particle interaction with the silicone lattice. Figure 4.2 illustrates the main process, taken from [23]:

(a) the ideal silicon lattice has regularly spaced atoms,

(b) an incident particle traverses the lattice,

(c) there is a probability that the particle strikes and dislodges an atom,

(d) this interaction can create Frenkel defects consisting of a vacancy and an interstitial defect.

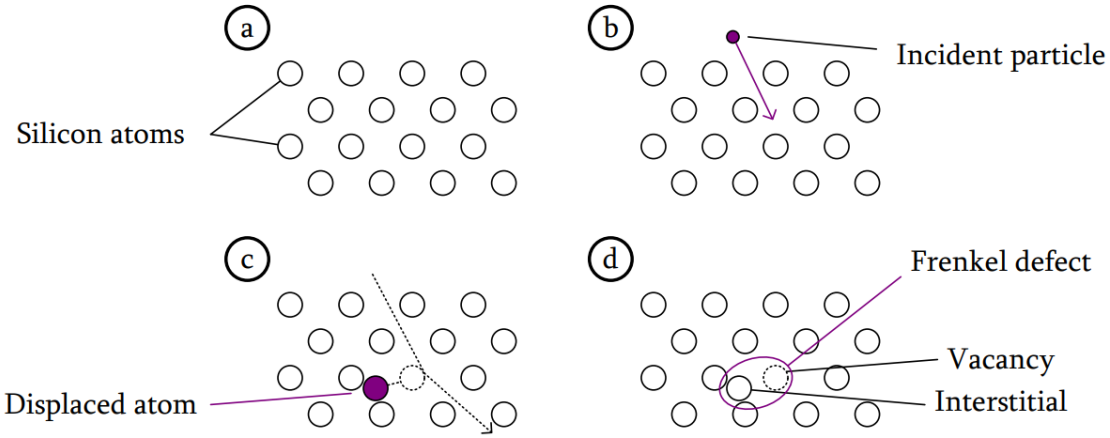

Figure 4.2: Illustration of the displacement damage process [23]. The interaction of incident particles is illustrated in several steps, described in the text.

The DD gradually increases over time, as the damage to the lattice is proportional to the integrated flux of particles (called fluence) that have passed through the atomic structure [23]. DD is measured as the total number of 1 MeV equivalent neutrons that have passed through a given surface area – 1 MeV eq. n/cm^2.

DD effects on electronics

The disturbance resulting from DD process causes changes in the operation of any affected device. This change may worsen the conduction in regions designed for flow or conversely add a current path that previously did not exist - allowing increased leakage current [10]. An example can be a solar cell diode becoming less effective at producing power with exposure to radiation, as its leakage current increases, generated electrons live for shorter time periods, and the internal electric field decreases [14].

While the effects of DD may be similar to the effects of TID, the defects usually lead to device degradation, for an overview see Table 4.2 [36]. This type of damage is not particularly applicable to CMOS microelectronics.

Technology	**Effects**
BJT	hFE degradation, particularly for low-current conditions (PNP devices more sensitive than NPN).
diodes	Increased leakage current, increased forward voltage drop.
CCDs	CTE degradation, Increased dark current, Increased hot spots, Increased bright columns, Random telegraph signals.
Photo diodes	Reduced photocurrents. Increased dark currents.
Opto-couplers	Reduced current transfer ratio.

Table 4.2: Technologies susceptible to DD effects [36][25].

4.1.3 Single Event Effects

A single event effect (SEE) is caused by the passage of a single heavy charged particle (such as proton or ion) through an EEEC such as a semiconductor material [10]. Contrary to TID or DD, SEEs are sudden and each particle passing through the semiconductor has a certain probability of interaction. In other words, a single event effect has a certain probability (cross-section) of occurring with every particle interaction [14]. While SEEs can manifest in several different ways, the usual root cause is illustrated in Figure 4.3, which considers the same interaction as in previous TID case - an incident particle acting on a semiconductor. In this case, however, the behaviour of electrons, not holes, is considered [23]:

(a) a charged particle passes through a semiconductor material and interacts,

(b) as the particle traverses the material, electrons are generated,

(c) electrons are highly mobile and flow through the MOSFET, and are collected at the reverse biased junction,

(d) these electrons create a pulse of current shortly after the particle's interaction. The current pulse is the root cause of SEE in almost all cases.

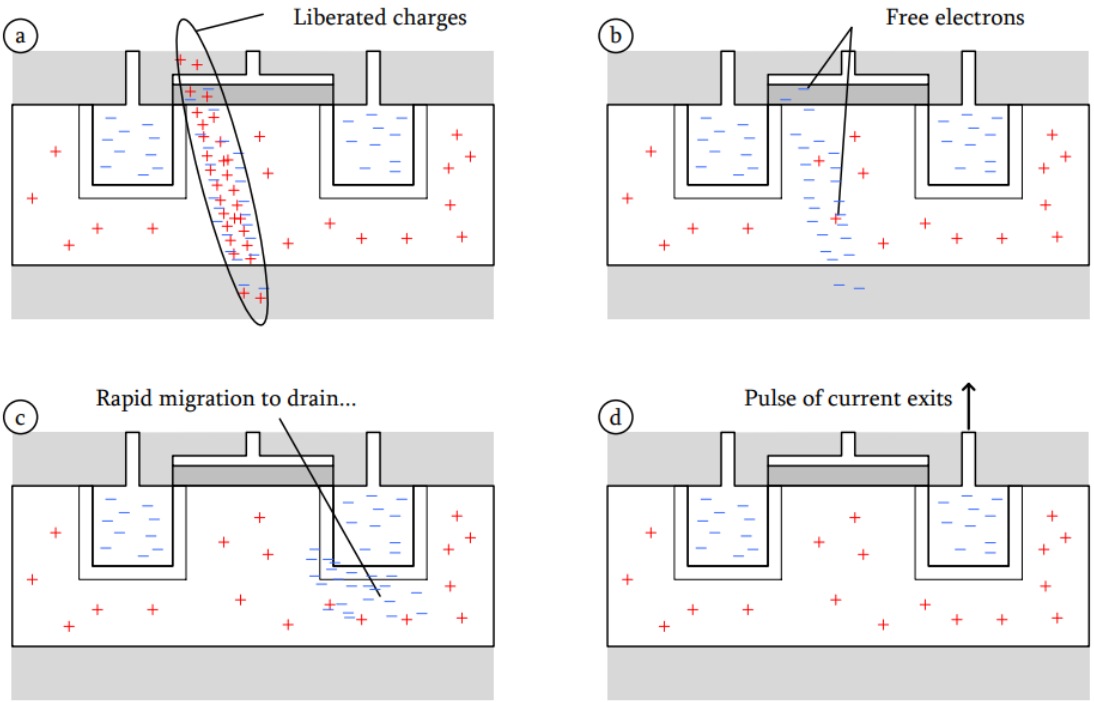

Figure 4.3: Illustration of the single event effect process (bias not shown, for simplicity) [23]. The interaction of incident particles is illustrated in several steps, described in the text.

The most important factor in SEE is the prediction of the rate of these events occurring. Currently, the only way for this prediction is by performing experiments on individual devices. The result of these experiments is the cross sections versus energy

data for protons and cross sections vs linear energy transfer (LET) for heavy ions. The cross section is an indication of the susceptibility of a device to the event in area units (cm^2). LET indicates how a particle loses energy as it passes through a material. Even though the term linear is used, LET is strongly non-linear as a function of particle energy. An ion typically loses most of its energy at the end of its range when it has the least kinetic energy remaining [37] [14]. LET is usually reported in units of megaelectron volts per square centimeters per milligram [$MeV \cdot mg^{-1} \cdot cm^{-2}$], or megaelectron volts per millimeter [$MeV \cdot mm^{-1}$].

As the heavy ions can change individual bits, it is also possible to express the damage in bit error rates or SEU Error Probability - see below. The SEU Error Probability is calculated by models and calculations based on the expected distribution of particles, LET, and the device cross-section for upset or latch-up. The result is a fixed number for the upset or latch up probability [37].

SEE effects on electronics

The term SEE encompasses all possible effects, however a distinction between destructive and non-destructive events should be made. The non-destructive events, or soft failures, include [23] [36]:

- **SEU (single event upset)**: A change in logic state of a bit or bits caused by the initial particle interaction. The value of the corrupted bit would persist until rewritten. The scope of the damage caused by this error depends on the location and therefore function of the erroneous bit.
- **SET (single event transient)**: The charge deposited by the passing particle causes a transient voltage disturbance on a signal path. The effect of this event depends on the path's function.

Other modes of failure can also occur, particularly in CMOS devices, where a parasitic NPN, PNP structure can be created and activated if the particle deposits sufficient charge. These destructive events, or hard failures, include [23] [36]:

- **SEL (single event latchup)**: A semiconductor component latchup can be stimulated by the transient current induced by the passage of a charged particle. Latchup is the transition of a semiconductor to a certain state that will persist as long as power is applied, caused by a low-impedance short-circuit between power supply and ground. If the latchup causes excessive current flow, a localized over-heating can cause irreparable damage and resetting power will have no perceptible effect. If the part is not damaged, functionality may be restored by resetting power.
- **SHE (single hard error)**: Heavy ions penetrating a transistor can establish leakage paths that permanently change the affected transistor to either an open or a closed state. These bits are unable to be changed by a write-process.
- **SEGR (single event gate rupture)**: A heavy ion interaction with material in conjunction with high voltage can cause a rupture of the gate oxide of a MOS technology semiconductor device. This event is generally associated with power metal oxide semiconductor (DMOS) or electrically erasable programmable read-only memory (EEPROM) devices.

- **SEB (single event burnout)**: Device burnout caused by the impact of a heavy ion usually associated with a power semiconductor device. An example of SEB damage can be seen in Figure 4.4.

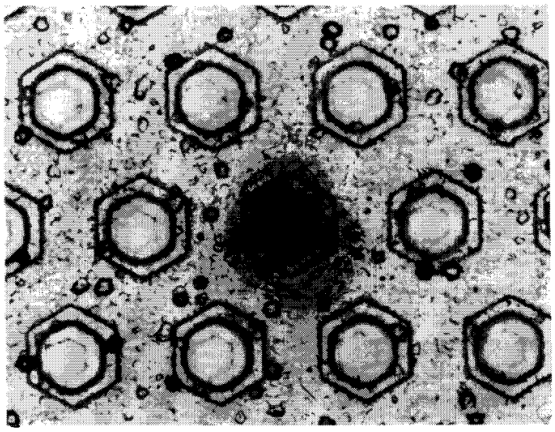

Figure 4.4: SEB damage on surface of power MOSFET [38].

Event	Effect	Technology
SEU	Corruption of information	Memories, latches in logic devices
SET	Impulse response of certain amplitude and duration	Analog and mixed signal circuits, Photonics
SEL	High-current conditions	CMOS, BiCMOS devices
SHE	Unalterable change of state in a memory element	Memories, latches in logic devices
SEGR	Rupture of gate dielectric due to high electrical field conditions	Power MOSFETs, Non-volatile NMOS structures, VLSIs, linear devices
SEB	Destructive burnout due to high-current conditions	BJT, N-channel Power MOSFET

Table 4.3: Technologies susceptible to different SEEs [36] [25].

4.2 Radiation damage mitigation

The two main mechanisms to protect electronics against radiation are *I*) by designing radiation tolerant devices or *II*) to provide radiation shielding. TID and DD effects can be partially mitigated with enhanced shielding of electrons and protons. With DD, it also depends on the location of the device. For example, to shield the aforementioned solar arrays, the material would need to be transparent for the optical photons, with good optical interface to minimize the refraction effects. Contrary to TID and DD, SEEs are almost impossible to shield against. The usual way to reduce single event effects is selection of radiation hard devices, or circuit level mitigation techniques [14] [7].

4.2.1 Radiation hardness of semiconductors

Components can be categorized into three groups based on following characteristics[1]:

1. Radiation Soft / COTS:
   - Process and design limit the radiation hardness
   - Hardness levels:
     - Total Dose: 2 to 10 krad (typical)
     - SEU Threshold LET: 5 MeV $\cdot$ mg^{-1} $\cdot$ cm^{-2}
     - SEU Error Rate: 10^{-5} errors per bit-day (typical)
   - Customer performs radiation testing, and assumes all risk
   - Customer evaluation and risk
2. Radiation Tolerant:
   - Design assures radiation hardness up to a certain level
   - Hardness levels:
     - Total Dose: 20 to 50 krad (typical)
     - SEU Threshold LET: 20 MeV $\cdot$ mg^{-1} $\cdot$ cm^{-2}
     - SEU Error Rate: 10^{-7} to 10^{-8} errors per bit-day
   - Usually tested for functional failure only
   - Customer evaluation and risk
3. Radiation Hard:
   - Designed and processed for particular radiation hardness level
   - Hardness levels:
     - Total Dose: $>$ 200 krad to $>$ 1 Mrad
     - SEU Threshold LET: 80–150 MeV $\cdot$ mg^{-1} $\cdot$ cm^{-2}
     - SEU Error Rate: 10^{-10} to 10^{-12} errors per bit-day

Using COTS components increases the risk of failure. However, in CubeSats the low cost, latest technology and fast procurement prevail [26]. For this reason, shielding is used as the more cost-effective radiation damage mitigation mechanism in many cost-efficient deployments in LEO [22].

4.2.2 Radiation shielding

Usually, radiation shielding consists of single or multiple walls of shielding material. The type of material used depends on the specific radiation environment - the type and energy spectrum of the radiation that needs to be shielded against [11]. The radiation shielding properties are based on the material type, mass (volume) and efficiency at reducing the intensity and/or energy of radiation in relation to its thickness. As shielding reduces

[1] https://llis.nasa.gov/lesson/824

the incident flux of radiation on electronics, it can partially mitigate especially TID and to limited extent SEEs [37] [39]. However, SEEs are rarely considered of interest when choosing shielding materials, and are usually attenuated by electronics design and/or operation.

Chapter 5

Shielding properties of materials

The most important parameters for shielding of a material are the material type (namely its density i.e. its Z-number), thickness and for assembled structures, the layout of the shielding layers. During interaction with a material, the incident radiation transfers energy to said material. This happens mostly by direct ionization. One resulting process is the generation of secondary radiation. The overall interaction and experimentally tested effects of ionization depend mainly on the atomic number (Z-number) of the shielding material and the type and energy of the interacting particles [39]. Since the energy transfer by direct ionization is given by the electron density, it is more prominent in high-Z materials. Measured data shows that when a heavy charged particle passes through a shielding target, Coulomb and nuclear interactions occur simultaneously. The nuclear fragmentation dominates in low-Z materials (PE), while ionization dominates in high-Z materials (Al, Cu) [40]. The shielding material and configuration of its layers needs to be experimentally tested and evaluated for different kinds of particles and energies.

5.1 Radiation effects in LEO

Table 5.1 summarizes the commonly encountered radiation effects in materials, EEECs and COTS components in LEO and their sources. As this thesis is dealing with shielding of space systems, the mass, density and volume of the shielding material plays an important role. This chapter explains how each particle type interacts with materials, what are the secondary radiations, and gives a brief introduction to carbon composites.

Radiation effect	**Important primary radiations**	**Important secondary radiations**
Total ionising dose	Trapped protons, light ions Trapped electrons Solar protons	X rays and gamma rays from electrons, electrons and neutrons from high-LET particles i.e. protons, ions
Displacement damage	Trapped protons, light ions Trapped electrons Solar protons	Neutrons, low-energy high-LET particles i.e. protons, ions
Single event effects	GCRs (protons, ions)	Spalling, fragmentation, nuclear reaction products

Table 5.1: Summary of the radiation effects in materials, EEECs and COTS components and the corresponding radiation environment that can be encountered in LEO.

5.2 Shielding of electrons

Electrons, which are low-interacting particles and have low mass, are easily deflected or scattered during interaction with a shielding material depending on the material density. The deflection is larger for high-Z materials, for which however occurs the bremmstrahlung or stopping radiation process. This results in the secondary production of X rays and gamma rays especially for high-energy electrons. In addition, electrons in matter exhibit the so-called multiscattering process in which the electrons lose energy but scatter and change their direction many times. Their trajectory and penetration range in matter depend on their energy and are expressed in terms of the electron free mean path [41]. Similarly to photons (X rays, gamma rays), electrons are attenuated across matter exponentially.

High energetic electrons at first stage are best shielded by low-Z materials, in order to suppress the production of secondary radiation/stopping radiation (X rays, gamma rays). As a second stage, for low energies, low-Z materials are more effective. The problem with X rays and especially gamma rays is that they are penetrating. Thus, it is recommended to avoid the production of secondary stopping radiation. Therefore, the ideal shielding for high energies is a combination of low-Z material (in front) and high-Z material at the back. The electron stopping power for commonly used shielding materials is shown in Figure 5.1. It shows that up until $\approx$ 4.5 MeV, aluminum (atomic number 13) and tantalum (atomic number 73) have better stopping power, but after 4.5 MeV, lead (atomic number 82) and tungsten (atomic number 74) show better results. The high-Z materials however for energetic electrons ($\geq$ 5 MeV) produce significant secondary radiation (stopping radiation X ray and gamma rays).

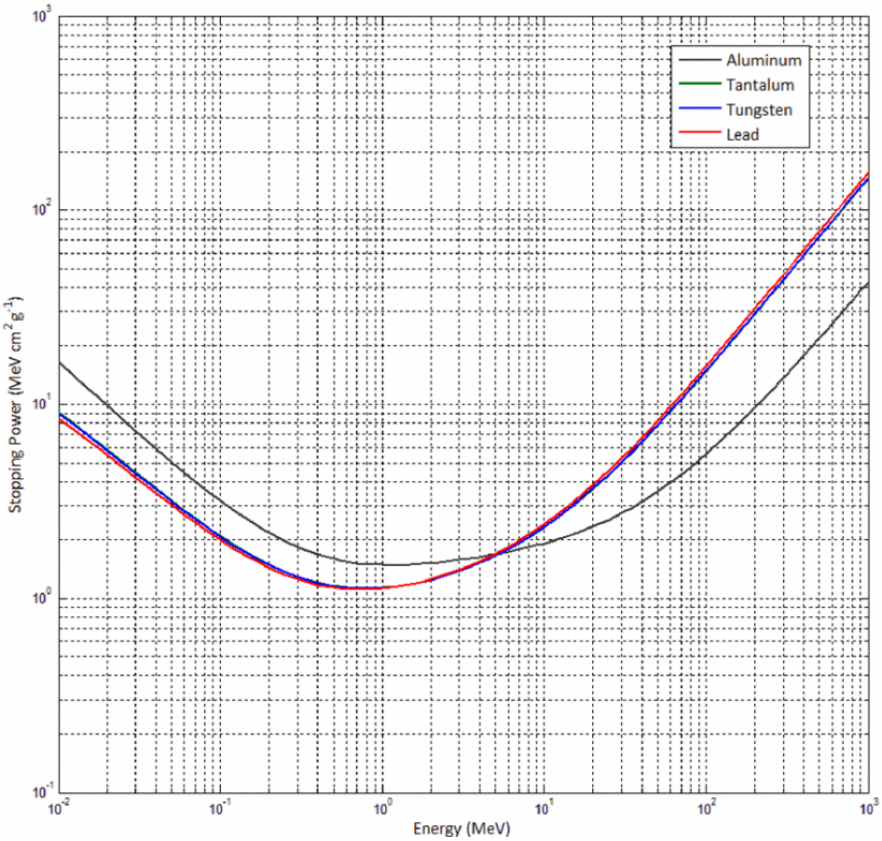

Figure 5.1: Electron stopping power for different materials [39]. Dependence on electron energy (x axis) in wide range. X-rays correspond to the range from few keV to 100 keV. Gamma rays are > few tons of keV.

5.3 Shielding of protons

Being highly interacting particles and having higher mass than electrons, protons exhibit different interaction and shielding properties in matter than electrons and photons (X rays, gamma rays). Protons and heavy charged particles such as ions gradually loose energy by ionization across the material and exhibit little or no scattering (unlike electrons) and exhibit well defined range which depends on the proton's (or ion's) energy [41]. Protons are shielded primarily by the density of the material - namely by the planar density i.e. by the mass/area of the material [39]. The proton stopping power for different materials can be seen in Figure 5.2. The graph shows that tungsten and aluminum have better stopping power than aluminum or lead. The stopping power decreases for all materials for high energy protons.

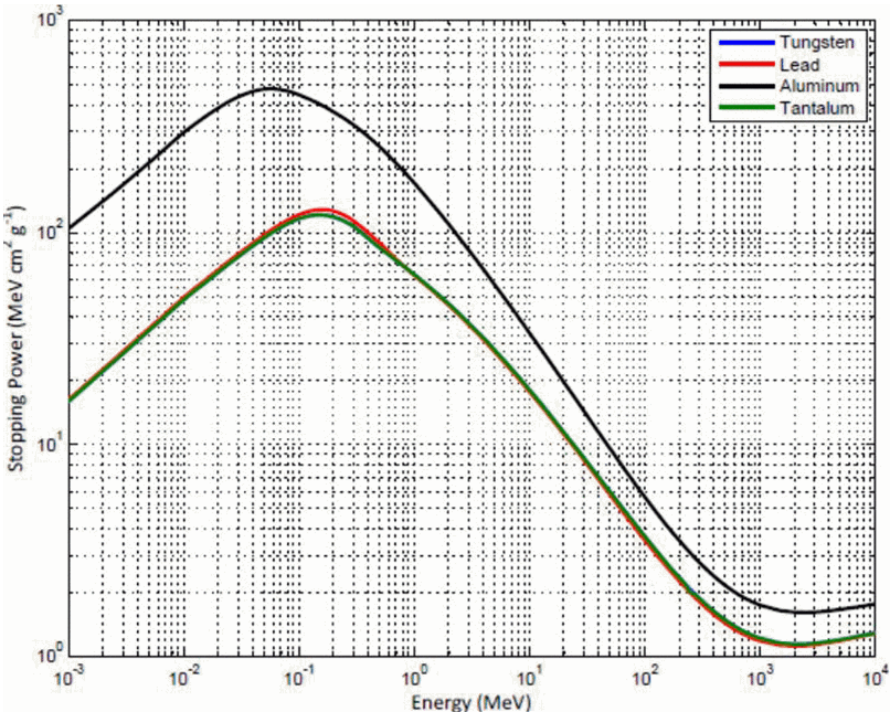

Figure 5.2: Proton stopping power for different materials [39].

5.4 Shielding of X-rays and gamma rays

X-rays and gamma rays are low intensity interacting particles and exhibit characteristic interaction and shielding properties across matter. This interaction in matter depends on the particle energy and proceeds over three processes (see Figure 5.3):

- **Photoelectric effect** - This effect is prevalent for photons of energies $\leq$ 100 keV and materials with high atomic number [42]. The photon's energy is absorbed, creating an excited photoelectron and leaving a positively charged vacancy (called *hole*). If the photon has higher energy, an inner electron can get excited, fill the created *hole* and create a secondary *characteristic* X-ray photon [37]. The energy of this secondary photon is characteristic to the interacting element.
- **Compton scattering** - This effect is prevalent for energies in range from 100 keV to 4 MeV [42]. A photon collides with an electron and loses some of its energy, creating a scattering reaction. The product is a free recoil electron and a redirected (scattered) photon, with less energy than the incident photon [37].
- **Pair production** - This effect occurs mostly for high energy photons above 4 MeV in heavy elements [42]. Pair production is the dominant energy-loss mechanism for high energy gamma rays. Incident gamma ray interacts with the nucleus and creates an electron and a positron (positively charged electron). The rate of the pair production increases approximately with the atomic number of the target element [37].

X-ray photons have low energy, therefore X-ray shielding depends mainly on the

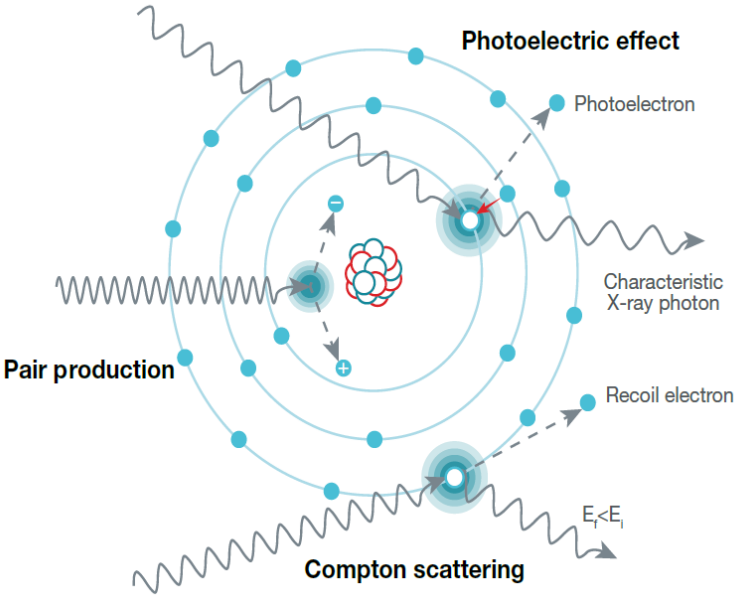

Figure 5.3: Illustration of the primary photon interaction mechanisms in matter - the photoelectric effect, Compton scattering and pair production, described in text [37].

probability of Compton scattering and photoelectric effects occurring when the incident photons traverse the shielding material [24].

Generally, the most used material for shielding X-rays is lead and tungsten. Due to their high Z number and high density, they are very efficient at shielding X-rays, with low cost and minimum or low production of secondary radiation. The downsides of lead-based shielding materials are high toxicity, heavy nature, poor flexibility, low chemical stability and poor mechanical and thermal properties unsuitable for space deployments [24].

5.5 Secondary radiation

The radiation environment for satellites in LEO is further complicated by secondary radiation, which is product of interaction of energetic primary radiation in matter and materials, including the shielding elements themselves, see Figure 3.3. One such example of secondary radiation is the so called *Bremmstrahlung* (stopping radiation) in the form of X-rays and gamma rays from the passage of light charged particles, namely energetic electrons across high-Z materials such as lead and tungsten, see Figure 3.3. This secondary effect is created by energetic electrons being scattered and slowed down, for example by the satellite's shielding material, as depicted in Figure 5.4. High-Z materials are more prone to creating secondary radiation to energetic electrons [41]. One 1 MeV gamma ray can penetrate up to 1 cm of aluminum with only 10 % intensity attenuation [25].

Another example of secondary radiation is nuclear reaction products such as neutrons and charged particles from high-LET energetic heavy charged particles traversing matter and materials including shielding elements themselves. High energy protons in interaction with satellite's materials thus produce secondary protons, neutrons, electrons and X-rays.

These particles can become relevant as they can further ionize and reach further beyond the path of the primary particle [25].

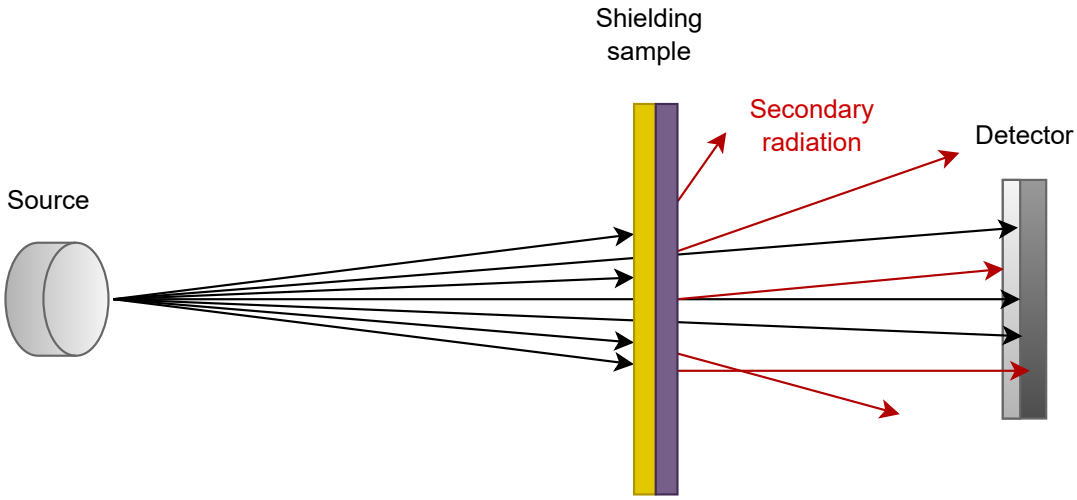

Figure 5.4: The shielding sample can consist of materials that cause significant secondary radiation. These secondary particles can contribute to the radiation dose and damage behind the shielding. They change the radiation field in terms of composition, spectrum, direction and penetration.

5.6 Carbon composites

Different materials have different and distinct shielding efficiency for different particles of different energies. Since LEO is made of different radiation fields, a convenient approach is to combine different materials of both low-Z and high-Z number into one composite sample. Moreover, rocket launches and satellite in-orbit deployment in open space place stringent requirements and limitations on the materials that can be used. They must survive and resist the harsh physical conditions in terms of not just radiation itself, but also thermal (huge temperature gradients e.g. -70°C to +80°C in LEO), high vacuum, mechanical stress and shock as well as plasma electrostatic charging. One more requirement is to use and keep the materials small and of low-Z number in order to minimize weight and size to keep compact and low-cost deployments.

Composite materials are usually made of resin and reinforced to enhance mechanical strength. By combining suitable materials and reinforcement, the composite material can become better at shielding radiation than single-matrix materials. The composition should also make the material more shock and heat resistant, while maintaining light weight [43]. The layout and orientation of the assembled samples are equally important too. Energetic electrons are overall best shielded by placing a low-Z material in the front (to slow down the energetic particles) and a high-Z element behind (to shield the slowed down electrons and the stopping radiation X-rays and gamma rays).

The resin is typically an organic polymer such as polyether ether ketone (PEEK), polyethylene (PE), polyimide (PI), or polypropylene (PP), selected based on its chemical and thermal properties [44]. The reinforcement can be for example Carbon fiber (CF),

Glass fiber (GF) or silicon carbide. The complete composites then can be for example carbon fiber reinforced epoxy resin (CFER), graphite fiber reinforced polymer (GFRP) or carbon fiber reinforced polymer (CFRP), all tested in this thesis. As a material like CFRP has a low specific weight, it acts as a good shield against particles with similar weight - alpha particles, protons or neutrons.

A study using Monte Carlo simulations was conducted, that found that a hydrogenous composite (PE) performed better than aluminum. It further showed, that with shielding thickness higher than 10 $g \cdot cm^{-3}$, the mass needed for shielding could be reduced by more than 77 % for GCRs and 33 % for SPEs [45]. Another study found the shielding effectiveness of polymer and composite materials better than aluminum's for GCR and SPE radiation conditions using simulations [46]. Furthermore, data from the study showed that the material's composition, density, and the ratio of number of nucleons to volume directly affect its performance.

Research already shows that carbon materials can provide suitable shielding from space radiation. The study of influence of structure on radiation shielding effectiveness of graphite fiber reinforced polyethylene (GFRP) composite was performed using simulations [47]. It suggests that pure graphite can have better shielding properties than aluminum for some radiation fields. Nevertheless, as its mechanical properties are insufficient, it needs to be combined with a different material. The study found the combination of PE at the surface layer, followed by graphite, provided better radiation shielding. The works supportive of further research of carbon composites as shielding materials are extensive (2004 [48], 2015 [47], 2019 [49], 2020 [43], 2021 [44]).

To support the simulations, in-orbit measurements of novel carbon fiber composite on board the CubeSat VZLUSAT-1 [19] [21] were reported. The composite was based on a combination of a carbon fibermesh and a radiation-protecting reinforced resin. They found that while the shielding ability of the composite stacked with tungsten reference sheet is almost constant with increasing energy, the carbon composite shows better results for lower energy of incident X-rays and electrons whereas its efficiency slightly falls with higher energies. It is however important to mention, that the weight of the composite shield was nearly 10 times lower. Further studies from experiments on board the VZLUSAT-1 suggest that the studied carbon composite is adequately resilient against the influence of mechanical stress, which was simulated by vibrations [20] [22].

Chapter 6

Methodology and design of measurements

To test and determine the shielding efficiency of a material and its suitability for space deployment, real and high-resolution experiments are valuable and are performed in this work. The shielding samples are ideally exposed to various radiation types of different energies. The accuracy of the measurement depends on the method, measurement design and setup, like the geometry of the detector to the radiation beam and placement of the shielding sample. This thesis deals with up to 41 samples for one experiment. This chapter explains the design of the measurements, the detectors used in the experimental measurements and the radiation fields to which the samples were exposed.

6.1 Geometry and setup

The basic setup for radiation detection and visualization is depicted in Figure 6.1. The radiation beam generated by a radiation-generating device (source) directly hits the detector. This type of setup was used for measurement of reference open beam values for many experiments. As can be seen in Figure 8.19 or Figure 8.25, in several experiments, the beam was smaller than the detector sensitive area, so a region of interest had to be selected to accurately calculate the reference values.

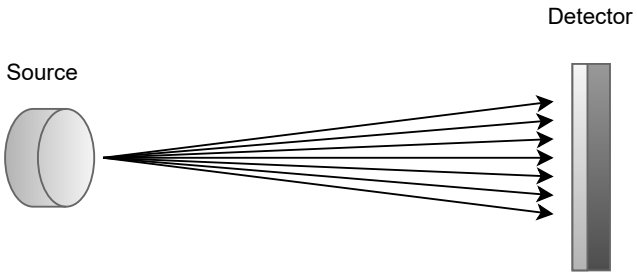

Figure 6.1: Open beam measurement setup. The radiation beam generated by the source directly hits the radiation detector.

In order to measure the effect of the shielding sample, the setup depicted in Figure 6.2 was used for measurement of shielded radiation beam in the electron and proton experiments. The radiation particles are absorbed, slowed down or deflected by the shielding sample, therefore fewer particles of lower energy pass through and reach the detector. The difference between values from the open beam measurement and this shielded measurement provide the shielding efficiency of a sample for a given radiation field.

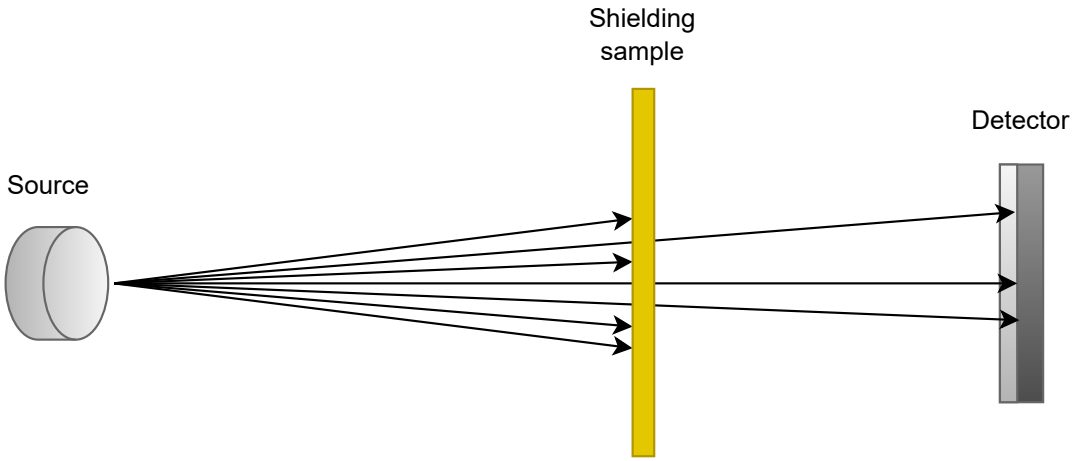

Figure 6.2: Shielded beam measurement setup. Part of the radiation beam generated by the source is absorbed, slowed down or deflected by the shielding sample.

As the radiation-generating devices are not perfect, the radiation beam intensity and flux can fluctuate throughout time. Therefore, another setup was also used for accurate shielding efficiency measurement as depicted in Figure 6.3 and Figure 6.4. This type of setup provides one data set for both the open beam value and the shielded beam value taken at the same time. This type of measurement is however time-consuming, as individual samples have to be precisely positioned to only cover a part of the detector, and the regions of interest have to be manually selected for every sample.

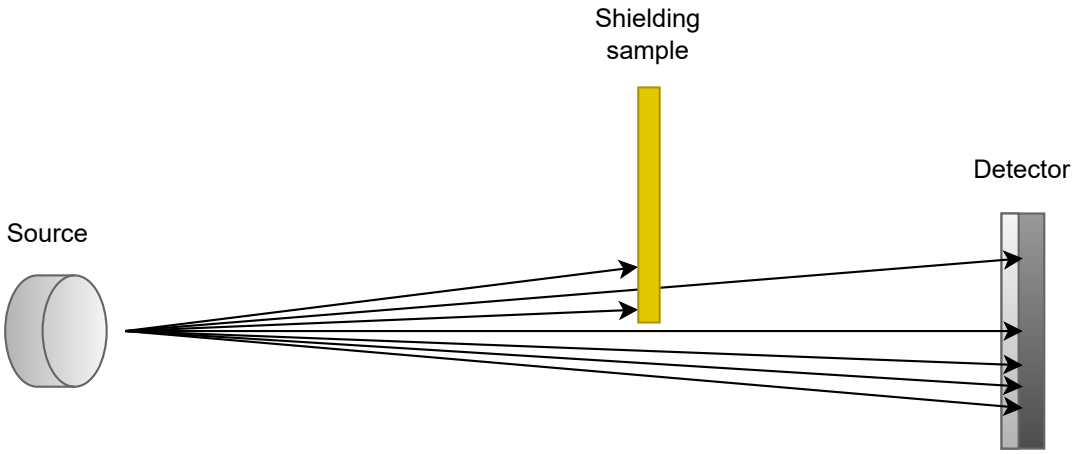

Figure 6.3: For certain measurements, only part of the detector was covered by the shielding sample. This results in one data set with both open beam and shielded areas, as illustrated in Figure 6.4. This setup provides the most accurate comparison of open beam to shielded beam values, but is time consuming to set up and also to process.

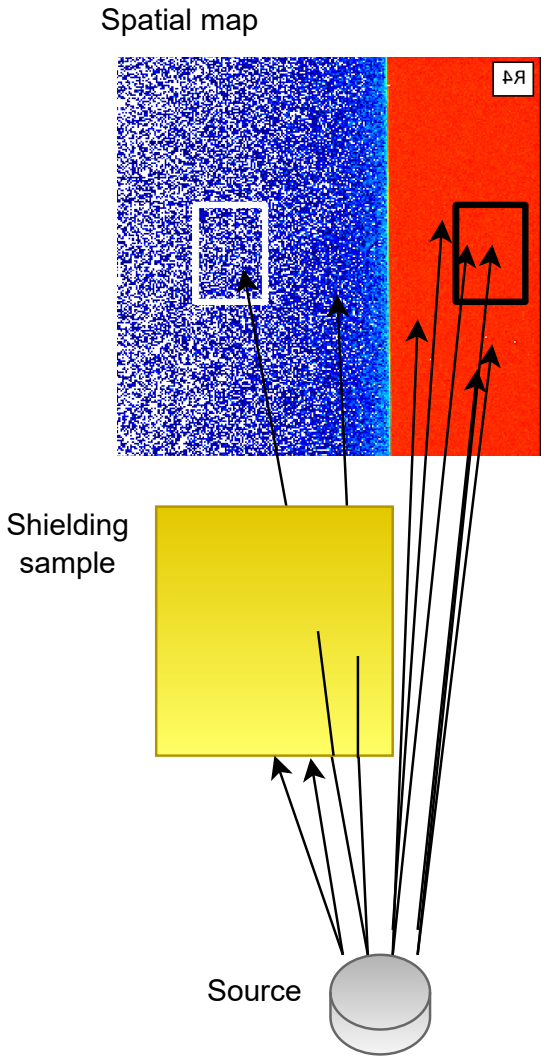

Figure 6.4: Detailed illustration of setup in Figure 6.3. The red part represents the open beam counts and the blue part represents the shielded beam. Each part has a defined region of interest - white and black. More detailed spatial maps are given in Chapter 8.3. The recorded data contains only a small part of the shielding sample.

6.2 Semiconductor pixel detectors

The hybrid pixel semiconductor detectors developed by Advacam (ADV) used in this thesis are all of the Medipix type, a photon counting and particle tracking pixel detector ASIC chip developed by the international collaboration Medipix based at CERN. The full device operates like a radiation camera, where each individual particle that hits the pixels is detected and counted with quantum imaging sensitivity and per-pixel spectral, counting and/or time response [50]. This results in high-resolution, high-contrast, noise hit free images, suitable for a wide range of radiation imaging and particle tracking applications [51].

Figure 6.5 shows the hybrid semiconductor pixel detector Timepix consisting of a semiconductor radiation-sensitive sensor bump-bonded to the ASIC Timepix readout chip. Various semiconductor sensors can be used of different material (Si, CdTe, GaAs) or thickness (e.g. 100, 300, 500, 700, 1000, 1500 µm). The detectors operate at room temperature and in vacuum including particle accelerators and open space.

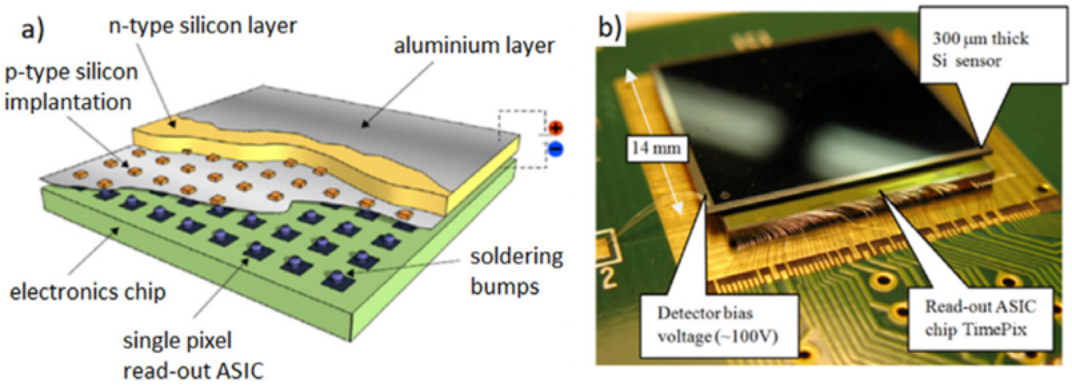

Figure 6.5: Illustration (a) and photo (b) of the hybrid semiconductor pixel detector Timepix consisting of a semiconductor radiation-sensitive sensor (300 µm silicon, full size 14 mm × 14 mm — shown in yellow) bump-bonded to the ASIC Timepix readout chip (shown in green) consisting of an array of 256 × 256 pixels (total 65,536 independent channels) [51].

The Medipix pixel detectors[1] provide direct conversion single photon counting for unique noiseless (i.e. without dark current) detection sensitivity. Every single radiation quanta such as a photon of X-ray radiation detected in individual pixels are processed and counted. Figure 6.6 depicts the difference between direct and indirect conversion, the latter being used by most other radiation detectors. In the indirect conversion detectors a scintillation layer is attached on top of a photodiode manufactured on a simple CMOS circuit. Here, the X-rays are first converted into visible light in the scintillation layer that is then converted into electric charge in the photodiodes. In direct conversion detectors, each pixel volume of the semiconductor sensor is directly connected to the highly integrated CMOS ASIC chip using a conductive solder bump. The X-rays are converted into electric charge in the semiconductor crystal and immediately processed and readout by the per-pixel analog and digital circuitry in the ASIC chip. This direct

[1] `https://advacam.com/technology`

conversion photon counting capability enables high sensitivity for enhanced resolving power to discriminate particle types (electrons, protons, ions, X rays, gamma rays) and accurately measure the energy of single particles. In addition, the pixelated architecture and high spatial granularity provide imaging, tracking and directional response.

Standard radiation detectors such as Space X-ray Detectors[2] (SXDs) exhibit limited resolution and limited sensitivity and thus were not used for measurements as Timepix detectors are superior and more technologically advanced, providing more accurate information in wider range for a different range of measurements and applications.

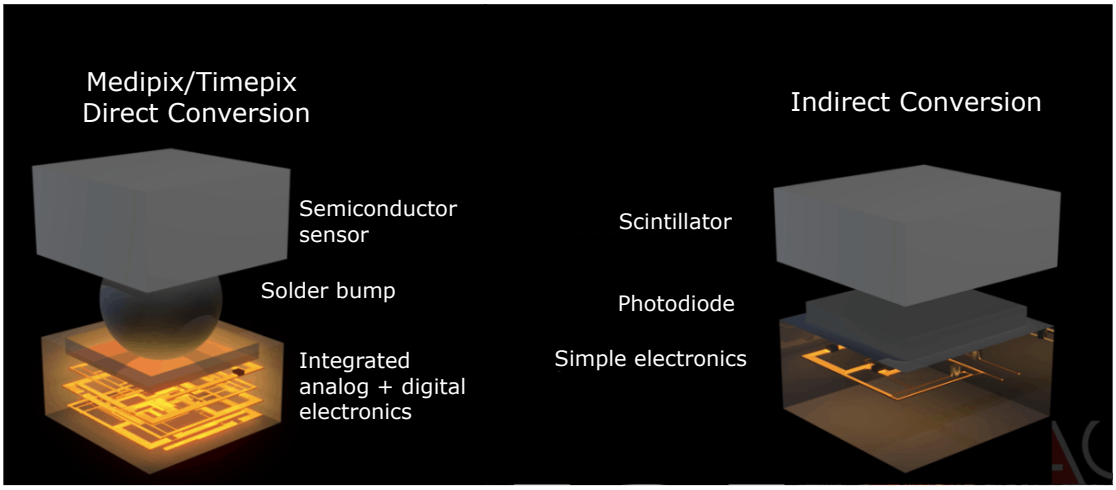

Figure 6.6: Illustration of comparison at the single pixel scale of a direct conversion (left) and indirect conversion (right) detection of radiation. Source: ADV.

The Timepix detector registers all particles coming from any direction as a wide field-of-view radiation camera of angular acceptance essentially full angle 2π field of view (FoV) [50]. Energetic radiation particles incident from the back of the chip are also registered, providing essentially a full 4π FoV. In the case of energetic charged particles, information on their direction can be registered from cluster pattern recognition analysis [51]. The vector of trajectory in 3D is derived from analysis of the micro-meter scale cluster track in the pixelated sensor illustrated in Fig. 6.7. The tracking directional information is expressed in the form of two angles: polar (in the plane of the sensor with respect to the axis of the pixel matrix) and elevation (angle between the vector of trajectory and the sensor plane) [51].

6.2.1 Timepix

The Timepix ASIC chip provides a high density matrix of 256 × 256 energy sensitive pixels (total of 65,536 pixels) [52]. The pixel pitch is 55 µm, resulting in a sensitive area of 14 mm × 14 mm = 2 cm^2. The chip is then bump-bonded to a radiation sensitive semiconductor sensor (such as Si, CdTe, GaAs) of certain thickness e.g. 100 µm to 1500 µm). The hybrid architecture provides dark-current free noiseless detection. Depending on the particle type and direction of incidence, omni-directional fluxes of up to 10^6 particles per second per cm^2 can be recorded in full spectrometric tracking

[2] https://www.serenumspace.com/products/space-X-ray-detector

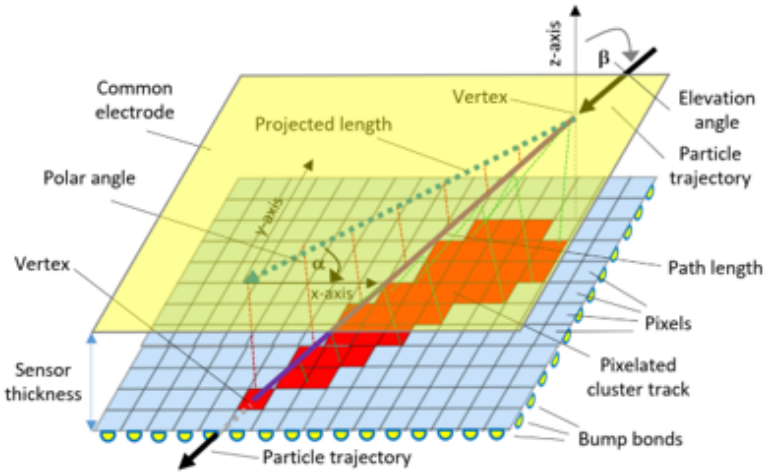

Figure 6.7: Illustration of particle tracking in Timepix for energetic charged particles. Microscale pattern recognition analysis of the registered signal (cluster of pixels—shown in red) enables deriving the path length in 3D (purple line) across the sensitive volume with entrance and exit points (labeled vertex points), the projected length (dash green line) on the plane of the sensor and the projected polar angle (α) and an elevation angle (β) of the particle trajectory. The asymmetric morphology of the cluster along the sensor thickness (broad cluster track on one end and narrow cluster track on the other), which is due to the charge sharing effect along the depth of the sensor (illustrated by dash green lines), is exploited to determine the particle direction in 3D [51].

mode. Control, configuration and readout can be performed by the PIXET software[3]. The detector provides one per-pixel channel which can measure the Energy, Count or Time in high resolution and wide range. In the measurements performed, it used the per-pixel energy mode, with frame based readout type, with the output being a .clog file, described further in this chapter. The Timepix detectors used in this work were equipped with Si or CdTe sensors and were operated with MiniPIX readout interfaces (described below), developed by ADV[3].

6.2.2 Timepix3

Timepix3 is a new generation pixel detector readout chip from Timepix for enhanced X-ray imaging and particle tracking developed by the Medipix3 collaboration. Compared to Timepix the Timepix3 detector offers two per-pixel signal readout channels (e.g. Energy and Time or Energy and Counting), zero dead time, and data driven readout for greatly faster data transfer. Similar to Timepix, the Timepix3 detector provides a high density matrix of 256 × 256 energy sensitive pixels (total of 65,536 pixels). The pixel pitch is 55 µm, resulting in sensitive area of 14 mm × 14 mm = 2 cm^2. Control, configuration and readout can be also performed by the PIXET software. Timepix3 detectors also provide full spectrometric tracking mode, with two per-pixel channels (combination of Energy, Count or Time) and are capable of operating in both frame based mode and data driven mode. The Timepix3 detectors used in this work were equipped with 500 µm

[3] Provided by Advacam, which is a Prague based spin-off of the CTU Prague and the CERN based Medipix collaboration

sensors and operated with AdvaPIX and MiniPIX readout interfaces, developed by ADV.

6.2.3 Medipix3

While Timepix detectors are fully spectral (precise and wide-range measurement of the deposited energy per-pixel) suitable for detailed event-by-event spectral-tracking measurement, Medipix detectors are designed for high-intensity energy sensitive photon counting suitable for radiation imaging. They are readout with fast data rate electronics such as the ModuPIX readout interface from Advacam. The Medipix3 detectors provide also a high density matrix of 256 × 256 energy sensitive pixels (total of 65,536 pixels). The pixel pitch is 55 µm, resulting in sensitive area of 14 mm × 14 mm = 2 cm^2. These detectors work on the principle of low-energy threshold or energy window and provide one per-pixel channel - counting. The Medipix3 detector used in this work is the `WidePIX 2×5 - MPX3 1000 µm CdTe`, developed by ADV. This large area detector (LAD) provides a high-resolution radiation camera of full sensitive area 28 mm × 70 mm = 2×5 TPX3 chips, equaling 512 px × 1,280 px.

6.2.4 Radiation Camera MiniPIX-TPX/TPX3

The radiation cameras are full devices which consist of a TPX ASIC chip/sensor assembly, chipboard and full readout board (chipboard and motherboard) with single USB output interface to connect to standard PC. The MiniPIX is a miniaturized camera, with low power and maximum rate of 2.35 million hit pixels per second.

The MiniPIX [53] camera shown in Figure 6.8 is a portable small USB camera that contains one Timepix chip detector. The detector in the measurements had a Silicon sensor of 500 µm thickness, the detection efficiency for photons (X rays, gamma rays) is shown in Figure 6.9. The resolution for X-ray imaging depending on the setup geometry is 9 lp/mm (i.e. 9 image bins per milimeter, i.e. ≃ 120 µm) and readout speed is 45 frames per second. The photon counting speed is up to 3 × 10^6 photons per second per pixel. Pixel modes of operation are Counting, Time-over-Threshold and Time-of-Arrival. It uses a USB 2.0 interface, has dimensions of 88.9 mm × 21 mm × 10 mm (L × W × H) and weights 25 g. Power, control and data readout use a single USB connector to PC. It operates in room temperature. Together with the software PIXET (see Section 6.2.7) it provides plug-and-play operability and online response.

Figure 6.8: The MiniPIX TPX radiation camera. Operation, control and readout require a single USB 2.0 connector/cable.

Figure 6.10 shows the MiniPIX TPX3 [54] camera, containing a Timepix3 detector. The detector in the measurements had a Silicon sensor of 500 µm thickness. The detection efficiency for photon detection is described in Figure 6.9, depends on the photon energy

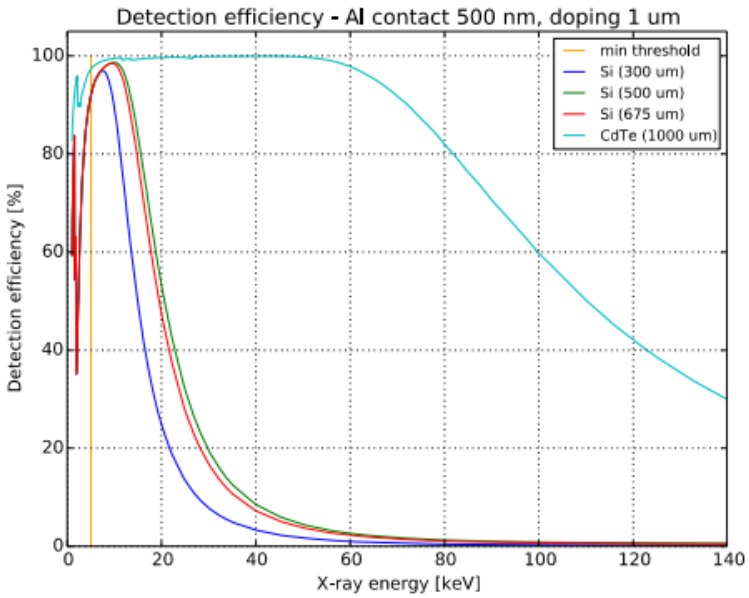

Figure 6.9: Detection efficiency for photon detection for the Timepix/Timepix3 detectors equipped with different semiconductor sensors - material, thickness (see label) [53]. The detection efficiency decreases for higher energies. CdTe thick sensors provide higher detection efficiency for photon detection.

and the sensor material and thickness as shown in wider energy range in Figure 6.11 (in Figure 6.11 the full 100 % detection efficiency is displayed as 1.0). This detector has two modes of data readout: *I*) data-driven mode - so called pixel mode, where individual single hit-pixels and thus the detected particle is readout immediately and continuously essentially without readout dead time or *II*) frame mode, supported also by the Timepix chip, where the particles are accumulated in images, so-called frames, which are readout at a speed up to 16 frames per second. The time resolution at the per-pixel level is 1.6 ns. The overall energy resolution is in the range of 5-8 %. Pixel modes of operation are energy (i.e. Time-over-Threshold) and time (i.e. Time-of-Arrival). It uses a µUSB 2.0 interface, has dimensions of 80 mm × 21 mm × 14 mm (L × W × H) and weights 41 g. The detector was mostly operated in frame mode, the output was a .clog file, described further in this chapter. Power, control and data readout use a single USB connector to PC. It operates in room temperature. Together with the software PIXET (see Section 6.2.7) it provides plug-and-play operability and online response.

Figure 6.10: The MiniPIX TPX3 radiation camera. Operation, control and readout require a single USB 2.0 connector/cable.

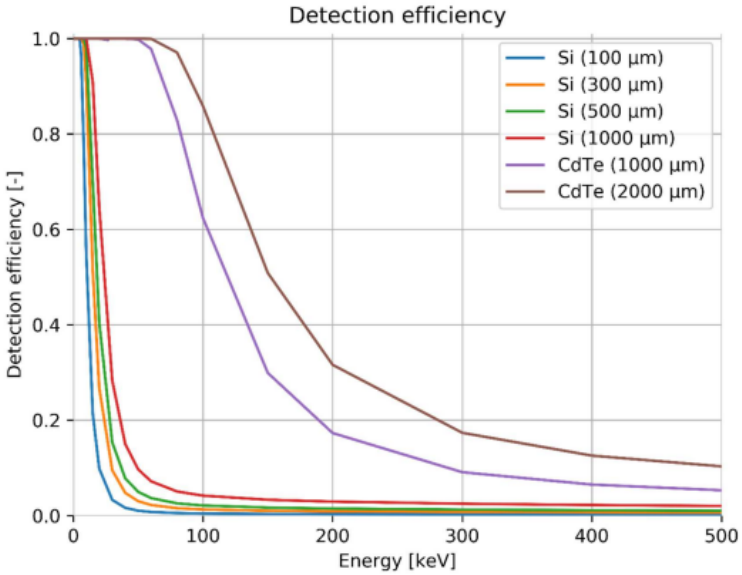

Figure 6.11: Detection efficiency for photon detection for the Timepix/Timepix3 detectors equipped with different semiconductor sensors - material, thickness (see label) [54]. A greater energy range is shown. Similar to Figure 6.9. Notation 1.0 on the y axis means full i.e. 100 % detection efficiency.

6.2.5 Radiation Camera AdvaPIX-TPX3

The AdvaPIX cameras are full performace, high speed radiation cameras with data readout able to acquire up to 40 million pixel hits per second.

The AdvaPIX TPX3 [55] shown in Figure 6.12 contains the Timepix3 detector. The detector in the measurements had a Silicon sensor of 500 µm thickness, for the detection efficiency of photons, see Figures 6.9 and 6.11. It operates in a data driven i.e. pixels mode, so every single particle hit is registered and readout into a continuous stream of data. The device also measures the position, energy and time-of-arrival of each detected quanta but with greater data rate speed. The time resolution is 1.6 ns. Pixel-level modes of operation are Time-over-Threshold, counting and Time-of -Arrival. It uses a USB 3.0 interface, has dimension of 125 mm × 79 mm × 25.5 mm (L × W × H) and weights 503 g. Furthermore, it requires cooling - at least passive (thermal conductive contact), but ideally active cooling e.g. with AdvaCOOLER system built and provided also by Advacam. This detector was operated in data driven mode, the output was a .t3pa file, described further in this chapter.

Figure 6.12: The TPX3 AdvaPIX radiation camera. Operation, control and readout require a single USB 3.0 connector/cable. Power is supplied by additional/separate DC +5 V connector/cable.

6.2.6 WidePIX 2x5 - MPX3

The WidePIX 2x5 - MPX3 [56] device shown in Figure 6.13 camera consists of 2×5 Medipix3 devices providing a so-called Large Area Detector (LAD). The camera used in the measurements is equipped with CdTe 1000 µm edgeless sensor tiles closely packed for smooth continuous radiation imaging of large samples. For the detection efficiency of photons which is given by the sensor (material, thickness) see Figures 6.9 and 6.11. The resolution is 9 lp/mm (i.e. 9 image bins per milimeter, i.e. $\simeq$ 120 µm) and readout speed is 20 frames per second. Pixel modes of operation are Counting in Single Pixel Mode (SPM) or Charge Summing Mode (CSM) [57]. It uses a USB 2.0 interface, has dimension of 213 mm × 60 mm × 40 mm (L × W × H) and weights 1,800 g. This device also requires cooling - at least passive (thermal conductive contact), but ideally active cooling e.g. with AdvaCOOLER system built and provided also by Advacam. For this

work, the detector was operated in Single Pixel Mode and the output was a .txt file with a matrix containing count values for pixels.

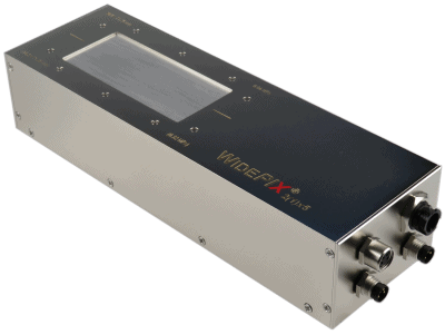

Figure 6.13: The WidePIX 2x5 - MPX3 device. It requires 3 connectors: 1 × USB 2.0 (control, operation, readout), 1 × +24 V DC connector (power), 1 × active liquid cooling.

6.2.7 Control and readout software PIXET

Control and operation of the detector including on-line response, data readout and limited data pre-processing are performed by the PIXET software [58]. Figure 6.14 shows photo of the software being used with a TPX3 detector for the X-ray micro-focus tube measurement.

The PIXET software is a multiplatform software developed by ADV for control and readout of data from the Medipix chip family. It supports most available Medipix chips - Medipix2, Medipix3, Timepix, Timepix Quad and Timepix3. PIXET has an open architecture that supports different and multiple detectors and supporting devices, for example for control of step motors. This software is provided with the detectors and is freely available. Besides control and data acquisition, PIXET is also able to visualize data online, configure the detector, save measured data in multiple formats, equalize and configure the various MPX/TPX chips, calibrate measured data and provide information about clusters.

6.2.8 Raw data formats

According to the measurement mode, the raw data from the pixel detectors can be stored in different file formats. For Timepix detectors, the data is stored as cluster log (clog) file. In the **clog** format, the data are arranged in frames, with the pixelated clusters, each of which corresponding to a single registered particle, represented as a sequence of individual pixels (each pixel within a `[]`) arranged in separate rows:

```
Frame 1 (UNIX_TIME, ACQ_TIME s)
[X_1, Y_1, ToT_1] [X_2, Y_2, ToT_2] \n
[X_1, Y_1, ToT_1] [X_2, Y_2, ToT_2] [X_3, Y_3, ToT_3] ...\n
...
Frame 2 (UNIX_TIME, ACQ_TIME s)
[X_1, Y_1, ToT_1] [X_2, Y_2, ToT_2] ... \n
....
```

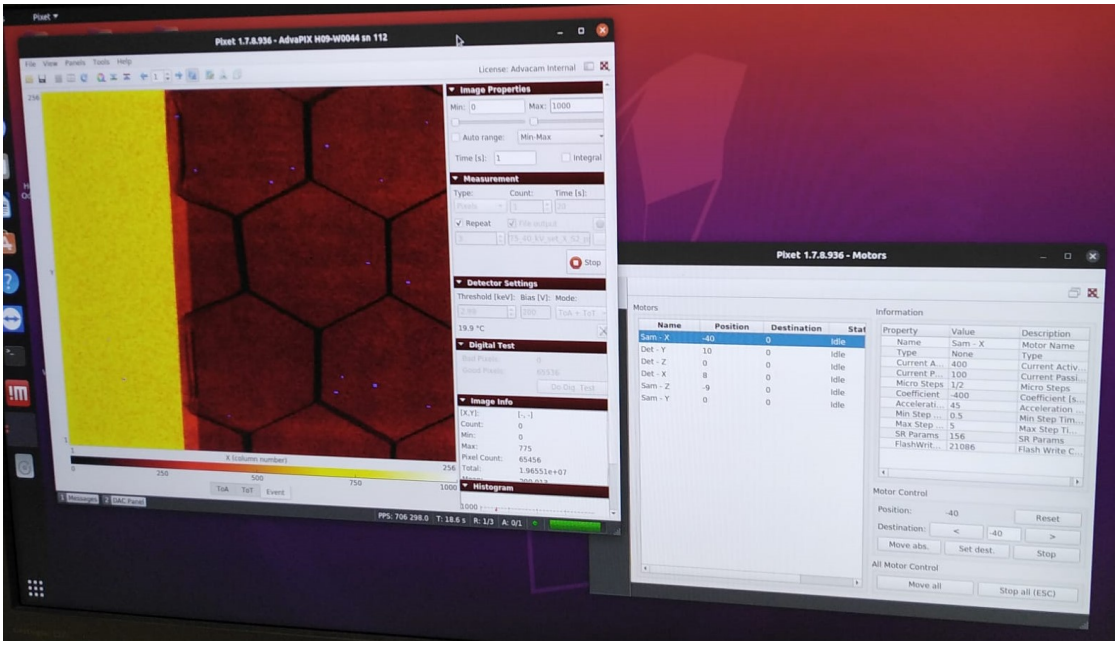

Figure 6.14: The software tool used for control of the measurements - PIXET. In the left window, an ongoing measurement with a single chip (TPX3) detector camera can be seen, with online non-calibrated visualization of registered radiation. The full sensor-chip pixel matrix is displayed showing the integrated per-pixel counting mode of the transmitted X-ray field across a shielding sample (composite in honeycomb sandwich layout). The right window shows an interface for controlling the step motors.

where `'ACQ_TIME'` is the acquisition time of the given frames in seconds and `'UNIX_TIME'` is absolute time stamp in format UNIX time stamp in seconds. Every line starting with `'['` is one cluster and in each square brackets is one pixel and its information `'[x coordinate, y coordinate, time over threshold]'`. The clog data format can be also generated for the Timepix3 detector, when used in frame mode. Additionally, the Timepix3 detector can be used in data-driven mode and generate pixel-readout data in the **t3pa** format:

```
Index   Matrix Index    ToA     ToT     FToA    Overflow
0       matrix_idx_0    ToA_0   ToT_0   FToA_0  overflow_0 \n
1       matrix_idx_1    ToA_1   ToT_1   FToA_1  overflow_1 \n
2       matrix_idx_2    ToA_2   ToT_2   FToA_2  overflow_2 \n
....
```

where each row represents one hit-pixel and its information `'[pixel index number, position on the matrix representing the detector, time of arrival (ToA), time over threshold (energy in ToT units), fast time of arrival (FToA), overflow]'`.

6.3 Radiation sources

For this work, four experiments were conducted and analyzed including extensive data processing: *I*) X-ray robotic scanner with 50 keV energy was used in Advacam and

Radalytica Prague laboratory. This technology is used to provide high-resolution, wide range and enhanced contrast X-ray images (2D radiographies and 3D CTs). *II*) and *III*) experiments also with X-ray radiation field, using a table-top setup (called coffin in Advacam), a micro-focus tube for 40 keV and 120 keV energies, respectively. *IV*) a microtron accelerator experiment, generating energetic electrons, like those encountered in LEO orbit (the Earth radiation belts) with energy 5 MeV. As the radiation environment in LEO in large part contains also protons, data from previous experiments performed on part of the same samples was used and analyzed, including extensive data processing. This final experiment *V*) was conducted with a cyclotron accelerator at the NPI CAS Rez near Prague, generating protons with energy 31 MeV.

6.3.1 X-ray robotic scanner

Radalytica's[4] Robotic Imaging System RadalyX[5] is an X-ray non-destructive non-invasive imaging system for large and bulky objects that combines single particle counting X-ray imaging detectors for high quality images with the flexibility of highly automated robots. The key parts of the scanner are two robotic arms with 6 joints. One arm holds an X-ray micro-focus tube. The second arm holds an LAD imaging detector assembled of various TPX3 or MPX3 chips in e.g. $5 \times 1 = 5$ or $5 \times 2 = 10$ chips array. The X-ray tube / detector pair can, thanks to the robots, move and rotate freely around the fixed sample. The robots are moving synchronously so that the mutual position of the X-ray tube and detector is well defined and registered under all circumstances.

In the experiment for this thesis, as can be seen in Figure 6.15, the rack with samples was stationary, while the robotic arms moved the X-ray source and the detector horizontally along the samples, to create images as seen in Figure 6.16.

The radiation beam had energy spectrum up to 50 keV and the beam was perpendicular to the detector. The detector used for this experiment was the WidePIX A06, which is a 2×5 array of MPX3 1000 µm CdTe sensor-chip assemblies. Each detection period of a given sample measurement was 10 s.

[4] A spinoff from Advacam, also based in Prague

[5] `https://www.radalytica.com/en/robotic-imaging-system.html`

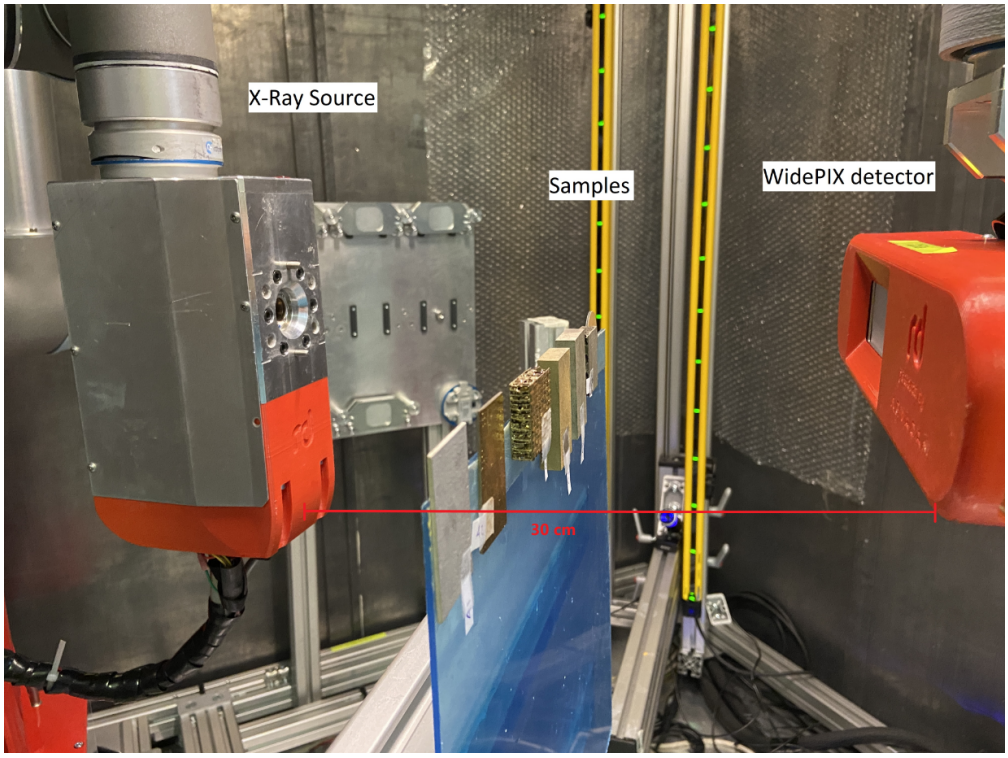

Figure 6.15: Setup for measurements with the X-ray robotic scanner. The rack with samples is stationary during the measurements, while the X-ray source and detector are operated via a computer application and moved in sync by the pair of robotic arms. The system provides high-resolution 2D X-ray radiographies and 3D X-ray micro CT imaging.

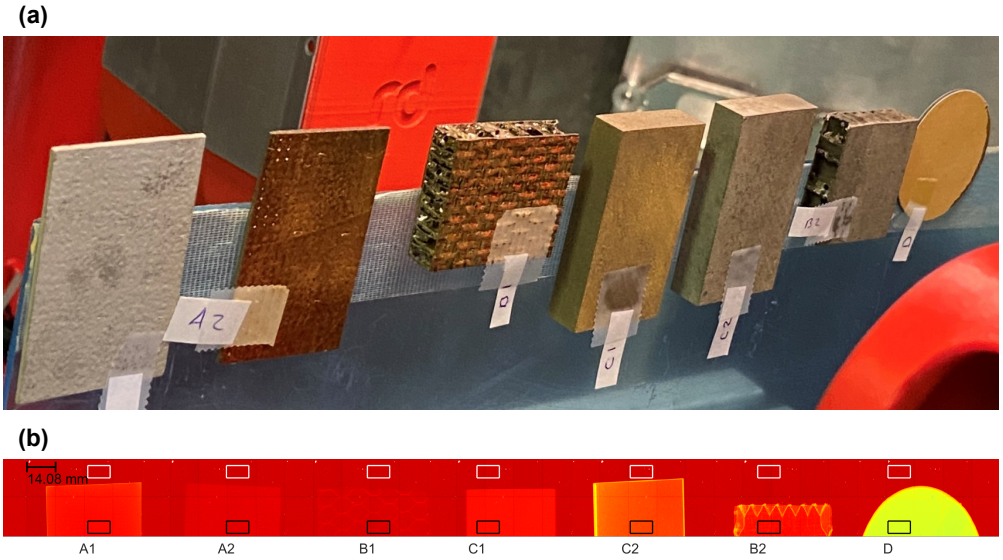

Figure 6.16: Example of a measurement done by the X-ray robotic scanner. Figure a) shows the rack with samples mounted for measurement. Figure b) shows the resulting X-ray micro-radiography with color-scale visualization of event counts (X-ray fluence) from the LAD MPX3 imaging detector for the given samples above (a).

6.3.2 X-ray micro-radiography table-top system

The imaging system used is seen in Figure 6.17. A stationary X-ray micro-focus tube generated X-rays of energy spectra up to 40 keV and 120 keV. For detail of the X-ray tube physics principle, see Appendix A.1. Along to the beam axis, a single-chip pixel detector was positioned (TPX3 H09 500 µm Si AdvaPIX). The samples were attached to a platform that was controlled by the PIXET SW application and moved by step motors, as shown in Figure 6.18 and Figure 6.14. Each data acquisition period of a sample measurement was 20 s. As shown in Figure 6.19, every sample was positioned so that it covered part of the detector (see Section 6.1, Figures 6.3 and 6.4). This way, the data recorded contains both the open beam and the shielded beam sections.

To filter out the low-energy components and to shape the spectrum of the X-ray field, a material filter was used. A 2.45 mm thick aluminum plate was used for the 40 keV and a 4.58 mm thick iron plate for 120 keV energies. This plate was laid down directly in front of the micro-focus source.

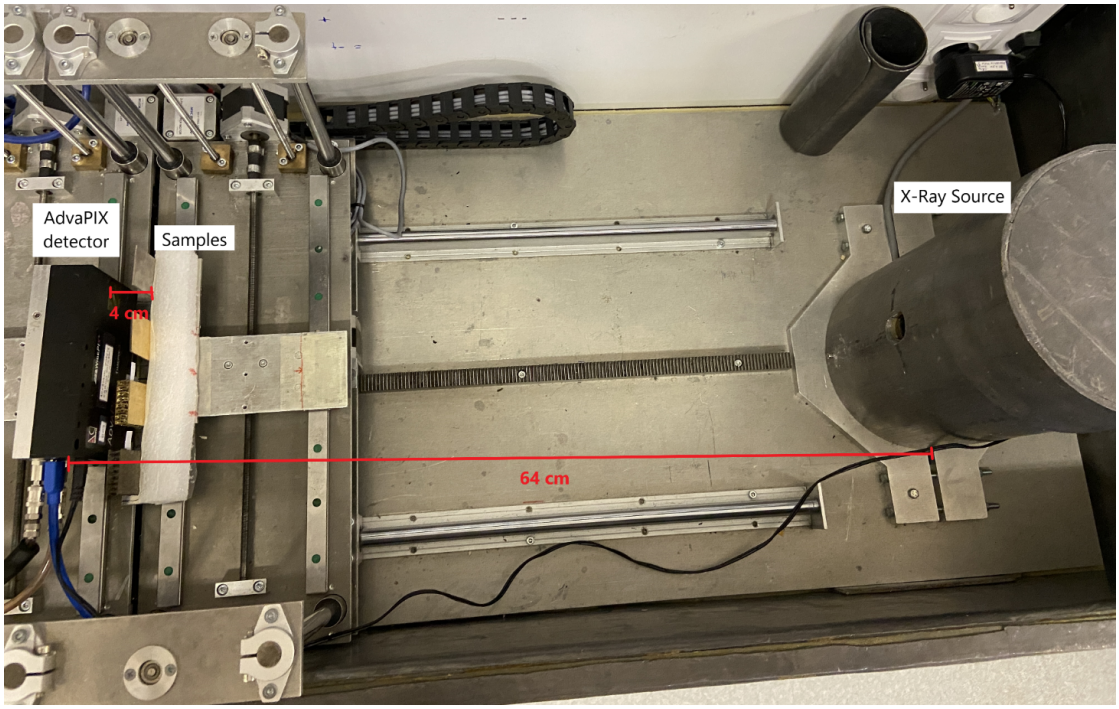

Figure 6.17: Setup for measurements using the X-ray micro-focus tube. The X-ray source (on the right) and the detector (on the left) are stationary, while the platform with samples (in between, close to the detector) is moved by stepper motors.

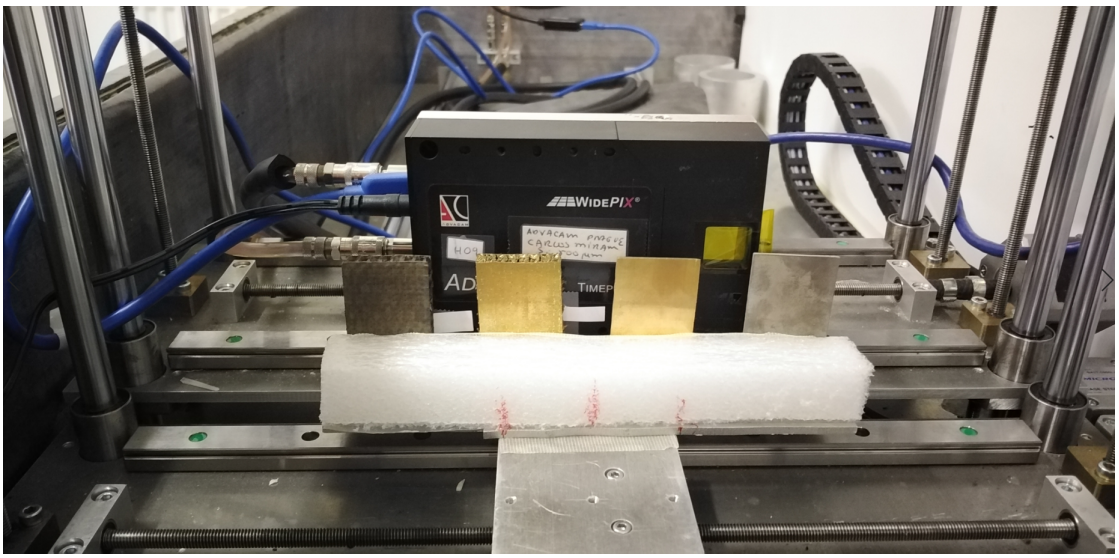

Figure 6.18: Close-up of the sample-detector setup for the X-ray micro-focus tube measurements. The samples are on a platform that is moved along the plane perpendicular to the beam axis by stepper motors.

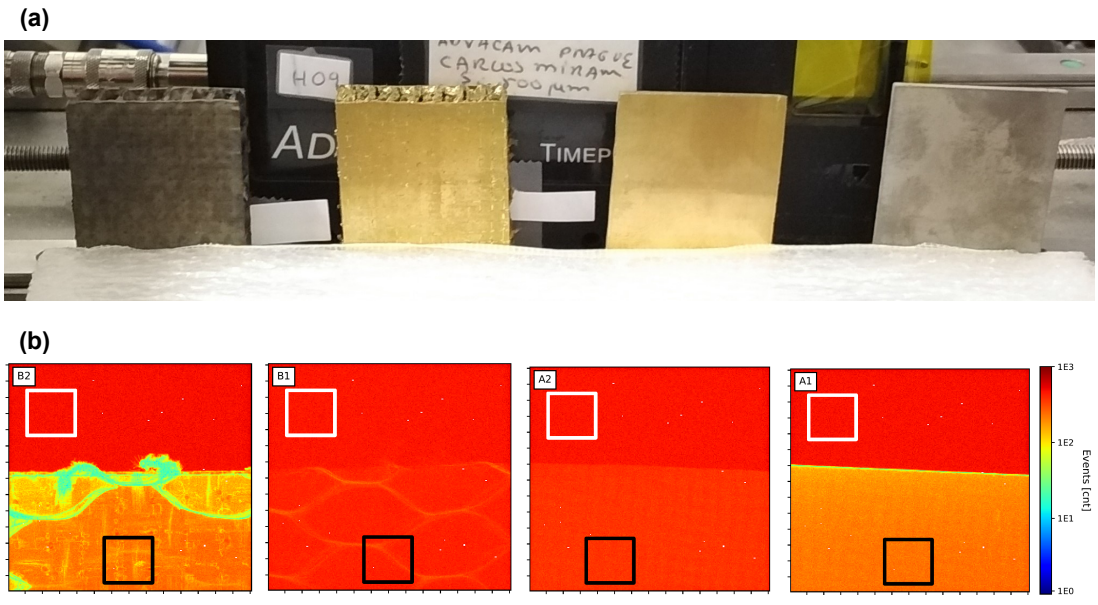

Figure 6.19: Example of a measurement done using the X-ray micro-focus tube. Figure a) shows a photo of sample array mounted for measurement. Figure b) shows the recorded micro-radiographies with color-scale visualization of event counts (X-ray fluence) from the pixel detector for the given samples above (a).

6.3.3 Electron microtron accelerator

For the measurement of shielding efficiency against electrons, a Microtron MT25 accelerator (NPI CAS Rez near Prague) was used, generating electrons of 5 MeV energy. Appendix A.2 provides detail about the accelerator. This whole measurement took place inside an underground room with the only exit made of two tones of lead-filled, hydraulic operated doors. The generated electron beam was directed inside a massive shielding bunker made of wide lead bricks (10 cm thick), to shield intense X-ray and gamma-ray background radiation (produced by the accelerator in close proximity). As seen in Figure 6.20, the electron beam coming from the accelerator entered the shielded setup through a small opening (narrow collimator of $\approx$ 10 mm diameter). Inside, a moving holder platform with the examined samples moved by stepper motors was positioned directly in front of the beam. The detector was positioned closely behind and tilted at a 45° angle to the electron beam axis.

The irradiation exposure for each sample measurement was 120 s. Every sample was positioned so that it covered the whole detector sensor. In this experiment, the electron beam had a size of several milimeters which didn't actually cover the whole area of the detectors used (mounted next to each other). Two detectors were used at the same time next to each other, as shown in Figure 6.21. One was the `TPX3 D05 500 µm Si MiniPIX`, data from which are evaluated in the next chapter. The other was a `TPX H09 300 µm Si MiniPIX` detector. After initial processing, it became clear that there was some error with this TPX detector and the data was too corrupted for reliable results.

6.3.4 Proton cyclotron accelerator

For the measurement with protons, a cyclotron accelerator U-120M (NPI CAS Rez near Prague) was used, generating protons of 31 MeV energy. Appendix A.3 provides detail about the accelerator. This experiment was performed earlier (in 2018 by Carlos Granja, Advacam).

As seen in Figure 6.22, the proton beam coming from the accelerator was also collimated (centered through a small hole opening of $\approx$ 3 mm diameter). The platform with samples was remotely moved by stepper motors positioned between the detector and the beam. The detector was positioned closely behind the samples and also tilted by a 45° angle to the proton beam axis.

Each irradiation exposure of a sample measurement was around 1 minute. Every sample was positioned so that it covered the whole sensor, same as in the electron experiment. As can be seen in Figure 6.24, the samples were also positioned so that a part of them was stacked with a neighbouring sample. This way, additional measurements were also done on these combinations of samples. However, this requires extensive corrections to normalize for density of such combinations. Evaluation of these measurements goes beyond the scope and extent of this thesis. However, the non-normalized values were evaluated and presented in Appendix D .

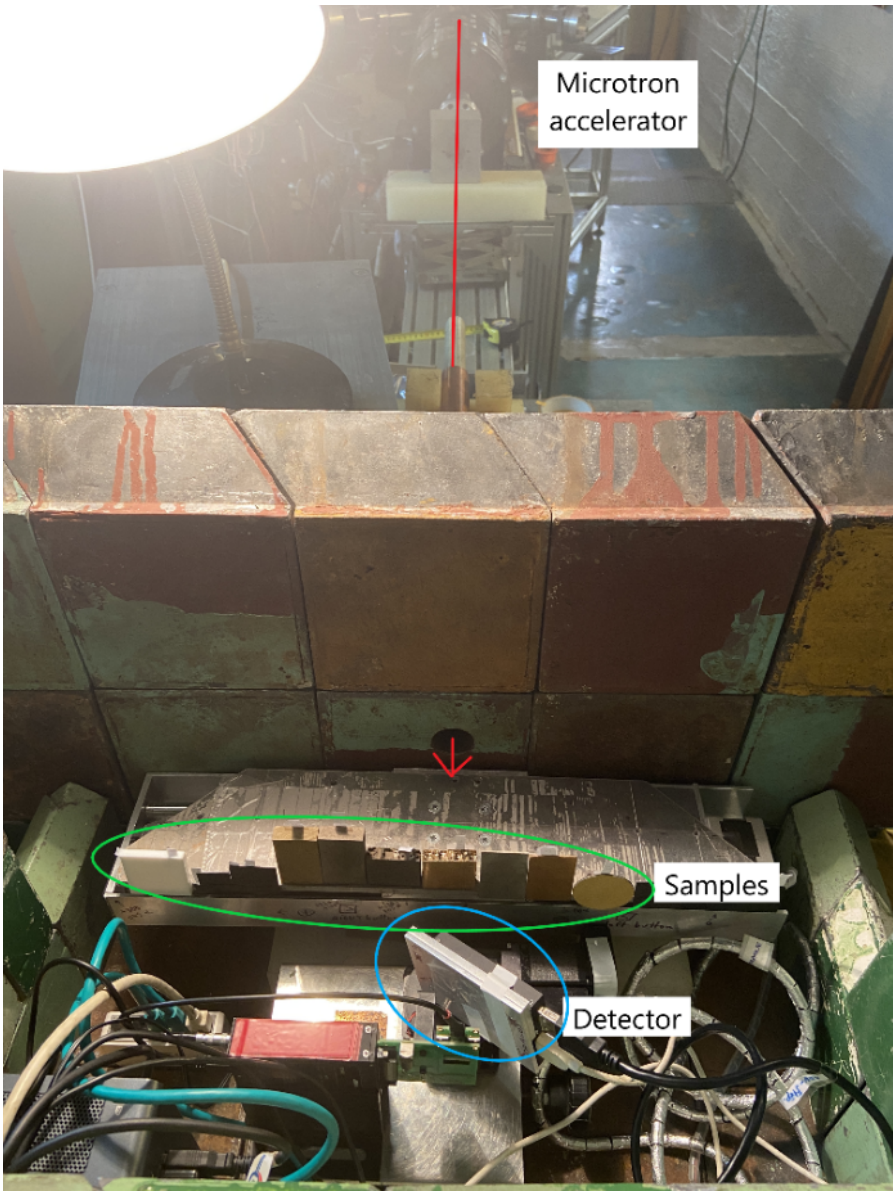

Figure 6.20: Setup for measurements using the electron microtron accelerator. The accelerator generates monoenergetic parallel electron beam, which enters the shielded bunker setup via the collimator hole at the bottom. The pixel detector is positioned at a 45° angle behind the irradiated samples along the beam axis. Between the opening collimator hole and the pixel detector, a platform holder with samples is remotely moved by stepper motors from outside of the measurement hall.

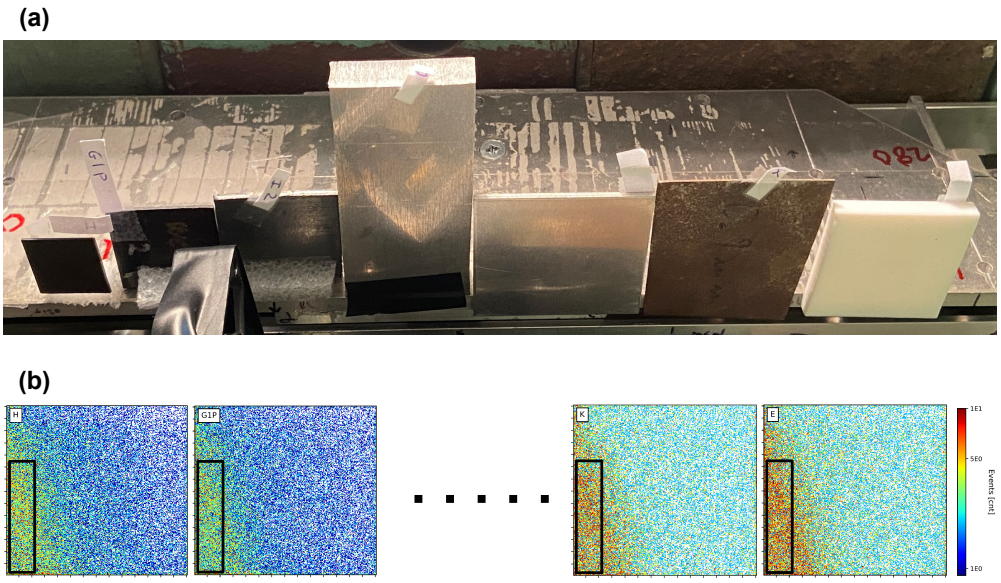

Figure 6.21: Example of a measurement done using the electron microtron accelerator. Figure a) shows the sample array mounted for irradiation. Figure b) shows the recorded images (electron radiographies) with color-scale visualization of event counts (event i.e. particle fluence) from the detector for the first two (from left) and the last two samples above (a) (from left).

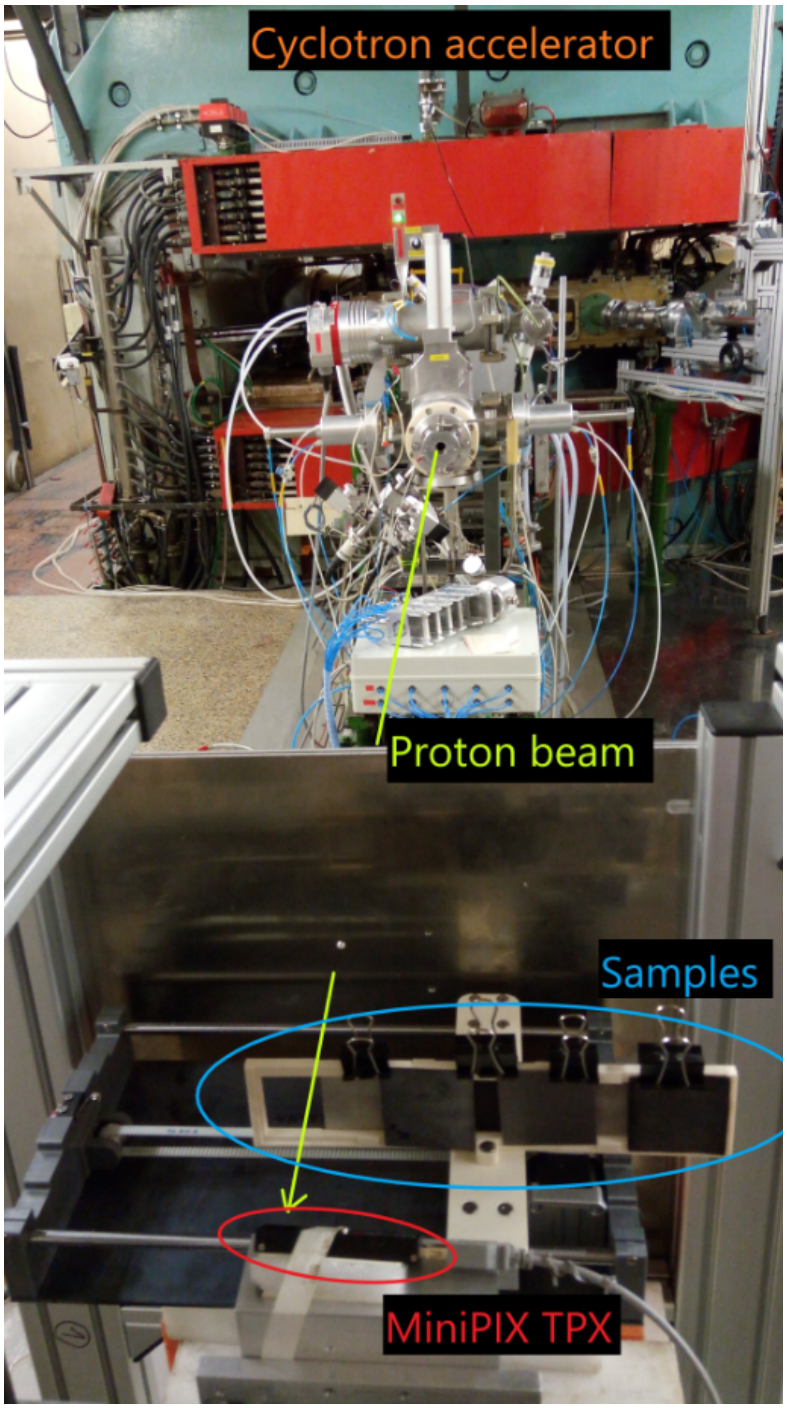

Figure 6.22: Setup for measurements using the proton cyclotron accelerator (seen in the back, on top of the photo). The accelerator generates a monoenergetic proton beam, which is centered by the collimator hole (seen in the bottom part of the photo). The detector is positioned at a 45° angle behind the irradiated samples along the beam axis. Between the collimator hole and the detector is a moving platform holder with the mounted samples moved by stepper motors controlled remotely from outside the measurement room.

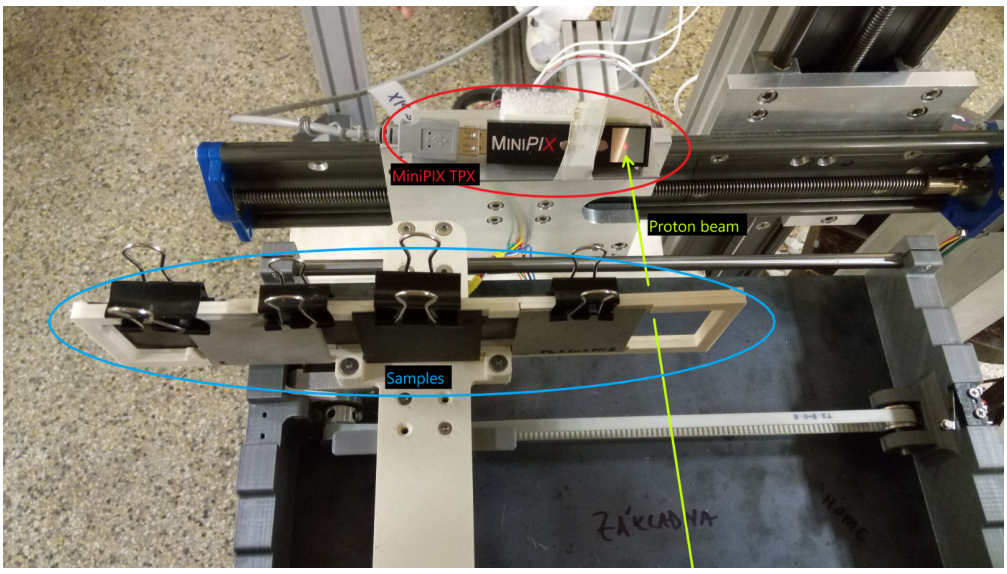

Figure 6.23: Close-up of the measurement setup for the proton cyclotron accelerator. The samples are on a platform that is moved horizontally along the plane perpendicular to the beam axis by a stepper motor, positioned between the beam and the detector. The red dot on the pixel detector shows where exactly the proton beam is.

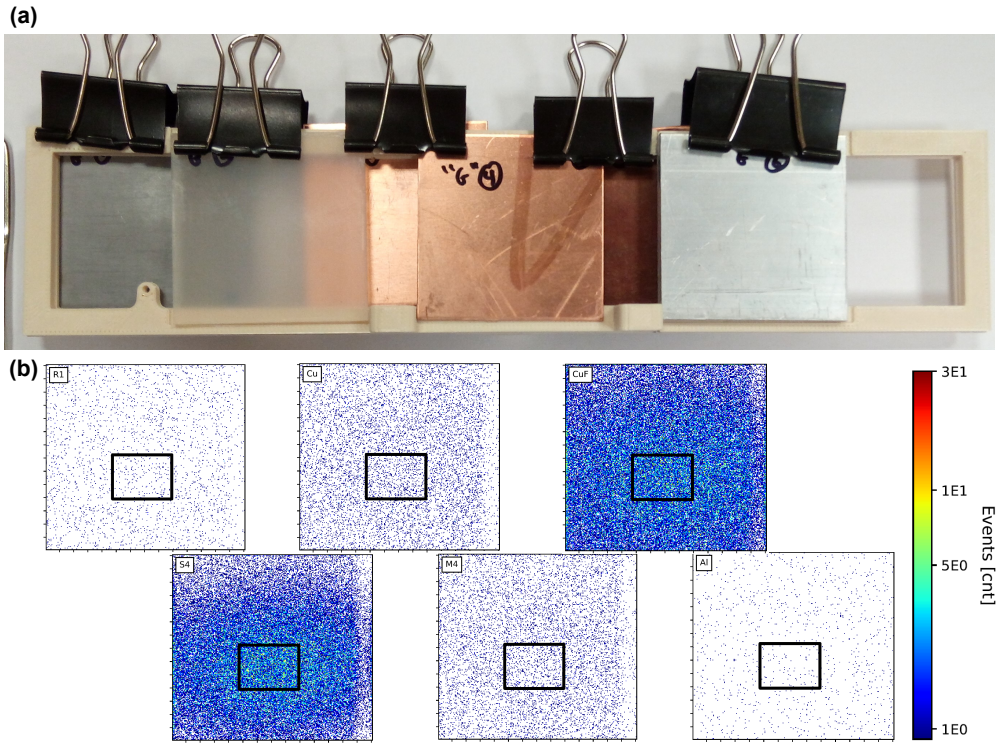

Figure 6.24: Example of a measurement done using the proton cyclotron accelerator. Figure a) shows the photo of the sample array mounted for measurement. Figure b) shows the proton radiographies showing in color-scale the visualization of event counts (event i.e. particle fluence) from the pixel detector for measurements of irradiated samples.

6.4 Shielding samples

This thesis primarily focuses on carbon composites with related and similar other materials also used in the measurements. Moreover, basic materials like steel, aluminum, lead and tantalum were additionally used to provide reference measurements, as these materials are usually used for radiation shielding in nuclear industry and ground based applications. In addition to the overview of samples in Figure 6.1, this section describes the samples used, including examples in the following chapters. For photos of all the samples, please see Appendix B.

All the samples used for the measurements and analysis in this thesis were assigned an ID, with which they are labeled and tracked throughout the experiments, results and plots presented. The list of the investigated samples is given in Table 6.1. Values of sample thickness (t), density (ρ) and planar i.e. surface density = $\rho \times$ t are included.

R4 - Tantalum

Tantalum is a chemical element with the symbol Ta and atomic number (Z–number) 73. Because of its high Z–number, it is prone to produce secondary stopping radiation (X rays, gamma rays) to energetic electrons. However, compared to lighter materials, its high density allows for thinner material for the same shielding efficiency for primary photons (X rays, gamma rays) and heavy charged particles (protons, ions). Figure 6.25 shows the photo of the sample R4 used for measurements.

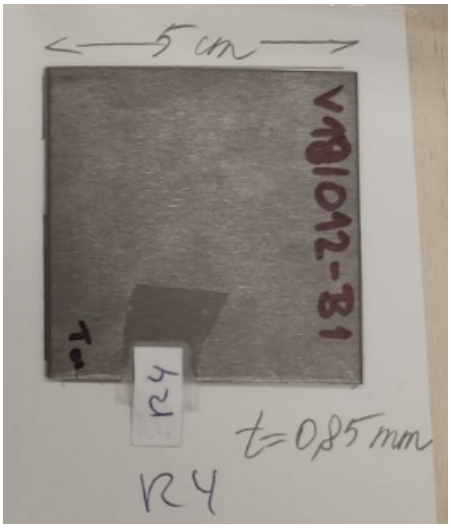

Figure 6.25: Sample R4 used for measurements - Tantalum. Thickness of the sample is 0.85 mm and density is 16.60 g·cm^{-3}.

R3 - Lead

Lead is a chemical element with the symbol Pb and Z–number 82. Similar to Tantalum, it is prone to produce secondary stopping radiation from high energy electrons for primary photons (X rays, gamma rays) and heavy charged particles (protons, ions).

It can be implemented in thinner layers. It has a high attenuation coefficient and is effective at stopping gamma rays and X rays. Figure 6.26 shows the sample R3 used for measurements.

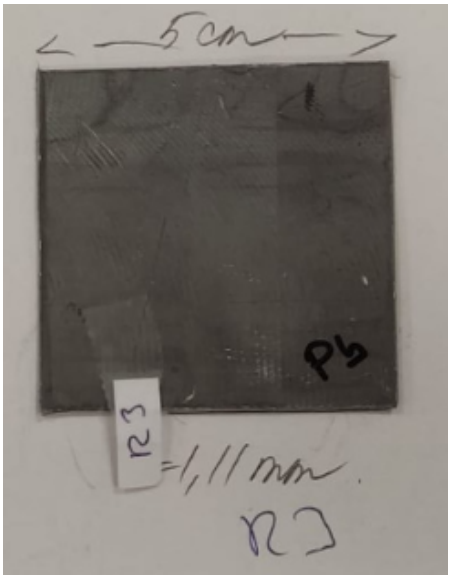

Figure 6.26: Sample R3 used for measurements - Lead. Thickness of the sample is 1.11 mm and density is 11.34 g·cm^{-3}.

S1 - Carbon Fiber Reinforced Polymer + Aluminum Honeycomb Sandwich

These composite samples are manufactured in honeycomb sandwich layout, which consists of two outer layers and a lightweight core, as illustrated in Figure 6.27 (a). The honeycomb structures allow for a minimum material used to reach minimal weight while keeping parameters of mechanical strength and stress resistance. The material of sample S1 is a carbon fiber reinforced polymer (CFRP) sandwich panel with an aluminum honeycomb core. Carbon has a low Z–number (Z = 6) useful for shielding of electrons with hindered production of stopping radiation. The CFRP aluminum honeycomb sandwich is widely used in aerospace applications. Figure 6.27 (b) shows the sample S1 used for measurements.

Q1 - Carbon composite

Sample Q1 is a simple Carbon composite. It is made in a compact dense matrix. Figure 6.28 shows the sample Q1 used for measurements.

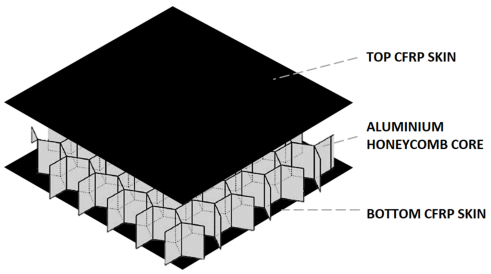

(a) : Honeycomb structure

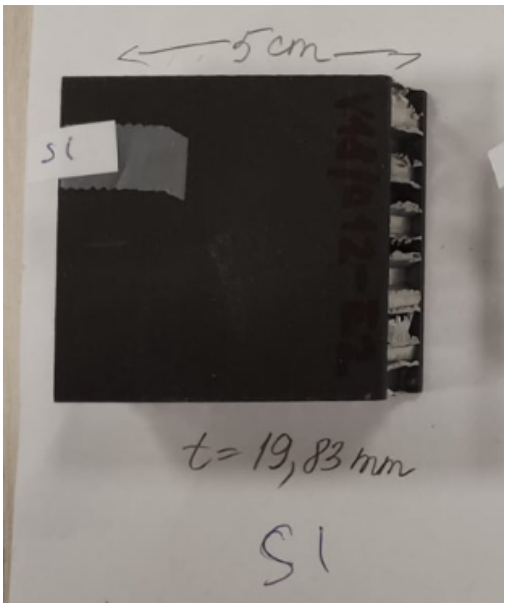

(b) : Sample S1

Figure 6.27: On the left - illustration of honeycomb sandwich structure, taken from [59]. On the right - the sample S1 used for measurements - Carbon Fiber Reinforced Polymer + Aluminum honeycomb sandwich. Thickness of the sample is 19.83 mm and density is 0.38 g·cm^{-3}.

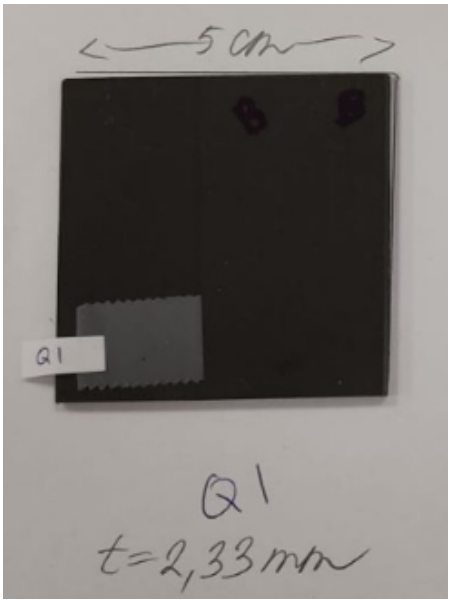

Figure 6.28: Sample Q1 used for measurements - Carbon Composite. Thickness of the sample is 2.33 mm and density is 1.54 g·cm^{-3}.

ID	Sample description	Thickness [cm]	Density [g/cm3]	Surface density [g/cm2]	Used in measurement			
					X-Ray scanner	X-Ray tube	Mikrotron	Cyclotron
A1	CFER + Ni	0.14	1.73	0.25	yes	yes	yes	no
A2	CFER + Au	0.13	1.42	0.18	yes	yes	yes	no
B1	CFER + Au	0.88	0.52	0.46	yes	yes	yes	no
B2	CFER + Ni	0.90	0.51	0.46	yes	yes	yes	no
C1	C + O + H + Au	0.97	0.85	0.82	yes	yes	yes	no
C2	C + O + H + Au + Ni	0.99	0.83	0.82	yes	yes	yes	no
D	Zr + Pb + Ti + O + Au + Ag	0.13	7.80	1.05	yes	yes	yes	no
E	F + C + H (PTFE)	0.48	2.20	1.06	yes	yes	yes	no
F	Al	0.20	2.70	0.55	yes	no	yes	no
G1	C composite	0.13	1.35	0.17	yes	yes	yes	no
G2	C composite	0.09	1.30	0.11	yes	yes	yes	no
H	C composite	0.09	1.58	0.14	yes	yes	yes	no
I1	Pb	0.13	11.34	1.49	yes	yes	yes	no
I2	Pb	0.22	11.34	2.44	yes	yes	yes	no
J	Al	1.00	2.70	2.70	yes	yes	yes	no
K	Steel	0.09	7.85	0.72	yes	yes	yes	no
L	PMMA	0.14	1.18	0.16	yes	yes	yes	no
M1	C composite + Pb	0.56	2.53	1.41	no	yes	yes	no
M2	C composite	0.32	1.66	0.53	no	yes	yes	yes
M3	Pb + Cu + Ni	0.09	9.23	0.78	no	yes	yes	yes
M4	Cu	0.10	8.96	0.90	no	yes	yes	yes
P1	C composite + Cu	0.23	0.68	0.16	no	yes	yes	yes
P2	Pb + Cu	0.07	9.72	0.64	no	yes	yes	yes
P3	Cr + C composite	0.23	1.56	0.36	no	yes	yes	yes
P4	WC + Pb + Ni	0.07	10.35	0.73	no	yes	yes	yes
Q1	C composite	0.23	1.54	0.36	no	yes	yes	yes
Q2	GFRP	0.30	1.92	0.58	no	yes	yes	no
Q3	C composite + Cu + Ni	0.24	1.86	0.45	no	yes	yes	yes
Q4	C composite + Ceramics	0.25	3.39	0.85	no	yes	yes	yes
R1	C composite + Ta	0.15	8.63	1.25	no	yes	yes	yes
R2	CFRP	0.27	1.65	0.45	no	yes	yes	yes
R3	Pb	0.11	11.34	1.26	no	yes	yes	yes
R4	Ta	0.09	16.60	1.41	no	yes	yes	yes
S1	CFRP + Al	1.98	0.38	0.76	no	yes	yes	yes
S2	GFRP + Al	2.20	0.59	1.30	no	yes	yes	no
S3	C composite	0.24	1.54	0.36	no	yes	yes	yes
S4	PP	0.30	0.92	0.28	no	yes	yes	yes
T1	Ta	0.09	16.60	1.43	no	yes	yes	yes
T2	GFRP	0.30	1.88	0.56	no	yes	yes	no
T3	CFRP	0.27	1.80	0.49	no	yes	yes	no
T4	C composite + Cr + Pb	0.07	9.56	0.66	no	yes	yes	yes

Table 6.1: List of samples used in measurements. The right part of the table describes which samples were used in which measurements. Light blue text in the sample description indicates that the material is used as coating of the sample.

Chapter 7

Data analysis

The data acquired by the pixel detectors during measurements is stored as raw, uncalibrated data as described in Chapter 6. To process and get relevant results regarding the shielding efficiency of the materials, a data processing flow is followed, as shown in Figure 7.1. After data acquisition, the process is as follows:

1. **Data pre-processing** - event list creation with detailed event-by-event (i.e. each particle track) information in the form of spectral-tracking parameters (see Section 7.1).

2. **Processing** - filtering, particle recognition, frame analysis, event and/or deposited energy integration per pixel, flux and dose rate derivation, region of interest selection (see Section 7.2).

3. **Post-processing** - image reconstruction, value normalization, shielding efficiency calculation (see Section 7.3).

The data acquired by pixel detectors is input for pre-processing done by a specific SW tool application called Clusterer developed by Advacam. It is a self compiled executable written in C++, which runs on Linux and Windows platforms. This application generates a detailed event-by-event (i.e. for all and each single particle detected) list with detailed spectral-tracking and pattern recognition characteristics [51] [60]. The event list is then processed by a python script, which provides output of detailed particle-type event classification, frame analysis and global data statistics. The generated files are then analyzed further to generate spatial maps and to analyze the evaluated flux and dose rates per pixel. These tasks can require significant computing power, as is described in sections below.

The computational power needed for processing of the extensive data experiments was efficiently solved by the use of an HPC Linux cluster (at the FEE CTU in Prague). This cluster provided large RAM for processing and multiple processors to finish the task in a manageable time frame.

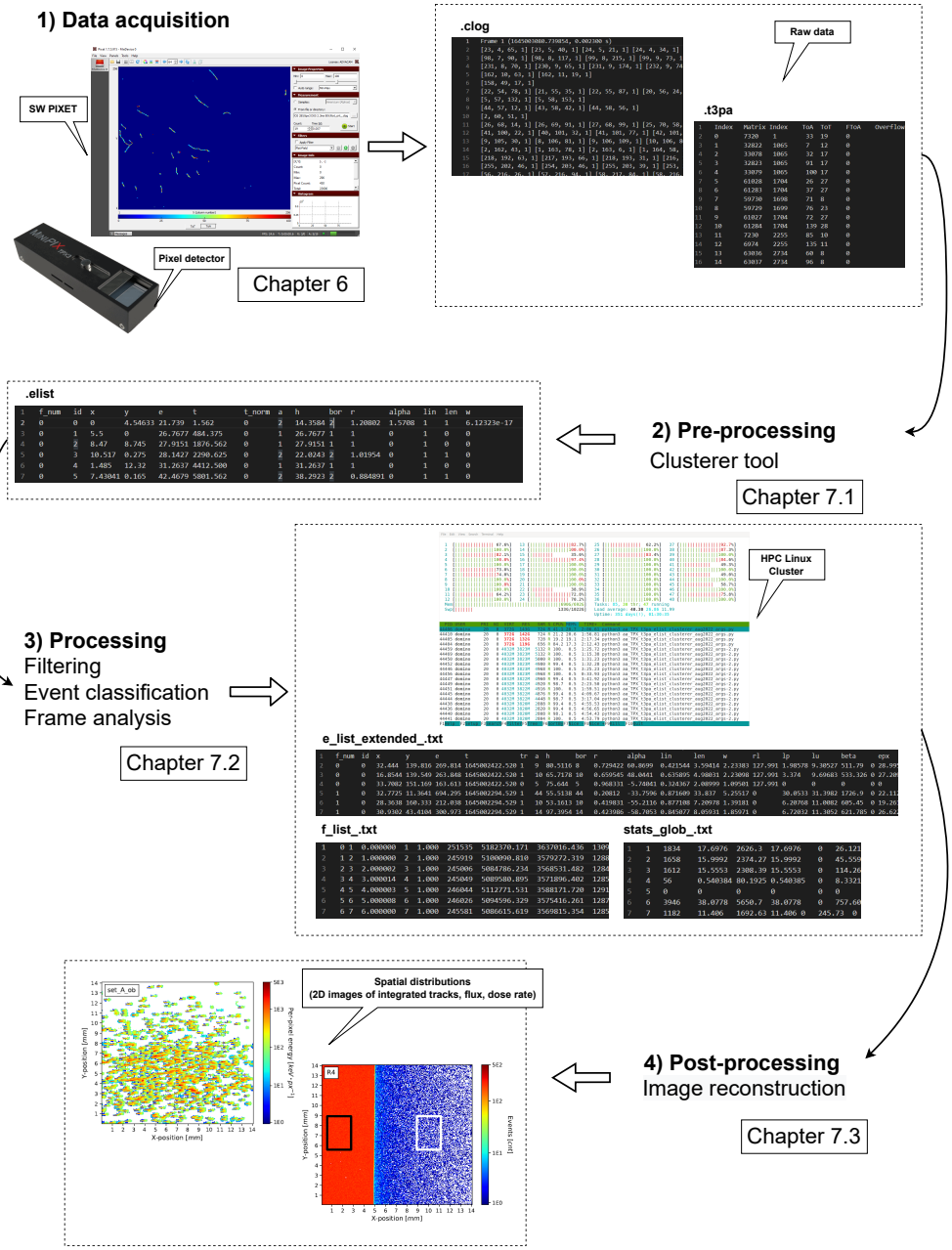

Figure 7.1: Illustration scheme and overview of the data processing flow. Data acquired by the pixel detector using the integrated SW tool PIXET is analyzed offline as input for pre-processing performed with a specific application SW package Clusterer developed and provided by Advacam. The generated files contained detailed information at the event-by-event level i.e. for each radiation particle (in the event list file so-called e-list table) and at the whole sensor level sampled in fixed time period e.g. 1 s (in the so-called frame file). The event list is further processed by a python script, which provides output of detailed event classification, frame analysis and global data statistics. The generated files are then post-processed to generate spatial maps and final results of flux and dose rates.

7.1 Data pre-processing

The first step in data analysis is to convert the raw data gathered from the pixel detectors into the detailed event-by-event list. This task was done by running an application (C++ compiled executable) called Clusterer developed and provided by Advacam. The application has the following functionality:

- **Clustering** - grouping pixels based on coordinates and if available also on detailed per-pixel time information.
- **Calibration and corrections** - application of per-pixel energy calibration calculation, and derivation of cluster analysis and pattern recognition parameters [60] for each particle track.
- **Cluster parameters** - calculation of spectral-tracking and morphology cluster parameters (deposited energy of one particle, roundness, etc.).

Input for the application is data in either *clog* or *t3pa* format, as described in Chapter 6, along with the calibration matrices specific for each pixel detector. The output is an event list - a text file where each row represents one event (one cluster i.e. one particle), with 15 columns, each representing a specific parameter of the event, in following order:

`id` = Event ID based on the order of detection,
`x` = x-position of the event on the detector pixel matrix [mm],
`y` = y-position of the event on the detector pixel matrix [mm],
`Energy` = event deposited energy [keV],
`t` = time stamp [s] or [ns],
`Flags` = flag indicating if the event will have tracking,
`Size` = area of the cluster [px],
`Height` = maximum energy per pixel in the cluster [keV],
`BorderPixCount` = number of pixels on the border of the cluster [px],
`Roundness` = 0–1 value indicating morphology roundness of the cluster,
`Angle` = polar angle of the track in the detector 2D plane [rad],
`Linearity` = 0–1 value indicating the morphology linearity of the cluster,
`Length` = track length = cluster vertex distance in 2D [px],
`Width` = width of the cluster [px].

As mentioned in Chapter 6, every measurement had a region of interest (ROI) selected. The ROI is represented as an area of pixels, with only events fitting into the area counted for the shielding efficiency calculation. The Pixet application, which can provide basic data visualization, was used for this purpose. The pixel coordinates were manually selected from the visualization. For the microtron and cyclotron experiments (see Figure 7.2), one ROI was selected for all measurements, as the samples covered the whole sensor and only the beam area had to be specified. However, as the samples in measurements from the X-ray tube experiments cover only a part of the sensor (see Figure 7.3), and they all have individual sample to open beam alignments, every one of the 41 data files had to have individual ROIs assigned manually. These ROIs were written into a JSON file for easy automated use in the next processing step.

For data from the microtron experiment, every measurement also had to have a time range selected for the final result calculation. As can be seen in Figure 7.4, the intensity of the electron beam fluctuated throughout the measurement. This happened mainly during the first measurements in a set, before the beam stabilized. The red arrow in Figure 7.4 highlights the region where the detector did not measure any data. These occurrences happened randomly throughout the measurements and also had to be filtered out. For the particular pattern in Figure 7.4, a time range 94 s – 120 s is selected. Some measurements were stable enough and did not have a range selected.

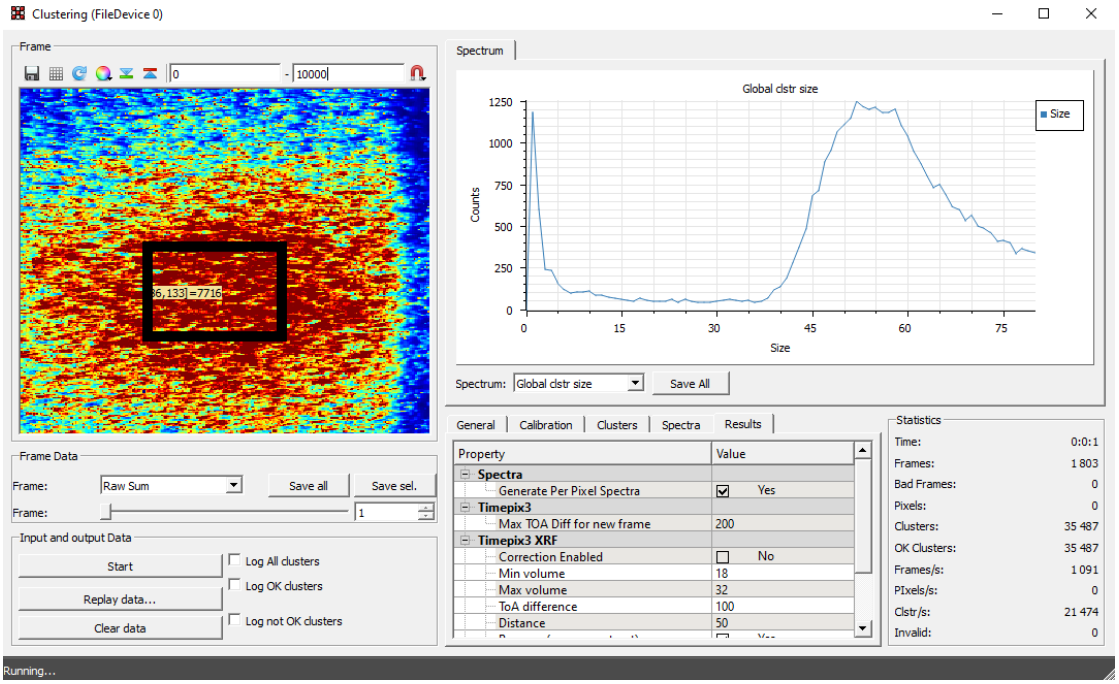

Figure 7.2: Pixet function Clustering used for visualization of *clog* data and ROI selection. The black frame represents the area selected where the proton beam directly hits the sensor.

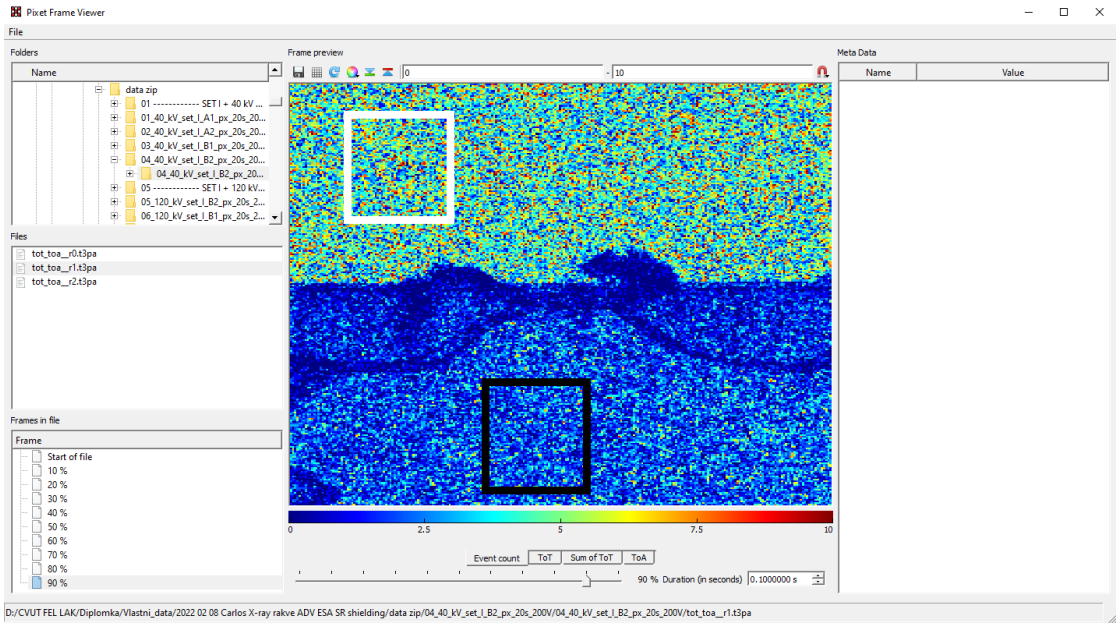

Figure 7.3: Pixet function Frame Viewer used for visualization of *t3pa* data and ROI selection. The white frame represents the area of sensor with unshielded open beam, while the black frame represents the shielded area of the sensor.

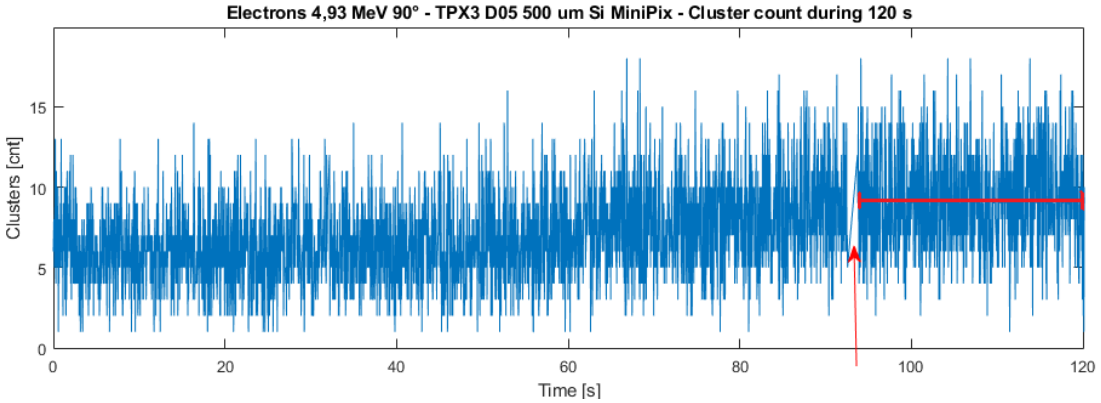

Figure 7.4: The graph depicts cluster count throughout time for the measurement of 5 MeV Electrons with the `TPX3 D05 500 µm Si MiniPix` detector. The measurement is of an open beam at the start of a set measurement. It can be seen that the intensity of the beam fluctuates throughout time and also shows a slight increasing trend. This happened mainly at the beginning of the sets, when the microtron accelerator had not stabilized yet. The red arrow points to an occurrence when the detector did not measure any data. Both the intensity change and the detector outage have to be filtered out. Final range selected, depicted by the red line, is 94 s – 120 s.

7.2 Data processing

Before running the main processing script (frame analysis), it is necessary to select the events from the event list (particle-type classification) that are relevant for a given ROI. In practice, the x-position and y-position value of every event is compared to the relevant area defined in the ROI json file. The events that belong in the region are stored as a separate event list. For each X-ray tube measurement, two new event lists are created - one for the open beam region and one for shielded region of interest. These event lists are then input for the main processing script (frame analysis).

The main processing script is written in python. The physics and algorithms are based on high resolution pattern recognition algorithms [60] [51]. Along with an event list, the script needs to specify: *I*) the frame acquisition time/sampling time - defined by measurement for *clog* data (typically 1 ms or 10 ms), or set manually for *t3pa* data (typically 1 s), *II*) the sensitive region - normally the whole sensor area, in this case calculated by the defined ROI, *III*) the sensor thickness (300 µm or 500 µm) and *IV*) sensor material density (2.3 g $\cdot$ cm^{-3} for Si or 5.85 g $\cdot$ cm^{-3} for CdTe). The frame acquisition time, sensor thickness and sensor density are always the same for each given experiment. The sensitive area stays the same for the microtron and cyclotron experiments measurements, but changes for every measurement for the X-ray tube (also for the X-ray scanner) experiments.

The frame analysis script creates an extended event-by-event list with 80 columns, analyzes and classifies events according to 26 particle-event types, calculates new parameters (such as the elevation angle β, particle LET and deposited dose), and converts values and results to physical units. The 26 particle-event types are then classified into three broad classes as:

Broad class 1 = electrons, X-rays, gamma rays,
Broad class 2 = protons,
Broad class 3 = ions.

Along with the identified classes, other values and parameters are calculated - track length in 3D, elevation angle β, Linear Energy Transfer (LET), energy per pixel, the particle deposited energy, absorbed dose and further spectral-tracking ratios. Many of the parameters are calculated values in different units, for convenience of use. The main physical products which can be found in the output files are:

- Flux [cnt $\cdot$ cm^{-2} $\cdot$ s^{-1}]
- Count rate of particles and pixels [cnt $\cdot$ s^{-1}]
- The particle deposited dose [µGy]
- Dose rate [µGy $\cdot$ s^{-1}]
- Deposited energy per pixel [keV $\cdot$ px^{-1}]
- The particle deposited energy [keV]

The algorithm's classification parameters and boundary values along with the formulas needed for the event classification and parameter calculation were provided by Carlos Granja from Advacam, in the form of a matlab script used for the data processing. One

task and work performed in this thesis was to convert the data processing scripts written in matlab into open source python programming language.

From the event list, the script creates a frame/sampling list. There is a time interval between the registration of individual frames, where the detector writes out data and thus does not detect new particles, which is referred to as dead time. This dead time should be taken into account for the full results i.e. complete values of physical products dependant on time such as the total absorbed dose. Therefore, the derived physical products in the sampling list are calculated based both on the sampling time and the dead time (together giving the total elapsed time). This means that all events/particles which are within a time interval of sampling time from some starting point contribute to the physical products.

Example[1], lets assume that a measurement of 10 s was done and 2,000 particles were registered in first 5 seconds and 3,000 particles in another 5 seconds. If the sampling time is chosen as 5 s, then 2 samples are created in the output file with two values for each sampled physical product. The values of flux, are then: 2,000 and 3,000 particles $\cdot$ s^{-1} $\cdot cm^{-2}$. The particle event flux is calculated based on the elapsed time and if the last event was detected at time of 9 s then the total flux is: (2,000 + 3,000 particles)/(2 cm^2 $\cdot$ 9 s) = 2,777.8 particles $\cdot$ s^{-1} $\cdot$ cm^{-2} which is not the same as the mean value of the class fluxes which is 2,500 particles $\cdot$ s^{-1} $\cdot$ cm^{-2}.

The final output, from which the physics results are calculated is a text file containing the summary of all calculated values - the global statistics. It contains values of count, flux, deposited energy and dose rate for the whole measurement with and without dead time, for partial event types as well as for all events.

As data from e.g. the microtron experiment are detected in frame mode, the time range filter is applied to the frame list. Frames that are detected in the time range specified, are logged into separate frame list file. The global statistics are then calculated from this new frame list.

7.2.1 High-performance computing

The X-ray tube measurements raw data sizes are in range of 1–2 GB per sample-beam geometry setup, which accounts to approximately 20 million events per file, each with 15 parameters. After the ROI selection, this becomes approximately two times 5 million events for one measurement (one file for open beam and one for shielded beam). During the processing, each of the 5 million events has to be compared to the previous one, to make sure that the time stamps are not distorted, and if so, it has to be corrected. Additionally, after pre-processing, each event has additional 65 parameters calculated. Calculations of this memory size and complexity were not practical to run on normal PC such as a 16 GB RAM laptop. This was solved by the use of an HPC Linux cluster available at FEE CTU in Prague (see specifications in Figure 7.5), which provided large RAM (e.g. 740 GB with 1 TB swap memory), as can be seen in screenshot in Figure 7.6. The cluster consists of two computers, Dalton and Dirac, each with its own RAM (740 GB and 540 GB respectively), both working with the same memory disks. As one such file could take up to two hours to calculate, the utilization of multiple processors of the cluster made this task manageable in appropriate time. Thus, a 2 GB data file could be

[1] `https://wiki.advacam.cz/index.php/DPE`

processed in 20 minutes.

(a)

```
[sieger@Dalton ~]$ inxi
CPU: 2x 12-Core Intel Xeon Gold 6136 (-MT MCP SMP-) speed/min/max: 1200/1200/3700 MHz
Kernel: 5.6.13-100.fc30.x86_64 x86_64 Up: 374d 7h 00m Mem: 5609.8/708921.5 MiB (0.8%)
Storage: 1.09 TiB (1.0% used) Procs: 500 Shell: bash 5.0.11 inxi: 3.1.00
[sieger@Dalton ~]$
```

(b)

```
[sieger@Dirac ~]$ inxi
CPU: 8-Core Intel Xeon W-2145 (-MT MCP-) speed/min/max: 1200/1200/4500 MHz
Kernel: 5.1.11-300.fc30.x86_64 x86_64 Up: 1248d 1m
Mem: 1783.2/515700.7 MiB (0.3%) Storage: 22.92 TiB (24.0% used) Procs: 264
Shell: bash 5.0.11 inxi: 3.1.00
[sieger@Dirac ~]$
```

Figure 7.5: The FEE CTU HPC Linux cluster specifications. Subfigure a) shows the specifications of the Dalton machine. Subfigure b) shows the specifications of the Dirac machine.

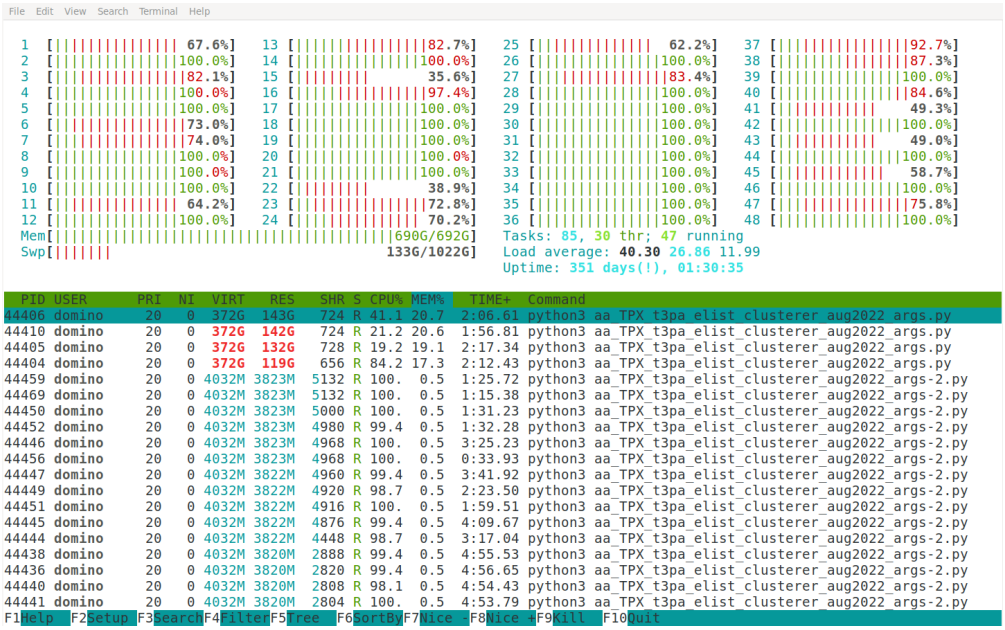

Figure 7.6: CPU and RAM computing resource utilization on the HPC Linux cluster. Output of the *htop* command on the Dalton machine. The processing of data from the X-ray tube measurements even required the use of the full RAM available and most of the available processors.

7.3 Post-processing

After processing the data and getting the values of relevant parameters, the results need to be processed into different high-level and suitable forms. The first form of results in Chapter 8.1 is the 2D spatial imaging track visualization of clusters. This visualization is constructed from the raw *clog* data together with the application of the per-pixel energy

calibration (part of pre-processing), displaying single particle tracks at the individual pixel level that form the clusters and their deposited energies. The image reconstruction works in the way that each pixel coordinates as registered in the *clog* file are transformed into a position in a spatial matrix to which the respective energy of the pixel is assigned. If there are more hits on the same position, the energy is integrated. For the purposes of the track visualization, only a few frames were integrated, so that the tracks overlay as little as possible. For the integrated cluster imaging in Chapter 8.2, the clusters from *clog* files were integrated for a longer period of time.

The 2D imaging of physical products in Chapter 8.3 is constructed from the event lists. It provides a convenient evaluation and clean look of the measured results. One step for the visualization, the spatial distributions of the event parameters are created. Similar to the track visualization, a matrix is created which is filled with integrated values of events that are mapped from their coordinates to the matrix. Specific spatial maps are created for count, deposited energy and dose. These are then used to calculate spatial maps for flux and dose rate based on the sampling time of the measurement. The maps are saved into separate files. As mentioned in the above chapter, the X-ray tube measurements logged a large amount of data - e.g. 20 million events for each measurement. Thus, the maps had to be calculated using the HPC Linux cluster.

These maps are then loaded into a separate python script that creates the physics evaluated plots and draws the region of interest frames. The evaluated quantity e.g. flux or deposited dose is displayed in color by the bar scale in logarithmic scale - to suitably handle and display a wide range of values covering many orders of magnitude. The colormap boundaries of the plots are fixed - set manually so that they are the same for given physical product for all measurements in a given experiment. This enhances and optimizes the evaluation and comparison of data in wide range and results of different samples. Pixels with no event hits are painted white.

For the calculation of final results, the measured values of physical products for each sample had to be additionally normalized. As seen in the sample overview in Appendix B, each sample has a different thickness. This leads to potential distortion of results in regards to the shielding efficiency. Therefore, the results were normalized for the surface density of 1 cm of Aluminum, as this well known material's shielding properties are often used for reference both in space / LEO deployment and in ground applications.

Chapter 8

Results

The shielding efficiency of samples presented in Chapter 6.4 was measured in the following experiments:

1. **X-ray scanner** – X-rays 50 keV,
2. **X-ray tube** – X-rays 40 keV,
3. **X-ray tube** – X-rays 120 keV,
4. **Microtron** – Electrons 5 MeV,
5. **Cyclotron** – Protons 31 MeV.

The measurements were evaluated for main physical products:

- Flux [cnt $\cdot$ cm^{-2} $\cdot$ s^{-1}]
- Dose rate (DR) [pGy $\cdot$ s^{-1}]

This chapter first presents the visualization of the radiation field for electrons and protons for both open beam measurement and shielded measurements for the selected samples. Then, the visualization of both physical products for the selected samples is presented. While looking at these visualizations, it is important to remember that all samples have a different thickness and these visualizations are not yet normalized (see Section 7.3), therefore the derived computed shielding efficiency may vary.

Next, an overview of measurements of flux and dose rate for the measured samples is given, showing the difference between measured and normalized values. Last, the final shielding efficiency is calculated and presented for all samples in given experiments including the normalization for surface density (see Section 7.3).

8.1 Radiation field visualization

Individual particles are registered in the pixel detector as characteristic pixelated tracks of specific geometric morphology and energetic properties. Based on high-resolution event-by-event pattern recognition analysis (see Section 7.2) and these properties, they can be recognized and classified into particle types. The figures in this subsection show only a few frames, recorded in short acquisition time - e.g. 70 ms, so that individual particle tracks can be displayed and visually recognized.

8.1.1 Electrons

Figure 8.2 shows the detection and radiation field visualization behind selected shielding samples. The measurement was done with the `TPX3 D05 500 µm Si Minipix` detector for 70 ms frame acquisition time. The beam was incident to the detector sensor plane at a 45° direction. The detector sensor plane is tilted to the beam axis in order to increase the resolving power of spectral-tracking analysis. It can be seen that sample R4 (Ta) in plot c) shields the most particles, not only lowering the number of particles passed, but also reduces the energy of the particles that pass through. It can be seen that even though the sample S1 (CFRP + Al honeycomb sandwich) in plot b) is less effective at shielding the particles completely, the particles are more spread throughout the whole sensor area than the open beam in Figure 8.1, which reveals that the particles are scattered (partly diverted in direction) after hitting the shielding material.

8.1.2 Protons

Figure 8.3 provides a detail view of 31 MeV proton detection and visualization. The measurement was done with the `TPX C08 500 µm Si Minipix` detector for 70 ms, at a 45° incident direction to the proton beam. Compared to electrons, it can be seen that the protons have a different beam-field geometry - better defined more round, wider and with single particle shorter tracks.

Figure 8.4 shows the track visualization behind shielding samples. It can be seen that sample R4 (Ta) in plot c) shields the most particles. The sample S1 (CFRP + Al honeycomb sandwich) in plot b) is more effective at shielding protons than the sample R3 (Pb) in plot a).

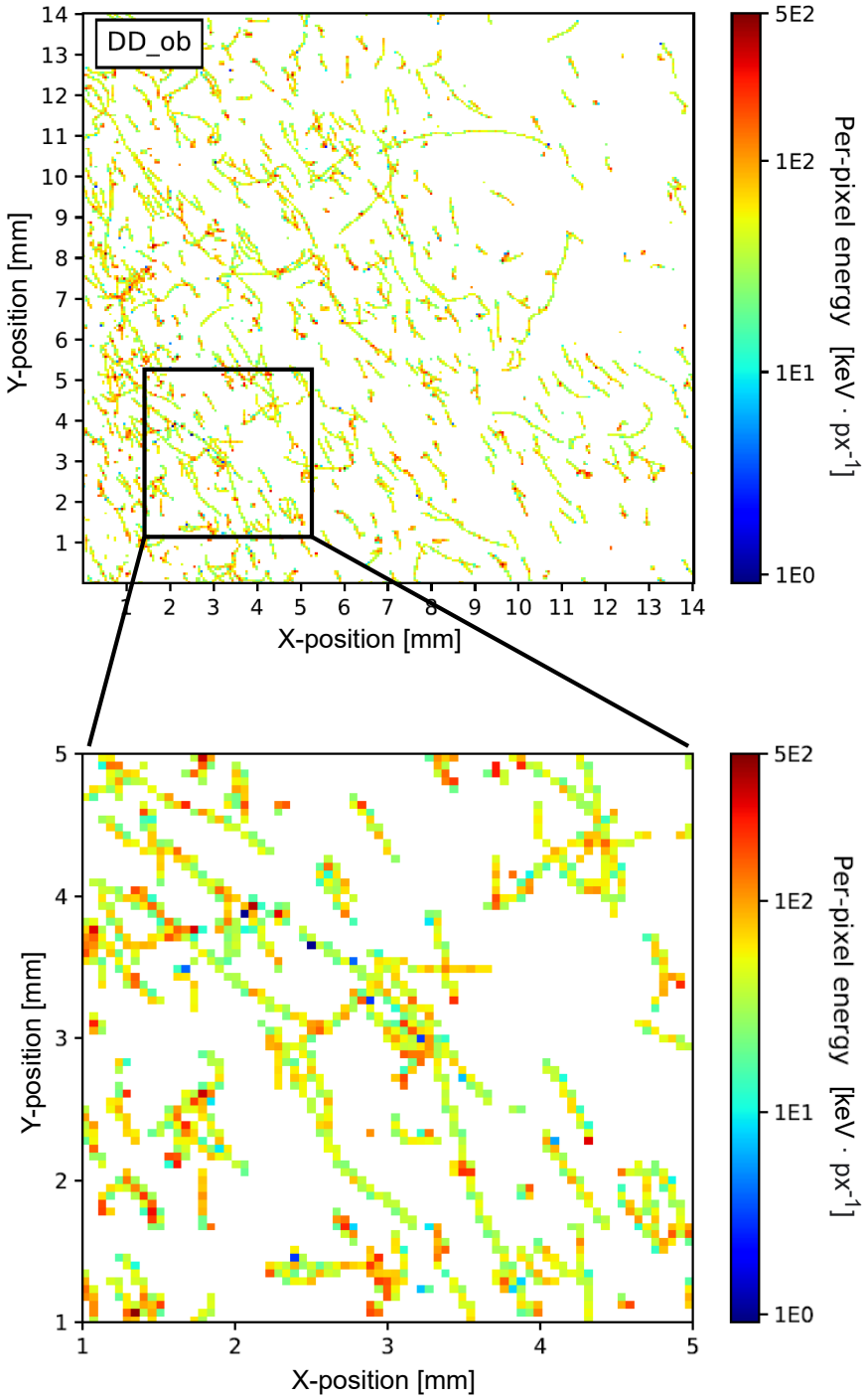

Figure 8.1: Detection and track visualization of 5 MeV electrons. Measured with `TPX3 D05 500 µm Si Minipix` detector in 70 ms acquisition time. The beam–detector plane geometry had a 45° tilt angle. Data is shown for open beam (no shielding sample used). The top image presents the whole detected area, while the bottom shows a detail of selected area. The per-pixel deposited energy is displayed by the colormap in logarithmic scale.

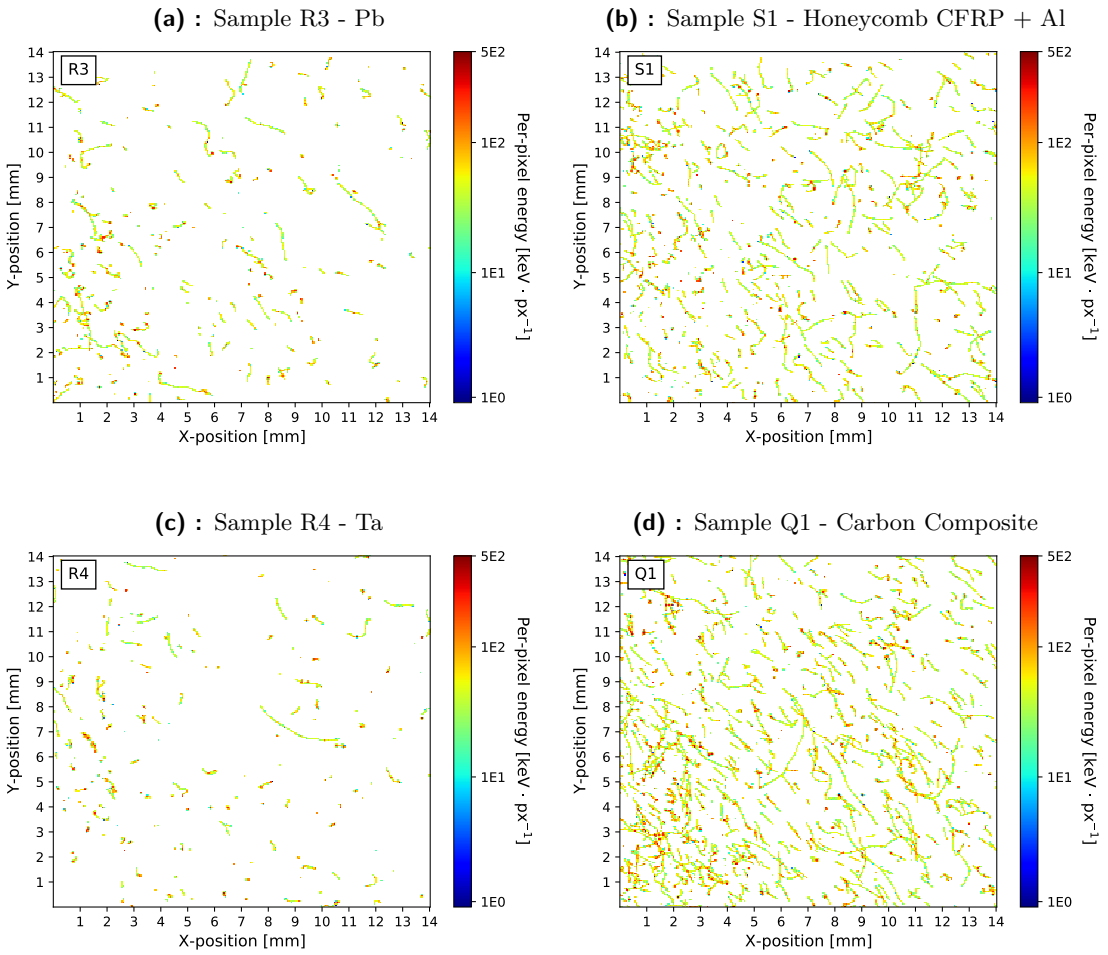

Figure 8.2: Detection and track visualization of 5 MeV electrons behind radiation shielding samples. Measured with `TPX3 D05 500 µm Si Minipix` detector in 70 ms acquisition time. The beam–detector plane geometry had a 45° tilt angle. Each plot shows a measurement for different shielding samples specified in the plot's captions. The primary beam was the same for all plots shown (same energy, intensity, beam size). It can be seen that sample R4 (Ta) in plot c) shields the most particles. It is however important to remember that the samples have a different thickness and these visualizations are not yet normalized, therefore the final computed shielding efficiency can vary.

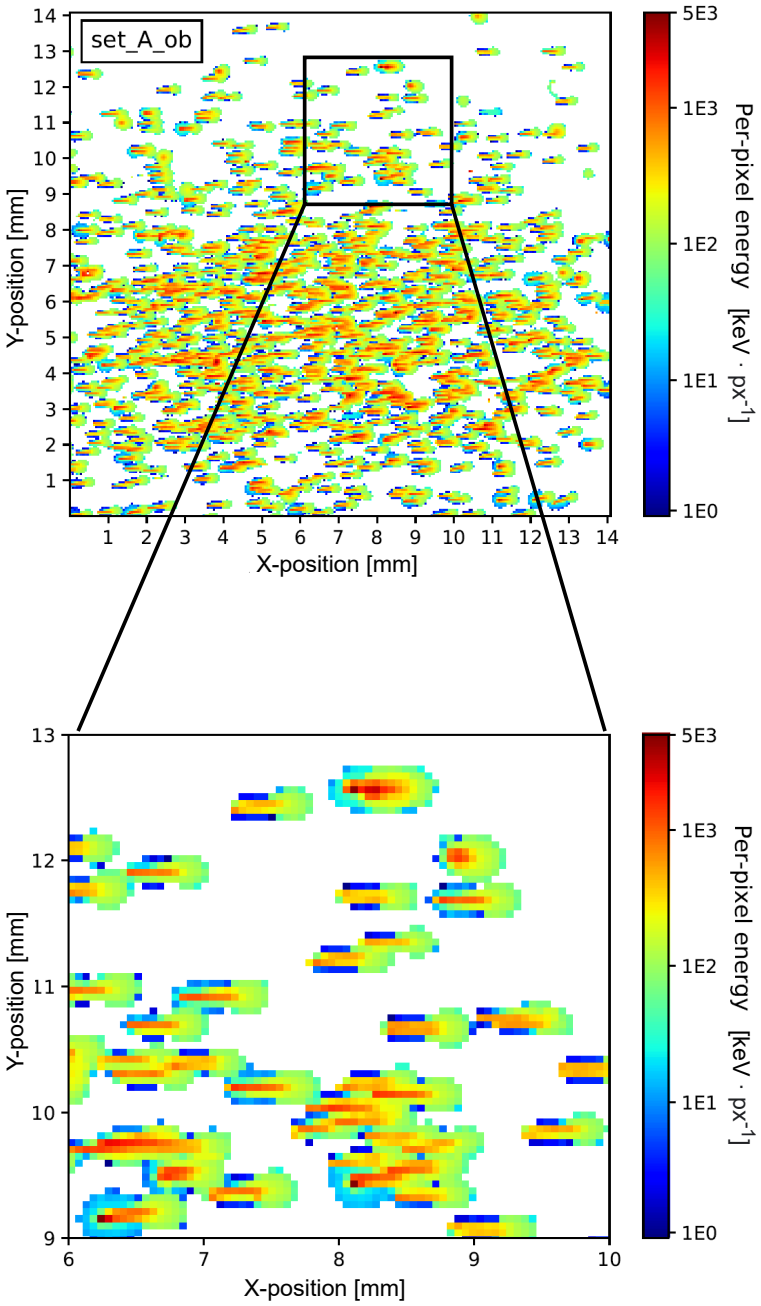

Figure 8.3: Similar to Figure 8.1 showing the detection and track visualization of 31 MeV protons. Measured with `TPX C08 500 µm Si Minipix` detector in 70 ms acquisition time, at a 45° incident direction to the proton beam. Data is shown for open beam (no shielding sample used). The top image presents the whole detected area, while the bottom shows a detail of selected area. The per-pixel deposited energy is displayed by the color bar in logarithmic scale.

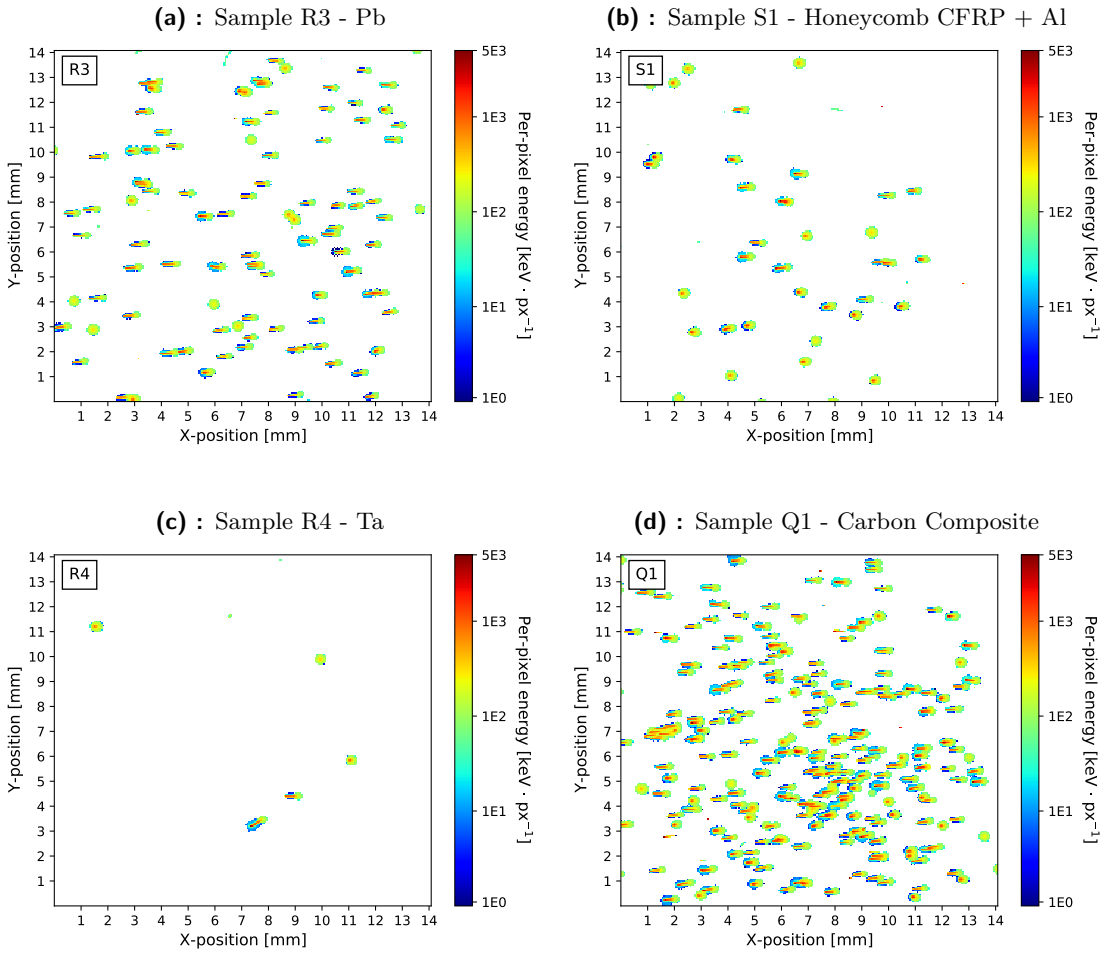

Figure 8.4: Similar to Figure 8.2 showing the detection and track visualization of 31 MeV protons behind four different shielding samples. Measured with `TPX C08 500 µm Si Minipix` detector in 70 ms acquisition time, at a 45° incident direction to the proton beam. Each plot shows the measurement for selected shielding sample specified in the plot's captions. The primary beam was the same for all plots shown (same energy, intensity, beam size). It can be seen that sample R4 (Ta) in plot c) shields the most particles.

8.2 Integrated 2D imaging of particle deposited energy

Previous figures depicted few measured frames displaying data acquired in short times, e.g. 70 ms. This section presents the same measurements displayed in integrated frames acquired in long frames, e.g. 7 s for electrons and 14 s for protons. The results and images present the integrated deposited energy of particles crossing selected shielding samples as well as the unshielded open beam.

8.2.1 Electrons

Figure 8.5 shows the integrated deposited energy field by 5 MeV electrons measured with the `TPX3 D05 500 µm Si Minipix` detector in 7 s acquisition time, at a 45° incident direction to the proton beam without shielding sample.

Figure 8.6 shows the deposited integrated energy behind selected shielding samples. It can be seen that the high-Z samples R3 (Pb) in plot a) and R4 (Ta) in plot c) shield more particles.

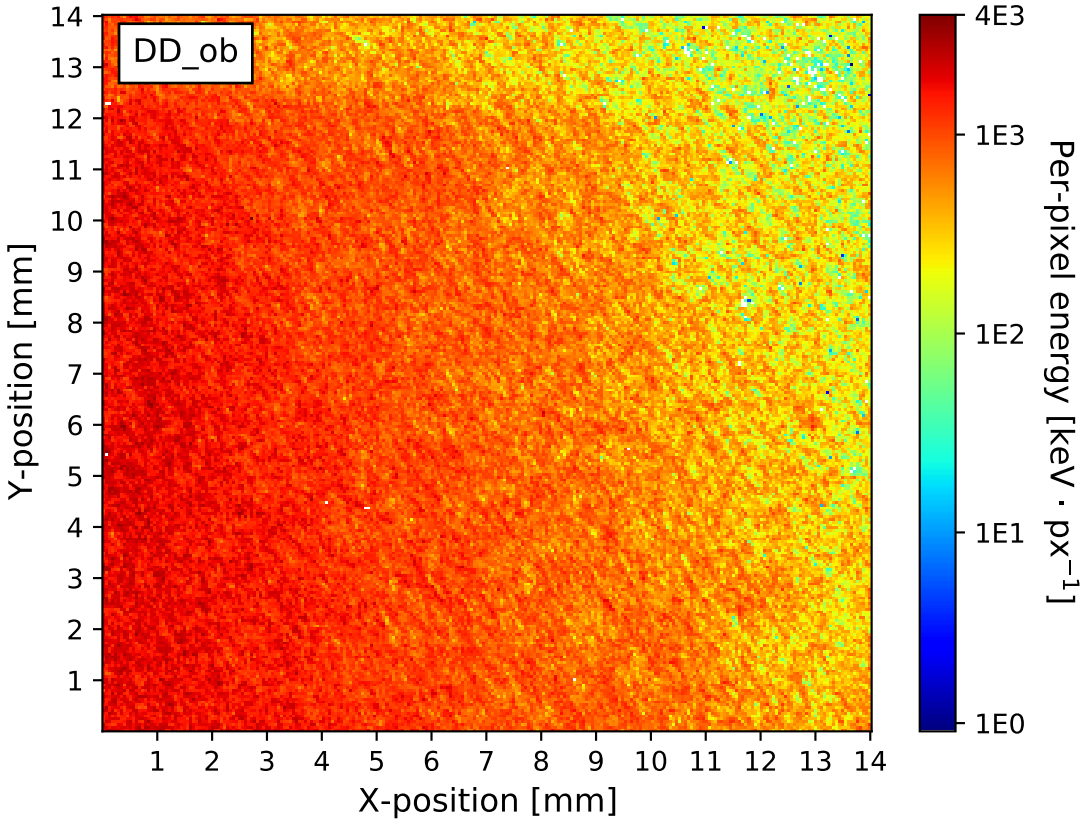

Figure 8.5: Detection and radiation field visualization of 5 MeV electrons. Measured with the `TPX3 D05 500 µm Si Minipix` detector in 7 s acquisition time, at a 45° incident direction to the proton beam without shielding sample. The per-pixel deposited energy is shown by the color bar in logarithmic scale.

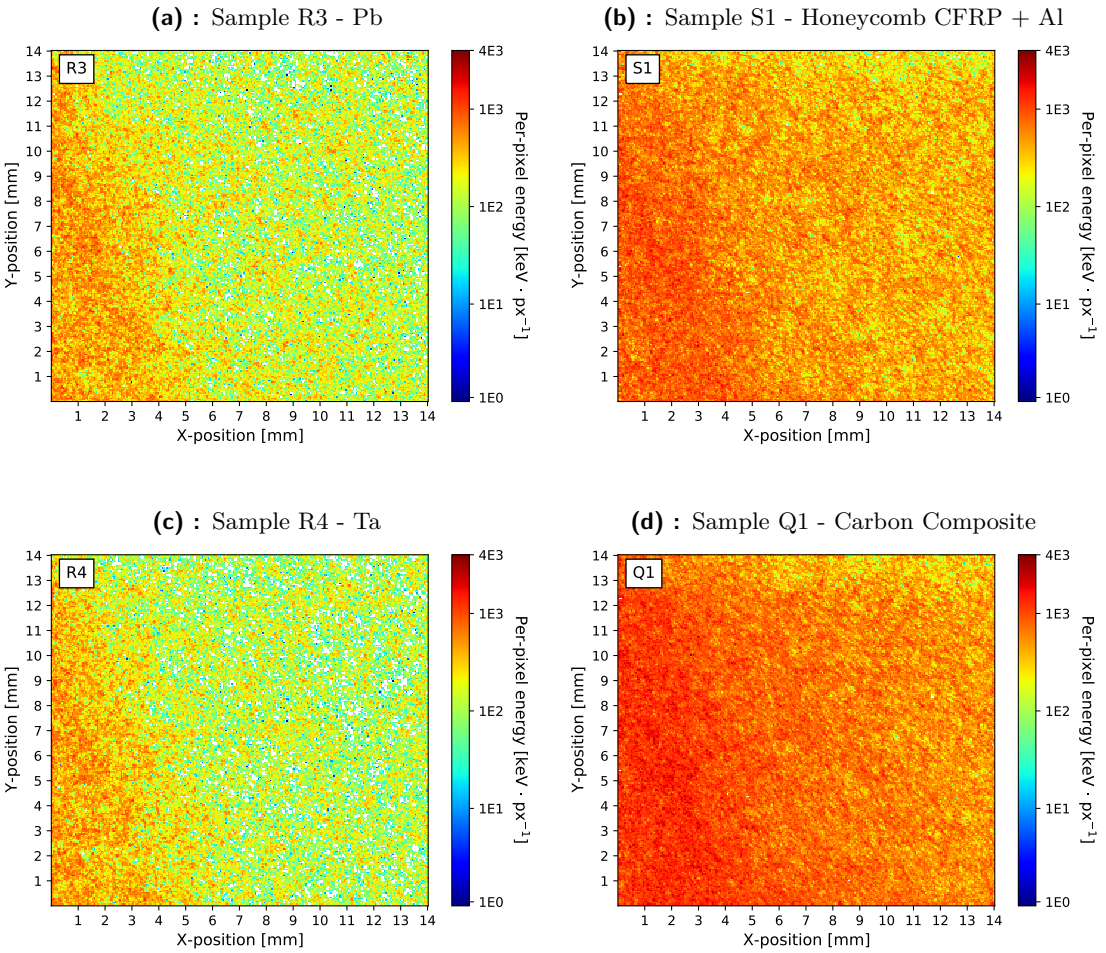

Figure 8.6: Similar to Figure 8.5 showing the detection and radiation field visualization of 5 MeV electrons. Measured with the `TPX3 D05 500 µm Si Minipix` detector in 7 s acquisition time, at a 45° incident direction to the proton beam. Each plot shows a measurement for different shielding sample specified in the plot's captions. It can be seen that sample R4 (Ta) in plot c) shield the most particles.

8.2.2 Protons

Figure 8.7 shows the integrated 31 MeV proton deposited energy measured with the `TPX C08 500 µm Si Minipix` detector for 14 s at 45° angle without a shielding sample.

Figure 8.8 shows the integrated deposited energy behind several shielding samples. It can be seen that the sample R4 (Ta) in plot c) shields the most particles. It can be also seen, that the low-Z sample S1 (CFRP + Al honeycomb sandwich) in plot b) is more effective at shielding protons than sample R3 (Pb) in plot a). The fact that the carbon composite sample Q1 in plot d) shows as a poor proton shield can be attributed namely to the sample's thickness.

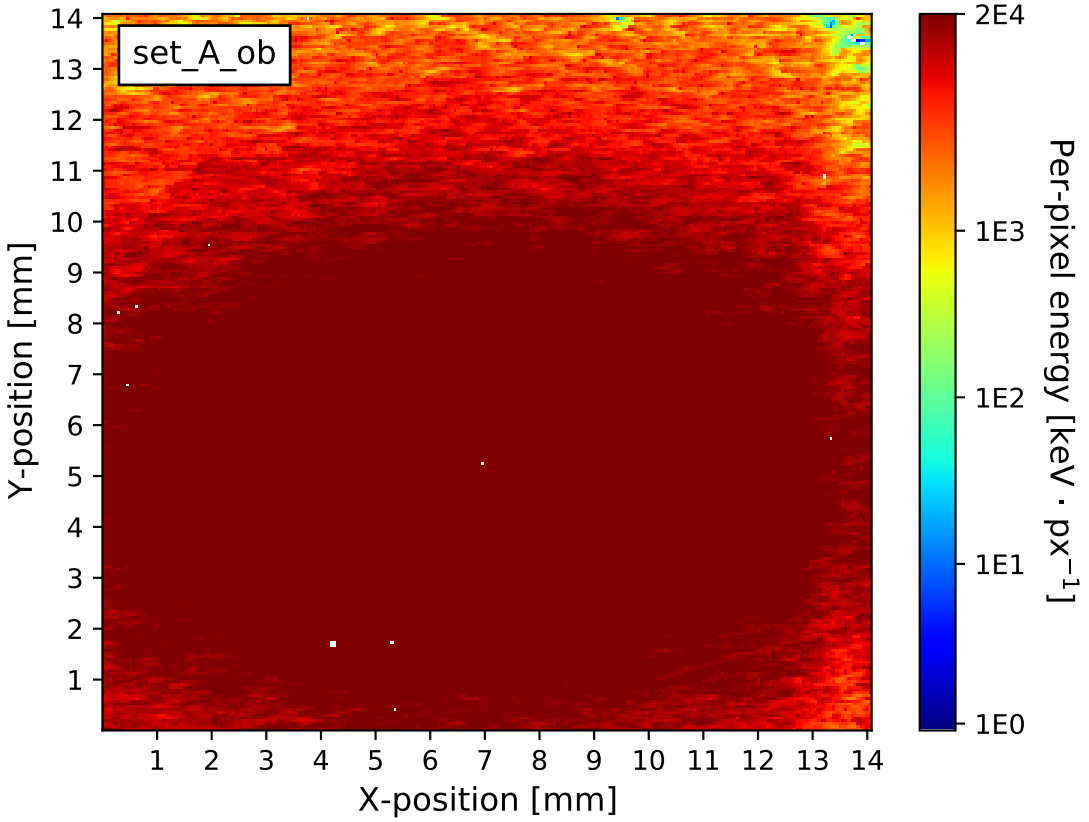

Figure 8.7: Similar to Figure 8.5 showing the detection and radiation field visualization of 31 MeV protons. Results shown for open beam - no shielding sample is used. Measured with the `TPX C08 500 µm Si Minipix` detector for 14 s at a 45° incident direction to the proton beam.

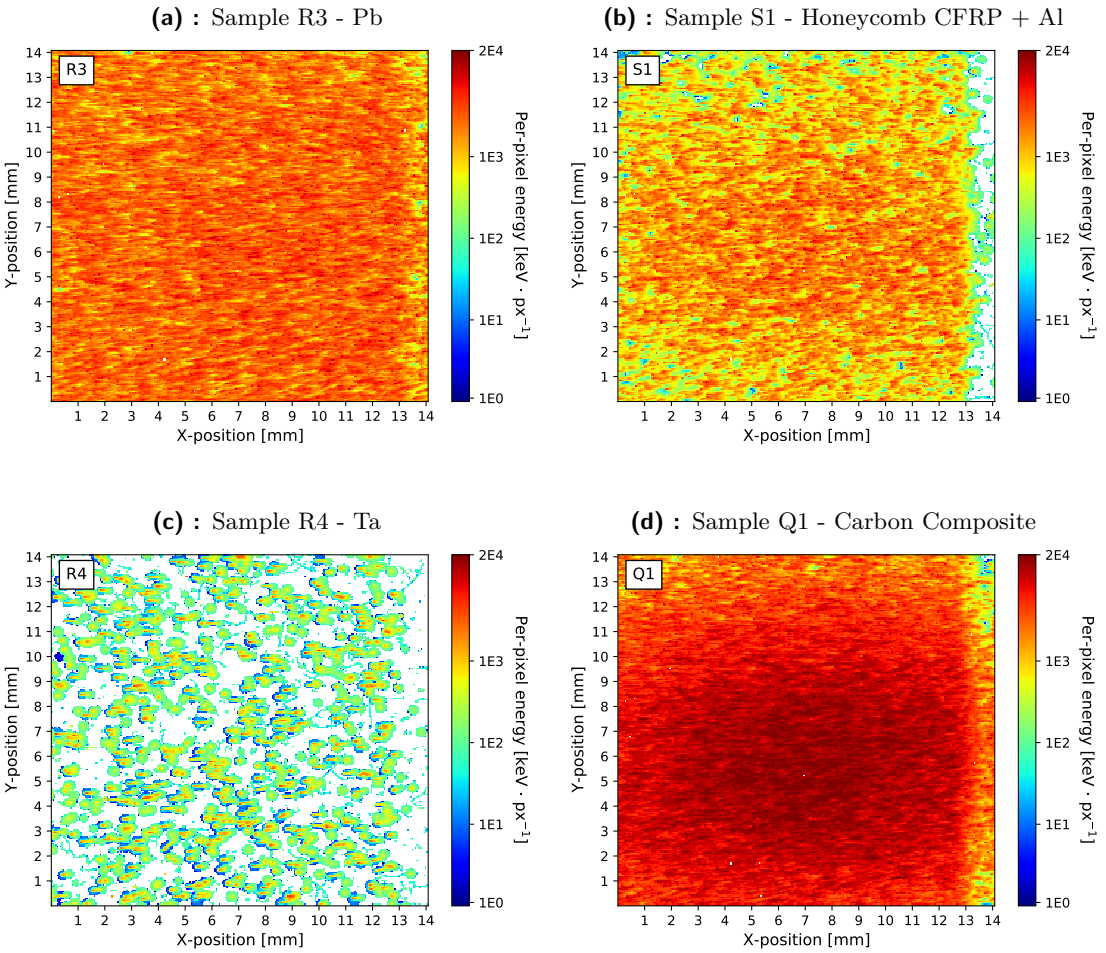

Figure 8.8: Similar to Figure 8.6d showing the detection and radiation field visualization of 31 MeV protons behind selected shielding samples. Measured with the `TPX C08 500 µm Si Minipix` detector for 14 s at a 45° incident direction to the proton beam. Each plot shows the measurement for selected shielding sample specified in plot's captions. It can be seen that sample R4 (Ta) in plot c) shields the most particles.

8.3 Integrated 2D imaging & Numerical comparison of physical products: flux, dose rate

While the sections above depicted individual or integrated particles, this section will consider only individual events from an event list, as described in Section 7.1. This type of imaging can provide more precise visualizations of the physical products. Besides the visualization of selected measured samples, graphs presenting the computed mean values of flux and dose rate for all samples in a given experiment are shown. These graphs show the importance of normalization of the measured values.

8.3.1 X-rays 50 keV

The measurements for the X-ray scanner 50 keV experiment were measured by the `WidePIX A06 (2×5 = 10× chips array MPX3 1000 µm CdTe )` LAD for 10 s. The beam was perpendicular to the detector. The X-ray scanner experiment measures simultaneously and shows all the measured samples. Due to the nature of the detector, the output of the measurement are only event counts for individual pixels, without detailed event-by-event information on particle deposited energy. The event count rate normalized per sensor area and unit time, called particle **flux** is visualized in Figure 8.9. The white ROI frames represent the selected open beam sensor areas. The black ROI frames represent the shielded sensor regions. The samples in the visualization are not normalized for their thickness. A bigger version of Figure 8.9 can be found in Appendix C.5. The Figure shows that the best shielding properties belong to samples I1, I2 (both aluminum), D (ceramics) and K (steel).

Figure 8.10 presents the resulting values of flux for all samples in the experiment. Black cross markers represent the flux value for the open beam area relevant for the given sample. Light blue square markers represent the flux value measured behind the shielding sample. Because every sample has a different thickness and density, the values have been normalized to the surface density of 1 cm of aluminum. This value is represented by the red cross marker for every sample. This is the same for every such figure in this thesis.

Looking at the graph in Figure 8.10, it is seen that the samples I1, I2, D and K have the best flux shielding properties even after normalization for density. Out of all the remaining samples, the best samples are A1 (CFER coated with Ni), H (carbon composite) and A2 (CFER coated with Au).

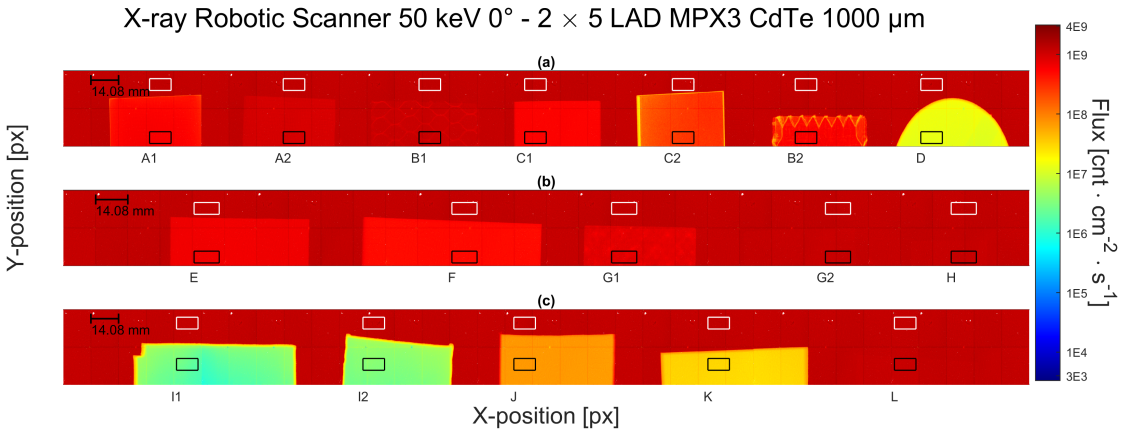

Figure 8.9: Flux visualization of 50 keV X-rays. Measured with the `WidePIX A06 (2×5 = 10× chips array MPX3 1000 µm CdTe)` LAD for 10 s. The beam was perpendicular (0°) to the detector. The white ROI frame specifies the region of interest for the open beam without any shielding, while the black ROI frame specifies the region of interest of detected beam behind the shielding sample. These regions are used in calculating the shielding efficiency. It can be seen that samples I1 and I2 (both alimunium), and D (ceramics) shield the most particles. A bigger version of the Figure can be found in Appendix C.5.

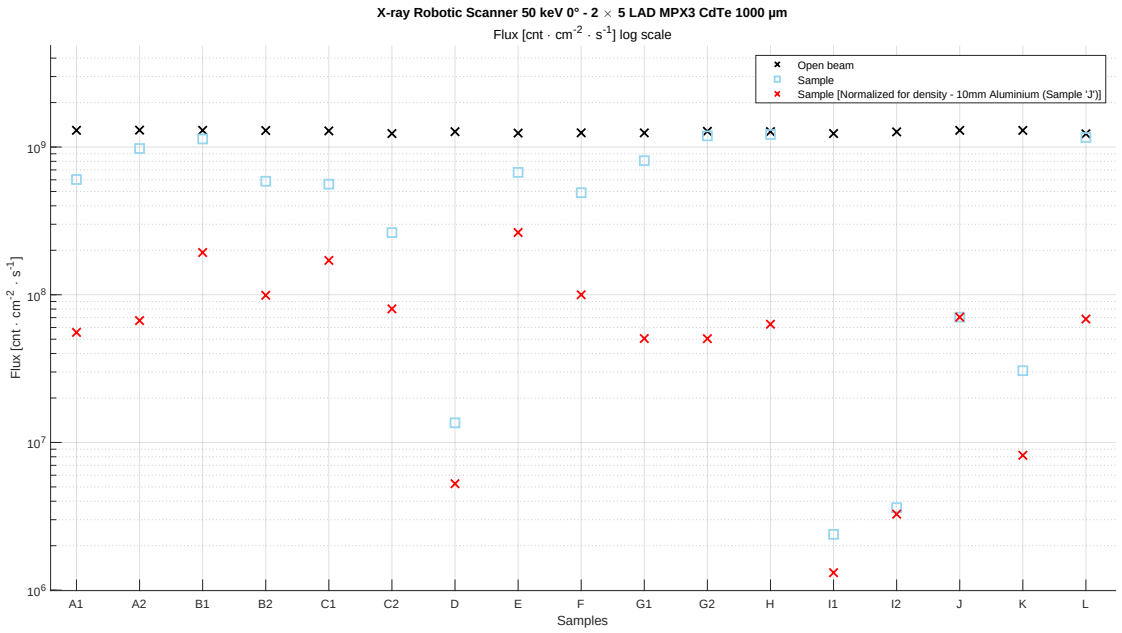

Figure 8.10: X-rays: 50 keV. The plot shows the flux in the region of interest of all samples in respect to the relevant open beam values for individual samples. Values are shown for open beam (black cross) and behind the given shielding sample non-normalized (blue square) and normalized (red cross). Note the logarithmic scale of the colormap.

8.3.2 X-rays 40 keV

The measurements for the table-top X-ray micro-focus tube 40 keV experiment were measured with the `TPX3 H09 500 µm Si AdvaPix` detector for 20 s. The beam was perpendicular to the detector. A detail of the measured samples is seen in Figure 8.11, which shows the **flux** visualization and Figure 8.12, which shows the **dose rate** visualization.

The white ROI frame specifies the region of interest for the open beam i.e. without any shielding. The black ROI frame specifies the region of interest of the measured radiation field behind the shielding sample. These regions are used in calculating given sample shielding efficiency.

Looking at the four figures, samples R4 (Ta) and R3 (Pb) shield many more particles, while also decreasing the deposited dose rate. The 2D imaging maps for more measured samples can be found in Appendix C.1.

Taking into account the normalized measurements for all the samples, as shown in Figure 8.13 and Figure 8.14, the samples can be divided into two groups based on how effective in shielding they are - low-Z and high-Z materials. As expected, all high-Z materials, or composites made primarily of high-Z materials have better shielding properties namely for X-rays (and also heavy charged particles such as protons).

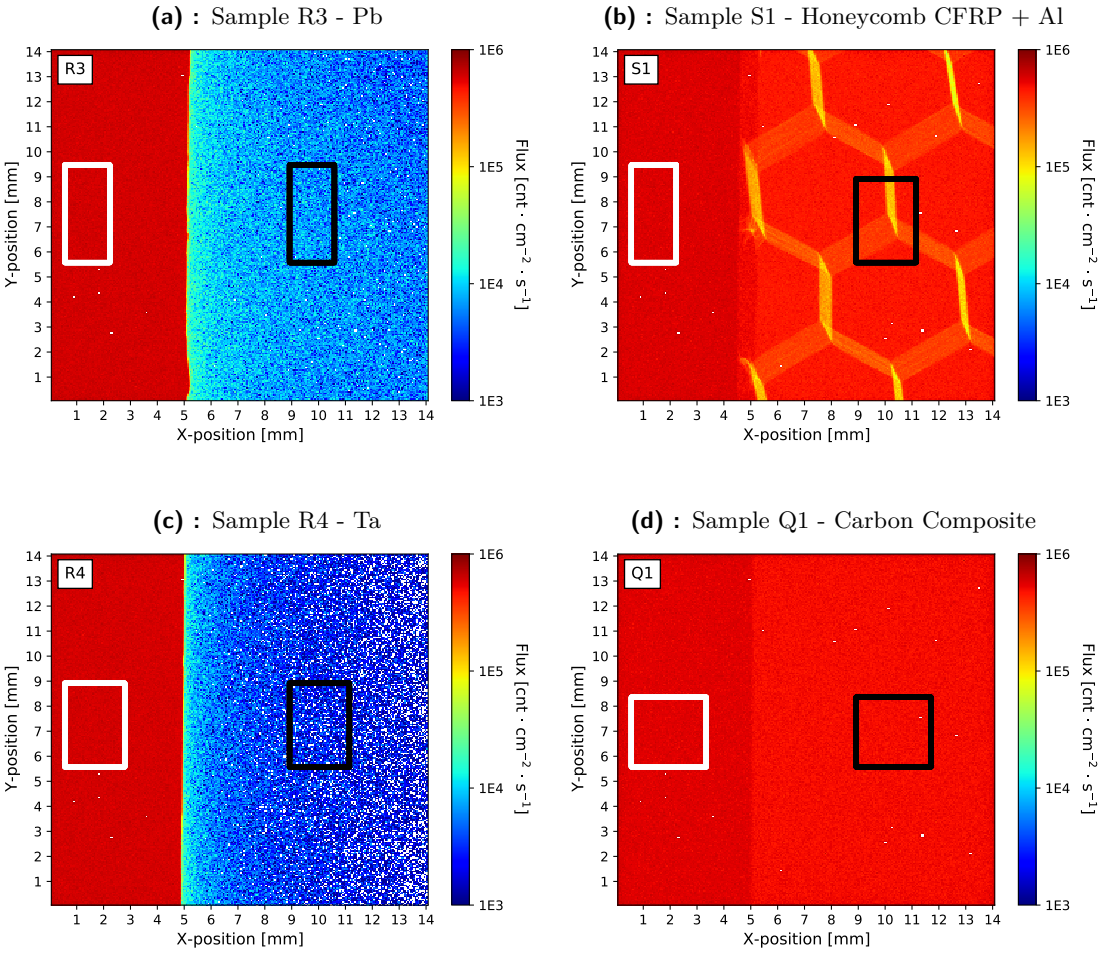

Figure 8.11: Particle **flux** visualization of 40 keV X-rays. Measured with the `TPX3 H09 500 µm Si AdvaPix` detector for 20 s. The beam was perpendicular to the detector. Each plot shows the measurement for selected shielding sample specified in the plot's caption. The white ROI frame specifies the region of interest for the open beam without shielding. The black ROI frame specifies the region of interest of the measured radiation field behind the shielding sample. These regions are used in calculating given sample shielding efficiency. Note the logarithmic scale of the colormap. It can be seen that sample R4 (Ta) in plot c) shields the most particles. The 2D imaging maps for more measured samples can be found in Appendix C.1.

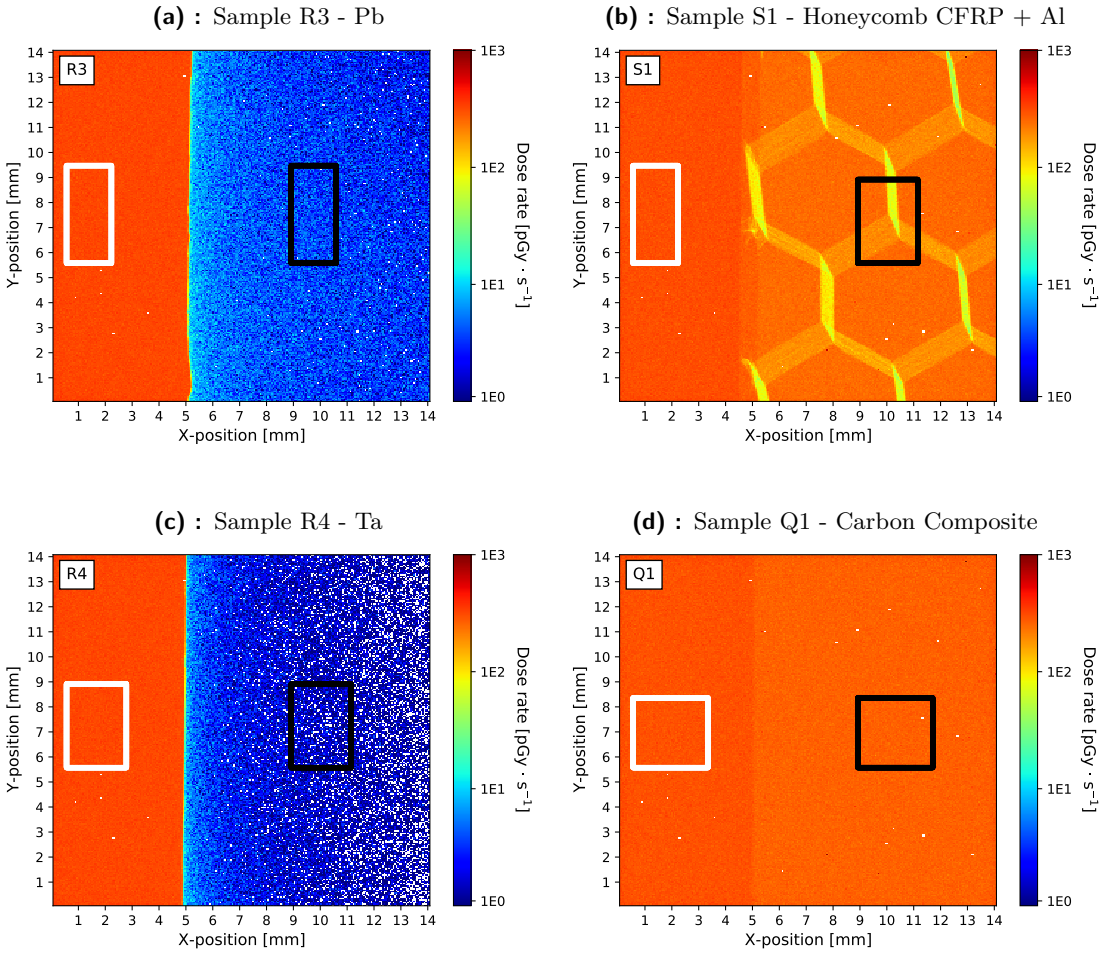

Figure 8.12: Similar to Figure 8.11 showing the **dose rate** visualization of 40 keV X-rays. The same primary radiation, detector, geometry, selected samples and raw data as in Figure 8.11 are used. Sample R4 (Ta) in plot c) shields the most deposited energy i.e. deposited dose.

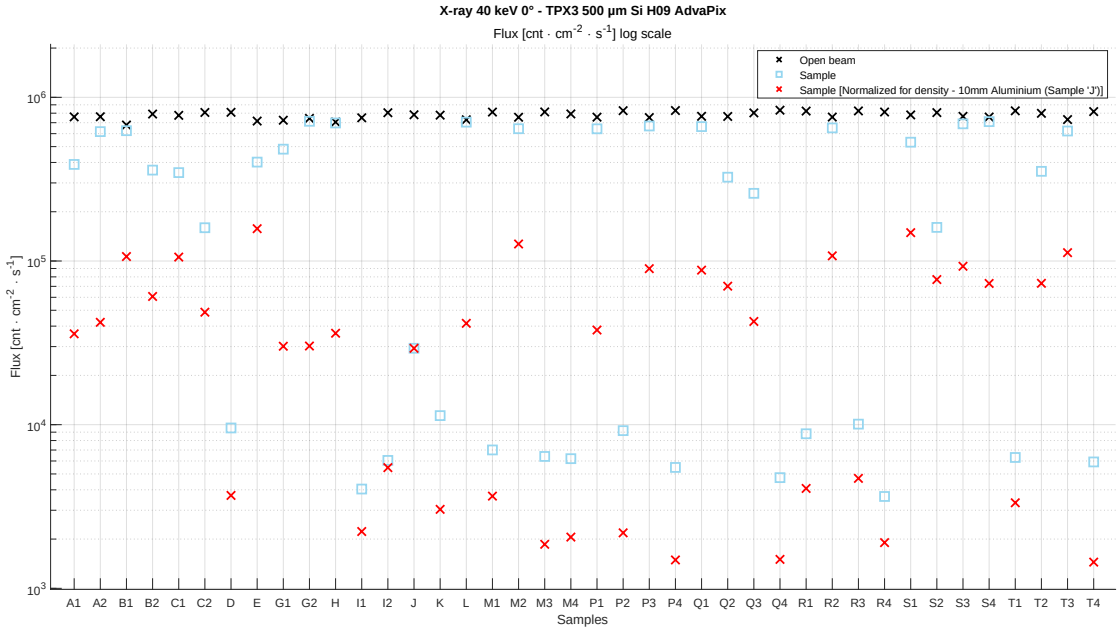

Figure 8.13: Similar to Figure 8.10 showing the shielding efficiency for 40 keV X-rays. The plot shows the particle flux in the region of interest of all samples in respect to the relevant open beam values for individual samples. Values shown for open beam (black cross), behind the given shielding sample non-normalized (blue square) and normalized (red cross). Note the logarithmic scale of the colormap.

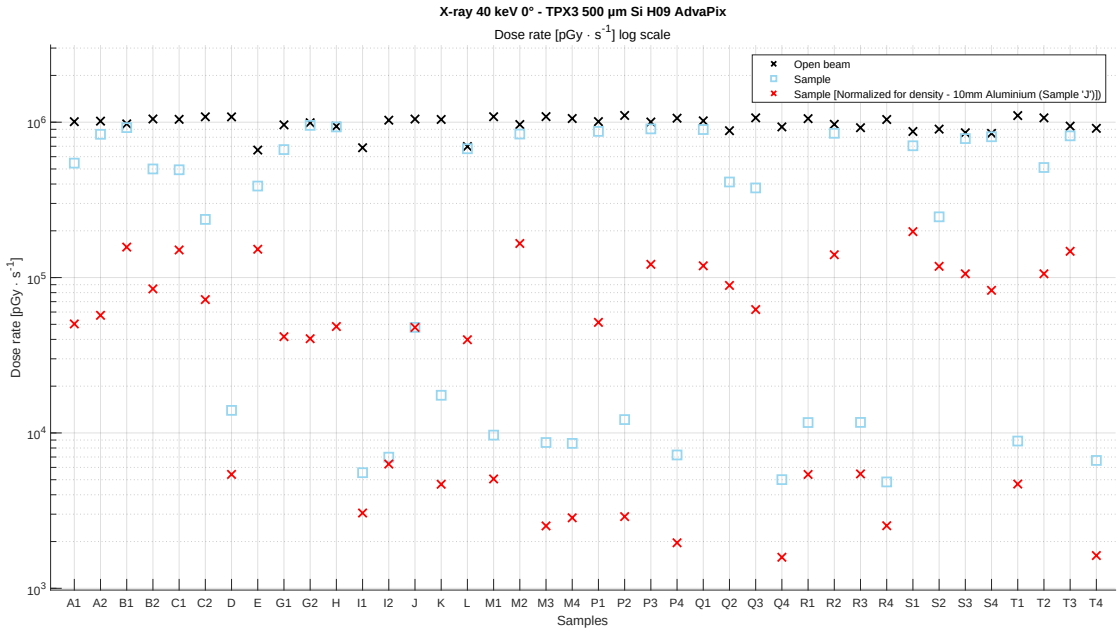

Figure 8.14: Similar to Figure 8.13 showing the dose rate.

8.3.3 X-rays 120 keV

The measurements for the X-ray tube 120 keV experiment were measured with the `TPX3 H09 500 µm Si AdvaPix` detector for 20 s frame acquisition time. The beam was perpendicular to the detector. Figure 8.15 shows the **flux** visualizations and Figure 8.16 shows the **dose rate** visualizations.

As can be seen in the open beam values of both figures, the 120 keV beam has lower flux and dose rate values than the 40 keV beam. This is a consequence of the primary beam (X-ray micro-focus unit) settings.

Looking at the four figures, samples R4 (Ta) and R3 (Pb) shield many more particles, while also decreasing the deposited dose rate. The 2D imaging maps for more measured samples can be seen in Appendix C.2.

Taking into account the normalized measurements for all the samples, shown in Figure 8.17 and Figure 8.18, it is seen that the 120 keV X-rays are harder to shield than 40 keV. This agrees with the expected physics - high-energy X-rays (called hard X-rays) are more penetrating than low-energy (soft) X-rays. While most of the high-Z materials that were efficient in shielding 40 keV X-rays could still be classified as the more efficient at shielding 120 keV X-rays, they are joined by some of the carbon composites and a clear distinction between high-Z and low-Z materials can no longer be easily made.

Moreover, as can be seen, some of the samples have the same or slightly higher value for flux or dose rate in the shielded area than in the open beam area. This is due to secondary radiation such as Compton scattered X-rays and scattered primary radiation.

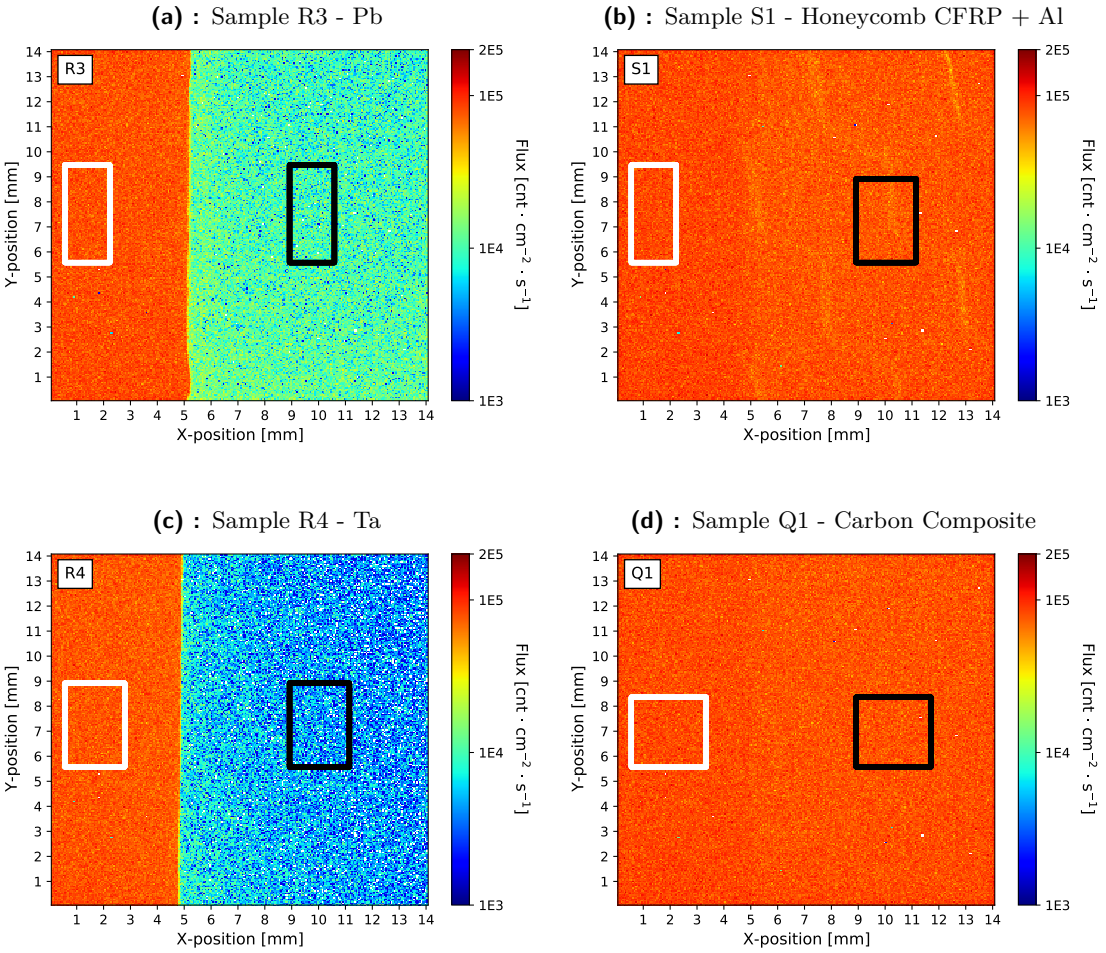

Figure 8.15: Similar to Figure 8.11 showing the particle **flux** visualization for the 120 keV X-rays. Measured with the `TPX3 H09 500 µm Si AdvaPix` detector for 20 s. The beam was perpendicular to the detector. Each plot shows the measurement for selected shielding samples specified in the plot's captions. The white ROI frame specifies the region of interest for the open beam without shielding, while the black ROI frame specifies the region of interest of the measured radiation field behind the shielding sample. These regions are used in calculating given sample shielding efficiency. Note the logarithmic scale of the colormap. Sample R4 (Ta) in plot c) shields the most particles. The 2D imaging maps for more measured samples are given in Appendix C.2.

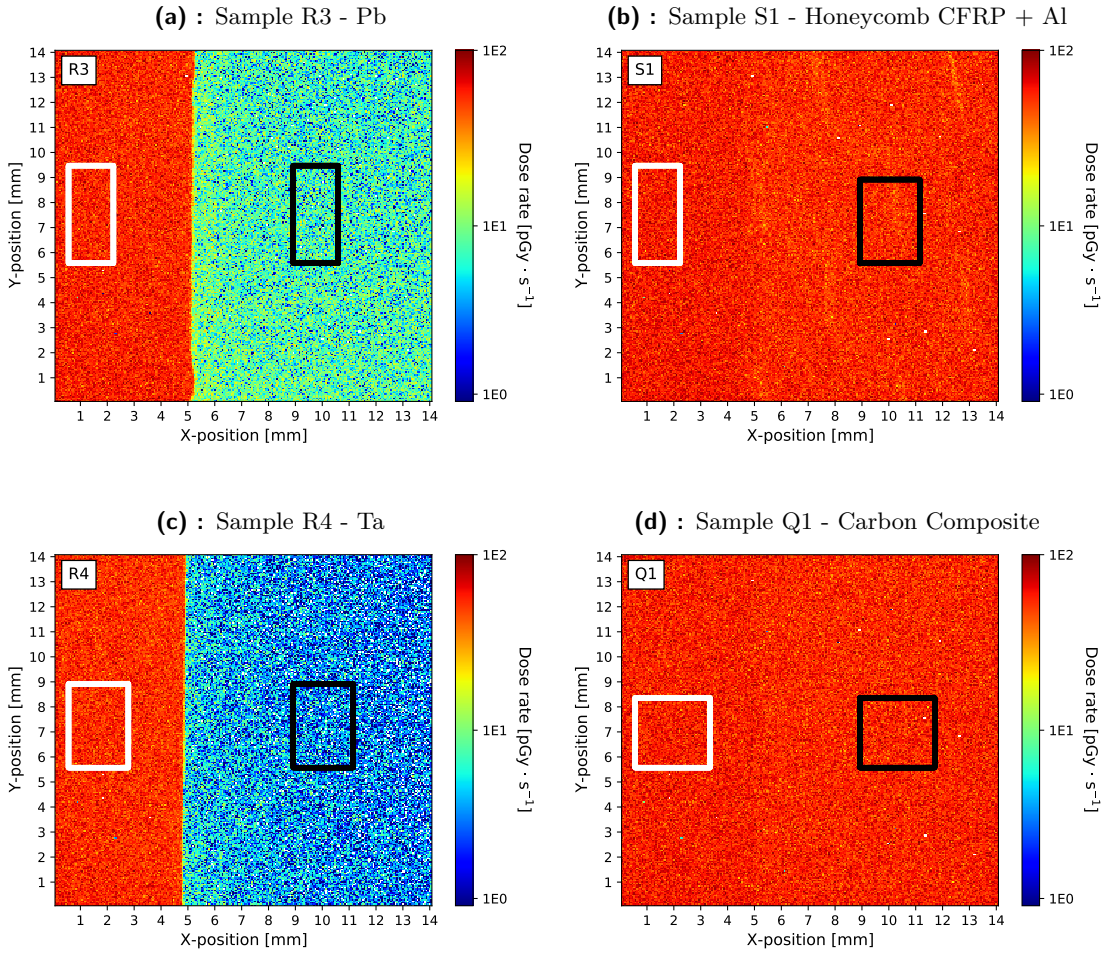

Figure 8.16: Similar to Figure 8.15 showing the **dose rate** visualization for the 120 keV X-rays. The same primary radiation, geometry, detector, selected samples and raw data as in Figure 8.15 are used. Sample R4 (Ta) in plot c) shields the most deposited energy.

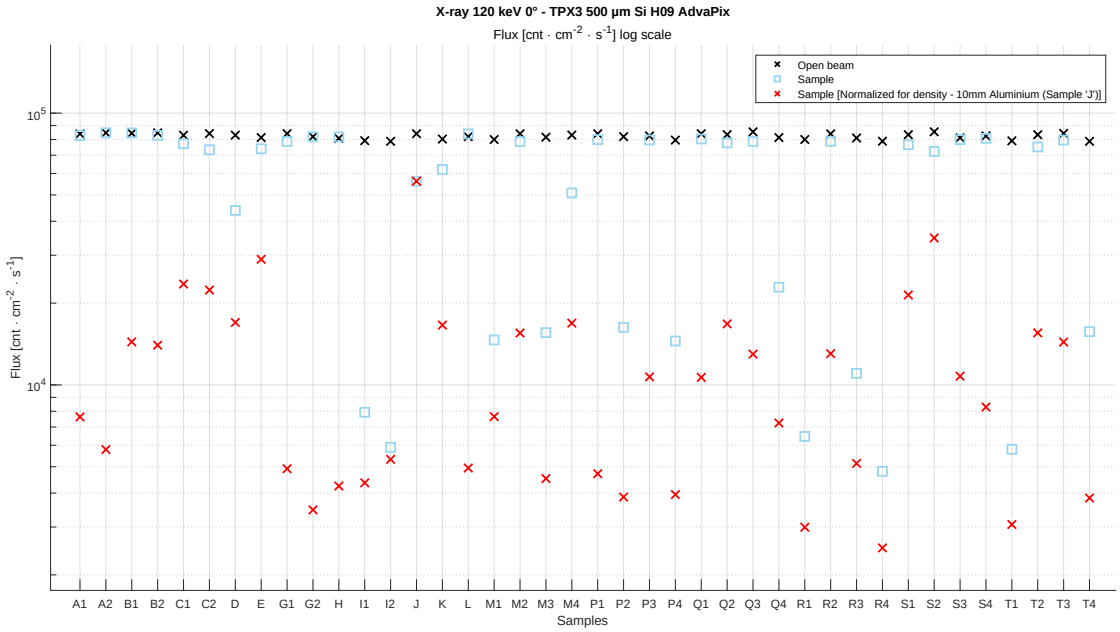

Figure 8.17: Similar to Figure 8.13 for 120 keV X-rays showing the particle flux in the region of interest of all samples in respect to the relevant open beam values for individual samples. Note the logarithmic scale of the y axis. Values shown for open beam (black cross), behind the given shielding sample non-normalized (blue square) and normalized (red cross).

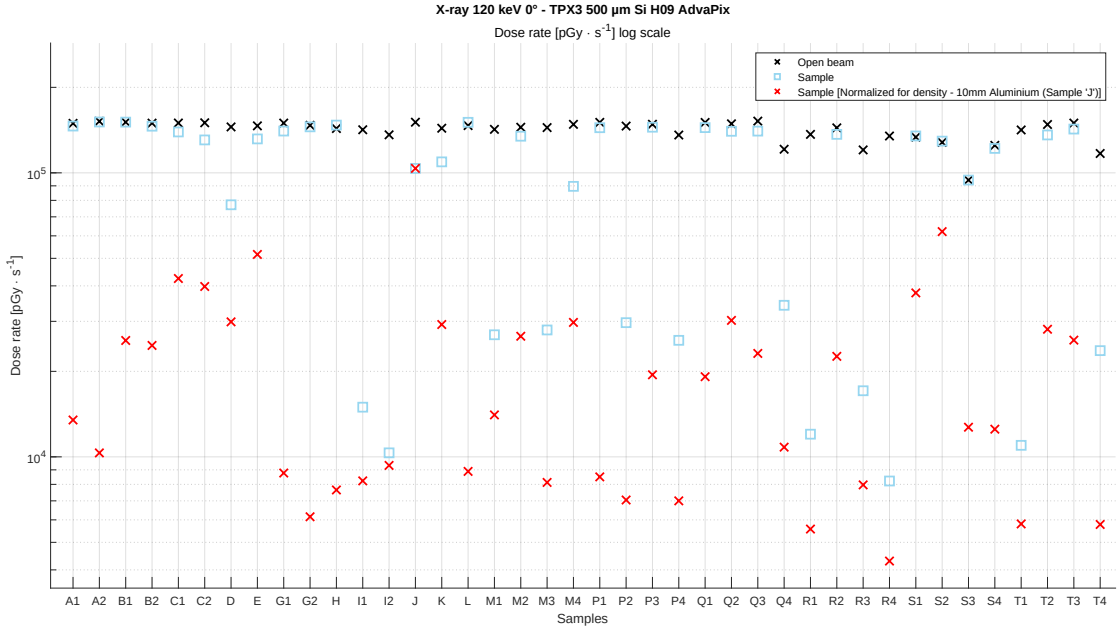

Figure 8.18: Similar to Figure 8.17 for 120 keV X-rays showing the dose rate.

8.3.4 Electrons

The measurements for the 5 MeV electrons experiment were measured with the `TPX3 D05 500 µm Si Minipix` detector for 120 s for each sample. The beam and the detector had a 45° angle tilt direction.

Contrary to X-ray experiments, the open beam was measured as a separate measurement. Figure 8.19 shows the detection and **flux** visualization for the open beam measurement, while Figure 8.20 shows the flux visualization for the four selected samples. Similarly, Figure 8.21 shows the **dose rate** visualization for open beam and Figure 8.22 for the selected shielding samples.

The white ROI frame in the open beam plots and the black ROI frame in the shielded beam plots represent the region of interest used for shielding efficiency calculations. As explained in previous chapters, only this area is used where the well-defined beam falls on the detector.

Looking at the four plots, samples R4 (Ta) and R3 (Pb) shield more particles, while also decreasing the deposited dose rate. The 2D imaging maps for more measured samples are given in Appendix C.3.

Taking into account the normalized measurements for all the samples, shown in Figure 8.23 and Figure 8.24, the best shielding materials are certain carbon composites and CFER (A1, A2, G1, G2, H, P1), with the addition of PMMA (L). The higher values for high-Z materials can also be attributed to created secondary radiation (Compton X-rays) and scattered primary X-rays.

As can be seen, samples A1, A2, C1, C2, G1 and G2 have higher values for flux or dose rate for the shielded area than the open beam area. This can be attributed to secondary radiation. A limitation can be the instability of the microtron generated electron beam intensity. All these samples, along with sample D, are part of the set "A" that was measured first during the microtron experiment. This set had the open beam measured only once, at the end of the measurement. Sample G2 was measured first and sample G1 last. It could be assumed that the beam intensity became progressively lower towards the end of the measurement. However, looking at average values of open beams for other sets, it was probably higher during the whole set "A" measurement, and only decreased towards the very end. The instability might have impacted more samples in other sets, but might not have been as evident. The best solution would be to set up future measurements as with the X-ray tube experiment, so that the open beam is measured at the same time as the shielded beam.

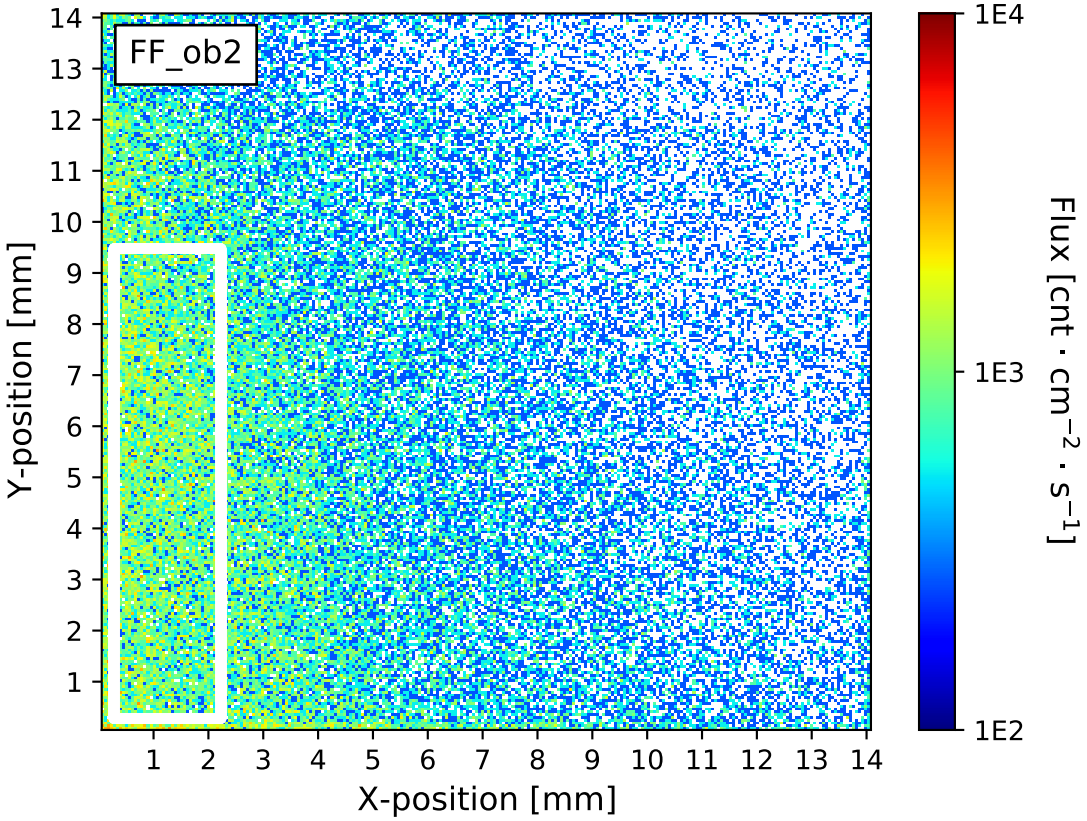

Figure 8.19: Similar to Figure 8.5 showing the particle **flux** visualization of 5 MeV electrons without shielding sample i.e. open beam. Measured with the `TPX3 D05 500 µm Si Minipix` detector for 120 s. The beam and the detector had a 45° angle tilt direction. The white ROI frame represents the region of interest used for the shielding efficiency calculations.

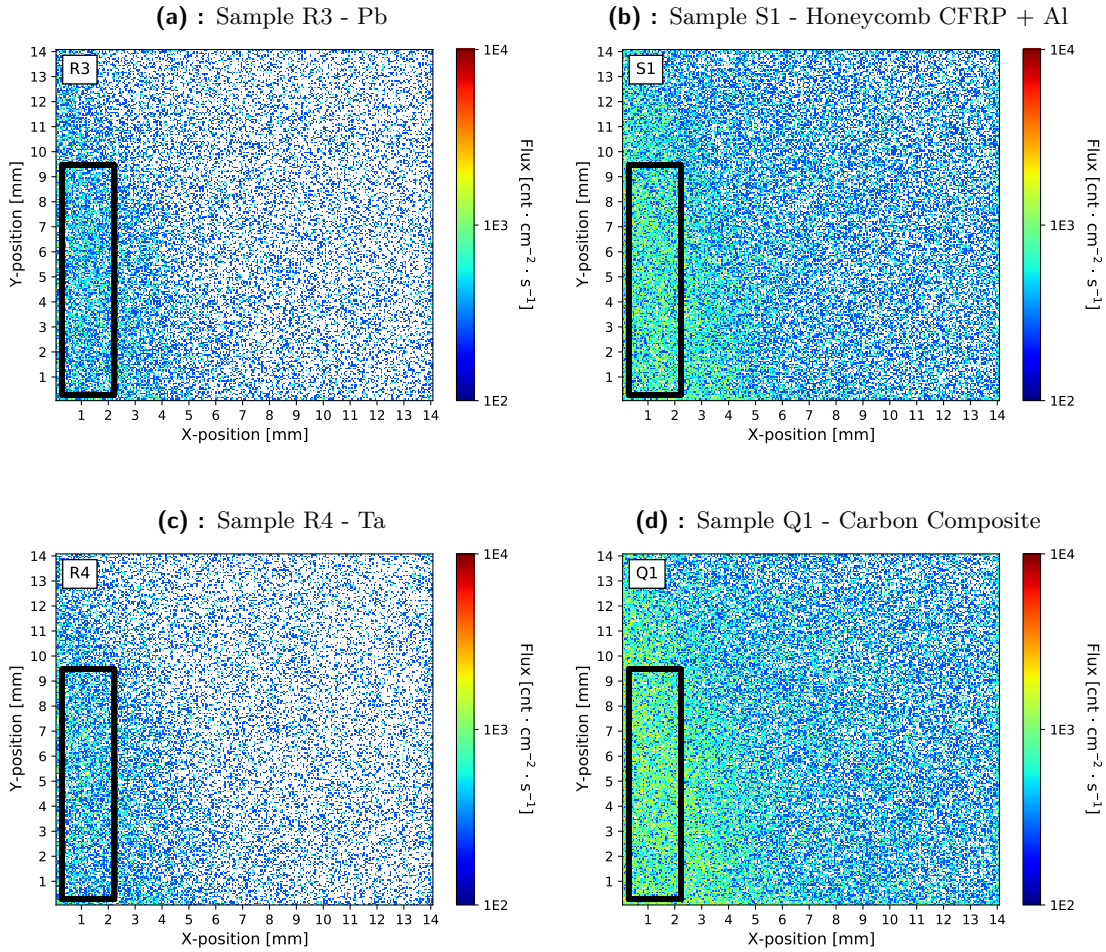

Figure 8.20: Similar to Figure 8.6 showing the particle **flux** visualization for 5 MeV electrons. Measured with the `TPX3 D05 500 µm Si Minipix` detector for 120 s. The beam and the detector had a 45° angle tilt direction. Each plot shows a measurement for selected shielding sample specified in the plot's caption. The black ROI frame represents the region of interest used for the shileding efficiency calculations. Note the logarithmic scale of the colormap. It can be seen that samples R3 (Pb) in plot a) and R4 (Ta) in plot c) shield the most particles. The 2D imaging maps for more measured samples are given in Appendix C.3.

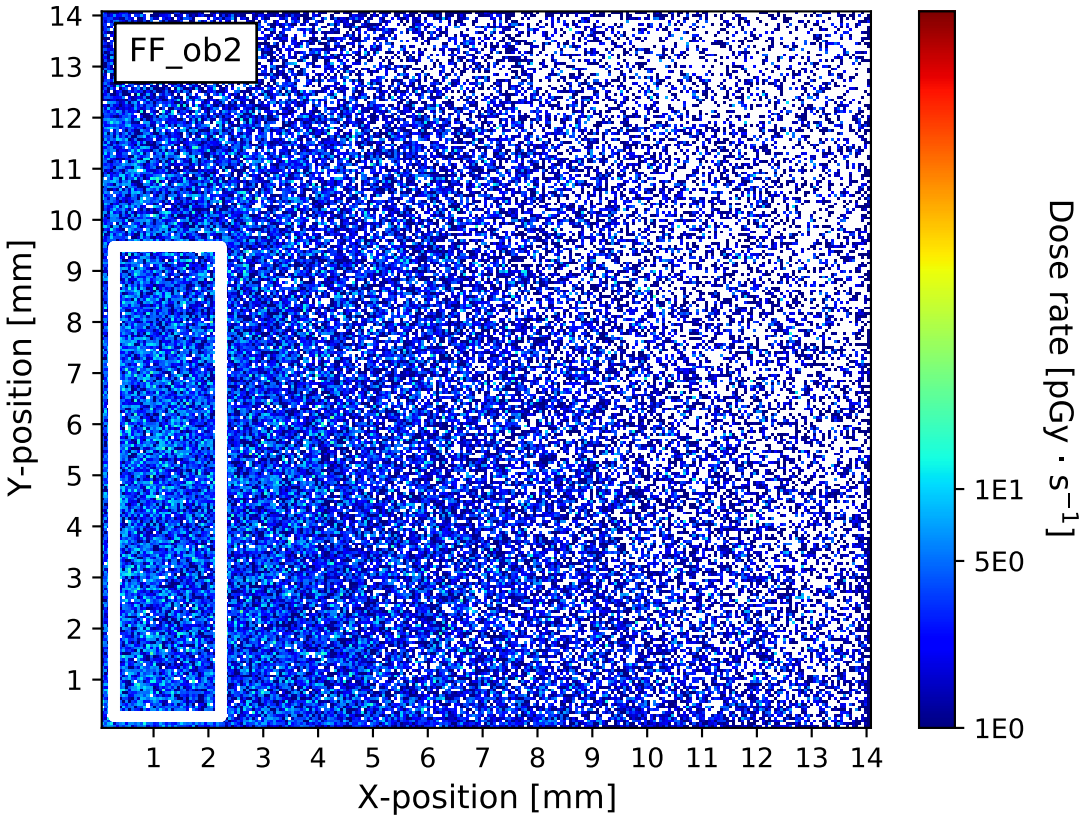

Figure 8.21: Similar to Figure 8.19 showing the **dose rate** visualization of 5 MeV electrons without shielding. The same samples, detector, radiation, geometry and raw data were used. The white ROI frame represents the region of interest used for the shielding efficiency calculations.

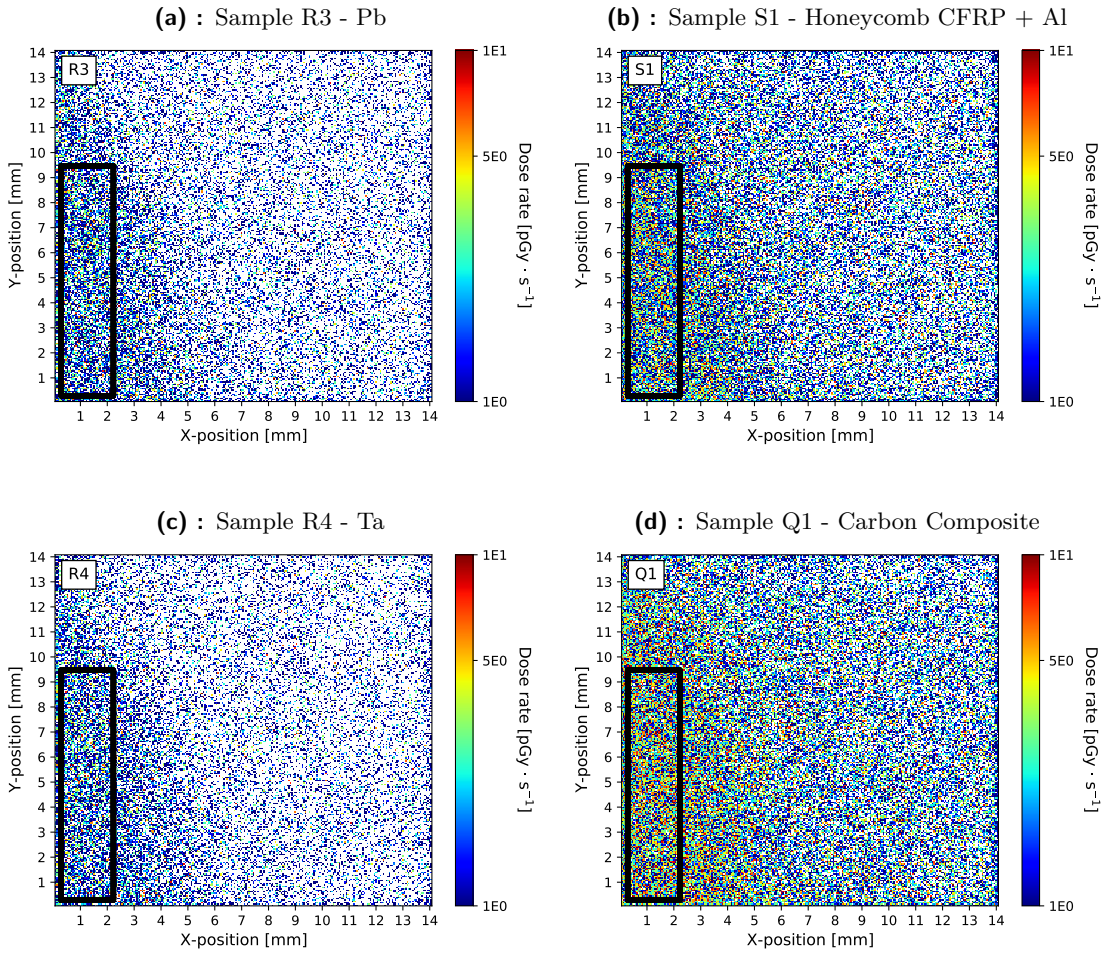

Figure 8.22: Similar to Figure 8.20 showing the **dose rate** visualization for 5 MeV electrons. The same samples, detector, radiation, geometry and raw data were used. The black ROI frame represents the region of interest used for the shielding efficiency calculations. It can be seen that samples R3 (Pb) in plot a) and R4 (T4) in plot c) shield the most deposited energy i.e. deposited dose.

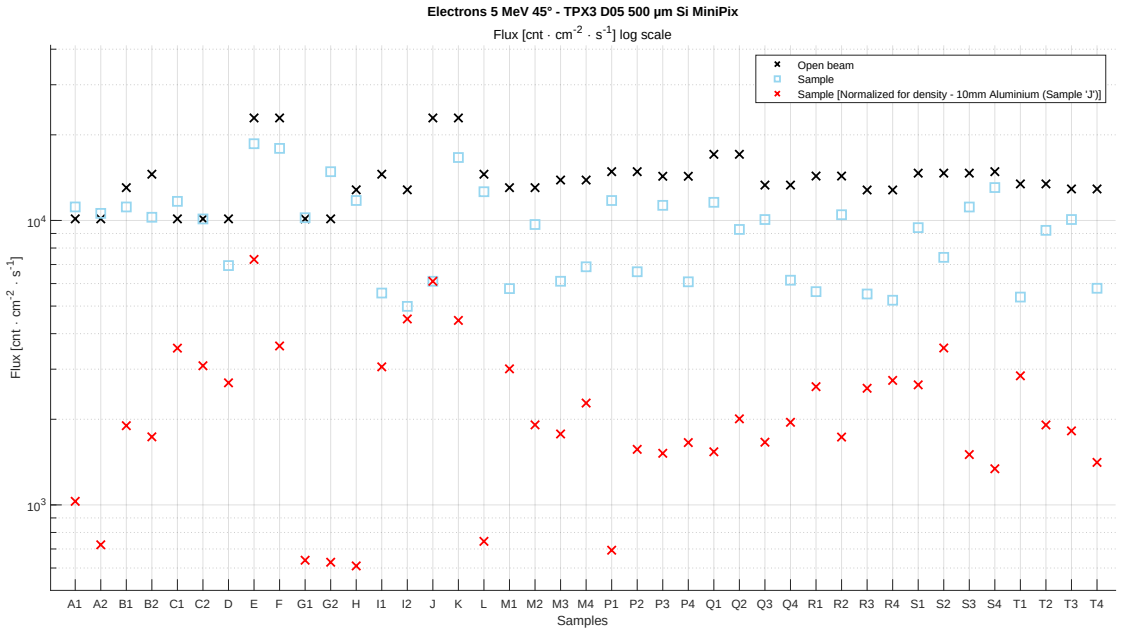

Figure 8.23: Similar to Figure 8.17 for 5 MeV electrons showing the particle flux in the region of interest of all samples in respect to the relevant open beam values for individual samples. Note the logarithmic scale of the y axis. Values shown for open beam (black cross), behind the given shielding sample non-normalized (blue square) and normalized (red cross).

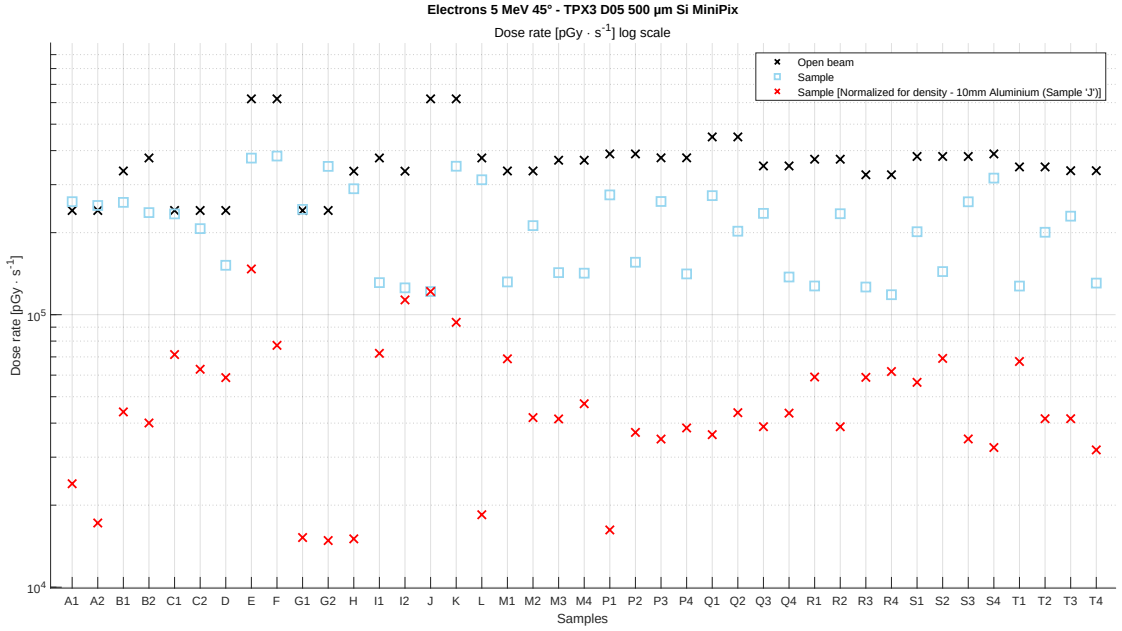

Figure 8.24: Similar to Figure 8.23 for 5 MeV electrons showing the dose rate.

8.3.5 Protons

The measurements for the 31 MeV protons experiment were measured with the `TPX C08 500 µm Si Minipix` detector for 50 s for each sample. The beam and the detector had a 45° angle tilt direction.

Similar to the microtron experiment, the open beam was measured as a separate measurement. Figure 8.25 shows the **flux** visualization for the open beam and Figure 8.26 for the selected shielding samples, while Figure 8.27 shows the **dose rate** visualization for the open beam and Figure 8.28 for the samples.

The white ROI frame in the open beam plots and the black ROI frame in the shielded beam plots represent the region of interest used for the shielding efficiency calculations. As explained in previous chapters, only this area is used where the well-defined beam falls on the detector.

Looking at the four plots, samples R4 (Ta) and S1 (CFRP + Al honeycomb sandwich) shield more particles, while also decreasing the deposited dose rate. The 2D imaging maps for more measured samples can be seen in Appendix C.4.

Taking into account the normalized measurements for all the samples, shown in Figure 8.29 and Figure 8.30, there don't seem to be any samples with outstanding shielding efficiency. Samples M1 (carbon composite + Pb) and S2 (GFRP + Al) exhibit the highest shielding efficiency. Looking at all measurements in Figure D.2 in Appendix D, the M1 sample is probably the combination of samples R4 (Ta) / M1 and S2 would be the T4 (carbon composite + Cr + Pb) / S2 measurement as they have almost identical values and were measured next to each other. This is supported by the fact that the classification into event classes in Table E.5 for these two samples shows values that can be seen in other measurements with the stacked samples.

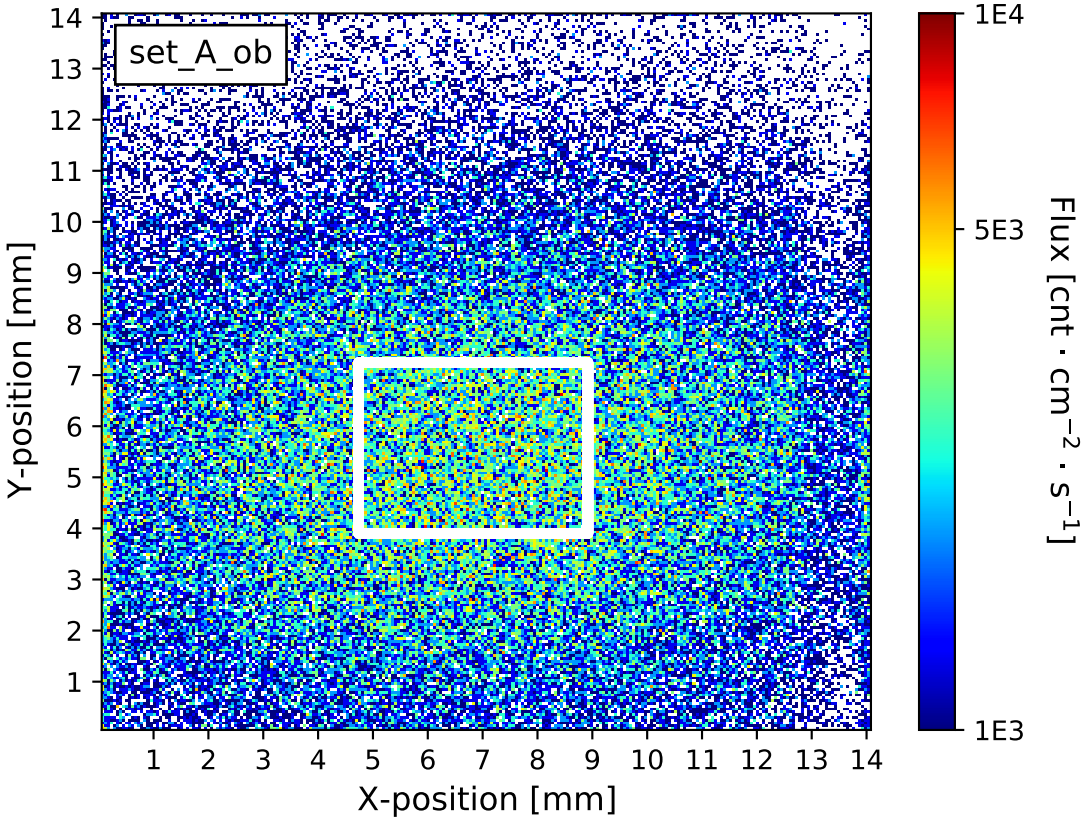

Figure 8.25: Similar to Figure 8.19 showing the particle **flux** visualization of 31 MeV protons without shielding sample i.e. open beam. Measured with the `TPX C08 500 µm Si Minipix` detector for 50 s at a 45° angle tilt direction. The white ROI frame represents the region of interest used for the shielding efficiency calculations.

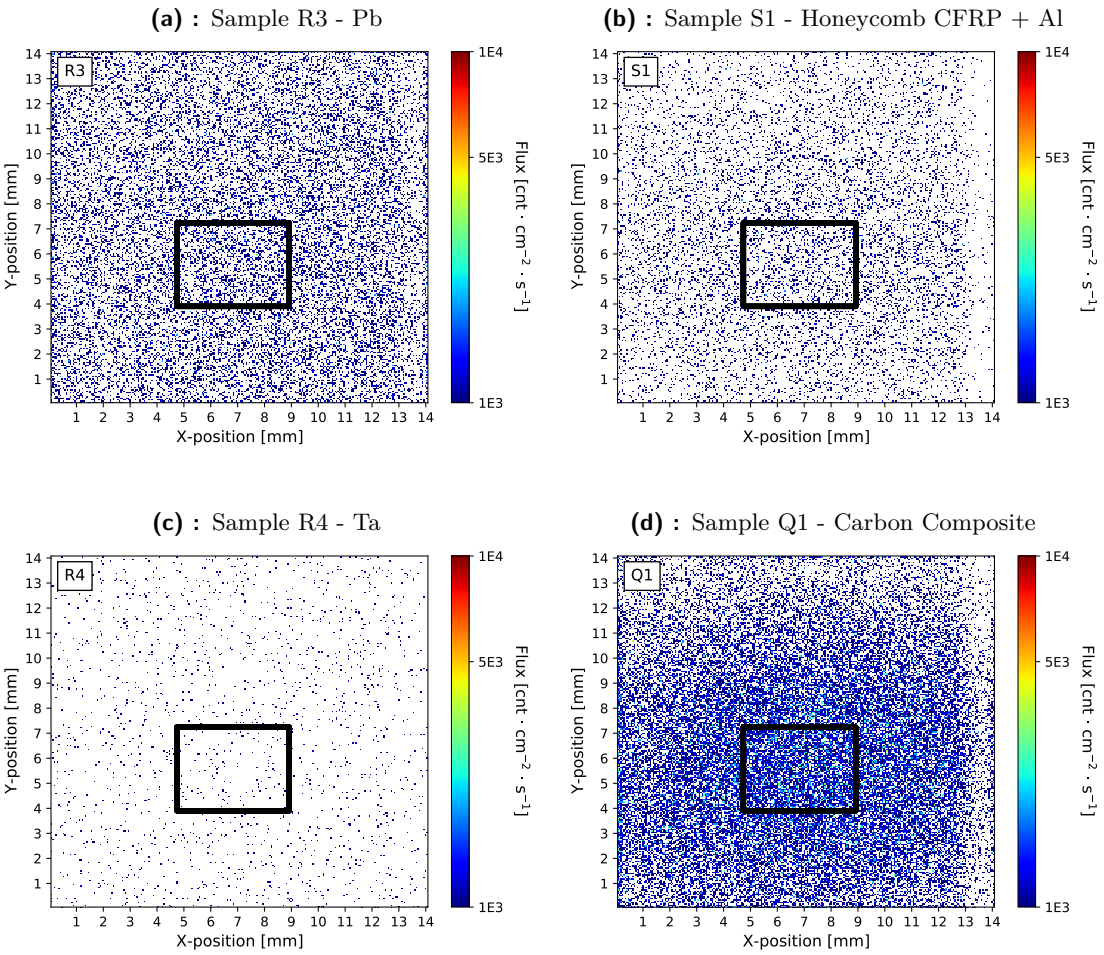

Figure 8.26: Similar to Figure 8.25 showing the particle **flux** visualization of 31 MeV protons behind four selected shielding samples. Measured with the `TPX C08 500 µm Si Minipix` detector for 50 s at a 45° angle tilt direction. Each plot shows the measurement for selected sample specified in the plot's caption. The black ROI frame represents the region of interest used for the shielding efficiency calculations. Only this area is used because that is where the well-defined beam falls on the detector through the shielding sample. It can be seen that samples S1 (CFRP + Aluminum honeycomb sandwich) in plot b) and R4 (Ta) in plot c) shield more particles. The 2D imaging maps for more measured samples can be seen in Appendix C.4.

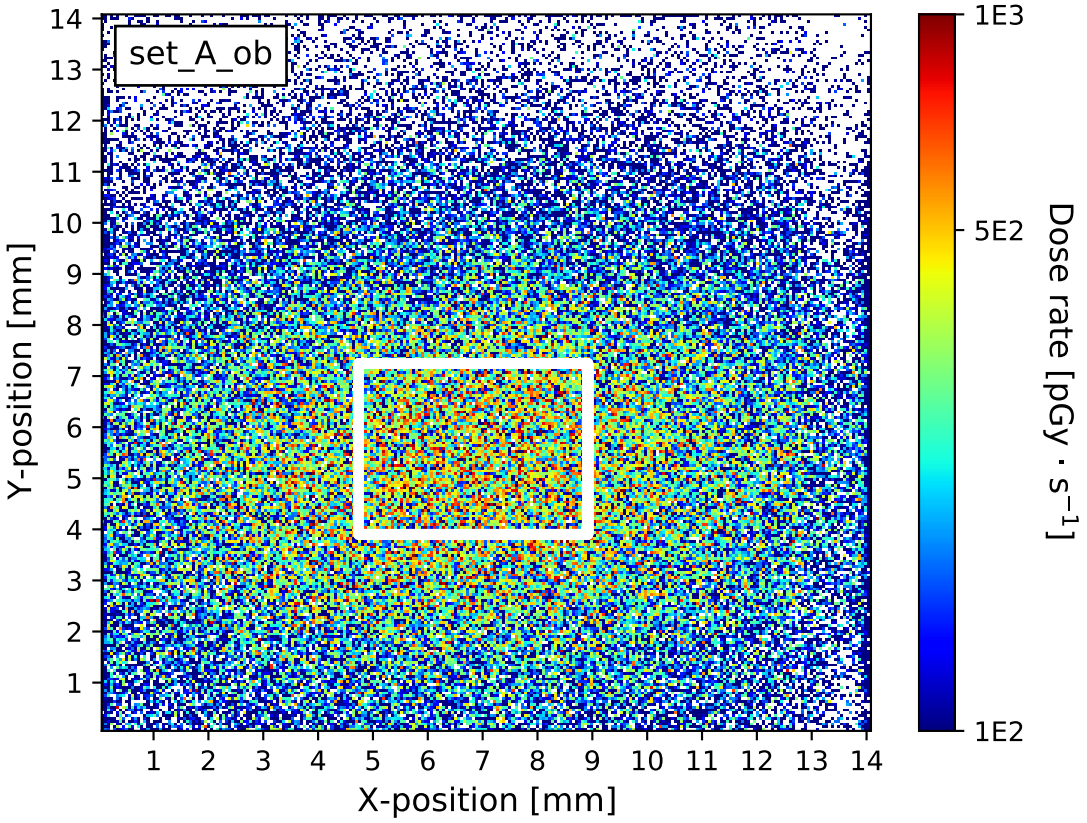

Figure 8.27: Similar to Figure 8.25 showing the **dose rate** visualization of 31 MeV protons. The same samples, primary radiation, geometry, detector and raw data were used. The white ROI frame represents the region of interest used for the shielding efficiency calculations.

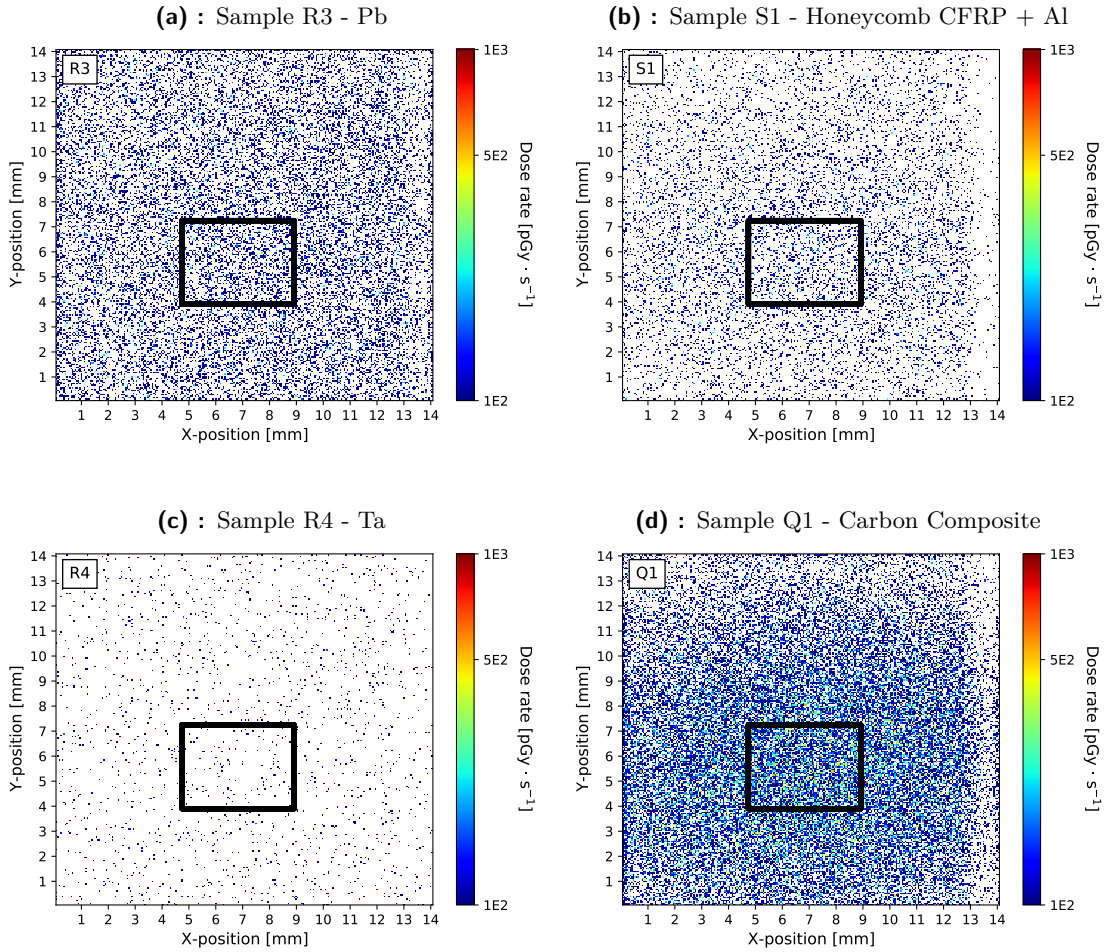

Figure 8.28: Similar to Figure 8.27 showing the **dose rate** visualization of 31 MeV protons. The same samples, primary radiation, geometry, detector and raw data were used. Each plot shows the measurement for selected sample specified in the plot's caption. The black ROI frame represents the region of interest used for the shielding efficiency calculations. Only this area is used because that is where the well-defined beam falls on the detector through the shielding sample. It can be seen that samples S1 (CFRP + Aluminum honeycomb sandwich) in plot b) and R4 (Ta) in plot c) shield more deposited energy.

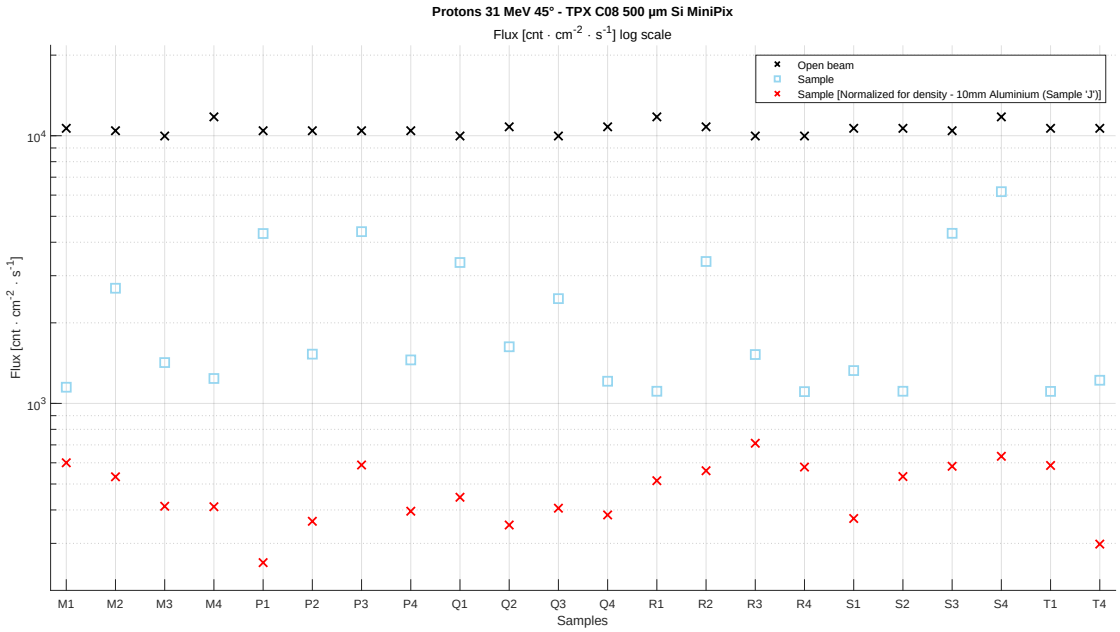

Figure 8.29: Similar to Figure 8.23 for 31 MeV protons showing the particle flux in the region of interest behind all samples in respect to the relevant open beam values for individual samples. Note the logarithmic scale of the y axis. Values shown for open beam (black cross), behind the given shielding sample non-normalized (blue square) and normalized (red cross)

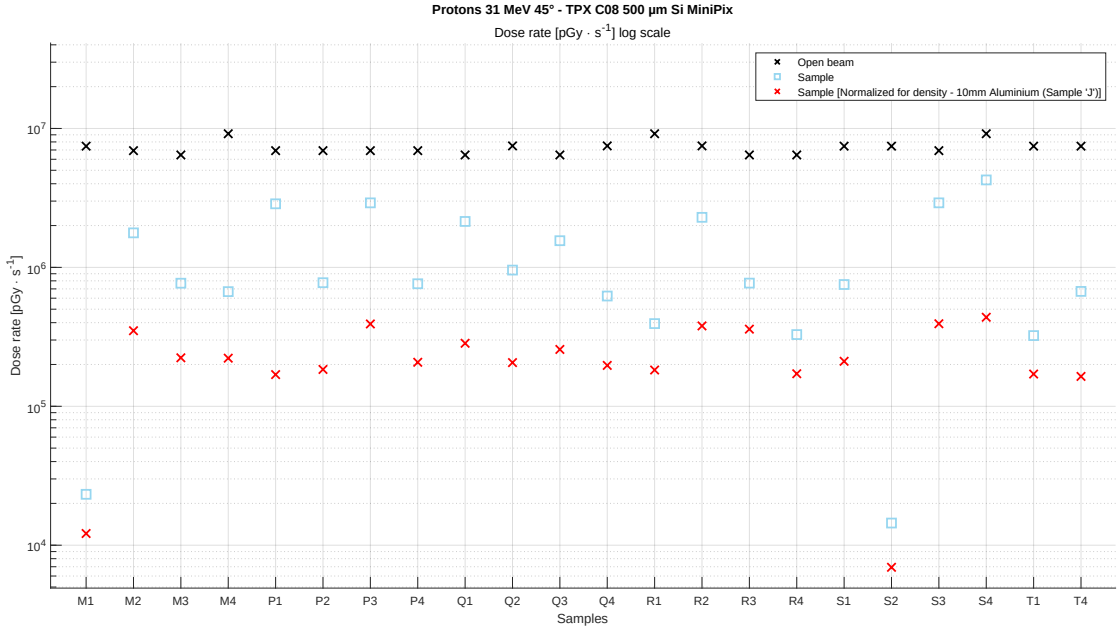

Figure 8.30: Similar to Figure 8.29 for 31 MeV protons showing the dose rate.

8.4 Evaluation

The following figures show and compare the shielding efficiency computed based on normalized values. The shielding efficiency represents the ratio of shielded flux or dose rate in respect to the open beam value.

The **flux** shielding efficiency of all samples from the **X-rays 50 keV** experiment can be seen in Figure 8.31. It shows that samples from materials with higher atomic number like lead, ceramics or steel have better shielding efficiency than low-Z materials. However, certain carbon composites show reasonable shielding efficiency.

Figure 8.32 shows the flux shielding efficiency of all samples from the **X-rays 40 keV** experiment. It can be seen that the high-Z materials like tantalum, lead, ceramics or steel, along with composites containing these materials, have shielding efficiency approaching 100 %. The worst shielding materials are the samples S1 (CFRP+Al Honeycomb sandwich) and E (PTFE), however these materials still have a shielding efficiency over 75 % for this radiation (soft X-rays).

Figure 8.33 shows the dose rate shielding efficiency of all samples from the **X-rays 40 keV** experiment. The results are almost identical to the flux shielding efficiency. The order of the samples approaching a 100 % shielding efficiency varies slightly in comparison to flux shielding. This can be attributed to some samples creating more secondary radiation and/or scattered primary radiation (Compton scattering) both of which result in a small increase of deposited dose.

Figure 8.34 shows the flux shielding efficiency for all samples in the **X-rays 120 keV** experiment. Compared to 40 keV X-rays, a distinction between low-Z and high-Z materials cannot be easily made anymore. The worst shielding efficiency belongs to sample J (Al) with only over 30 % followed by sample S2 (GFRP + Al honeycomb sandwich) approaching 60 %. Figure 8.35 shows the dose rate shielding efficiency for samples in the **X-rays 120 keV** experiment. From all X-ray results, it can be seen that 120 keV X-rays are harder to shield against than the 40 keV X-rays. This agrees with the physics of interaction and shielding of photons/X-rays in matter which is determined primarily by the material density i.e. Z-number.

Figure 8.36 shows the flux shielding efficiency and Figure 8.37 the dose rate shielding efficiency for all samples in the **electrons 5 MeV** experiment. The 5 MeV electrons are best shielded by the measured carbon composites with addition of PMMA. While the worst shielding efficiency belongs to samples I2 (Pb) and C1 (polyurethane foam), all samples show above 60 % shielding efficiency. It should be noted, that samples A1, A2, C1, C2, D, G1 and G2 probably have better shielding efficiency, however due to aforementioned issues with measurement of open beam for this set, the shielded value is compared to a lower open beam value.

Figure 8.38 shows the flux shielding efficiency for all samples in the **protons 31 MeV** experiment. All samples show above 92 % shielding efficiency, with samples having very small differences between them. Figure 8.39 shows the dose rate shielding efficiency, which is higher, above 94 % for all samples.

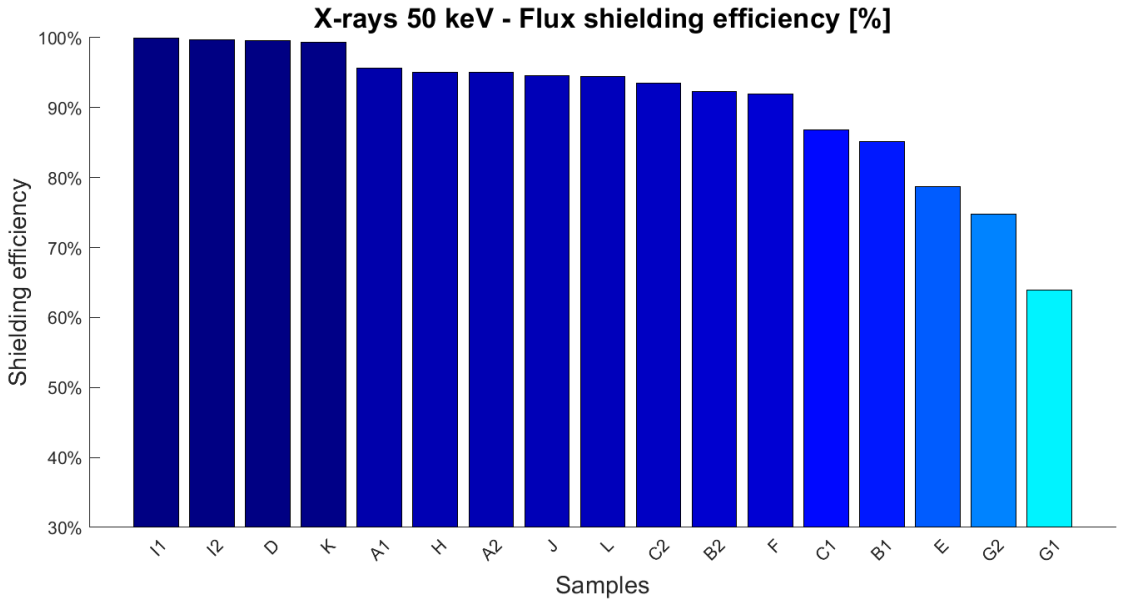

Figure 8.31: **Flux** shielding efficiency for all samples in the **X-ray 50 keV** experiment. The high-Z materials have shielding efficiency approaching 100 %, with the worst shielding material being from sample G1 (carbon composite) at 64 %.

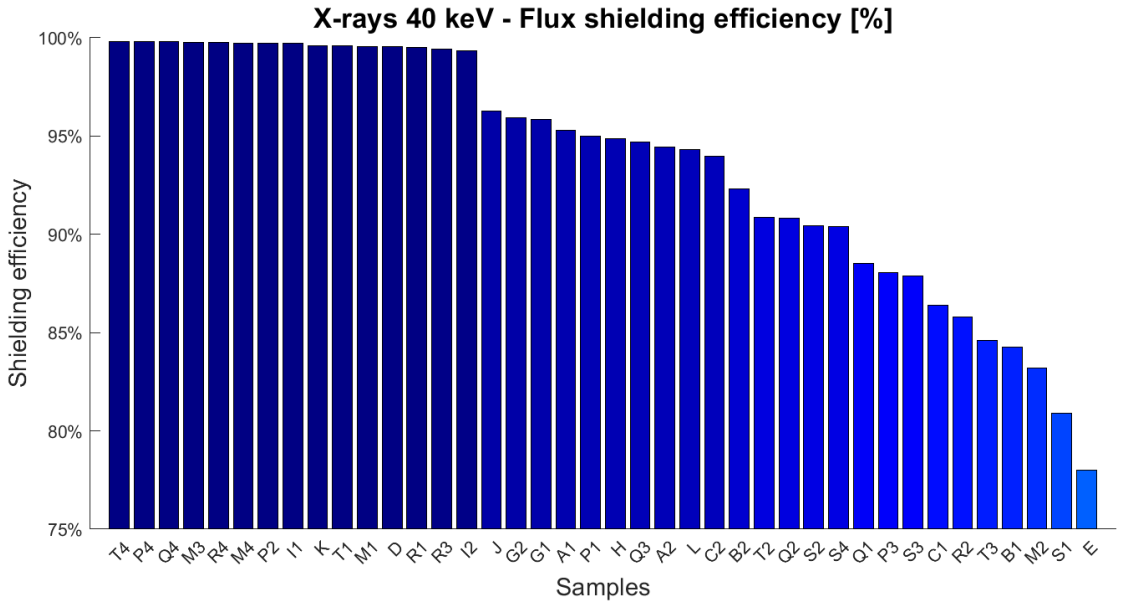

Figure 8.32: **Flux** shielding efficiency for all samples in the **X-ray 40 keV** experiment. The high-Z materials have shielding efficiency approaching 100 %, with the worst shielding materials being from samples S1 (CFRP+Al honeycomb sandwich) and E (PTFE).

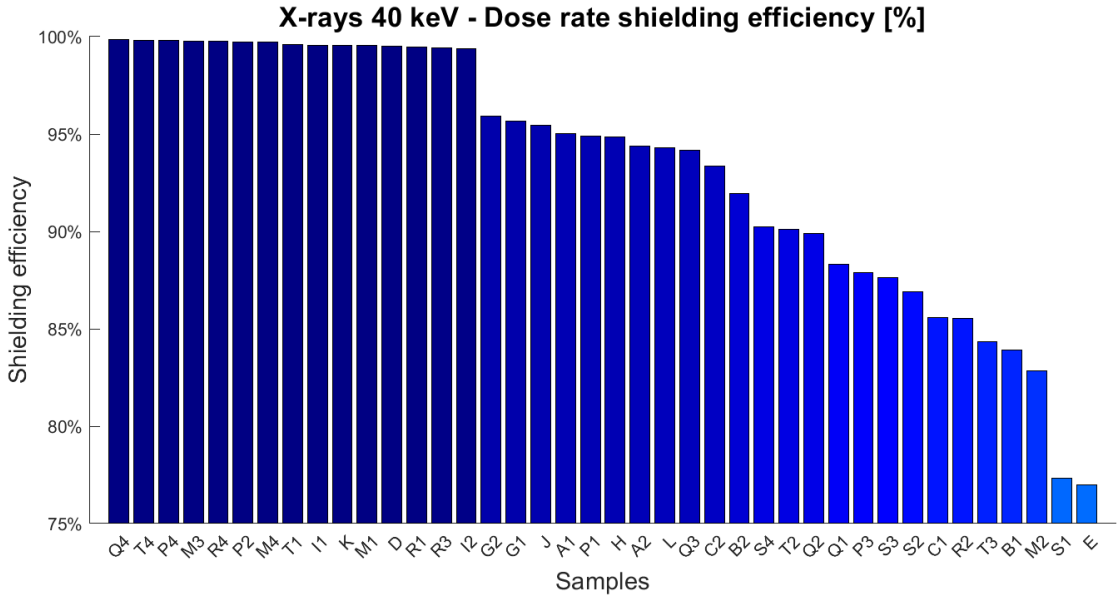

Figure 8.33: Dose rate shielding efficiency for all samples in the **X-ray 40 keV** experiment. The high-Z materials have shielding efficiency approaching 100 %, with the worst shielding materials being from samples S1 (CFRP+Al honeycomb sandwich) and E (PTFE).

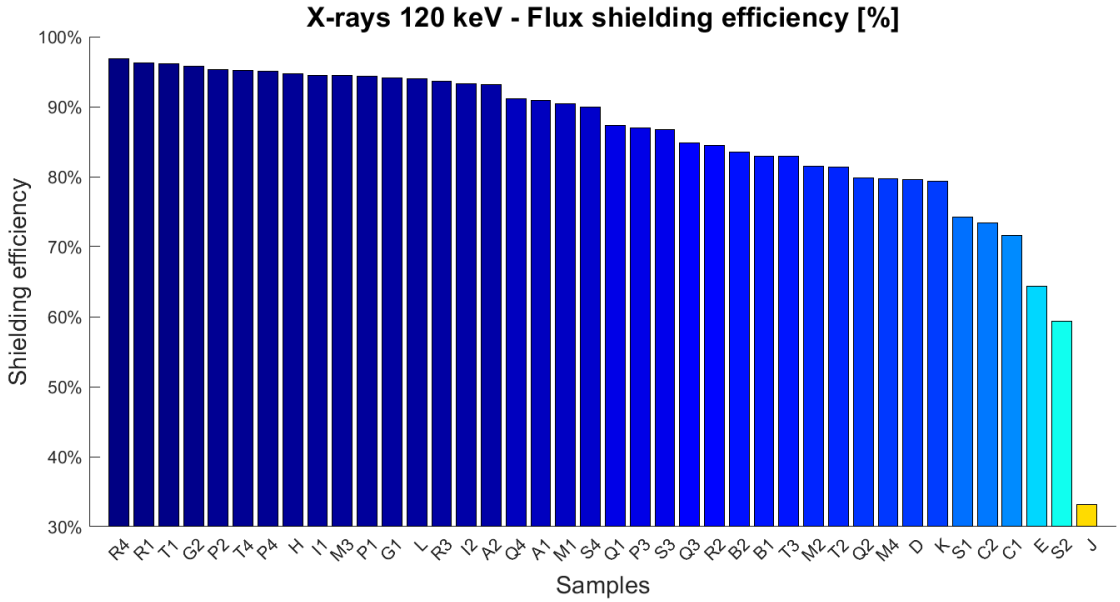

Figure 8.34: Flux shielding efficiency for all samples in the **X-ray 120 keV** experiment. For 120 keV X-rays, a distinction between low-Z and high-Z materials cannot be easily made. The worst shielding efficiency belongs to sample J (Al) followed by sample S2 (GFRP + Al honeycomb sandwich).

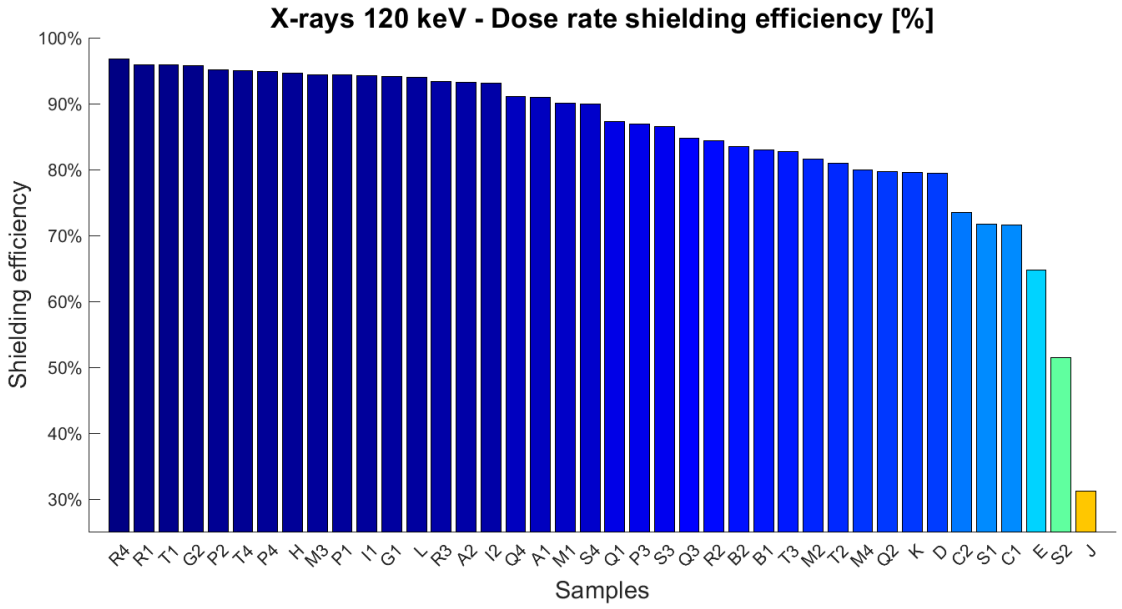

Figure 8.35: Dose rate shielding efficiency for all samples in the **X-ray 120 keV** experiment. For 120 keV X-rays, a distinction between low-Z and high-Z materials cannot be easily made. The worst shielding efficiency belongs to sample J (Al) followed by sample S2 (GFRP + Al honeycomb sandwich).

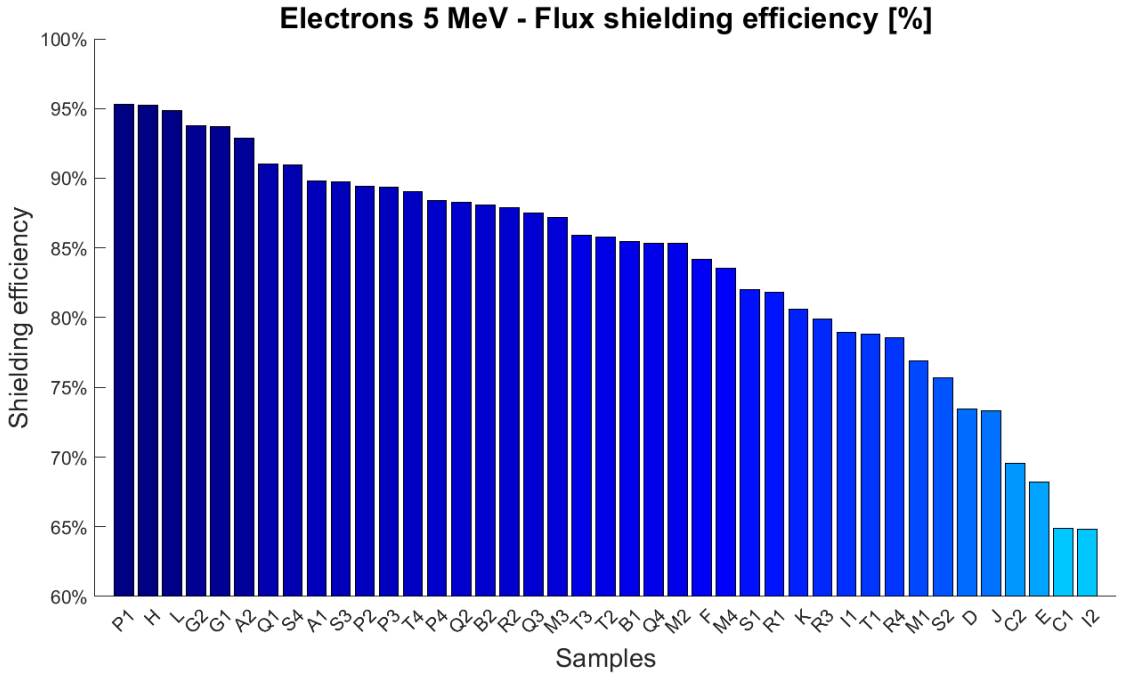

Figure 8.36: Flux shielding efficiency for all samples in the **electron 5 MeV** experiment. The 5 MeV electrons are evidently best shielded by low-Z materials, particularly the measured carbon composites. The worst shielding efficiency belongs to samples I2 (Pb) and C1 (polyurethane foam). However, all samples show above 60 % shielding efficiency.

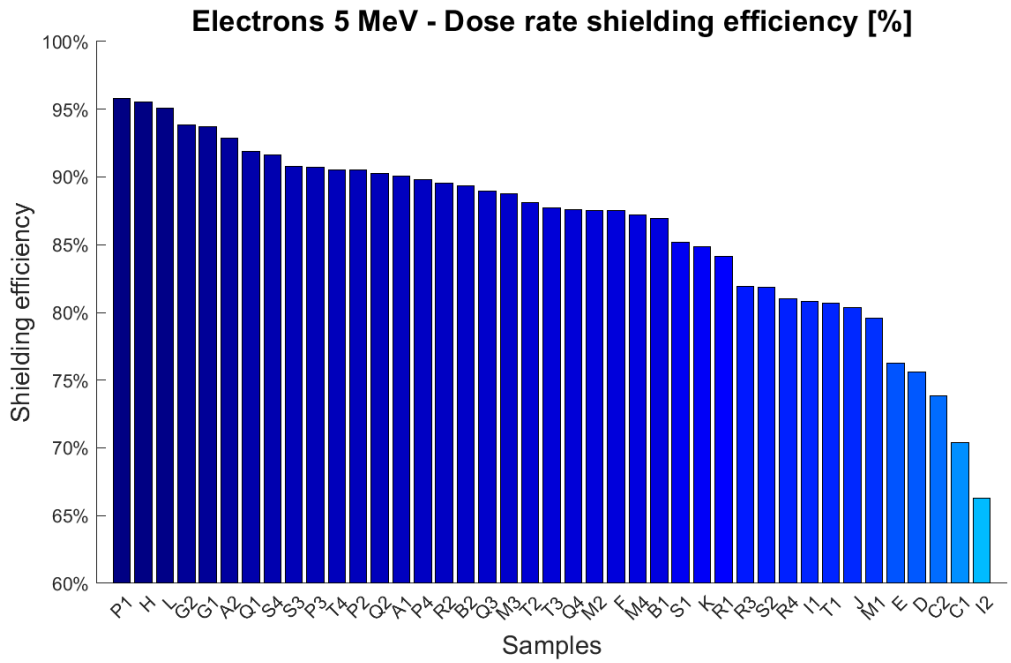

Figure 8.37: Dose rate shielding efficiency for all samples in the **electron 5 MeV** experiment. The 5 MeV electrons are evidently best shielded by low-Z materials, particularly the measured carbon composites. The worst shielding efficiency belongs to samples I2 (Pb) and C1 (polyurethane foam). However, all samples show above 65 % shielding efficiency.

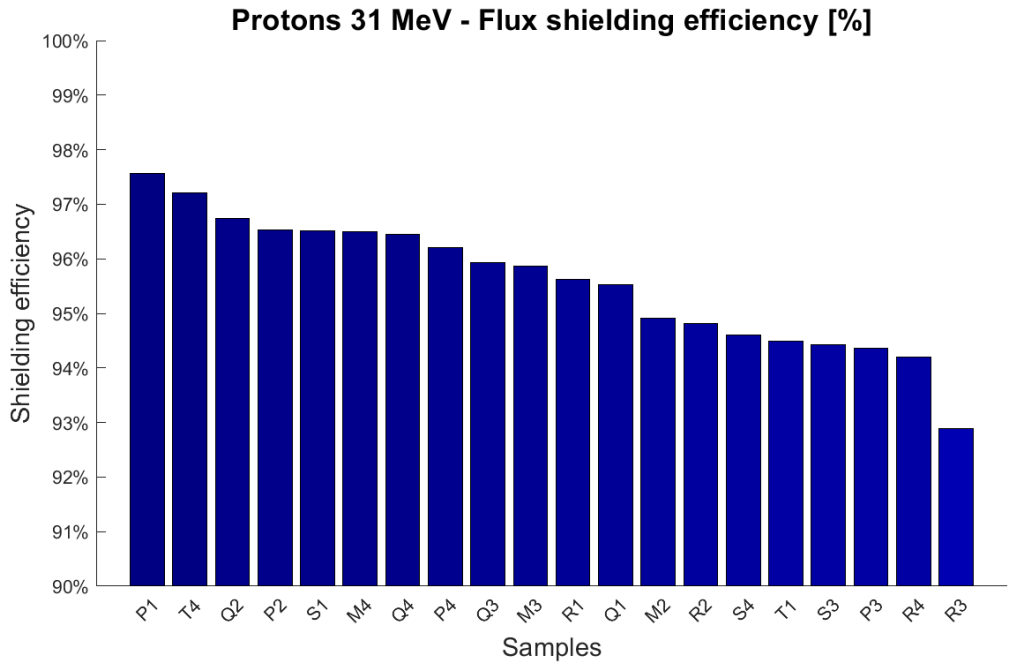

Figure 8.38: Dose rate shielding efficiency for all samples in the **protons 31 MeV** experiment. All samples show above 92 % shielding efficiency, with samples having very small differences.

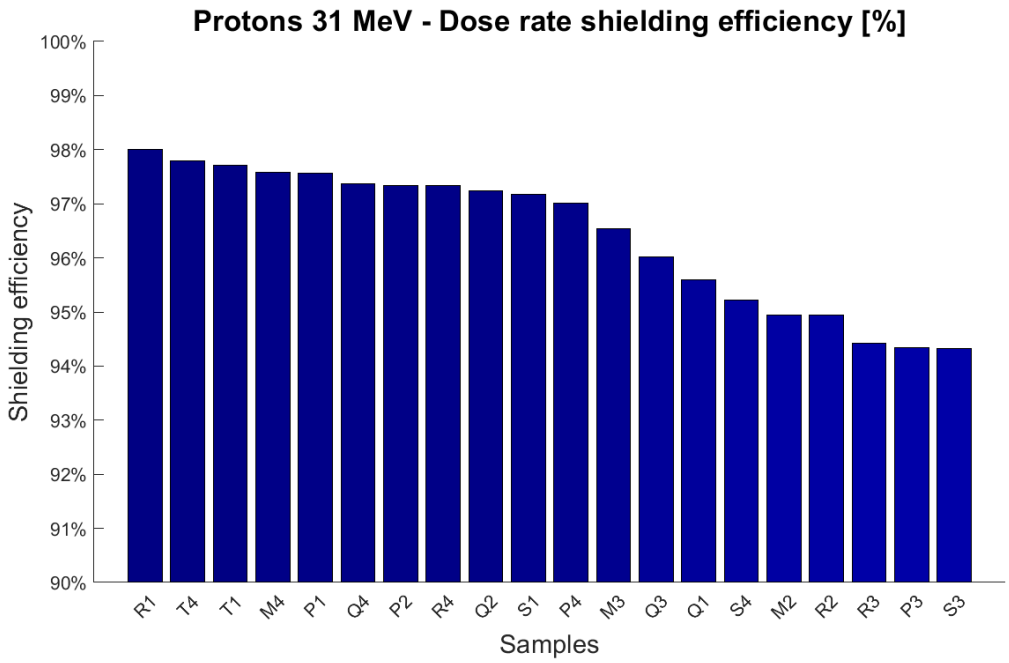

Figure 8.39: **Dose rate** shielding efficiency for all samples in the **protons 31 MeV** experiment. All samples show above 94 % shielding efficiency, with samples having very small differences.

Figure 8.40 compares and shows the overview of the **flux** shielding efficiency of all samples in four experiments as shown in the figure's legend - 40 keV and 120 keV X-rays, electrons and protons. Figure 8.41 shows the same overview for **dose rate** measurements. Both figures show the shielding efficiency computed from normalized values. Measurements from the X-ray 50 keV experiment are not shown for readability, as they very closely follow results from the X-ray 40 keV experiment.

Samples that have the flux or dose rate shielding efficiency above 90 % in all experiments are:

- **A1, A2** - Carbon Fiber Epoxy Resin; A1 coated with Ni, A2 coated with Au,
- **G1, G2, H** - pure carbon composites,
- **L** - PMMA and **S4** - polypropylene,
- **P1** - carbon composite + copper,
- **P2** - lead + copper,
- **T4** - carbon composite + chromium + lead.

Samples A1, A2, G1, G2, H and L were not measured for shielding efficiency against the proton beam. However, considering they are low-Z materials like carbon composites and PMMA, it can be assumed that they would have comparable proton shielding efficiency as similar measured samples.

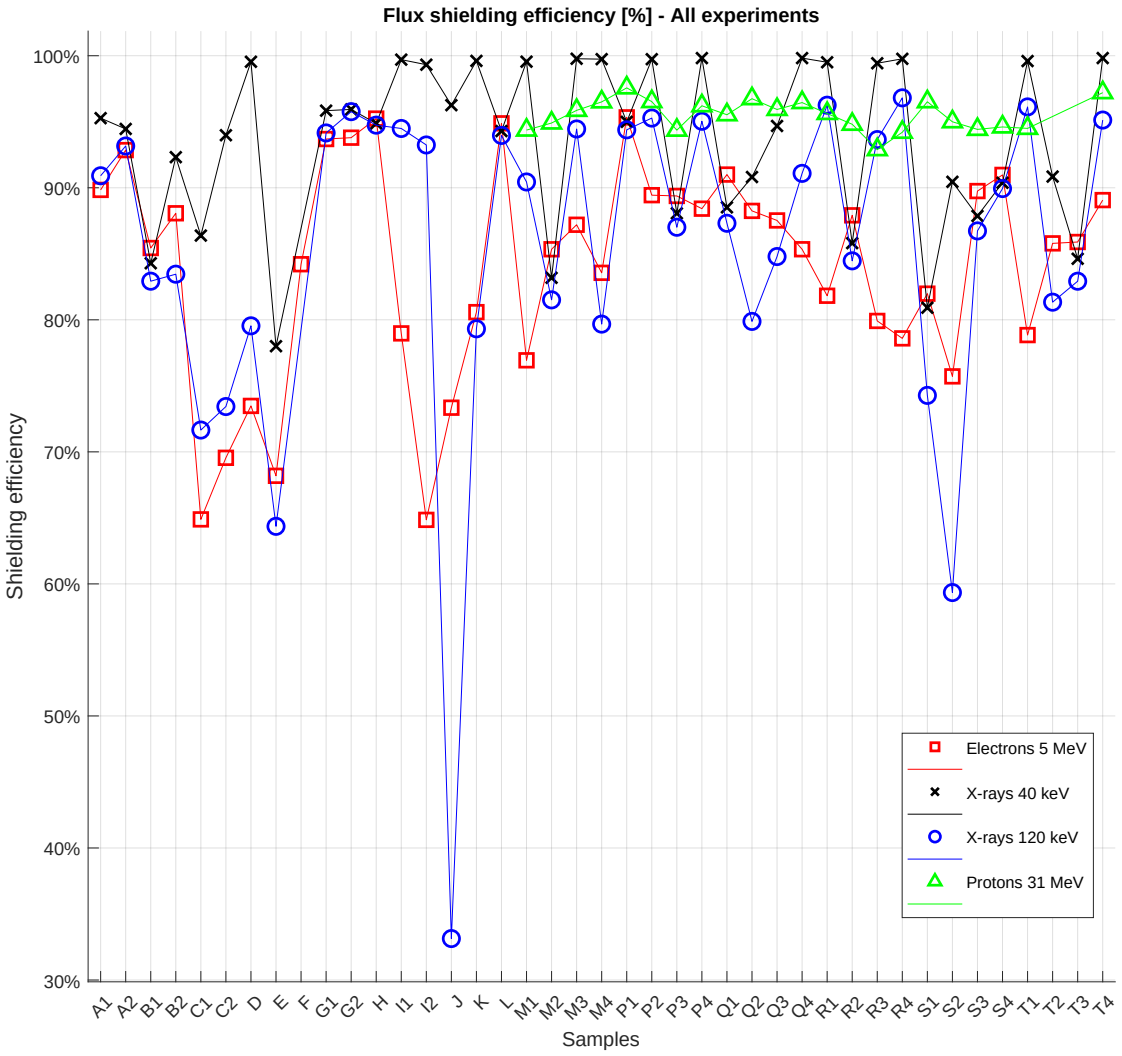

Figure 8.40: **Flux** shielding efficiency of all samples in all experiments, as shown in the legend. Measurements from the X-ray 50 keV experiment are not shown for readability, as they closely follow results from the X-ray 40 keV experiment.

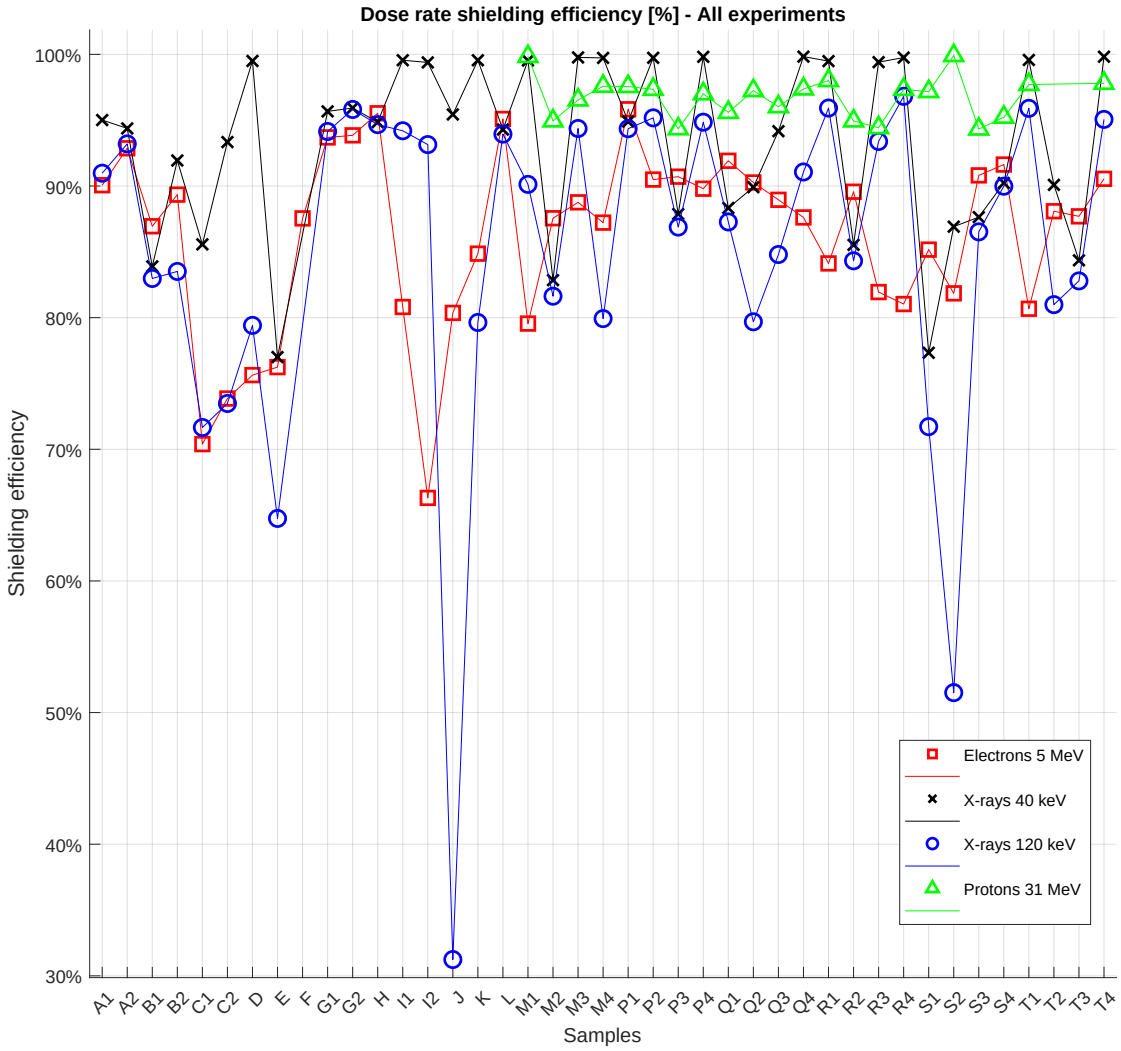

Figure 8.41: Dose rate shielding efficiency of all samples in all experiments, as shown in the legend. Measurements from the X-ray 50 keV experiment are not shown for readability, as they closely follow results from the X-ray 40 keV experiment.

Chapter 9

LEO radiation environment

ESA's SPace ENVironment Information System[1] (SPENVIS) was used to simulate the radiation environment for a typical CubeSat LEO mission specified by parameters in Table 9.1. The radiation components calculated are the trapped radiation both protons and electrons as well as the solar protons (SPEs). The mission duration was chosen at duration 1 day providing several (about 15) orbits to cover most geographic locations. The simulated orbits can be seen in Figure 9.1. In the Figure is displayed the spacecraft altitude which appears to vary (over about 20 km) due to the small asymmetry in the Earth's roundness.

Orbit around	Earth
Mission start	13/01/2022
Mission end	14/01/2022
Apogee altitude	540.90 km
Perigee altitude	522.00 km
Inclination	97.47°
R. A. Ascending Node	43.13°
Argument of Perigee	197.97°
True Anomaly	40.00°
Period	1.59 hrs
Number of orbits	15.14
Duration	1.00 day

Table 9.1: Mission parameters used for simulating radiation fluxes. Mission duration was chosen to get enough satellite orbits to cover all geographic locations.

Using NASA's AP-8 [61] radiation environment model, the **trapped proton** average flux assuming solar maximum was calculated for the specified mission orbit. The calculated proton flux values can be seen in Figure 9.2. The proton energy varies from 0.1 MeV to 400 MeV, with integral flux decreasing from 1,000 $cm^{-2} \cdot s^{-1}$ to as low as 0.3 $cm^{-2} \cdot s^{-1}$. Energetic (i.e. >10's MeV) protons are more properly shielded by massive (i.e. > few centimeters) shielding of dense materials. Low energy protons are easier to shield than high energy protons (few milimeters).

Looking at the integral proton flux map in Figure 9.3, it is seen that the majority of the trapped protons come from the South Atlantic Anomaly for the selected LEO at $\approx$ 520 km altitude.

Using NASA's AE-8 [62] radiation environment model, the **trapped electrons** average flux assuming solar minimum was calculated for the specified mission. The

[1] `https://www.spenvis.oma.be/`

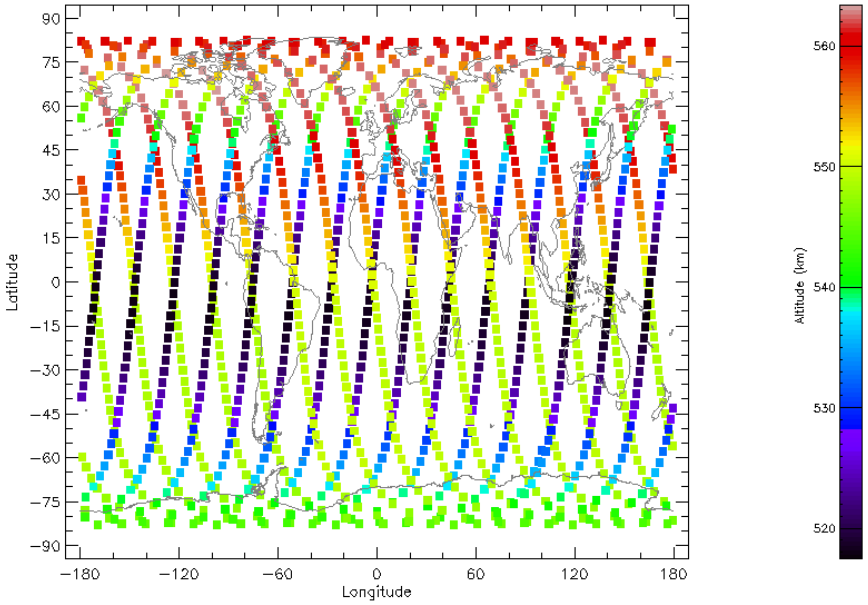

Figure 9.1: Simulated **orbit map** for the mission specified in Table 9.1. The colors represent the changing **altitude** of the satellite along the 1 day orbit.

calculated electron flux values can be seen in Figure 9.4. The electron energy varies from 0.04 MeV to 7 MeV, with integral flux decreasing from 10^6 cm^{-2} · s^{-1} to as low as 10^{-2} cm^{-2} · s^{-1}. Electrons, which in LEO have much higher integral flux values for the lower energies, are more properly shielded by low-Z materials.

Looking at the integral electron flux map in Figure 9.5, it is seen that the majority of the trapped electrons come from the South Atlantic Anomaly and from the polar horn regions, where field lines from the outer electron belt reach down to low altitudes.

Using the Solar Accumulated and Peak Proton and Heavy Ion Radiation Environment (SAPPHIRE) [63] total fluence and worst case models with confidence level 95 %, the **solar protons** total fluence during the given mission was calculated. The calculated values can be seen in Figure 9.6. The energy varies from 0.01 MeV to 1,000 MeV, with integral fluence decreasing from 10^{11} cm^{-2} to 10^5 cm^{-2}. Fluence is the integrated flux over a period of time e.g. 1 day.

Taking into account the simulated trapped proton and electron flux values, together with the solar proton fluence values, it seems the best shielding for this type of mission, at low altitude, passing through the SAA and polar horn regions, are customized carbon composites.

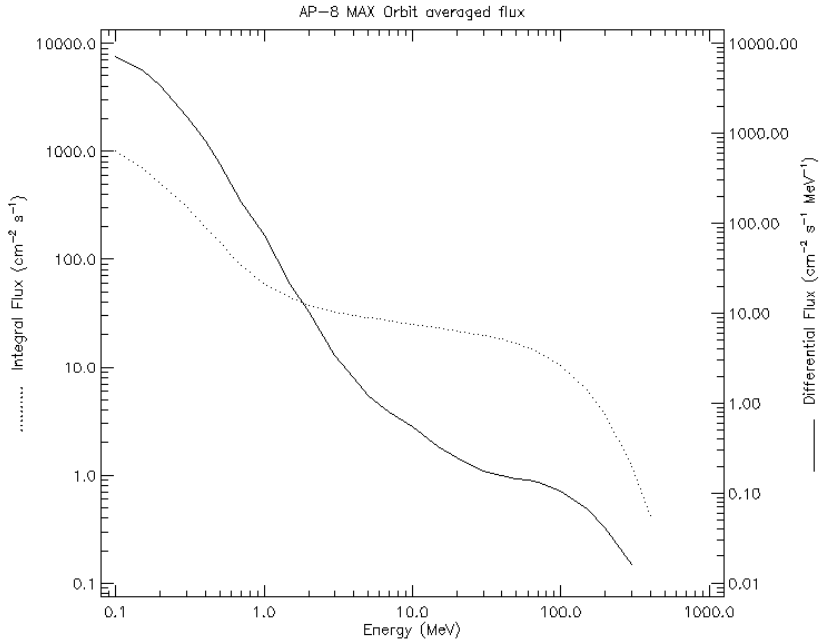

Figure 9.2: Simulated average **proton flux** for the mission specified in Table 9.1. The model used is AP-8 assuming solar maximum. Note the logarithmic scale in both x and y axis.

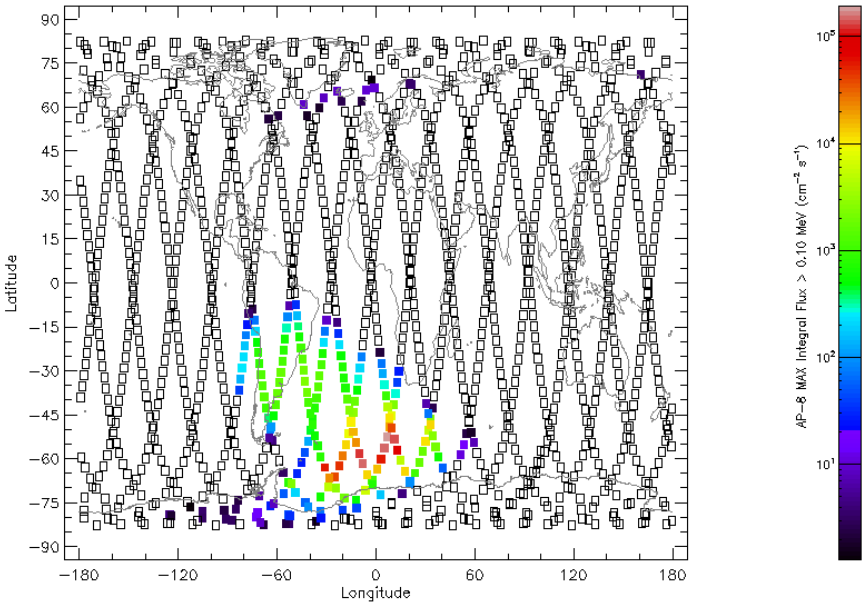

Figure 9.3: Simulated average **proton flux** (displayed by the colorbar in logarithmic scale) for the mission specified in Table 9.1 in relation to geographic location.

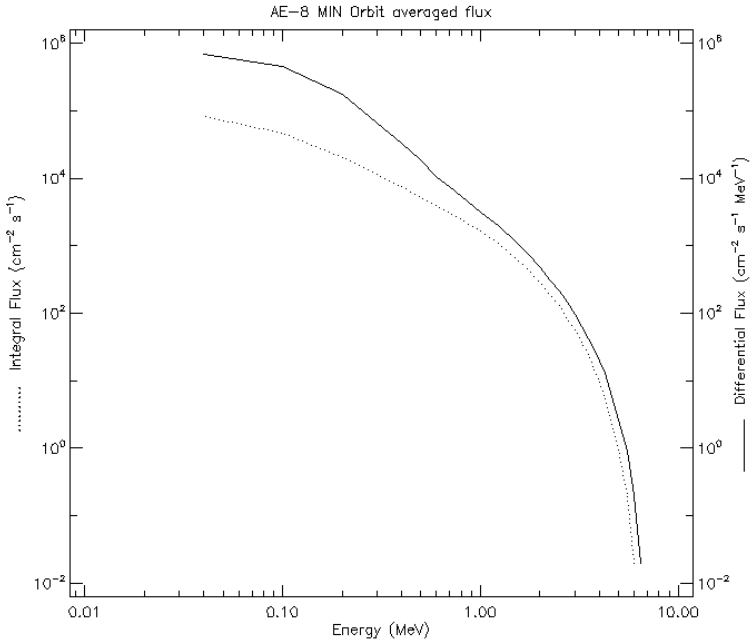

Figure 9.4: Similar to Figure 9.2 showing the simulated average **electron flux** for the mission specified in Table 9.1. The model used is AE-8 assuming solar minimum.

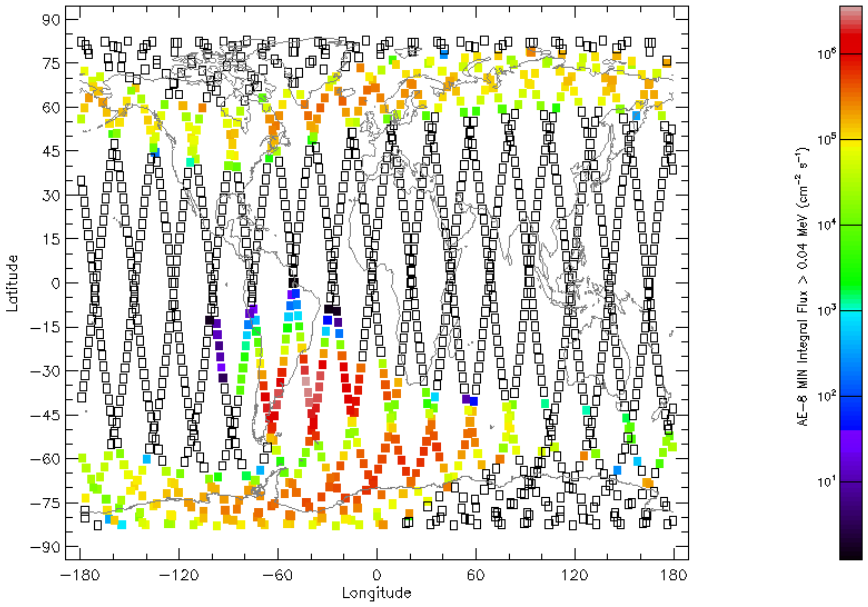

Figure 9.5: Similar to Figure 9.3 showing the simulated average **electron flux** for the mission specified in Table 9.1 in relation to geographic location.

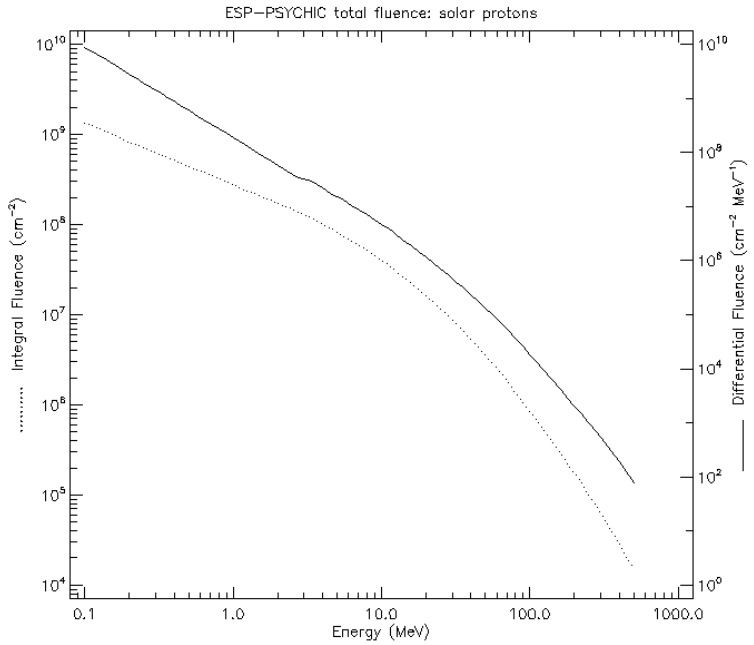

Figure 9.6: Similar to Figure 9.2 and Figure 9.4 showing the simulated **solar protons fluence** for the mission specified in Table 9.1. The model used is SAPPHIRE with confidence level 95 %.

Chapter 10
Discussion

The main components of space radiation that irradiate and threaten electronics and satellites in LEO are primarily trapped protons, trapped electrons and solar protons of broad energy spectra, along with secondary X rays and gamma rays partly generated by energetic electrons as stopping radiation in the spacecraft elements. Also present are the energetic galactic cosmic rays (GCRs) - protons and ions. These types of radiation can cause Total Ionising Dose (TID), Displacement Damage (DD) and Single Event Effects (SEEs) to electronics. The shielding efficiency to multiple radiation sources has been examined and experimentally measured for different materials, especially novel composite samples designed for radiation shielding in LEO. The evaluated materials consisted mostly of low-Z materials like carbon composites, polypropylene or PMMA as well as aluminum and high-Z materials like tantalum or lead, which are standard shielding materials used as reference. Results were also normalized to the sample planar density.

Evaluating the shielding efficiency of tested materials for low Earth orbit given in Chapter 9, the following material shielding samples exhibit the best shielding properties for this type of radiation environment:

- **A1, A2** - Carbon Fiber Epoxy Resin; A1 coated with Ni, A2 coated with Au,
- **G1, G2, H** - pure carbon composites,
- **L** - PMMA,
- **P1** - carbon composite + copper.

These materials are overall of low-Z density and of novel composite structure layout. They are additionally convenient for space deployment as they are light (low density) with suitable thermal and mechanical parameters and can be manufactured in customized geometry and design. The GCR component was not covered by the experimental work undertaken as the radiation interaction and shielding properties are complex and reach beyond the scope of this work and of the radiation facilities available in Czech Republic.

10.1 Future work

As presented in Chapter 3 and simulated in Chapter 9, the radiation environment in LEO is more complex than the four experiments covered. The composition, energy spectrum and flux range greatly vary and it is not possible to completely and/or accurately examine how the materials perform in different environments. It is possible to compare the results of this thesis to particle interaction models and Monte-Carlo simulations of particle

interactions through matter (future work, partly also done by other groups elsewhere). The shielding efficiency of the samples used can be experimentally investigated also at high-energy particle accelerators (existing outside Czech Republic, such as GSI in Darmstadt, Germany and CERN in Geneva, Switzerland - future work).

Presented in Chapter 2, materials used in satellites in LEO are subject to further hazards and damage of the space environment, like vaccuum, plasma charging, temperature fluctuation or outgassing. These other structural parameters of the materials and their distortion after irradiation have to be also taken into account and are beyond the scope of this thesis. Composite materials are intended to resist also these harsh non-radiation conditions.

The output of the measurement processing scripts provides more information than just flux or dose rate values evaluated in this work such as the direction of the radiation and the change in composition (primary, secondary components). It would be valuable to analyze the materials in regards to more specific particle-type event classification, to examine and classify how the radiation particles interact with the materials, etc.

A scientific article in an international journal to publish the results and developed technique in this thesis will be written, with the possibility of presenting the results to the expert community at an international conference by the thesis author (D.L.).

Chapter 11

Conclusions

The goal of this thesis was to develop an innovative experimental technique to examine and evaluate the radiation shielding properties of novel shielding samples including composite materials, some of which are already deployed on board Czech CubeSats in LEO, along with other conventional reference materials. The samples were chosen based on their radiation, mass and mechanical properties for space and LEO deployment.

The measurements were conducted as part of this thesis using several radiation sources with various energies available in Czech Republic like the microtron accelerator (5 MeV electrons), the cyclotron accelerator (31 MeV protons) and X-ray micro-focus tubes (40 keV, 50 keV, 120 keV X-rays). High-resolution semiconductor pixel detectors were used for these experiments (Timepix, Timepix3, Medipix3) developed in Prague by Advacam[1]. A detailed study of radiation parameters and radiation composition was done on the investigated samples with different radiations, particle beam sizes and detector-sample-beam positions.

Large amounts of high-resolution data were obtained and analyzed. Complex and extensive data processing analysis was realized, using advanced algorithms and also a high-performance computing cluster available at the FEE CTU in Prague which was provided with the support of the project CAAS MATE[2]. In total, 41 samples were studied, most of which with three different radiation experiments, accounting to 700 GB of processed data. Under supervision of expert advisor Carlos Granja from Advacam, an advanced and innovative technique to experimentally investigate the radiation properties of the materials was developed and applied. The experimental results of data processing were evaluated in terms of physical products (flux, dose rate, composition) and presented as visual interpretation and imaging of results, including high-resolution wide-range 2D plots and tables.

The samples with the best radiation shielding properties are overall the samples **A1, A2** - Carbon Fiber Epoxy Resin coated with Ni and Au respectively, **G1, G2, H** - pure carbon composites and **L** - PMMA or **P1** - carbon composite with copper. The best shielding properties against **X-rays** belong to samples consisting of materials with high atomic number, while the worst shielding properties belong to carbon composites combined with materials of low atomic number. On the other hand, **electrons** are best shielded by carbon composites, while high atomic materials like lead or tantalum perform significantly worse. This is due to the production of secondary radiation by energetic electrons in high-Z materials in the form of stopping radiation (X-rays, gamma rays). The shielding of **protons** is best achieved with composites containing admixtures of high-Z

[1] Advacam is a Prague based spin-off of the CTU Prague and the CERN based Medipix collaboration

[2] This work was supported by the Ministry of Education, Youth and Sports and the European Union through CAAS project CZ.02.1.01/0.0/0.0/16-019/0000778

materials such as lead or copper which provide slightly better shielding performance.

Appendix A

Radiation sources

This section provides basic information and short description about the radiation sources used for the experiments evaluated in this thesis.

A.1 X ray tube

For generation of X-rays, a modern table-top X-ray micro-focus tubes were used. As illustrated in Figure A.1, a current is passed through a filament (the cathode) and heats it up, which releases electrons. The thermal i.e. low-energy electrons are then attracted towards the positively charged anode and hit the tungsten target with a maximum energy determined by the tube potential (voltage). The interaction of electrons hitting the tungsten results in conversion of energy into heat (99 %) and photons (X-rays and gamma rays from stopping radiation) (1 %). The resulting X-ray beam has broad spectrum (see Figure A.2) at maximum energy given by the X-ray tube voltage and is released out of the tube window [64]. Typical X-ray tubes have voltages up to few hundred kV yielding correspondingly X-rays with spectrum up to few hundred keV.

Figure A.2 shows the resulting energy spectrum of the emitted X-ray photons. The spectrum is given by the stopping i.e. Bremsstrahlung radiation, which contains photons with a broad range of energies. The broad continuous spectrum is superposed by discrete 'K' energy peaks, which are characteristic of the target material [65].

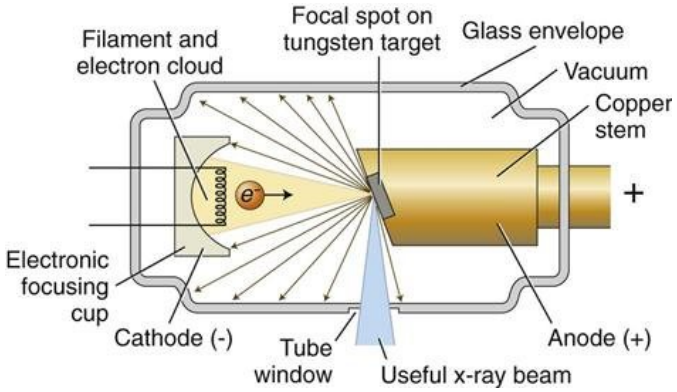

Figure A.1: Illustration of an X-ray tube. Electrons are emitted in vacuum from the cathode and are accelerated and hit the anode releasing X-rays [64].

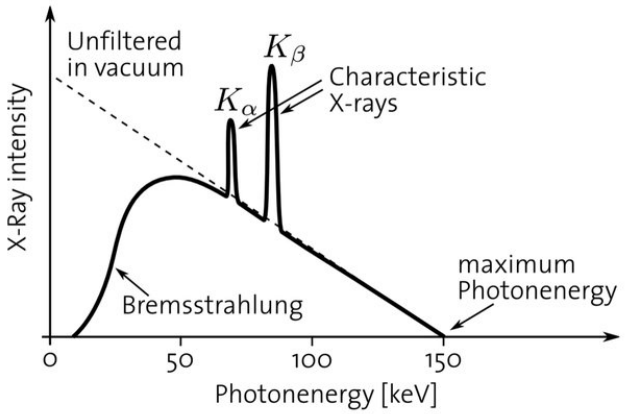

Figure A.2: Energy spectrum of emitted X-rays in X-ray tubes. The spectrum consists of a broad continuous energy spectrum Bremsstrahlung i.e. stopping radiation and discrete 'K' energy peaks, which are characteristic to the anode material - usually high-Z e.g. tungsten [65].

A.2 Microtron accelerator

For generation of high-energy electrons, the MT 25 microtron accelerator of the NPI CAS Rez near Prague was used [66]. It is a cyclic electron accelerator with a Kapitza type resonator, the schematic layout can be seen in Figure A.3. The particles are accelerated by an RF electric field of constant frequency in a constant uniform magnetic field. In the vacuum chamber, the electrons follow circular paths with a common tangent point. The accelerating cavity, which is excited by the RF field, is located at this point. The energy of accelerated electrons depends on the number of electron turns in the microtron vacuum chamber as well as on the magnitude of the magnetic field [66]. This allows to configure the accelerator and extract beams of electrons at several fixed energies in the range from 3 MeV to 25 MeV. Table A.1 describes the main parameters of the MT 25 microtron. Beams are extracted from the accelerator vacuum and can be used in air near to the beam nozzle guide. For the measurements performed in this work the intensity of the extracted beams had to be significantly decreased (by 6 to 10 orders of magnitude).

Electron Energy	3–25 MeV
Electron beam energy increment per turn	about 0.9 MeV
Number of orbit turn	25
Pulse current of the accelerated electrons	maximum 20 mA (24 MeV)
Magnetron operating frequency	2796 ± 5 MHz
Magnetron pulse power	3 MW
Length of RF macropulse	3.9 μs
Repetition rate of RF macropulse	423 Hz

Table A.1: Main parameters of the MT 25 microtron accelerator [66].

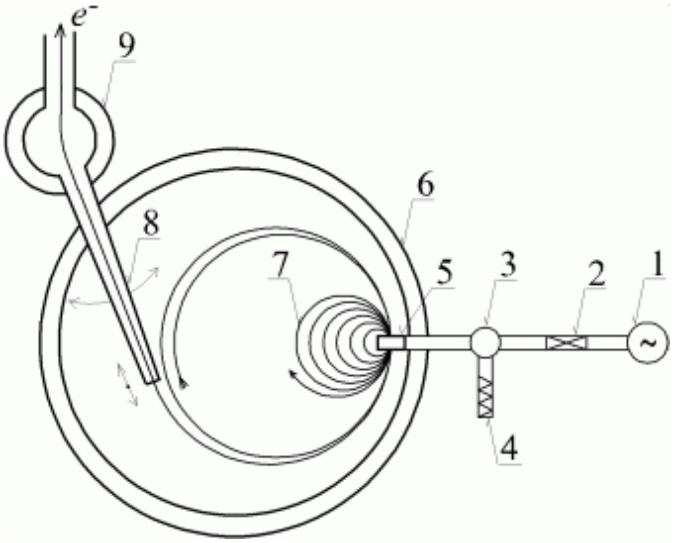

Figure A.3: Schematic layout of the MT 25 microtron. 1 — magnetron, 2 — phase shifter, 3 — circulator, 4— water load, 5 — accelerating cavity, 6 — vacuum chamber, 7 — electron orbits, 8 — adjustable beam extractor, 9 — beam deflector [66].

A.3 Cyclotron accelerator

For generation of energetic medium-energy (i.e. few tens MeV) protons (and light ions - e.g. ^{3}He ions), the U-120M cyclotron accelerator of the NPI CAS Rez near Prague was used. The U-120M cyclotron is a four-sector isochronous cyclotron which was developed at the Joint Institute of Nuclear Research (JINR) in Dubna (Russia) and installed in the Nuclear Physics Institute of the Czech Academy of Sciences (NPI CAS) in Rez in 1977.

The U-120M cyclotron's ion source is a Penning Ion Gauge (PIG) with a cold cathode, operating in continuous regime, creating both positive and negative ions. The ions are extracted by an alternating RF high voltage field. The desired type of ions to be accelerated is determined by the polarity of the cyclotron magnetic field [67].

The subsequent beam extraction is done by means of an about 1 µm thick carbon stripping foil placed at the required final beam orbit. The negative ions lose (with a high probability) both valence electrons when going through the foil, resulting in protons or deuterons. These are then directed in the cyclotron magnetic field to a short, 3 m long beamline located in the cyclotron hall. At the end of the beamline, protons are passing through an aluminum exit window (thickness 55 µm, diameter 16 mm) into the air. The energies of extracted monoenergetic proton beams are in the range from 6 to 37 MeV with the maximal current reaching several tens of microampere [68]. For the measurements performed in this work the intensity of the extracted beams had to be significantly decreased (by 6 to 10 orders of magnitude). The schematic view of the cyclotron accelerator principle can be seen in Figure A.4.

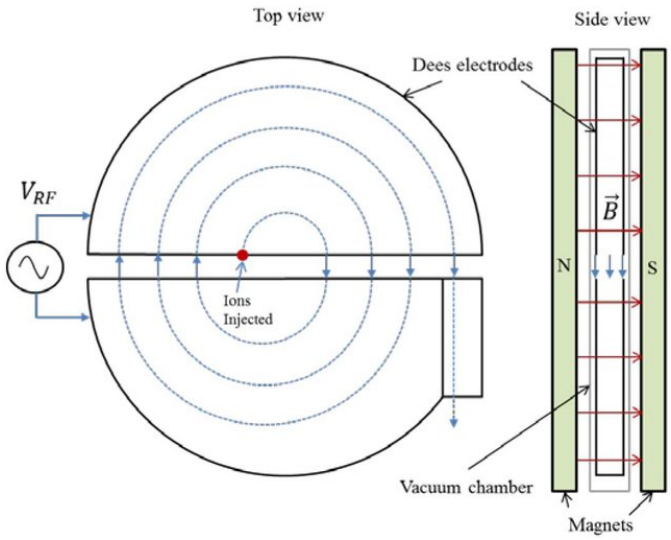

Figure A.4: Schematic view of the cyclotron principle [69].

Appendix B

Samples

This appendix shows photographs of all samples used in the measurements. The sets of samples were assembled individually for every experiment based on mounting and experimental logistic, depending on geometry and available space in the measurement setup. The first three sets in Figures B.1, B.2 and B.3 consist of novel composites obtained specifically for this thesis, along with new reference materials. Sets in Figures B.4, B.5, B.6, B.7, B.8 and B.9 contain older samples that were also used for the cyclotron measurement in 2018.

The samples were labeled and given a specific ID, sometimes grouped based on similar materials. Specific information about the samples can be seen in Table 6.1. This identification of samples provided easy way to track the samples throughout the measurements, processing and result interpretation.

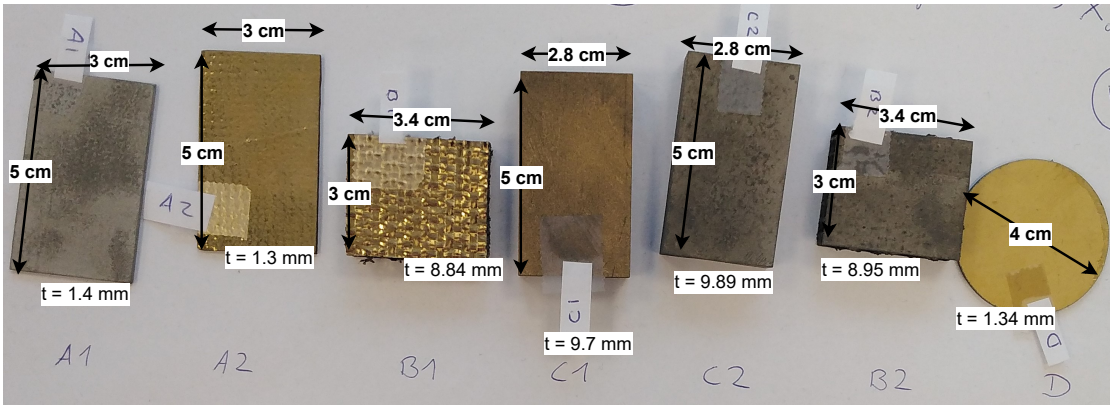

Figure B.1: Samples A1, A2, B1, C1, C2, B2, D (left to right).

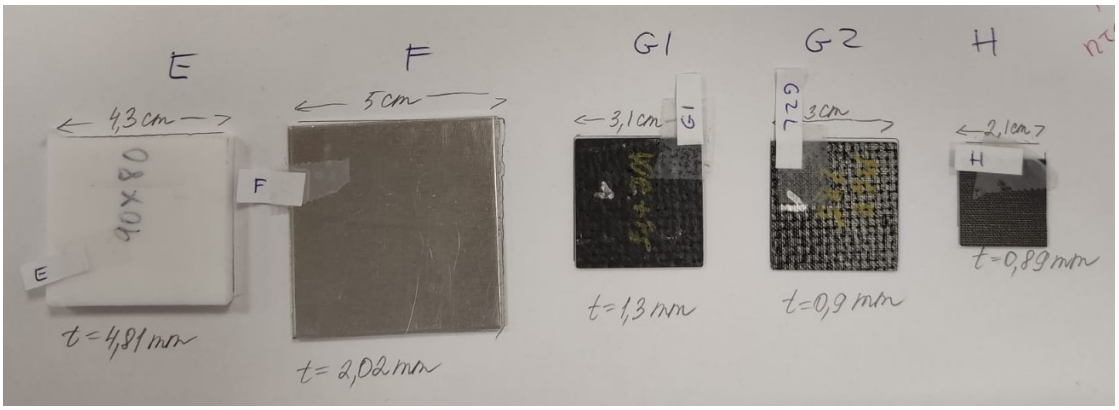

Figure B.2: Samples E, F, G1, G2, H (left to right).

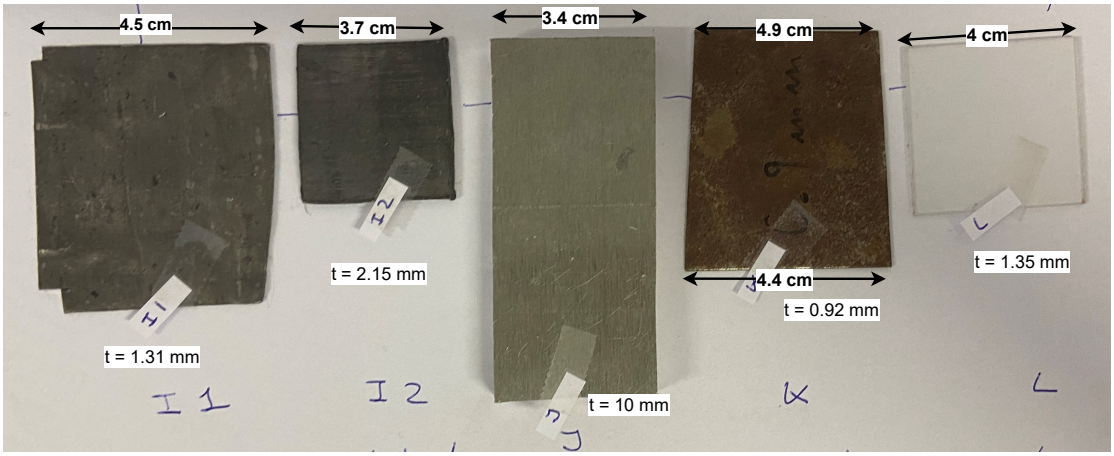

Figure B.3: Samples I1, I2, J, K, L (left to right).

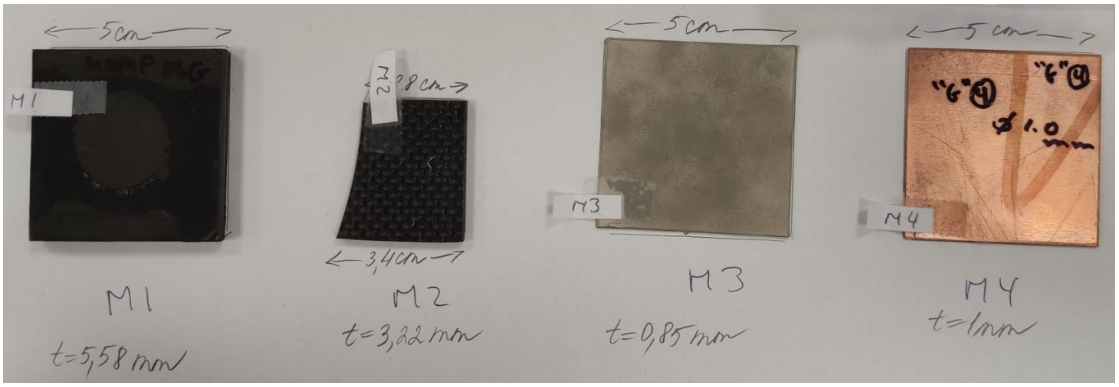

Figure B.4: Samples M1, M2, M3, M4 (left to right).

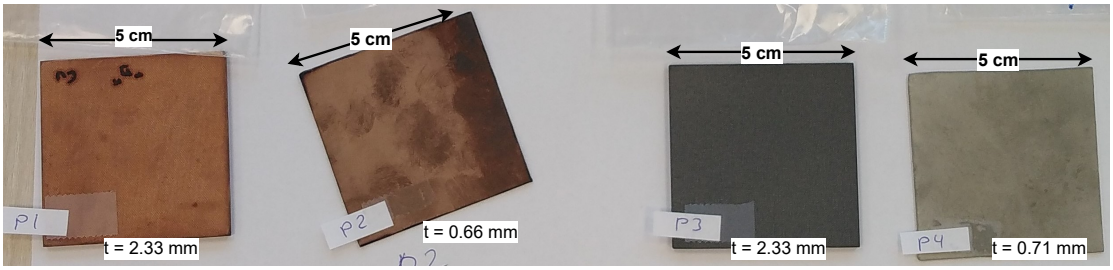

Figure B.5: Samples P1, P2, P3, P4 (left to right).

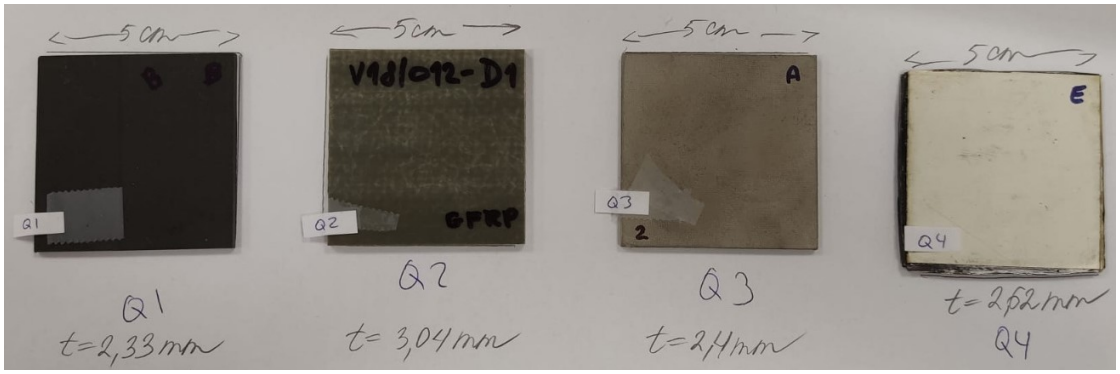

Figure B.6: Samples Q1, Q2, Q3, Q4 (left to right).

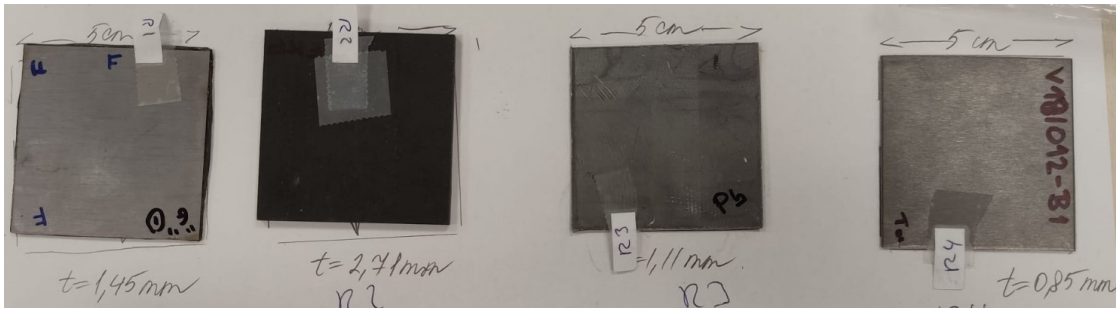

Figure B.7: Samples R1, R2, R3, R4 (left to right).

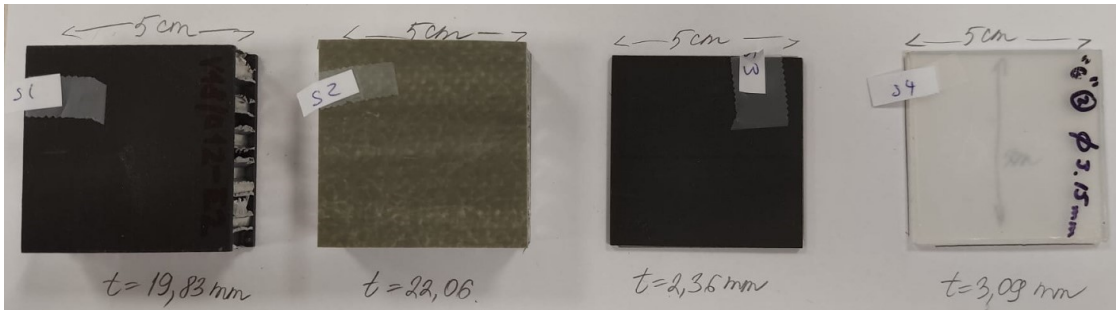

Figure B.8: Samples S1, S2, S3, S4 (left to right).

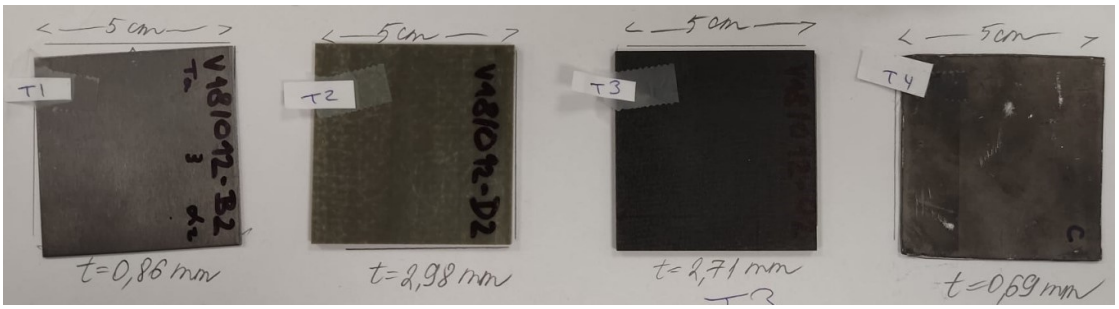

Figure B.9: Samples T1, T2, T3, T4 (left to right).

Appendix C

2D Radiation Imaging Maps

This appendix provides spatial maps from the irradiations (X ray, electron, proton) presenting particle flux values for significant samples used in the experiments, that were not discussed in the main part of this thesis. They are organized based on alphabetical order of the sample IDs. The caption for every subfigure provides the sample ID along with a simple material composition information. Significant specific information for samples can be seen in Table 6.1. The method used in measurements is described in Section 6.1, the pixel detectors used in Section 6.2 and overview of the radiation sources in Section 6.3. The detailed interpretation of results is described in Chapter 8.

C.1 X-ray micro-focus tube 40 keV

This section provides the spatial maps presenting particle flux values for significant samples from the 40 keV X-ray micro-focus tube experiment.

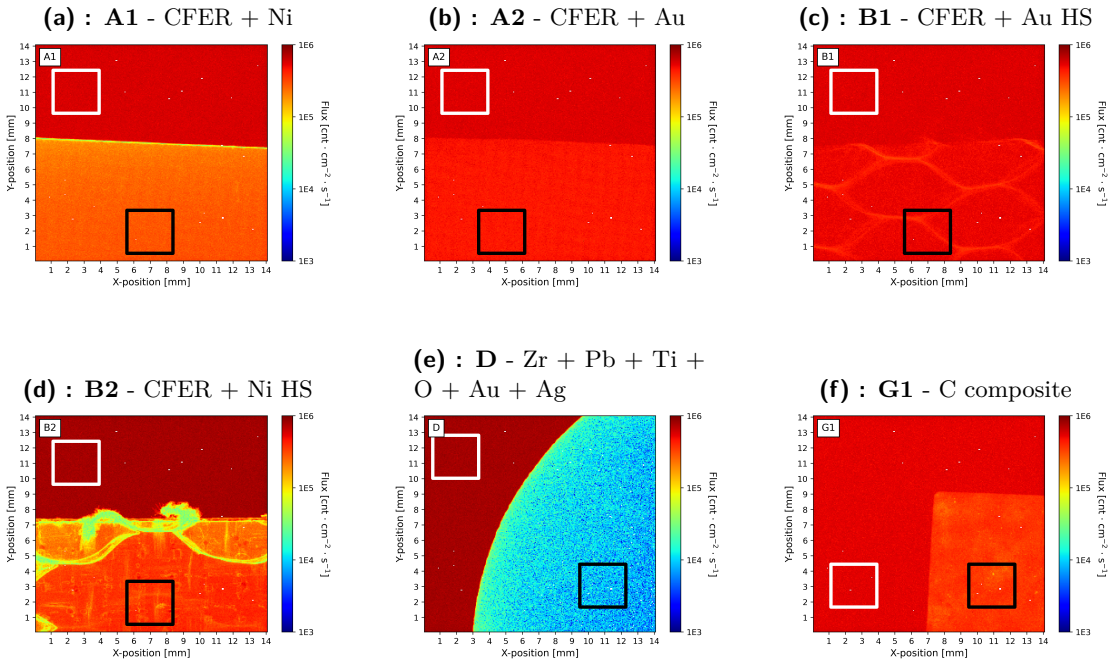

Figure C.1: Similar to Figure 8.11 showing the **particle flux** spatial maps for significant samples from the **X-ray 40 keV** experiment. The ROI regions are shown by squares for open beam (white) and shielded behind the samples (black).

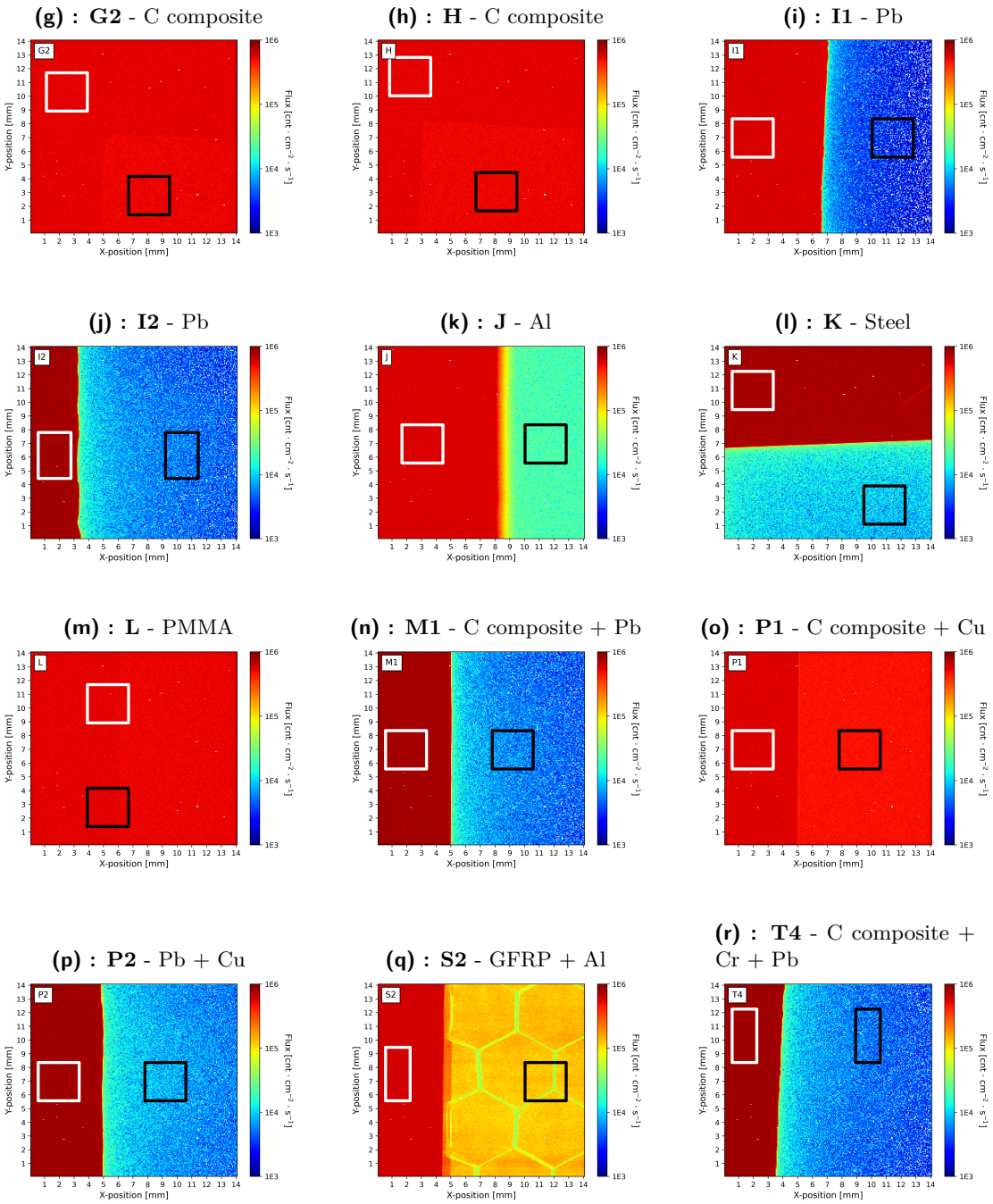

Figure C.1: Similar to Figure 8.11 showing the **particle flux** spatial maps for significant samples from the **X-ray 40 keV** experiment. The ROI regions are shown by squares for open beam (white) and shielded behind the samples (black).

C.2 X-ray micro-focus tube 120 keV

This section provides the spatial radiation maps presenting particle flux values for significant samples from the 120 keV X-ray micro-focus tube experiment.

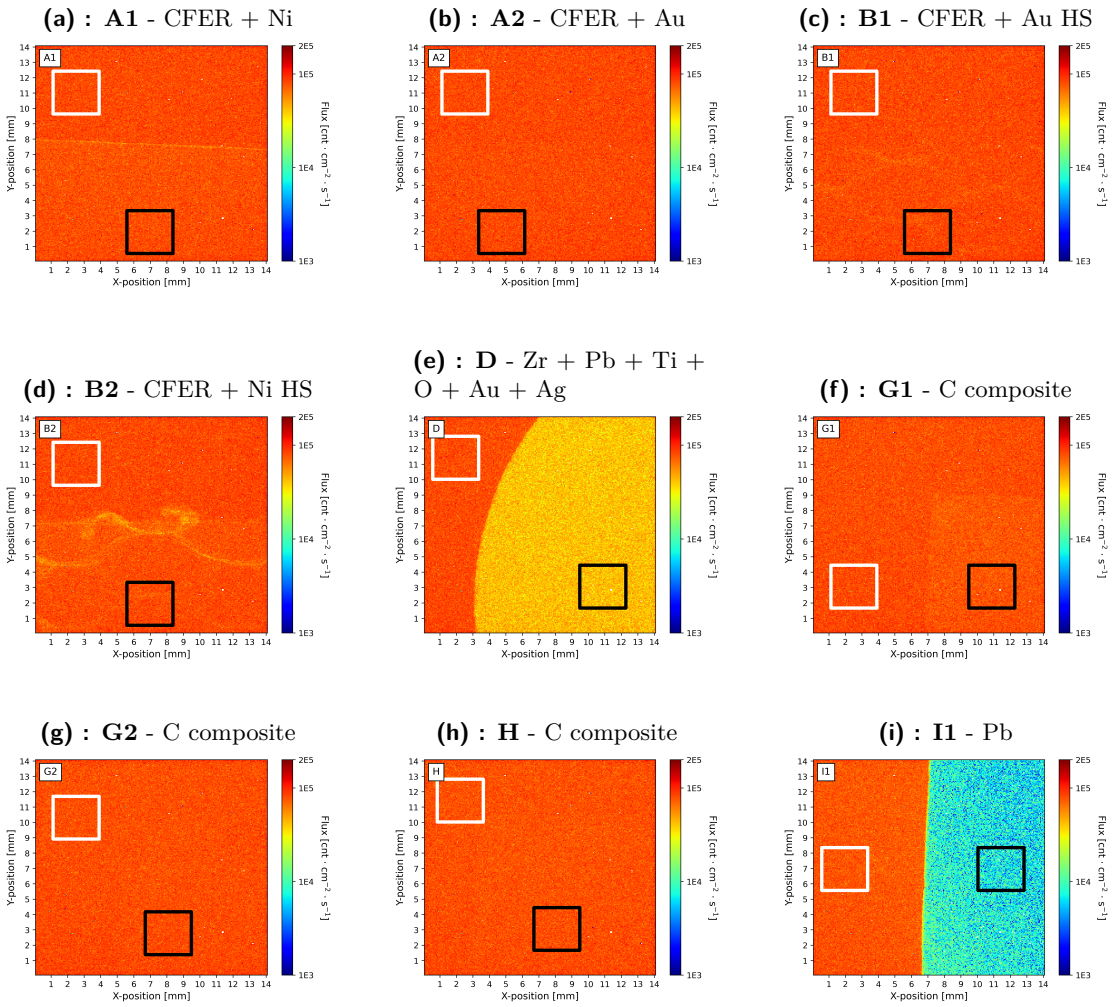

Figure C.2: Similar to Figure C.1 and Figure 8.15 showing the **particle flux** spatial maps for significant samples from the **X-ray 120 keV** experiment. The ROI regions are shown by squares for open beam (white) and shielded behind the samples (black).

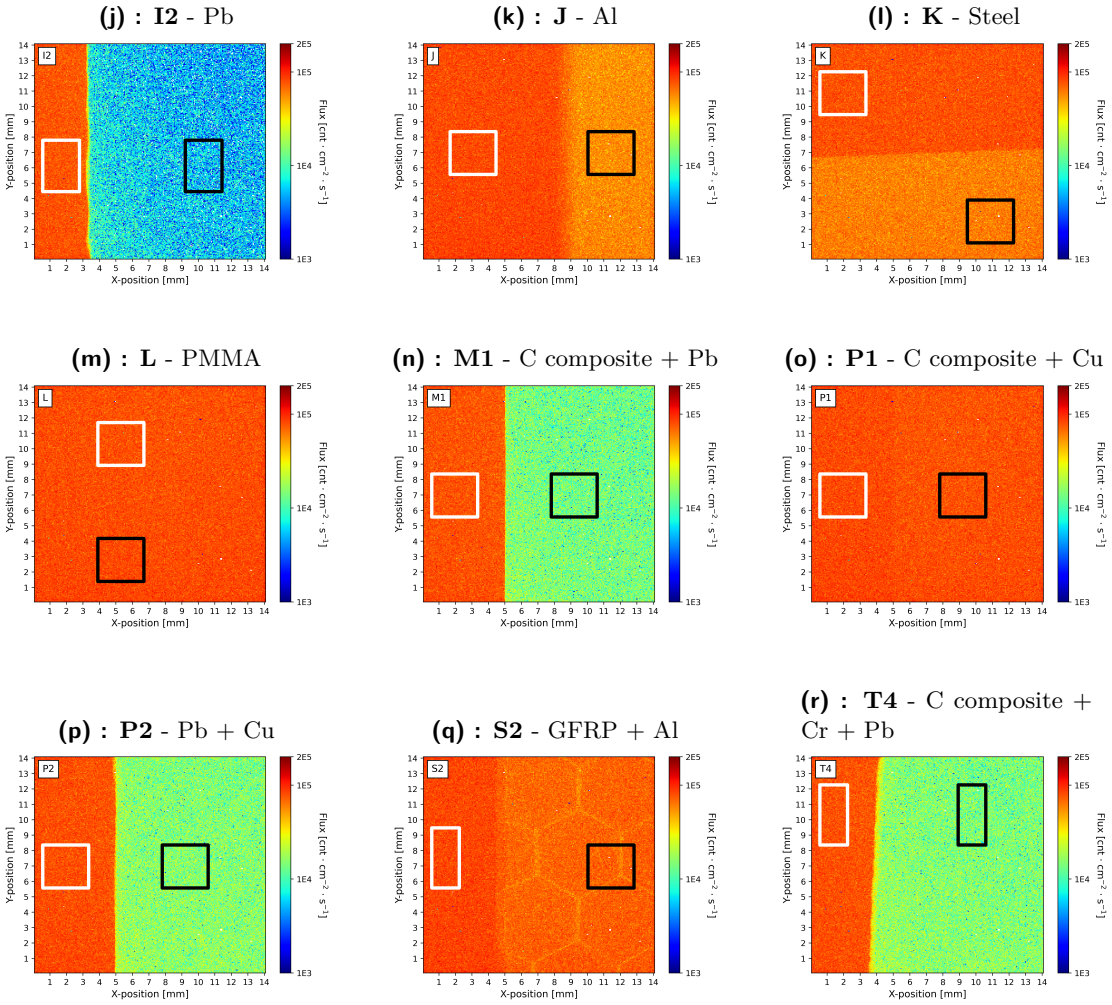

Figure C.2: Similar to Figure C.1 and Figure 8.15 showing the **particle flux** spatial maps for significant samples from the **X-ray 120 keV** experiment. The ROI regions are shown by squares for open beam (white) and shielded behind the samples (black).

C.3 Electrons

This section provides spatial radiation maps presenting the particle flux values for significant samples from the 5 MeV microtron accelerator experiment.

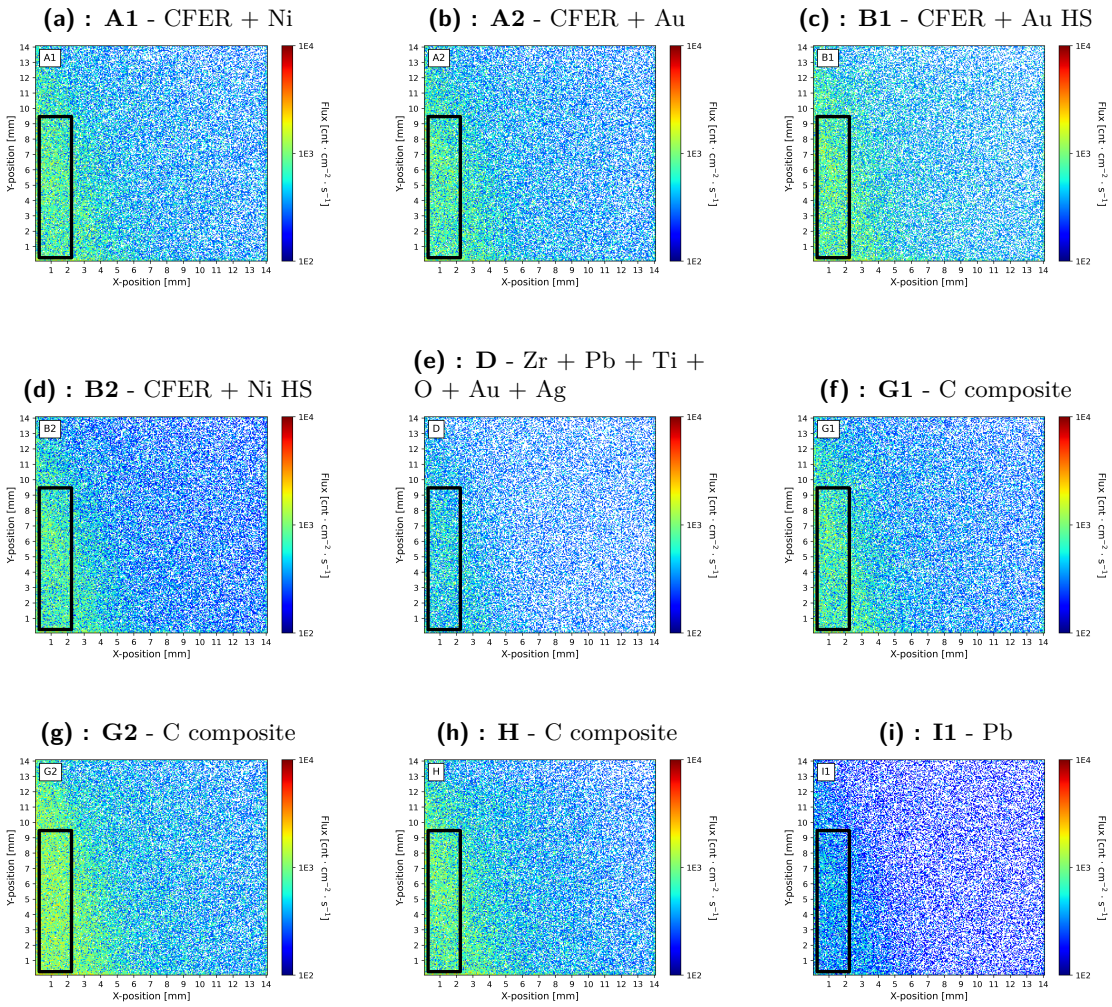

Figure C.3: Similar to Figure 8.20 showing the **particle flux** spatial maps for significant samples from the **electron 5 MeV** experiment. The ROI used for the shielding efficiency calculations is indicated (black frame).

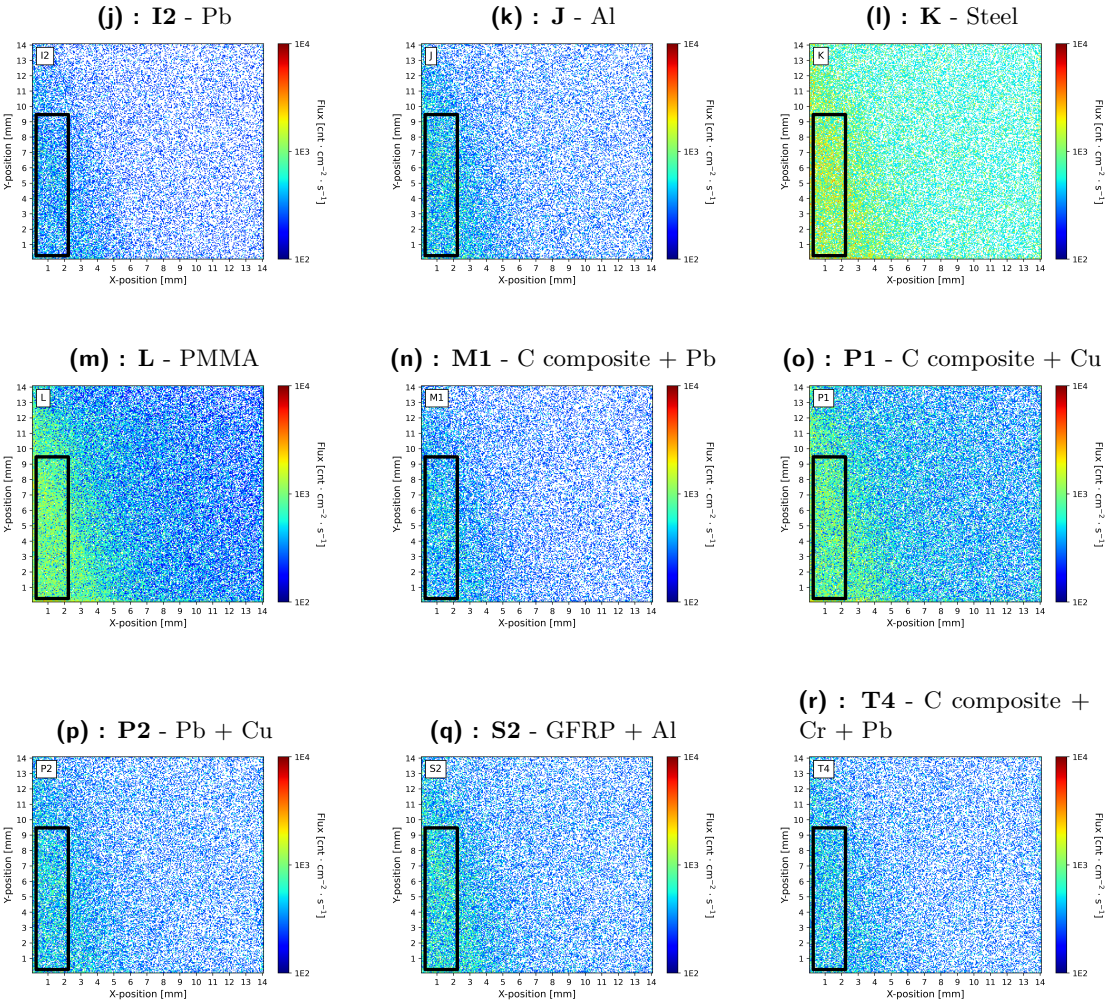

Figure C.3: Similar to Figure 8.20 showing the **particle flux** spatial maps for significant samples from the **electron 5 MeV** experiment. The ROI used for the shielding efficiency calculations is indicated (black frame).

C.4 Protons

This section provides the spatial radiation maps presenting the particle flux values for significant samples from the 31 MeV cyclotron accelerator experiment.

(a) : M2 - C composite

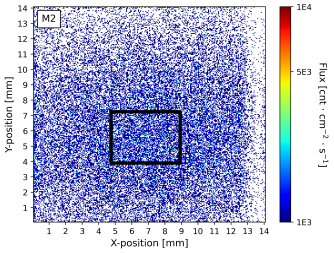

(b) : P1 - C composite + Cu

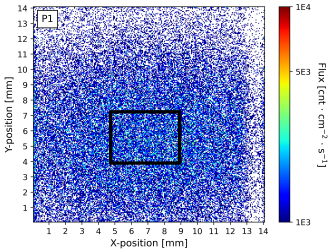

(c) : P2 - Pb + Cu

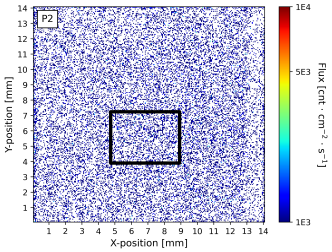

(d) : P3 - Cr + C composite

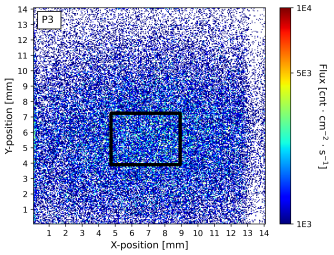

(e) : Q1 - C composite

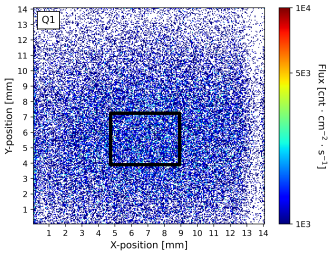

(f) : Q3 - C composite + Cu + Ni

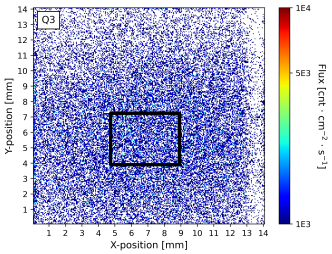

(g) : Q4 - C composite + Ceramics

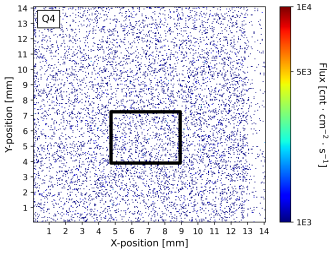

(h) : S3 - C composite

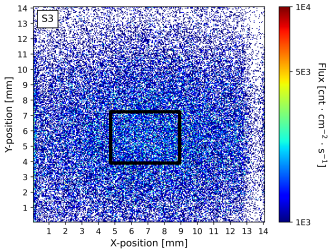

(i) : T4 - C composite + Cr + Pb

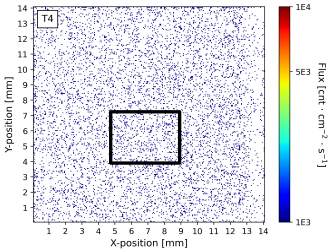

Figure C.4: Similar to Figure 8.26 showing the **particle flux** spatial maps for significant samples from the **protons 31 MeV** experiment. The ROI used for the shielding efficiency calculations is indicated (black frame).

C.5 X-ray scanner 50 keV

This section provides the spatial radiation map presenting the particle flux values for all samples from the 50 keV X-ray scanner experiment.

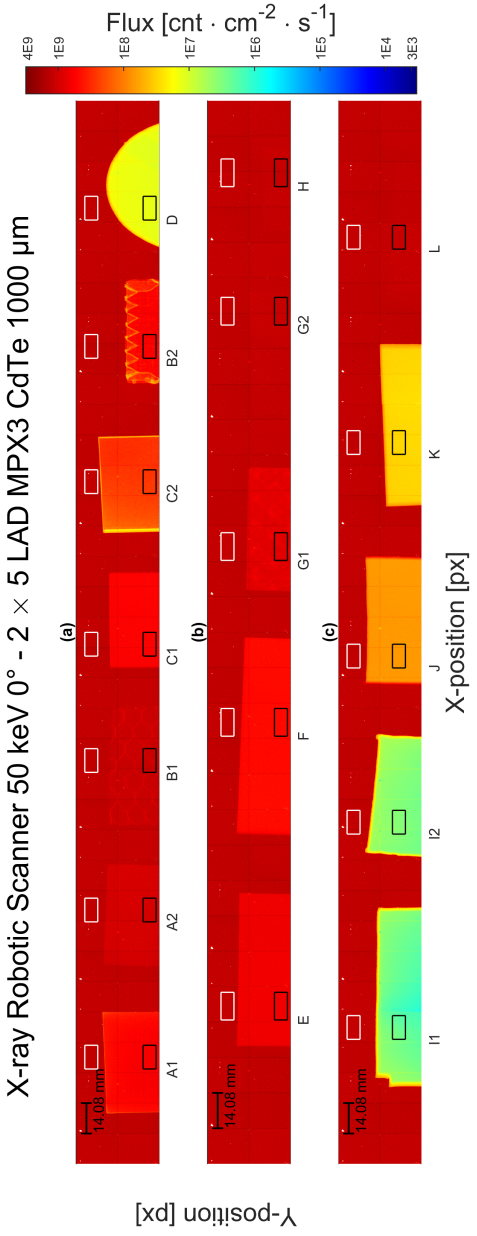

Figure C.5: Same as Figure 8.10 showing flux visualization of 50 keV X-rays. Measured with the `WidePIX A06 (2 × 5 LAD MPX3 1000 µm CdTe)` detector. The ROI regions are shown by squares for open beam (white) and shielded behind the samples (black).

Appendix D

Protons single-sample and two-sample stacked measurements

Figures D.1 and D.2 show the values of physical products (particle flux, dose rate) for all samples measured in the proton experiment including additional measurements combining two neighbouring stacked samples. The individual isolated samples were evaluated separately in this work - see Section 8. In the figures in this appendix, the samples and the double combinations of the samples do not show values normalized for planar thickness, as it would not be accurate with the stacked samples. The purpose is to show the added shielding effect when two samples are stacked on top of each other.

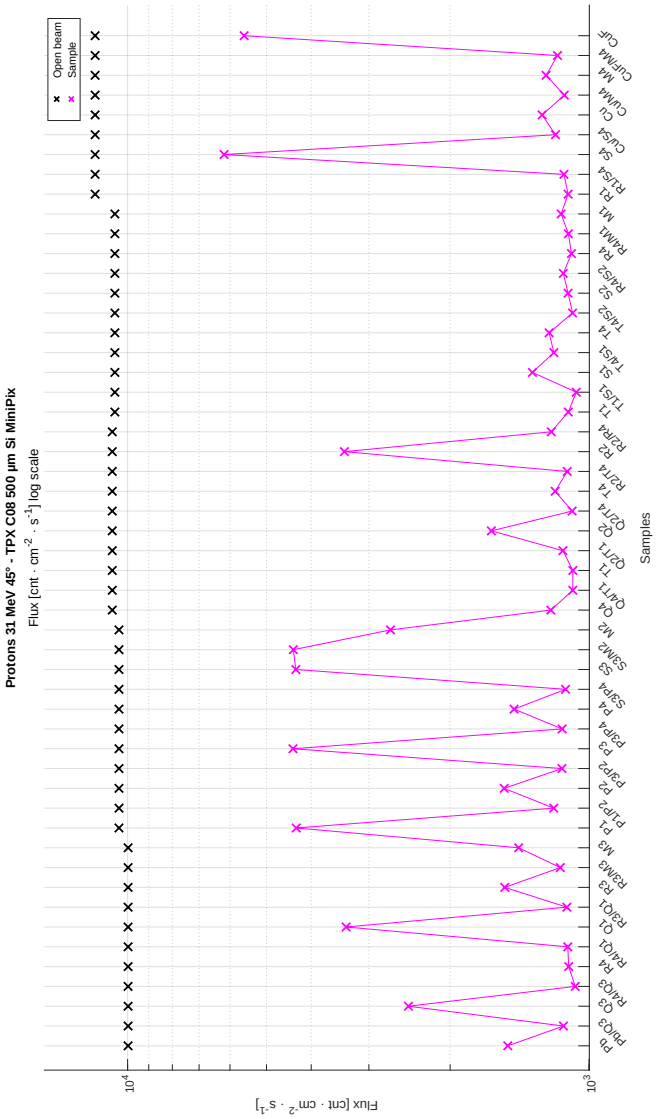

Figure D.1: Similar to Figure 8.29 for the **31 MeV protons** experiments showing the **particle flux** behind the region of interest of all samples in respect to the open beam values for individual samples (as in Figure 8.29) together with the two-sample stacked measurements. The values are not normalized for sample thickness.

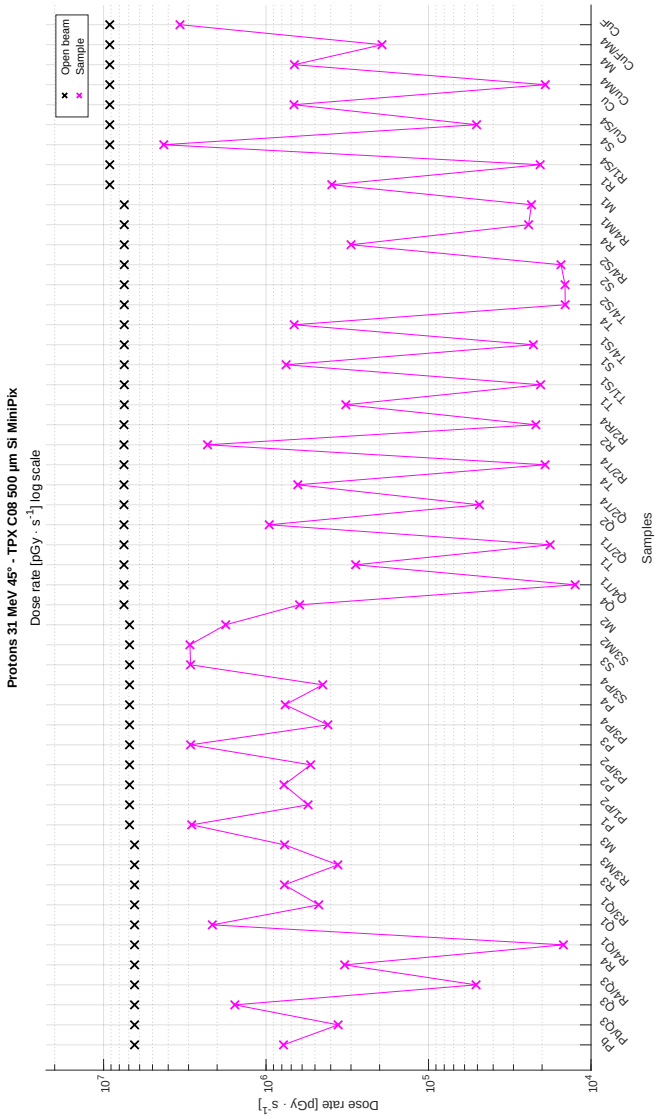

Figure D.2: Similar to Figure D.1 and Figure 8.30 for the **31 MeV protons** experiments showing the **dose rate** behind the region of interest of all samples in respect to the open beam values for individual samples (as in Figure 8.30) together with the two-sample stacked measurements. The values are not normalized for sample thickness.

Appendix E

Results tables

The tables in this annex provide the exact numerical values of the results for all samples measured in the various individual experiments: Robotic scanner 50 keV (Table E.1). micro-focus X-rays at 40 keV (Table E.2) and 120 keV (Table E.3), 5 MeV electrons (Table E.4) and 31 MeV protons (Table E.5). The broad event classes are explained in Chapter 7.2 as follows:

Broad class 1 = electrons, X-rays, gamma rays,
Broad class 2 = protons,
Broad class 3 = ions.

The classification parameters of the event classes are specified by experimental approach. The method of classification is described by Granja (2018) [70] and the tuned parameters used for this thesis are described by Granja (2022) [71].

The color range of cells in the following tables represents the range of values for the given column description, where green is the lowest physical product (flux or dose rate) value and red the highest. The sample values are normalized to the sample thickness/planar i.e. surface density (labeled in tables as *Shielded (II)*), and additionally also for the surface density of 1 cm of Aluminium (labeled in tables as *Shielded (I)*). These additional values were used for creation of comparison graphs in Chapter 8.

50 keV X-rays

ID	Flux [cnt · cm^{-2} · s^{-1}]		
	Shielded (I)	Shielded (II)	Open Beam
A1	5.56E+07	1.50E+08	1.30E+09
A2	6.68E+07	1.80E+08	1.30E+09
B1	1.93E+08	5.21E+08	1.30E+09
B2	9.91E+07	2.68E+08	1.29E+09
C1	1.71E+08	4.61E+08	1.29E+09
C2	8.03E+07	2.17E+08	1.23E+09
D	5.26E+06	1.42E+07	1.27E+09
E	2.64E+08	7.13E+08	1.24E+09
F	1.00E+08	2.70E+08	1.25E+09
G1	5.05E+07	1.36E+08	1.25E+09
G2	5.04E+07	1.36E+08	1.28E+09
H	6.31E+07	1.70E+08	1.27E+09
I1	1.31E+06	3.55E+06	1.23E+09
I2	3.27E+06	8.83E+06	1.27E+09
J	7.05E+07	1.90E+08	1.30E+09
K	8.19E+06	2.21E+07	1.30E+09
L	6.85E+07	1.85E+08	1.23E+09

Table E.1: The particle flux values for all samples in the 50 keV X-ray scanner experiment. The measurements from detector used (MPX3) in the X-ray scanner only provide the counts of events from which only the particle flux can be derived. The dose rate values or event classes are not available. Green color represents the lowest physical product (flux or dose rate) value and red the highest. The sample values are normalized to the sample thickness/planar i.e. surface density (*Shielded (II)*), and additionally also for the surface density of 1 cm of Aluminium (*Shielded (I)*)

40 keV X-rays

ID	Event classes [%]			Flux [cnt · cm^{-2} · s^{-1}]			Dose rate [pGy· s^{-1}]		
	Class 1	Class 2	Class 3	Shielded (I)	Shielded (II)	Open Beam	Shielded (I)	Shielded (II)	Open Beam
A1	100.00	0.00	0.00	3.59E+04	9.69E+04	7.59E+05	5.03E+04	1.36E+05	1.01E+06
A2	100.00	0.00	0.00	4.22E+04	1.14E+05	7.61E+05	5.71E+04	1.54E+05	1.02E+06
B1	100.00	0.00	0.00	1.06E+05	2.88E+05	6.78E+05	1.57E+05	4.24E+05	9.76E+05
B2	100.00	0.00	0.00	6.07E+04	1.64E+05	7.90E+05	8.46E+04	2.28E+05	1.05E+06
C1	100.00	0.00	0.00	1.06E+05	2.85E+05	7.76E+05	1.51E+05	4.07E+05	1.04E+06
C2	100.00	0.00	0.00	4.87E+04	1.31E+05	8.08E+05	7.22E+04	1.95E+05	1.08E+06
D	100.00	0.00	0.00	3.70E+03	9.98E+03	8.10E+05	5.41E+03	1.46E+04	1.08E+06
E	100.00	0.00	0.00	1.58E+05	4.25E+05	7.16E+05	1.52E+05	4.11E+05	6.62E+05
F	*N/A*	*N/A*	*N/A*	*N/A*	*N/A*	*N/A*	*N/A*	*N/A*	*N/A*
G1	100.00	0.00	0.00	3.01E+04	8.14E+04	7.25E+05	4.17E+04	1.12E+05	9.62E+05
G2	100.00	0.00	0.00	3.02E+04	8.17E+04	7.44E+05	4.04E+04	1.09E+05	9.92E+05
H	100.00	0.00	0.00	3.62E+04	9.77E+04	7.06E+05	4.84E+04	1.31E+05	9.41E+05
I1	100.00	0.00	0.00	2.22E+03	6.01E+03	7.50E+05	3.05E+03	8.24E+03	6.85E+05
I2	100.00	0.00	0.00	5.46E+03	1.47E+04	8.05E+05	6.31E+03	1.70E+04	1.03E+06
J	100.00	0.00	0.00	2.93E+04	7.91E+04	7.83E+05	4.78E+04	1.29E+05	1.05E+06
K	100.00	0.00	0.00	3.04E+03	8.20E+03	7.78E+05	4.67E+03	1.26E+04	1.04E+06
L	100.00	0.00	0.00	4.16E+04	1.12E+05	7.30E+05	3.98E+04	1.07E+05	6.97E+05
M1	100.00	0.00	0.00	3.66E+03	9.88E+03	8.13E+05	5.06E+03	1.37E+04	1.08E+06
M2	100.00	0.00	0.00	1.27E+05	3.43E+05	7.55E+05	1.66E+05	4.47E+05	9.66E+05
M3	100.00	0.00	0.00	1.86E+03	5.02E+03	8.14E+05	2.52E+03	6.81E+03	1.09E+06
M4	100.00	0.00	0.00	2.06E+03	5.55E+03	7.92E+05	2.84E+03	7.68E+03	1.06E+06
P1	100.00	0.00	0.00	3.79E+04	1.02E+05	7.57E+05	5.15E+04	1.39E+05	1.01E+06
P2	100.00	0.00	0.00	2.18E+03	5.90E+03	8.29E+05	2.89E+03	7.82E+03	1.11E+06
P3	100.00	0.00	0.00	8.98E+04	2.42E+05	7.52E+05	1.22E+05	3.29E+05	1.00E+06
P4	100.00	0.00	0.00	1.49E+03	4.03E+03	8.31E+05	1.96E+03	5.30E+03	1.06E+06
Q1	100.00	0.00	0.00	8.79E+04	2.37E+05	7.66E+05	1.19E+05	3.21E+05	1.02E+06
Q2	100.00	0.00	0.00	7.02E+04	1.89E+05	7.64E+05	8.90E+04	2.40E+05	8.82E+05
Q3	100.00	0.00	0.00	4.27E+04	1.15E+05	8.03E+05	6.23E+04	1.68E+05	1.07E+06
Q4	100.00	0.00	0.00	1.50E+03	4.06E+03	8.35E+05	1.58E+03	4.28E+03	9.33E+05
R1	100.00	0.00	0.00	4.08E+03	1.10E+04	8.24E+05	5.41E+03	1.46E+04	1.05E+06
R2	100.00	0.00	0.00	1.08E+05	2.90E+05	7.58E+05	1.40E+05	3.79E+05	9.69E+05
R3	100.00	0.00	0.00	4.70E+03	1.27E+04	8.26E+05	5.45E+03	1.47E+04	9.22E+05
R4	100.00	0.00	0.00	1.90E+03	5.14E+03	8.14E+05	2.53E+03	6.83E+03	1.04E+06
S1	100.00	0.00	0.00	1.49E+05	4.02E+05	7.81E+05	1.98E+05	5.33E+05	8.72E+05
S2	100.00	0.00	0.00	7.70E+04	2.08E+05	8.07E+05	1.18E+05	3.19E+05	9.03E+05
S3	100.00	0.00	0.00	9.29E+04	2.51E+05	7.65E+05	1.06E+05	2.86E+05	8.55E+05
S4	100.00	0.00	0.00	7.29E+04	1.97E+05	7.58E+05	8.28E+04	2.23E+05	8.47E+05
T1	100.00	0.00	0.00	3.33E+03	9.00E+03	8.27E+05	4.69E+03	1.27E+04	1.10E+06
T2	100.00	0.00	0.00	7.31E+04	1.97E+05	7.98E+05	1.06E+05	2.86E+05	1.07E+06
T3	100.00	0.00	0.00	1.12E+05	3.04E+05	7.32E+05	1.48E+05	3.99E+05	9.43E+05
T4	100.00	0.00	0.00	1.45E+03	3.91E+03	8.18E+05	1.63E+03	4.39E+03	9.13E+05

Table E.2: Similar to Table E.1 for the 40 keV X-ray tube experiment, the ratio of broad event classes (explained in Chapter 7.2) in the measured samples is included. Besides the particle flux also the dose rate values are derived (possible by the use of the TPX3 detector). N/A in the value cell means the sample was not measured in the experiment or has not been measured correctly.

120 keV X-rays

ID	Event classes [%]			Flux [cnt · cm^{-2} · s^{-1}]			Dose rate [pGy· s^{-1}]		
	Class 1	Class 2	Class 3	Shielded (I)	Shielded (II)	Open Beam	Shielded (I)	Shielded (II)	Open Beam
A1	**100.00**	0.00	0.00	7.63E+03	2.06E+04	8.39E+04	1.35E+04	3.64E+04	1.49E+05
A2	**100.00**	0.00	0.00	5.79E+03	1.56E+04	8.46E+04	1.03E+04	2.79E+04	1.52E+05
B1	**100.00**	0.00	0.00	1.44E+04	3.89E+04	8.43E+04	2.57E+04	6.94E+04	1.51E+05
B2	**100.00**	0.00	0.00	1.40E+04	3.78E+04	8.46E+04	2.47E+04	6.66E+04	1.50E+05
C1	**100.00**	0.00	0.00	2.35E+04	6.35E+04	8.29E+04	4.25E+04	1.15E+05	1.50E+05
C2	**100.00**	0.00	0.00	2.23E+04	6.03E+04	8.41E+04	3.98E+04	1.07E+05	1.50E+05
D	**100.00**	0.00	0.00	1.70E+04	4.58E+04	8.30E+04	2.99E+04	8.07E+04	1.45E+05
E	**100.00**	0.00	0.00	2.90E+04	7.82E+04	8.13E+04	5.16E+04	1.39E+05	1.46E+05
F	*N/A*	*N/A*	*N/A*	*N/A*	*N/A*	*N/A*	*N/A*	*N/A*	*N/A*
G1	**100.00**	0.00	0.00	4.92E+03	1.33E+04	8.41E+04	8.77E+03	2.37E+04	1.50E+05
G2	**100.00**	0.00	0.00	3.47E+03	9.36E+03	8.19E+04	6.15E+03	1.66E+04	1.47E+05
H	**100.00**	0.00	0.00	4.25E+03	1.15E+04	8.08E+04	7.65E+03	2.06E+04	1.43E+05
I1	**100.00**	0.00	0.00	4.36E+03	1.18E+04	7.92E+04	8.23E+03	2.22E+04	1.42E+05
I2	**100.00**	0.00	0.00	5.32E+03	1.44E+04	7.88E+04	9.33E+03	2.52E+04	1.36E+05
J	**100.00**	0.00	0.00	5.62E+04	1.52E+05	8.40E+04	1.04E+05	2.80E+05	1.51E+05
K	**100.00**	0.00	0.00	1.66E+04	4.48E+04	8.03E+04	2.92E+04	7.89E+04	1.44E+05
L	**100.00**	0.00	0.00	4.95E+03	1.34E+04	8.19E+04	8.89E+03	2.40E+04	1.47E+05
M1	**100.00**	0.00	0.00	7.65E+03	2.06E+04	8.00E+04	1.41E+04	3.79E+04	1.42E+05
M2	**100.00**	0.00	0.00	1.55E+04	4.19E+04	8.40E+04	2.66E+04	7.18E+04	1.45E+05
M3	**100.00**	0.00	0.00	4.53E+03	1.22E+04	8.16E+04	8.13E+03	2.19E+04	1.44E+05
M4	**100.00**	0.00	0.00	1.69E+04	4.56E+04	8.30E+04	2.97E+04	8.03E+04	1.48E+05
P1	**100.00**	0.00	0.00	4.71E+03	1.27E+04	8.40E+04	8.50E+03	2.30E+04	1.51E+05
P2	**100.00**	0.00	0.00	3.87E+03	1.04E+04	8.19E+04	7.05E+03	1.90E+04	1.46E+05
P3	**100.00**	0.00	0.00	1.07E+04	2.89E+04	8.24E+04	1.95E+04	5.25E+04	1.48E+05
P4	**100.00**	0.00	0.00	3.95E+03	1.07E+04	7.96E+04	7.00E+03	1.89E+04	1.36E+05
Q1	**100.00**	0.00	0.00	1.07E+04	2.88E+04	8.40E+04	1.92E+04	5.17E+04	1.50E+05
Q2	**100.00**	0.00	0.00	1.68E+04	4.53E+04	8.34E+04	3.02E+04	8.16E+04	1.49E+05
Q3	**100.00**	0.00	0.00	1.30E+04	3.51E+04	8.54E+04	2.31E+04	6.24E+04	1.52E+05
Q4	**100.00**	0.00	0.00	7.24E+03	1.96E+04	8.13E+04	1.08E+04	2.92E+04	1.21E+05
R1	**100.00**	0.00	0.00	3.00E+03	8.09E+03	8.00E+04	5.57E+03	1.50E+04	1.37E+05
R2	**100.00**	0.00	0.00	1.30E+04	3.52E+04	8.39E+04	2.26E+04	6.10E+04	1.44E+05
R3	**100.00**	0.00	0.00	5.14E+03	1.39E+04	8.10E+04	7.97E+03	2.15E+04	1.20E+05
R4	**100.00**	0.00	0.00	2.51E+03	6.79E+03	7.88E+04	4.30E+03	1.16E+04	1.35E+05
S1	**100.00**	0.00	0.00	2.14E+04	5.79E+04	8.33E+04	3.78E+04	1.02E+05	1.34E+05
S2	**100.00**	0.00	0.00	3.47E+04	9.38E+04	8.54E+04	6.21E+04	1.68E+05	1.28E+05
S3	**100.00**	0.00	0.00	1.08E+04	2.91E+04	8.12E+04	1.27E+04	3.43E+04	9.43E+04
S4	**100.00**	0.00	0.00	8.29E+03	2.24E+04	8.24E+04	1.25E+04	3.38E+04	1.25E+05
T1	**100.00**	0.00	0.00	3.07E+03	8.28E+03	7.91E+04	5.81E+03	1.57E+04	1.42E+05
T2	**100.00**	0.00	0.00	1.55E+04	4.20E+04	8.33E+04	2.81E+04	7.60E+04	1.48E+05
T3	**100.00**	0.00	0.00	1.44E+04	3.88E+04	8.42E+04	2.58E+04	6.96E+04	1.50E+05
T4	**100.00**	0.00	0.00	3.84E+03	1.04E+04	7.88E+04	5.78E+03	1.56E+04	1.17E+05

Table E.3: Similar to Table E.2 for the 120 keV X-ray micro-focus tube experiment.

5 MeV Electrons

ID	Event classes [%]			Flux [cnt · cm^{-2} · s^{-1}]			Dose rate [pGy· s^{-1}]		
	Class 1	Class 2	Class 3	Shielded (I)	Shielded (II)	Open Beam	Shielded (I)	Shielded (II)	Open Beam
A1	**99.96**	0.04	0.00	1.03E+03	2.78E+03	1.01E+04	2.40E+04	6.47E+04	2.41E+05
A2	**99.92**	0.08	0.00	7.24E+02	1.96E+03	1.01E+04	1.72E+04	4.65E+04	2.41E+05
B1	**99.95**	0.05	0.00	1.90E+03	5.13E+03	1.30E+04	4.40E+04	1.19E+05	3.37E+05
B2	**99.92**	0.08	0.00	1.73E+03	4.68E+03	1.45E+04	4.00E+04	1.08E+05	3.76E+05
C1	**99.93**	0.07	0.00	3.56E+03	9.60E+03	1.01E+04	7.14E+04	1.93E+05	2.41E+05
C2	**99.95**	0.05	0.00	3.08E+03	8.33E+03	1.01E+04	6.31E+04	1.70E+05	2.41E+05
D	**99.92**	0.08	0.00	2.69E+03	7.25E+03	1.01E+04	5.88E+04	1.59E+05	2.41E+05
E	**99.95**	0.05	0.00	7.29E+03	1.97E+04	2.29E+04	1.47E+05	3.97E+05	6.19E+05
F	**99.94**	0.05	0.01	3.62E+03	9.78E+03	2.29E+04	7.72E+04	2.08E+05	6.19E+05
G1	**99.99**	0.01	0.00	6.39E+02	1.73E+03	1.01E+04	1.52E+04	4.11E+04	2.41E+05
G2	**99.88**	0.12	0.00	6.29E+02	1.70E+03	1.01E+04	1.48E+04	4.01E+04	2.41E+05
H	**99.93**	0.07	0.00	6.10E+02	1.65E+03	1.28E+04	1.50E+04	4.06E+04	3.36E+05
I1	**99.89**	0.11	0.00	3.06E+03	8.25E+03	1.45E+04	7.21E+04	1.95E+05	3.76E+05
I2	**99.87**	0.13	0.00	4.51E+03	1.22E+04	1.28E+04	1.13E+05	3.06E+05	3.36E+05
J	**99.95**	0.05	0.00	6.11E+03	1.65E+04	2.29E+04	1.22E+05	3.28E+05	6.19E+05
K	**99.89**	0.11	0.00	4.45E+03	1.20E+04	2.29E+04	9.38E+04	2.53E+05	6.19E+05
L	**99.91**	0.09	0.00	7.45E+02	2.01E+03	1.45E+04	1.84E+04	4.98E+04	3.76E+05
M1	**99.92**	0.08	0.00	3.01E+03	8.12E+03	1.30E+04	6.89E+04	1.86E+05	3.37E+05
M2	**99.93**	0.07	0.00	1.91E+03	5.16E+03	1.30E+04	4.19E+04	1.13E+05	3.37E+05
M3	**99.90**	0.10	0.00	1.78E+03	4.79E+03	1.39E+04	4.14E+04	1.12E+05	3.69E+05
M4	**99.89**	0.11	0.00	2.28E+03	6.16E+03	1.39E+04	4.71E+04	1.27E+05	3.69E+05
P1	**99.92**	0.08	0.00	6.93E+02	1.87E+03	1.48E+04	1.62E+04	4.38E+04	3.89E+05
P2	**99.83**	0.17	0.00	1.57E+03	4.23E+03	1.48E+04	3.70E+04	9.99E+04	3.89E+05
P3	**99.96**	0.04	0.00	1.52E+03	4.10E+03	1.43E+04	3.50E+04	9.44E+04	3.76E+05
P4	**99.89**	0.11	0.00	1.66E+03	4.47E+03	1.43E+04	3.84E+04	1.04E+05	3.76E+05
Q1	**99.93**	0.07	0.00	1.54E+03	4.15E+03	1.71E+04	3.63E+04	9.80E+04	4.49E+05
Q2	**99.90**	0.10	0.00	2.01E+03	5.42E+03	1.71E+04	4.37E+04	1.18E+05	4.49E+05
Q3	**99.92**	0.08	0.00	1.66E+03	4.49E+03	1.33E+04	3.88E+04	1.05E+05	3.51E+05
Q4	**99.88**	0.12	0.00	1.95E+03	5.27E+03	1.33E+04	4.35E+04	1.18E+05	3.51E+05
R1	**99.95**	0.05	0.00	2.60E+03	7.03E+03	1.43E+04	5.91E+04	1.59E+05	3.72E+05
R2	**99.94**	0.06	0.00	1.73E+03	4.68E+03	1.43E+04	3.88E+04	1.05E+05	3.72E+05
R3	**100.00**	0.00	0.00	2.57E+03	6.94E+03	1.28E+04	5.89E+04	1.59E+05	3.26E+05
R4	**99.91**	0.09	0.00	2.74E+03	7.40E+03	1.28E+04	6.19E+04	1.67E+05	3.26E+05
S1	**99.91**	0.09	0.00	2.64E+03	7.14E+03	1.47E+04	5.65E+04	1.52E+05	3.81E+05
S2	**99.90**	0.10	0.00	3.56E+03	9.62E+03	1.47E+04	6.91E+04	1.87E+05	3.81E+05
S3	**99.93**	0.07	0.00	1.50E+03	4.06E+03	1.47E+04	3.50E+04	9.45E+04	3.81E+05
S4	**99.93**	0.07	0.00	1.34E+03	3.62E+03	1.48E+04	3.25E+04	8.79E+04	3.89E+05
T1	**99.89**	0.11	0.00	2.84E+03	7.68E+03	1.34E+04	6.73E+04	1.82E+05	3.48E+05
T2	**99.92**	0.08	0.00	1.91E+03	5.16E+03	1.34E+04	4.15E+04	1.12E+05	3.48E+05
T3	**99.89**	0.11	0.00	1.82E+03	4.92E+03	1.29E+04	4.15E+04	1.12E+05	3.38E+05
T4	**99.88**	0.12	0.00	1.41E+03	3.81E+03	1.29E+04	3.19E+04	8.61E+04	3.38E+05

Table E.4: Similar to Table E.3 for the 5 MeV electron microtron experiment.

31 MeV Protons

ID	Event classes [%]			Flux [cnt · cm^{-2} · s^{-1}]			Dose rate [pGy· s^{-1}]		
	Class 1	Class 2	Class 3	Shielded (I)	Shielded (II)	Open Beam	Shielded (I)	Shielded (II)	Open Beam
M1	*98.61*	*1.39*	*0.00*	*N/A*	*N/A*	*N/A*	*N/A*	*N/A*	*N/A*
M2	5.75	**80.90**	12.02	5.32E+02	1.44E+03	1.04E+04	3.50E+05	9.45E+05	6.92E+06
M3	7.68	**86.09**	5.18	4.13E+02	1.11E+03	9.98E+03	2.23E+05	6.03E+05	6.45E+06
M4	16.31	**75.94**	6.68	4.11E+02	1.11E+03	1.18E+04	2.22E+05	5.99E+05	9.16E+06
P1	2.73	**83.17**	12.82	2.54E+02	6.86E+02	1.04E+04	1.69E+05	4.57E+05	6.92E+06
P2	5.69	**90.16**	3.81	3.63E+02	9.80E+02	1.04E+04	1.84E+05	4.97E+05	6.92E+06
P3	2.97	**82.96**	12.87	5.89E+02	1.59E+03	1.04E+04	3.92E+05	1.06E+06	6.92E+06
P4	6.44	**88.54**	4.07	3.96E+02	1.07E+03	1.04E+04	2.07E+05	5.60E+05	6.92E+06
Q1	3.25	**85.34**	10.52	4.46E+02	1.20E+03	9.98E+03	2.84E+05	7.67E+05	6.45E+06
Q2	11.67	**77.84**	8.53	3.51E+02	9.49E+02	1.08E+04	2.06E+05	5.57E+05	7.49E+06
Q3	3.38	**85.56**	9.56	4.06E+02	1.10E+03	9.98E+03	2.57E+05	6.93E+05	6.45E+06
Q4	19.97	**73.27**	5.86	3.83E+02	1.03E+03	1.08E+04	1.97E+05	5.32E+05	7.49E+06
R1	45.33	**50.93**	2.80	5.14E+02	1.39E+03	1.18E+04	1.83E+05	4.93E+05	9.16E+06
R2	4.26	**80.53**	13.72	5.60E+02	1.51E+03	1.08E+04	3.79E+05	1.02E+06	7.49E+06
R3	4.93	**90.85**	3.70	7.10E+02	1.92E+03	9.98E+03	3.59E+05	9.70E+05	6.45E+06
R4	**54.22**	40.36	4.22	5.78E+02	1.56E+03	9.98E+03	1.72E+05	4.63E+05	6.45E+06
S1	16.81	**72.58**	9.14	3.72E+02	1.00E+03	1.07E+04	2.11E+05	5.69E+05	7.46E+06
S2	*98.70*	*1.30*	*0.00*	*N/A*	*N/A*	*N/A*	*N/A*	*N/A*	*N/A*
S3	2.72	**82.75**	13.22	5.82E+02	1.57E+03	1.04E+04	3.93E+05	1.06E+06	6.92E+06
S4	2.79	**82.33**	14.04	6.34E+02	1.71E+03	1.18E+04	4.37E+05	1.18E+06	9.16E+06
T1	**50.61**	43.29	4.27	5.86E+02	1.58E+03	1.07E+04	1.71E+05	4.61E+05	7.46E+06
T2	*N/A*	*N/A*	*N/A*	*N/A*	*N/A*	*N/A*	*N/A*	*N/A*	*N/A*
T3	*N/A*	*N/A*	*N/A*	*N/A*	*N/A*	*N/A*	*N/A*	*N/A*	*N/A*
T4	11.91	**81.87**	5.41	2.98E+02	8.05E+02	1.07E+04	1.64E+05	4.43E+05	7.46E+06

Table E.5: Similar to Table E.4 for the 31 MeV cyclotron proton experiment. Some single particle events were classified as noisy pixels and not counted in either event class. Samples R4 and T1 (both Ta) show higher percentage of events from event class 1 (electrons, X-rays, gamma rays) due to secondary and/or scattered primary radiation.

Appendix F

Contents of attached CD

The attached CD contains the main processing scripts in python used in this work (see Section 7.2) and samples of the data files used in processing (see Section 6.2.8 and Figure 7.1):

- `processing_scripts/` – containing the main processing scripts in python:
  - `TPX_elist_clusterer_april2022.py` - script used for processing data in the proton experiment - reads in event list from Clusterer (see Section 7.1) created from .clog data file (see Section 6.2.8) measured by detector with a TPX chip operated in frame mode (see Section 6.2)
  - `TPX3_f_itot_cnt_elist_clusterer_july2022.py` - script used for processing data in the electron experiment - reads in event list from Clusterer (see Section 7.1) created from .clog data file (see Section 6.2.8) measured by detector with a TPX3 chip operated in frame mode (see Section 6.2)
  - `TPX3_t3pa_elist_clusterer_aug2022.py` - script used for processing data in the table-top X-ray micro-focus tube experiment - reads in event list from Clusterer (see Section 7.1) created from .t3pa data file (see Section 6.2.8) measured by detector with a TPX3 chip operated in data driven mode (see Section 6.2)
- `data/` – containing samples of data files used in processing

Appendix G

Acronyms

μm Micrometre.

2D Two dimensional spatial planar imaging.

3D Two dimensional spatial volume/full space imaging.

ADV Advacam.

ASIC Application-Specific Integrated Circuit.

BiCMOS Bipolar Complementary Metal Oxide Semiconductor.

BJT Bipolar Junction Transistor.

CAAS MATE Centre of Advanced Applied Sciences, Material Science and Engineering.

CCD Charge-Coupled Device.

CdTe Cadmium Telluride.

CF Carbon Fiber.

CFER Carbon Fiber Reinforced Epoxy Resin.

CFRP Carbon Fiber Reinforced Polymer.

CME Coronal Mass Ejection.

CMOS Complementary Metal Oxide Semiconductor.

cnt Count.

COTS Commercial Of The Shelf.

CSM Charge Summing Mode.

CT Computed Tomography.

CTE Charge Transfer Efficiency.

CTU Czech Technical University.

DD Displacement Damage.

DMOS Depletion-mode MOSFET.

DR Dose Rate.

EEEC Electrical, Electronic and Electro-mechanical Component.

EEPROM Electrically Erasable Programmable Read-Only Memory.

ESA European Space Agency.

eV Electron Volt.

EVA Extra Vehicular Activity.

FEE Faculty of Electrical Engineering.

FoV Field of View.

FToA Fast Time of Arrival.

GaAs Gallium Arsenide.

GCR Galactic Cosmic Rays.

GEO Geosynchronous Equatorial Orbit.

GeV Giga Electron Volt.

GF Glass Fiber.

GFRP Graphite Fiber Reinforced Polymer.

GPS Global Positioning System.

Gy Gray.

HCP Heavy Charged Particle.

hFE Hybrid parameter Forward current gain, common Emitter.

HPC High Performance Computing.

ID Identification.

IR Infrared.

ISS International Space Station.

JFET Junction-gate Field Effect Transistor.

keV Kilo Electron Volt.

LAD Large Area Detector.

LCP Light Charged Particle.

LEO Low Earth Orbit.

LET Linear Energy Transfer.

log Logarithmic.

MEMS Micro-Electro-Mechanical Systems.

MEO Medium Earth Orbit.

MeV Mega Electron Volt.

MOS Metal Oxide Semiconductor.

MOSFET Metal Oxide Semiconductor Field Effect Transistor.

MPX Medipix.

NASA National Aeronautics and Space Administration.

NMOS N-type Metal Oxide Semiconductor.

NPI CAS Nuclear Physics Institute of the Czech Academy of Sciences.

PC Personal Computer.

PE Polyethylene.

PEEK Polyether Ether Ketone.

PI Polyimide.

PMMA Polymethyl Methacrylate.

PMOS P-channel Metal Oxide Semiconductor.

PP Polypropylene.

PTFE Polytetrafluoroethylene.

RAM Random Access Memory.

ROI Region Of Interest.

SAA South Atlantic Anomaly.

SAPPHIRE Solar Accumulated and Peak Proton and Heavy Ion Radiation Environment.

SATRAM Space Application of Timepix based Radiation Monitor.

SD Specific Dose.

SEB Single Event Burnout.

SEE Single Event Effect.

SEGR Single Event Gate Rupture.

SEL Single Event Latchup.

SET Single Event Transients.

SEU Single Event Upset.

SHE Single Hard Error.

SNR-CR Supernova Remnants Cosmic Ray.

SOI/SOS Silicon-On-Insulator/Silicon-On-Sapphire.

SPE Solar Particle Event.

SPENVIS Space Environment Information System.

SPM Single Pixel Mode.

STS Space Transportation System.

SW Software.

SXD Space X-ray Detector.

TID Total Ionizing Dose.

ToA Time of Arrival.

ToT Time over Threshold.

TPX Timepix.

UV Ultraviolet.

VLSI Very Large-Scale Integration.

VZLU Výzkumný a Zkušební Letecký Ústav.

Appendix H

Bibliography

[1] Vainio R, Desorgher L, Heynderickx D, Storini M, Fluckiger E, Horne RB, et al. Dynamics of the Earth's Particle Radiation Environment. Space Science Reviews. 2009 03;147(3-4):187-231. Available from: https://doi.org/10.1007/s11214-009-9496-7.

[2] Kudela K. Space weather near Earth and energetic particles: selected results. Journal of Physics: Conference Series. 2013 02;409:012017. Available from: https://doi.org/10.1088/1742-6596/409/1/012017.

[3] Bourdarie S, Xapsos M. The Near-Earth Space Radiation Environment. IEEE Transactions on Nuclear Science. 2008 08;55(4):1810-32. Available from: https://doi.org/10.1109/tns.2008.2001409.

[4] Benton ER, Benton EV. Space radiation dosimetry in low-Earth orbit and beyond. Nuclear Instruments and Methods in Physics Research Section B: Beam Interactions with Materials and Atoms. 2001;184(1):255-94. Advanced Topics in Solid State Dosimetry. Available from: https://doi.org/10.1016/S0168-583X(01)00748-0.

[5] Reitz G. Characteristic of the radiation field in low earth orbit and in deep space. Zeitschrift für Medizinische Physik. 2008 12;18(4):233-43. Available from: https://doi.org/10.1016/j.zemedi.2008.06.015.

[6] Badhwar GD. The Radiation Environment in Low-Earth Orbit. Radiation Research. 1997;148(5):S3-S10. Available from: https://doi.org/10.2307/3579710.

[7] Durante M, Cucinotta FA. Physical basis of radiation protection in space travel. Reviews of Modern Physics. 2011 11;83(4):1245-81. Available from: https://doi.org/10.1103/revmodphys.83.1245.

[8] Kudela K. On energetic particles in space. Acta Physica Slovaca Reviews and Tutorials. 2009 10;59(5). Available from: https://doi.org/10.2478/v10155-010-0098-4.

[9] Baker DN, Erickson PJ, Fennell JF, Foster JC, Jaynes AN, Verronen PT. Space Weather Effects in the Earth's Radiation Belts. Space Science Reviews. 2017 12;214(1). Available from: https://doi.org/10.1007/s11214-017-0452-7.

[10] Nwankwo VUJ, Jibiri NN, Kio MT. The Impact of Space Radiation Environment on Satellites Operation in Near-Earth Space. In: Satellites Missions and Technologies for Geosciences. IntechOpen; 2020. Available from: https://doi.org/10.5772/intechopen.90115.

[11] Boudjemai A, Hocine R, Guerionne S. Space environment effect on earth observation satellite instruments. In: 2015 7th International Conference on Recent Advances in Space Technologies (RAST). IEEE; 2015. Available from: https://doi.org/10.1109/RAST.2015.7208419.

[12] Koons H, Mazur J, Selesnick R, Blake J, Fennell J, Roeder J, et al. The Impact of the Space Environment on Space Systems. paper presented at 6th Spacecraft Charging Technology. 1998 10:7-11.

[13] Horne RB, Glauert SA, Meredith NP, Boscher D, Maget V, Heynderickx D, et al. Space weather impacts on satellites and forecasting the Earth's electron radiation belts with SPACECAST. Space Weather. 2013 04;11(4):169-86. Available from: https://doi.org/10.1002/swe.20023.

[14] Howard JW. Spacecraft environments interactions: Space radiation and its effects on electronic systems. NASA; 1999.

[15] Samwel SW, El-Aziz EA, Garrett HB, Hady AA, Ibrahim M, Amin MY. Space radiation impact on smallsats during maximum and minimum solar activity. Advances in Space Research. 2019 07;64(1):239-51. Available from: https://doi.org/10.1016/j.asr.2019.03.025.

[16] Tompros D, Mouzakis DE. Space environment effects on equipment and structures—current and future technologies. The Journal of Defense Modeling and Simulation: Applications, Methodology, Technology. 2021 08:154851292110330. Available from: https://doi.org/10.1177/15485129211033038.

[17] Suparta W, Zulkeple SK. Investigating Space Radiation Environment Effects on Communication of Razaksat-1. Journal of Aerospace Technology and Management. 2018 05;10. Available from: https://doi.org/10.5028/jatm.v10.815.

[18] Broccia G. Cubesats in Low Earth Orbit: Perils and Countermeasures. arXiv; 2021. Available from: https://doi.org/10.48550/ARXIV.2105.00107.

[19] Stehlikova V, Urban M, Nentvich O, Sieger L. Radiation resistance monitor on VZLUSAT-1: Preliminary results. Astron Nachr. 2018 06;339(5):382-5. Available from: https://doi.org/10.1002/asna.201813510.

[20] Urban M, Nentvich O, Stehlikova V, Baca T, Daniel V, Hudec R. VZLUSAT-1: Nanosatellite with miniature lobster eye X-ray telescope and qualification of the radiation shielding composite for space application. Acta Astronautica. 2017 11;140:96-104. Available from: https://doi.org/10.1016/j.actaastro.2017.08.004.

[21] Daniel V, Inneman A, Vertat I, Baca T, Nentvich O, Urban M, et al. In-Orbit Commissioning of Czech Nanosatellite VZLUSAT-1 for the QB50 Mission with a Demonstrator of a Miniaturised Lobster-Eye X-Ray Telescope and Radiation Shielding Composite Materials. Space Science Reviews. 2019 07;215(5). Available from: https://doi.org/10.1007/s11214-019-0589-7.

[22] Daniel V, Urban M, Nentvich O, Stehlikova V. VZLUSAT-1: verification of new materials and technologies for space. In: Pagano TS, editor. SPIE Proceedings. SPIE; 2016. Available from: https://doi.org/10.1117/12.2244035.

[23] Todd B, Uznanski S. Radiation Risks and Mitigation in Electronic Systems. CERN; 2015. Available from: https://doi.org/10.5170/CERN-2015-003.245.

[24] Li Z, Zhou W, Zhang X, Gao Y, Guo S. High-efficiency, flexibility and lead-free X-ray shielding multilayered polymer composites: layered structure design and shielding mechanism. Sci Rep. 2021 02;11(1):4384. Available from: https://doi.org/10.1038/s41598-021-83031-4.

[25] PSS-01-609 ESA. The Radiation Design Handbook. ESA Publications Division, ESTEC, Noordwijk, The Netherlands; 1993.

[26] NASA. CubeSat101 Basic Concepts and Processes for First-Time CubeSat Developers; NP-2017-10-2470-HQ. NASA, Headquarters/Media Fusion: Washington, DC, USA, 2017; 2017.

[27] A N. Fluctuation of Satellite Charging in the Low Earth Orbit Regime due to Interaction with Ionospheric Plasma. Journal of Physics: Conference Series. 2022 02;2214(1):012015. Available from: https://doi.org/10.1088/1742-6596/2214/1/012015.

[28] Anderson PC. Characteristics of spacecraft charging in low Earth orbit. Journal of Geophysical Research: Space Physics. 2012 07;117(A7). Available from: https://doi.org/10.1029/2011ja016875.

[29] Leach RD. Failures and anomalies attributed to spacecraft charging. vol. 1375. NASA, Marshall Space Flight Center; 1995.

[30] Tribble AC, Boyadjian B, Davis J, Haffner J, McCullough E. Contamination control engineering design guidelines for the aerospace community. In: Optical System Contamination V, and Stray Light and System Optimization. vol. 2864. International Society for Optics and Photonics. SPIE; 1996. p. 4 15. Available from: https://doi.org/10.1117/12.258298.

[31] Anwar A, Elfiky D, Hassan G, Albona M, Marchetti M. Outgassing Effect on Spacecraft Structure Materials; 2015.

[32] Bedingfield KL, Leach RD, Alexander MB. Spacecraft System Failures and Anomalies Attributed to the Natural Space Environment. NASA RP. National Aeronautics and Space Administration, Marshall Space Flight Center; 1996. Available from: https://doi.org/10.2514/6.1995-3564.

[33] Thoudam, S , Rachen, J P , van Vliet, A , Achterberg, A , Buitink, S , Falcke, H , et al. Cosmic-ray energy spectrum and composition up to the ankle: the case for a second Galactic component. A&A. 2016;595:A33. Available from: https://doi.org/10.1051/0004-6361/201628894.

[34] Anderson PC, Rich FJ, Borisov S. Mapping the South Atlantic Anomaly continuously over 27 years. Journal of Atmospheric and Solar-Terrestrial Physics. 2018 10;177:237-46. Available from: https://doi.org/10.1016/j.jastp.2018.03.015.

[35] Dachev T. Profile of the ionizing radiation exposure between the Earth surface and free space. Journal of Atmospheric and Solar-Terrestrial Physics. 2013 09;102:148–156. Available from: https://doi.org/10.1016/j.jastp.2013.05.015.

[36] IEEE Standard for Environmental Specifications for Spaceborne Computer Modules. IEEE Std 11564-1997. 1997:1-37. Available from: https://doi.org/10.1109/IEEESTD.1997.82876.

[37] Baumann R, Kruckmeyer K. Radiation handbook for electronics. Texas Instruments: Dallas, TX, USA. 2019.

[38] Stassinopoulos EG, Brucker GJ, Calvel P, Baiget A, Peyrotte C, Gaillard R. Charge generation by heavy ions in power MOSFETs, burnout space predictions and dynamic SEB sensitivity. IEEE Transactions on Nuclear Science. 1992;39(6):1704-11. Available from: https://doi.org/10.1109/23.211357.

[39] Uzel R, Özyildirim A. A study on the local shielding protection of electronic components in space radiation environment. In: 2017 8th International Conference on Recent Advances in Space Technologies (RAST); 2017. p. 295-9. Available from: https://doi.org/10.1109/RAST.2017.8003007.

[40] DeWitt JM, Benton ER, Uchihori Y, Yasuda N, Benton EV, Frank AL. Assessment of radiation shielding materials for protection of space crews using CR-39 plastic nuclear track detector. Radiation Measurements. 2009 10;44(9-10):905-8. Available from: https://doi.org/10.1016/j.radmeas.2009.10.041.

[41] Steffens M, Hepp F, Hoffgen SK, Krzikalla P, Metzger S, Pellowski F, et al. Characterization of novel lightweight radiation shielding materials for space applications. IEEE Trans Nucl Sci. 2017 08;64(8):2325-32. Available from: https://doi.org/10.1109/TNS.2017.2703312.

[42] van Lint VAJ. Mechanisms of Transient Radiation Effects. IEEE Transactions on Nuclear Science. 1963;10(5):11-9. Available from: https://doi.org/10.1109/TNS.1963.4323299.

[43] Naito M, Kodaira S, Ogawara R, Tobita K, Someya Y, Kusumoto T, et al. Investigation of shielding material properties for effective space radiation protection. Life Sciences in Space Research. 2020;26:69-76. Available from: https://doi.org/10.1016/j.lssr.2020.05.001.

[44] Naito M, Kitamura H, Koike M, Kusano H, Kusumoto T, Uchihori Y, et al. Applicability of composite materials for space radiation shielding of spacecraft. Life Sciences in Space Research. 2021;31:71-9. Available from: https://doi.org/10.1016/j.lssr.2021.08.004.

[45] Cai M, Yang T, Li H, Yang H, Han J. Experimental and Simulation Study on Shielding Performance of Developed Hydrogenous Composites. Space: Science & Technology. 2022 01;2022:1-11. Available from: https://doi.org/10.34133/2022/9754387.

[46] Bond DK, Goddard B, Singleterry RC, y León SB. Comparing the Effectiveness of Polymer and Composite Materials to Aluminum for Extended Deep Space Travel. Nuclear Technology. 2019 12;206(8):1120-39. Available from: https://doi.org/10.1080/00295450.2019.1681221.

[47] Emmanuel A, Raghavan J. Influence of structure on radiation shielding effectiveness of graphite fiber reinforced polyethylene composite. Advances in Space Research. 2015;56(7):1288-96. Available from: https://doi.org/10.1016/j.asr.2015.06.028.

[48] Cohen MM. Carbon radiation shielding for the habot mobile lunar base. In: SAE Technical Paper Series. 2004-01-2323. 400 Commonwealth Drive, Warrendale, PA, United States: SAE International; 2004. Available from: https://doi.org/10.4271/2004-01-2323.

[49] Wu Z, Ma Y, Lu J, Sun H, Liu G, Zhao H, et al. Comparison of the radiation shielding properties of wall materials for the manned spacecraft for future China space exploration missions. J Korean Phys Soc. 2019 11;75(9):666-71. Available from: https://doi.org/10.3938/jkps.75.666.

[50] Granja C, Jakubek J, Martisikova M, Kodaira S, Polansky S, Krist P, et al. Dynamic range and resolving power of the Timepix detector to heavy charged particles. J Instrum. 2018 11;13(11):C11003-3. Available from: https://doi.org/10.1088/1748-0221/13/11/C11003.

[51] Granja C, Jakubek J, Polansky S, Zach V, Krist P, Chvatil D, et al. Resolving power of pixel detector Timepix for wide-range electron, proton and ion detection. Nuclear Instruments and Methods in Physics Research Section A: Accelerators, Spectrometers, Detectors and Associated Equipment. 2018;908:60-71. Available from: https://doi.org/10.1016/j.nima.2018.08.014.

[52] Ballabriga R, Campbell M, Llopart X. Asic developments for radiation imaging applications: The medipix and timepix family. Nuclear Instruments and Methods in Physics Research Section A: Accelerators, Spectrometers, Detectors and Associated Equipment. 2018;878:10-23. Radiation Imaging Techniques and Applications. Available from: https://doi.org/10.1016/j.nima.2017.07.029.

[53] MiniPIX Datasheet. ADVACAM s.r.o.; 2022.

[54] MiniPIX TPX3 Datasheet. ADVACAM s.r.o.; 2022.

[55] ADVAPIX TPX3 Datasheet. ADVACAM s.r.o.; 2022.

[56] WidePIX 2(1)×5 - MPX3 Datasheet. ADVACAM s.r.o.; 2022.

[57] Ballabriga R, Blaj G, Campbell M, Fiederle M, Greiffenberg D, Heijne EHM, et al. Characterization of the Medipix3 pixel readout chip. Journal of Instrumentation. 2011 01;6(01):C01052-2. Available from: https://doi.org/10.1088/1748-0221/6/01/c01052.

[58] Turecek D, Jakubek J. PIXET Software package tool for control, readout and online display of pixel detectors Medipix/Timepix. ADVACAM s.r.o.; 2015.

[59] Mills JA, Hamilton AW, Gillespie DI, Ando11ic I, Michie C, Burnham K, et al. Identifying Defects in Aerospace Composite Sandwich Panels Using High-Definition Distributed Optical Fibre Sensors. Sensors. 2020;20(23). Available from: https://doi.org/10.3390/s20236746.

[60] Jakubek J, Cejnarova A, Holy T, Pospisil S, Uher J, Vykydal Z. Pixel detectors for imaging with heavy charged particles. Nuclear Instruments and Methods in Physics Research Section A: Accelerators, Spectrometers, Detectors and Associated Equipment. 2008;591(1):155-8. Radiation Imaging Detectors 2007. Available from: https://doi.org/10.1016/j.nima.2008.03.091.

[61] Vette JI. The AE-8 trapped electron model environment. vol. 91. National Space Science Data Center (NSSDC), World Data Center A for Rockets; 1991.

[62] Sawyer DM, Vette JI. AP-8 Trapped Proton Environment. NSSDC WDC-AR &S. 1991:76-06.

[63] Jiggens P, Heynderickx D, Sandberg I, Truscott P, Raukunen O, Vainio R. Updated model of the solar energetic proton environment in space. Journal of Space Weather and Space Climate. 2018;8:A31. Available from: https://doi.org/10.1051/swsc/2018010.

[64] Roque R. X-ray imaging using 100 µm thick Gas Electron Multipliers operating in Kr-CO2 mixtures [Ph.D. thesis]; 2018. Available from: https://doi.org/10.13140/RG.2.2.16794.49600.

[65] Keyes S. X-ray Computed Tomography and image-based modelling of plant, root and soil systems, for better understanding of phosphate uptake [Ph.D. thesis]; 2013.

[66] Krist P, Bila J. A mathematical model of the MT 25 microtron. Journal of Instrumentation. 2011 10;6(10):T10005. Available from: https://dx.doi.org/10.1088/1748-0221/6/10/T10005.

[67] Matlocha T. Ion source for a single particle accelerator. Acta Polytechnica CTU Proceedings. 2016 12;4:50–55. Available from: https://doi.org/10.14311/AP.2016.4.0050.

[68] Křížek F, Ferencei J, Matlocha T, Pospíšil J, Príbeli P, Raskina V, et al. Irradiation setup at the U-120M cyclotron facility. Nuclear Instruments and Methods in Physics Research Section A: Accelerators, Spectrometers, Detectors and Associated Equipment. 2018;894:87-95. Available from: https://doi.org/10.1016/j.nima.2018.03.066.

[69] Nassiri A, Chase B, Craievich P, Fabris A, Frischholz H, Jacob J, et al. History and Technology Developments of Radio Frequency (RF) Systems for Particle Accelerators. IEEE Transactions on Nuclear Science. 2015 11;63:1-1. Available from: https://doi.org/10.1109/TNS.2015.2485164.

[70] Granja C, Kudela K, Jakubek J, Krist P, Chvatil D, Stursa J, et al. Directional detection of charged particles and cosmic rays with the miniaturized radiation camera MiniPIX Timepix. Nuclear Instruments and Methods in Physics Research Section A: Accelerators, Spectrometers, Detectors and Associated Equipment. 2018;911:142-52. Available from: https://doi.org/10.1016/j.nima.2018.09.140.

[71] Granja C, Jakubek J, Soukup P, Jakubek M, Turecek D, Marek L, et al. Spectral tracking of energetic charged particles in wide field-of-view with miniaturized telescope MiniPIX Timepix3 1 × 2 stack. Journal of Instrumentation. 2022 03;17(03):C03028. Available from: https://doi.org/10.1088/1748-0221/17/03/c03028.